

**WA School of Mines: Minerals, Energy and Chemical Engineering
Faculty of Science and Engineering**

**Development of Functional Transition Metal Oxide and Sulfide
Cathodes for Aqueous Zinc-Based Rechargeable Batteries**

Yijun Zhong

0000-0003-4112-7115

**This thesis is presented for the Degree of
Doctor of Philosophy
of
Curtin University**

September 2020

Declaration

To the best of my knowledge and belief this thesis contains no material previously published by any other person except where due acknowledgment has been made. This thesis contains no material which has been accepted for the award of any other degree or diploma in any university.

Signature: _____ (Yijun Zhong)

Date: 7 September 2020

Acknowledgements

I would like to express my foremost thanks to my supervisor, Prof. Zongping Shao. He provided his full support throughout my PhD project. I learned from him how to be a researcher from every fruitful discussion with him. His authentic passion and deep insight in scientific research have conveyed to many of his students and with no doubt motivated my research and life I also owe my sincere gratitude to my associate-supervisors, Prof. Moses O. Tadé and Dr. Wei Wang. Thanks for their professional guidance, suggestions and support in the past few years.

I would also like to express my sincere thanks to Dr. Chao Su for her kind suggestions and encouragements for my research life in Australia. I am thankful to my friends and colleagues in the research group, Mr. Xiaomin Xu, Dr. Yu Liu, Ms. Pengyun Liu, Ms. Yangli Pan, Dr. Paulo Sérgio Barros Julião, Dr. Huangang Shi, Dr. Muhammad Azhar, Mr. Yasir Arafat, Dr. Li Yang, Dr. Jiafeng Cao, Dr. Yong Jiao, Dr. Wenting An, Mr. Jijin Mai, Dr. Hong Chang and Dr. Jiahuan Xu, for their support and the great time we had together. I would like to give my thanks to my previous group members, Dr. Yinlong Zhu, Mr. Qian Lu, Dr. Jie Yu, Dr. Yufei Song, Dr. Xiang Deng, Dr. Shiyong Chu, Mr. Jie Dai, Mr. Daqin Guan, Dr. Jie Miao, Mr. Liang Zhu, Dr. Yanping Zhu, Dr. Gao Chen, Dr. Yuan Zhang and Dr. Juan He, for their great help even we are now chasing our different careers all around the world. I also wish to give my gratitude to the technician team, Ms. Roshanak Doroushi, Mr. Xiao Hua, Ms. Jennifer Wang, Ms. Ann Carroll and Mr. Andrew Chan for their daily technical support on the research. I would like to thank Prof. Martin Saunders, Dr. Jean-Pierre Veder, Dr. Alexandra Suvorova, Ms. Elaine Miller, Dr. Matthew Rowles and Ms. Veronica Avery for their training and generous support on material characterizations.

My sincere gratitude also goes to Prof. San Ping Jiang, Prof. Wei Zhou, Prof. Meng Ni, Dr. Zhiwei Hu, Dr. Ran Ran, Prof. Shaobin Wang, Prof. Shaomin Liu, Prof. Rui Cai, Dr. Guangming Yang, Dr. Kaiming Liao and Dr. Xiaoguang Duan, for all the kind suggestions and great help for the benefits of my research and career.

At last, I would like to express my deepest love to my family for their endless love and support throughout my life. Their understanding and encouragements always keep my spirit up whenever I face a great challenge and have a depressing time.

Abstract

The utilization of renewable resources (e.g., solar, wind and hydro resources) to generate electricity is a promising pathway for sustainable development. To buffer the fluctuated electric power supply and uneven power utilization from renewable resources, advanced electrochemical energy storage technologies are very necessary. Aqueous zinc (Zn)-based batteries have recently attracted increasing attention owing to the abundant Zn resource and the high rechargeability of Zn. Transition metal oxides and sulfides are promising multi-functional cathode materials for a variety of Zn-based batteries. They not only show good capabilities of cation redox for Zn-ion batteries with neutral (weakly acidic) electrolytes and Zn-transition metal compound batteries with alkaline electrolytes, but also present excellent catalytic activities for oxygen redox as the catalysts for Zn-air batteries with alkaline electrolytes.

In the PhD research project, a series of new cathode materials (e.g., cobalt-modified δ -MnO₂ nanosheets, Ni-Co-S clusters decorated MnS and La_{1.6}Sr_{0.4}MnCoO₆ perovskite-type cubic nanocrystallites) and a new function-separated MnS-Ni_xCo_{1-x}S₂ electrode are developed, demonstrating improved performance and stability of Zn-based batteries. Such improvements are based on the rational designs (e.g., function-oriented composition designs, nanosizing, wettability tuning) of the material and electrode for promoting kinetics of redox reactions and facilitating electronic and mass transfer within the cathode. Multiple material characterization techniques combined with electrochemical analysis are utilized to investigate material properties and provide a better understanding of mechanisms behind the improved results. The new materials and the design strategies proposed in this thesis provide opportunities for the future development of functional transition metal compounds for Zn-based batteries and other electrochemical energy storage and conversion devices.

Publications by the Author

Published refereed papers

1. **Yijun Zhong**, Xiaomin Xu, Pengyun Liu, Ran Ran, San Ping Jiang, Hongwei Wu, Zongping Shao, A function-separated design of electrode for realizing high-performance hybrid zinc battery. *Adv. Energy Mater.* **2020**, 10, 2002992. doi:10.1002/aenm.202002992
2. **Yijun Zhong**, Xiaomin Xu, Jean-Pierre Veder, Zongping Shao, Self-recovery chemistry and cobalt-catalyzed electrochemical deposition of cathode for boosting performance of aqueous zinc-ion batteries. *iScience* **2020**, 23, 100943. doi:10.1016/j.isci.2020.100943
3. **Yijun Zhong**, Jie Dai, Xiaomin Xu, Chao Su, Zongping Shao, Facilitating oxygen redox on manganese oxide nanosheets by tuning active species and oxygen defects for zinc-air batteries. *ChemElectroChem* **2020**, 7, 4949-4955. doi:10.1002/celec.202001419
4. **Yijun Zhong**, Xiaomin Xu, Wei Wang, Zongping Shao, Recent advances in metal-organic framework derivatives as oxygen catalysts for zinc-air batteries. *Batteries Supercaps* **2019**, 2, 272-289. doi:10.1002/batt.201800093
5. **Yijun Zhong**, Xiaomin Xu, Yu Liu, Wei Wang, Zongping Shao, Recent progress in metal-organic frameworks for lithium-sulfur batteries. *Polyhedron* **2018**, 155, 464-484. doi:10.1016/j.poly.2018.08.067
6. Jie Yu, Ran Ran, **Yijun Zhong**, Wei Zhou, Meng Ni, Zongping Shao, Advances in porous perovskites: Synthesis and electrocatalytic performance in fuel cells and metal-air batteries. *Energy Environ. Mater.* **2020**, 3, 121-145. doi:10.1002/eem2.12064
7. Yasir Arafat, Muhammad Rizwan Azhar, **Yijun Zhong**, Xiaomin Xu, Moses O. Tadé, Zongping Shao, A porous nano-micro-composite as a high-performance bi-functional air electrode with remarkable stability for rechargeable zinc-air batteries, *Nano-Micro Lett.* **2020**, 12, 130. doi:10.1007/s40820-020-00468-4
8. Shiyong Chu, **Yijun Zhong**, Kaiming Liao, Zongping Shao, Layered Co/Ni-free oxides for sodium-ion battery cathode materials. *Curr. Opin. Green Sustainable Chem.* **2019**, 17, 29-34. doi:10.1016/j.cogsc.2019.01.006

9. Xiaomin Xu, **Yijun Zhong**, Zongping Shao, Double perovskites in catalysis, electrocatalysis, and photo(electro)catalysis. *Trends in Chemistry* **2019**, 1, 410-424. doi:10.1016/j.trechm.2019.05.006
10. Jie Yu, **Yijun Zhong**, Xinhao Wu, Jaka Sunarso, Meng Ni, Wei Zhou, Zongping Shao, Bifunctionality from synergy: CoP nanoparticles embedded in amorphous CoO_x nanoplates with heterostructures for highly efficient water electrolysis. *Adv. Sci.* **2018**, 5, 1800514. doi:10.1002/advs.201800514
11. Yangli Pan, Xiaomin Xu, **Yijun Zhong**, Lei Ge, Yubo Chen, Jean-Pierre Marcel Veder, Daqin Guan, Ryan O'Hayre, Mengran Li, Guoxiong Wang, Hao Wang, Wei Zhou, Zongping Shao, Direct evidence of boosted oxygen evolution over perovskite by enhanced lattice oxygen participation, *Nat. Commun.* **2020**, 11, 2002. doi:10.1038/s41467-020-15873-x
12. Xiaomin Xu, Yangli Pan, **Yijun Zhong**, Ran Ran, Zongping Shao, Ruddlesden–Popper perovskites in electrocatalysis, *Mater. Horiz.* **2020**, 7, 2519-2565. doi:10.1039/D0MH00477D
13. Xiaomin Xu, Yangli Pan, **Yijun Zhong**, Lei Ge, San Ping Jiang, Zongping Shao, From scheelite BaMoO₄ to perovskite BaMoO₃: Enhanced electrocatalysis toward the hydrogen evolution in alkaline media, *Compos. Part B-Eng.* **2020**, 198, 108214. doi:10.1016/j.compositesb.2020.108214
14. Yu Liu, Zhenbin Wang, **Yijun Zhong**, Xiaomin Xu, Jean-Pierre Marcel Veder, Matthew R. Rowles, Martin Saunders, Ran Ran, Zongping Shao, Activation-free supercapacitor electrode based on surface-modified Sr₂CoMo_{0.1-x}Ni_xO_{6-δ} perovskite, *Chem. Eng. J.* **2020**, 390, 124645. doi:10.1016/j.cej.2020.124645
15. Yu Liu, Shuai He, **Yijun Zhong**, Xiaomin Xu, Zongping Shao, Rational design of NiCo₂O₄/g-C₃N₄ composite as practical anode of lithium-ion batteries with outstanding electrochemical performance from multiple aspects. *J. Alloy Compd.* **2019**, 805, 522-530. doi:10.1016/j.jallcom.2019.07.044
16. Jie Dai, Yinlong Zhu, **Yijun Zhong**, Jie Miao, Bowen Lin, Wei Zhou, Zongping Shao, Enabling high and stable electrocatalytic activity of iron-based perovskite oxides for water splitting by combined bulk doping and morphology designing. *Adv. Mater. Interfaces* **2019**, 6, 1801317. doi:10.1002/admi.201801317
17. Xiaohong Zou, Qian Lu, **Yijun Zhong**, Kaiming Liao, Wei Zhou, Zongping Shao, Flexible, Flame-resistant, and dendrite-impermeable gel-polymer

- electrolyte for Li–O₂/air batteries workable under hurdle conditions. *Small* **2018**, 14, 1801798. doi:10.1002/sml.201801798
18. Yanping Zhu, Gao Chen, **Yijun Zhong**, Yubo Chen, Nana Ma, Wei Zhou, Zongping Shao, A surface-modified antiperovskite as an electrocatalyst for water oxidation. *Nat. Commun.* **2018**, 9, 2326. doi:10.1038/s41467-018-04682-y
 19. Xiang Deng, Wenxiang Shi, **Yijun Zhong**, Wei Zhou, Meilin Liu, Zongping Shao, Facile strategy to low-cost synthesis of hierarchically porous, active carbon of high graphitization for energy storage. *ACS Appl. Mater. Interfaces* **2018**, 10, 21573-21581. doi:10.1021/acsami.8b04733
 20. Yanping Zhu, Gao Chen, **Yijun Zhong**, Wei Zhou, Zongping Shao, Rationally designed hierarchically structured tungsten nitride and nitrogen-rich graphene-like carbon nanocomposite as efficient hydrogen evolution electrocatalyst. *Adv. Sci.* **2018**, 5, 1700603. doi:10.1002/advs.201700603
 21. Jie Yu, Xinhao Wu, **Yijun Zhong**, Guangming Yang, Meng Ni, Wei Zhou, Zongping Shao, Multifold nanostructuring and atomic-scale modulation of cobalt phosphide to significantly boost hydrogen production. *Chem. Eur. J.* **2018**, 24, 13800-13806. doi:10.1002/chem.201802667
 22. Yinlong Zhu, Jie Dai, Wei Zhou, **Yijun Zhong**, Huanting Wang, Zongping Shao, Synergistically enhanced hydrogen evolution electrocatalysis by in situ exsolution of metallic nanoparticles on perovskites. *J. Mater. Chem. A* **2018**, 6, 13582-13587. doi:10.1039/C8TA02347F

Manuscripts in preparation

1. **Yijun Zhong**, Zongping Shao, Promoting bifunctional oxygen catalyst activity of perovskite-type cubic nanocrystallites for aqueous and quasi-solid-state rechargeable zinc-air batteries, (To be submitted).

Content

Declaration	i
Acknowledgements	ii
Abstract	iii
Publications by the Author	iv
Content	vii
Chapter 1 Introduction	1
1.1 Background of Zn-based batteries	1
1.2 Research objectives	2
1.3 Thesis organization	3
References	5
Chapter 2 Literature review	7
2.1 Introduction	7
2.2 Concept and fundamentals of Zn-based batteries	9
2.3 Zn-ion batteries with neutral or mild acidic aqueous electrolyte	12
2.3.1 Fundamentals of Zn-ion battery	12
2.3.2 Cathode materials for Zn-ion batteries	13
2.4 Alkaline Zn-MX batteries	15
2.4.1 Fundamentals of alkaline Zn-MX batteries	15
2.4.2 Cathode materials for alkaline Zn-MX batteries	16
2.5 Zn-air batteries	17
2.5.1 Fundamentals of Zn-air batteries	17
2.5.2 Cathode materials for Zn-air batteries	19
2.5.3 Optimizations of the cathodes	21
2.6 Hybrid Zn batteries	23
2.6.1 Fundamentals of hybrid Zn batteries	23
2.6.2 Cathode materials for hybrid Zn batteries	24
References	25

Chapter 3 Self-recovery chemistry on cobalt-modified δ-MnO₂ nanosheets as high-performance and durable aqueous zinc-ion battery cathodes §	46
Abstract	46
3.1 Introduction	47
3.2 Experimental sections	49
3.3 Results and discussions	51
3.3.1 Self-recovery chemistry in MnO ₂ electrodes of Zn-ion batteries	51
3.3.2 The catalytic effect of cobalt components in the deposition process of active Mn compound	58
3.3.3 The dynamic movement of cobalt components for self-recovery of the Mn-based cathode	64
3.3.4 Cycling performance and more practical battery configurations	69
3.4 Conclusion	70
References	71
Chapter 4 Cobalt-modified MnO₂ as an oxygen catalyst for zinc-air battery cathode §	75
Abstract	75
4.1 Introduction	76
4.2 Experimental Sections	77
4.3 Results and Discussions	79
4.3.1 Characterization of modified MnO ₂ samples	79
4.3.2 Bifunctional catalytic activity for ORR and OER	81
4.3.3 Performance of the Zn-air batteries	84
4.4 Conclusion	88
References	89
Chapter 5 A function-separated MnS-Ni_xCo_{1-x}S₂ electrode for realizing high-performance hybrid zinc batteries §	93
Abstract	93
5.1 Introduction	94
5.2 Experimental Sections	95
5.3 Results and Discussions	98
5.3.1 Preparation and characterization of the function-separated electrode	98
5.3.2 Bifunctional catalytic activity for ORR-OER and performance of the Zn-air battery function	103
5.3.3 Performance of the Zn-MX battery function and optimization of the function-separated electrode	107

5.3.4 Important role of the asymmetric wettability design in the function-separated electrode.....	111
5.4 Conclusion.....	112
References	113
Chapter 6 Promoting bifunctional oxygen catalyst activity of perovskite-type cubic nanocrystallites for rechargeable zinc-air batteries	119
Abstract	119
6.1 Introduction	120
6.2 Experimental sections.....	121
6.3 Results and discussions	124
6.3.1 Synthesis and characterization.....	124
6.3.2 Bifunctional catalytic activity for ORR and OER	127
6.3.3 Performance of the Zn-air batteries	130
6.3.4 Integration of small amount of Pt/C for optimization of oxygen catalysis	134
6.4 Conclusion.....	136
References	136
Chapter 7 Conclusion and recommendations	142
7.1 Conclusion.....	142
7.2 Recommendations	143
Appendix 1 Permission of reproduction from the copyright owner	146
Appendix 2 Co-author attribution statement.....	152

Chapter 1 Introduction

1.1 Background of Zn-based batteries

Conventional electricity generation that relies on the combustion of unrenewable fossil fuels poses a low efficiency of converting energy from the fuels to electricity.^{1,2} Its negative effects on the environment, e.g., greenhouse gas emissions, have also raised attentions to seek more sustainable pathways for power generation.^{3,4} Renewable power sources, e.g., solar, wind, tidal and hydroelectric, will become the fastest-growing energy sources with international projection to 2050.⁵ However, the unstable supply of these renewable resources may not match the on-time demand, which may arise great challenges for the power grid.^{6,7} Advanced large-scale electrochemical energy storage systems are promising techniques that can buffer the fluctuated electricity supply and the electricity utilization in a high-efficiency, low-energy-loss way. Among the different energy storage techniques, rechargeable lithium-ion (Li-ion) batteries which have decent energy density and high energy efficiency have become the major electricity storage devices, especially, for portable applications and electrical vehicles.⁸ However, due to the increasing price of Li and the safety issues due to the flammable organic electrolytes,^{9,10} Li-ion batteries may not be the best candidate for the large-scale electricity storage.¹¹

Aqueous Zn-based rechargeable batteries represent a promising alternative that can meet the needs for large-scale electricity storage, owing to the advantages including low cost and abundance of Zn resources and high safety with nonflammable aqueous electrolytes.¹¹ Different types of Zn-based rechargeable batteries have been developed, including Zn-ion batteries, Zn-transition metal compound batteries, Zn-air batteries, hybrid Zn-battery and Zn-based flow batteries.¹² Despite the above benefits, most Zn-based batteries still face many challenges, e.g., lower output voltages and relatively inferior cycling stability as compared to Li-ion batteries.¹³ In Zn-based batteries, multiple types of redox reactions (e.g., reduction and oxidation of transition metal compounds, oxygen reduction reaction (ORR), oxygen evolution reaction (ORR)) can take place or be facilitated on the transition metal compounds.^{14,15} Developing low-cost, eco-friendly functional transition metal-containing compounds (e.g, oxides, sulphides, nitrides, phosphides) and composite materials for Zn-based batteries is important for lowering the overpotentials, improving energy density, increasing

energy efficiency and enhancing the cycling stability. The research is expected to develop new materials, methods and strategies for improving the performance of the Zn-based batteries and provide better understandings behind these improvements, which may facilitate the practical applications of the Zn-based rechargeable batteries.

1.2 Research objectives

The aim of this PhD research project is to develop new functional transition metal oxides and sulfides for advanced aqueous rechargeable Zn-based batteries. In different chapters, the integration of Mn-based compound and Co-/Ni-based compound to establish a bifunctional or multifunctional material are investigated to take the advantage of their corresponding capability for Faradaic cation redox and catalysis for oxygen redox (**Figure 1.1**), which promotes the performance of Zn-based battery. Multiple material characterizations, electrochemical testing and evaluation techniques are utilized to support the proposed ideas and analysis. Objectives of this PhD project include:

1. To summarize the advances of cathode materials for different types of Zn-based batteries in recent years.
2. To propose a new self-recovery strategy for alleviating the capacity deterioration during cycling of Mn-based cathode in aqueous neutral/weak acidic Zn-ion batteries and developing a new δ -MnO₂ material based on this strategy.
3. To investigate the influence of modification of δ -MnO₂ with different transition metal elements on the oxygen defects of the δ -MnO₂ and how these modifications affect the catalytic activity for ORR and OER and the performance of aqueous alkaline Zn-air batteries.
4. To develop a new electrode structure that can facilitate the mass (gas and ionic) transfers for a high-performance hybrid Zn battery, and verify this design with a transition metal sulfide combination.
5. To design a perovskite-type oxide material that integrated Mn and Co cations with an atomic ordered arrangement, which demonstrates improved catalysis for ORR-OER and performance of the Zn-air batteries.

1.3 Thesis organization

The main contents of this thesis are allocated to 7 chapters, the relationship between each chapter is present in **Figure 1.1**. Start with an Introduction (**Chapter 1**) that briefly provide the background of the Zn-based rechargeable battery and objective of this research project, the thesis gives a Literature Review (**Chapter 2**) on the development of Zn-based battery and cathode materials for the battery. **Chapter 3-6** are specific research topics and results. The thesis is ended with conclusion and perspectives in **Chapter 7**.

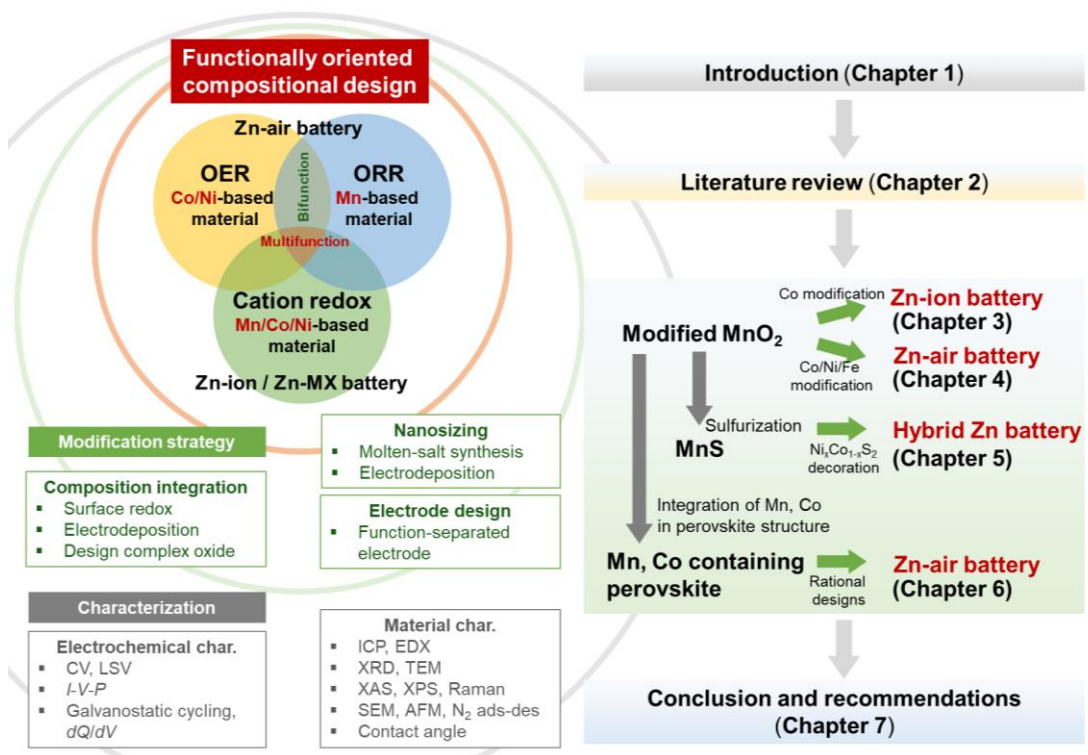


Figure 1.1 Objectives and organization of this thesis. Note: MX = transition metal compound.

Chapter 1 Introduction

Briefly introduce the background of the development of Zn-based rechargeable batteries, followed by demonstrating the motivation, aim objectives and organization of this PhD thesis.

Chapter 2 Literature review

This chapter provides an essential and timely review on the concept, catalogue, fundamentals, and progress of the research of some representative types of Zn-based batteries.

Chapter 3 Self-recovery chemistry on cobalt-modified δ -MnO₂ nanosheets as high-performance and durable aqueous zinc-ion battery cathodes

This chapter reveals the importance of deposition behavior of the Mn compound on performance and stability of neutral/weak acidic aqueous rechargeable Zn-ion batteries. This chapter also proposes a cobalt-catalyzed recovery strategy for improving cycling stability.

Chapter 4 Cobalt-modified MnO₂ as an oxygen catalyst for zinc-air battery cathode

Based on the modification strategy from **Chapter 3**, this chapter extends the modification cation to some of the reactive elements (i.e. Co, Ni and Fe) for facilitating the ORR and OER in alkaline electrolyte, which aims at lowering the overpotential and promoting the round-trip efficiency of aqueous rechargeable Zn-air batteries.

Chapter 5 A function-separated MnS-Ni_xCo_{1-x}S₂ electrode for realizing high-performance hybrid zinc batteries

In this chapter, a greater amount of Co and Ni species (NiCo-LDH) is introduced in the MnO₂ nanosheets (proposed in **Chapter 3**) using an electrodeposition method to construct a cathode for hybrid Zn-batteries to achieve a higher power density and energy efficiency than conventional Zn-air batteries. Sulfurization of the MnO₂-NiCo-LDH is conducted to promote the electronic conductivity. A function-separated electrode design is proposed. The function-separated electrode demonstrates significant benefits for enhancing the gas and ionic transfers in the air electrode and shows excellent high-rate performance and cycling stability.

Chapter 6 Promoting bifunctional oxygen catalyst activity of perovskite-type cubic nanocrystallites for rechargeable zinc-air batteries

Different from the cation hybridizing strategies studied in **Chapter 3-5**, in this chapter, Mn cation and Co cation were integrated into a complex oxide with a perovskite-type structure. The $\text{La}_{1.6}\text{Sr}_{0.4}\text{MnCoO}_6$ nanocrystallites with ultra-small cubic morphology and high specific surface areas were rationally designed as bifunctional catalysts for Zn-air batteries.

Chapter 7 Conclusion and recommendations

The main conclusion of each chapter and the overall conclusion of this PhD project are summarized. Perspectives of future work are also provided.

References

1. Cho J, Jeong S, Kim Y. Commercial and research battery technologies for electrical energy storage applications. *Prog Energy Combust Sci.* 2015;48:84-101. doi:10.1016/j.pecs.2015.01.002
2. Gür TM. Critical review of carbon conversion in "carbon fuel cells". *Chem Rev.* 2013;113(8):6179-206. doi:10.1021/cr400072b
3. D'Alessandro DM, Smit B, Long JR. Carbon dioxide capture: Prospects for new materials. *Angew Chem Int Ed.* 2010;49(35):6058-82. doi:10.1002/anie.201000431
4. Winter M, Brodd RJ. What are batteries, fuel cells, and supercapacitors? *Chem Rev.* 2004;104(10):4245-70. doi:10.1021/cr020730k
5. United States Department of Energy. International Energy Outlook 2019 with projections to 2050. Washington (United States): United States Department of Energy; 2019 [cited 2020 August 29]. Report No.: #IEO2019. Available from <https://www.eia.gov/outlooks/ieo/>
6. Yang Z, Zhang J, Kintner-Meyer MCW, Lu X, Choi D, Lemmon JP, et al. Electrochemical Energy Storage for Green Grid. *Chem Rev.* 2011;111(5):3577-613. doi:10.1021/cr100290v

7. Gür TM. Review of electrical energy storage technologies, materials and systems: Challenges and prospects for large-scale grid storage. *Energy Environ Sci.* 2018;11(10):2696-767. doi:10.1039/C8EE01419A
8. Tarascon J-M, Armand M. Issues and challenges facing rechargeable lithium batteries. *Nature.* 2001;414(6861):359-67. doi:10.1038/35104644
9. Luo J-Y, Cui W-J, He P, Xia Y-Y. Raising the cycling stability of aqueous lithium-ion batteries by eliminating oxygen in the electrolyte. *Nat Chem.* 2010;2(9):760-5. doi:10.1038/nchem.763
10. Zeng X, Hao J, Wang Z, Mao J, Guo Z. Recent progress and perspectives on aqueous Zn-based rechargeable batteries with mild aqueous electrolytes. *Energy Storage Mater.* 2019;20:410-37. doi:10.1016/j.ensm.2019.04.022
11. Kim H, Jeong G, Kim Y-U, Kim J-H, Park C-M, Sohn H-J. Metallic anodes for next generation secondary batteries. *Chem Soc Rev.* 2013;42(23):9011-34. doi:10.1039/C3CS60177C
12. Deng Y-P, Liang R, Jiang G, Jiang Y, Yu A, Chen Z. The current state of aqueous Zn-based rechargeable batteries. *Acs Energy Lett.* 2020;5(5):1665-75. doi:10.1021/acseenergylett.0c00502
13. Li H, Ma L, Han C, Wang Z, Liu Z, Tang Z, et al. Advanced rechargeable zinc-based batteries: Recent progress and future perspectives. *Nano Energy.* 2019;62:550-87. doi:10.1016/j.nanoen.2019.05.059
14. Wang H-F, Xu Q. Materials design for rechargeable metal-air batteries. *Matter.* 2019;1(3):565-95. doi:10.1016/j.matt.2019.05.008
15. Shang W, Yu W, Liu Y, Li R, Dai Y, Cheng C, et al. Rechargeable alkaline zinc batteries: Progress and challenges. *Energy Storage Mater.* 2020;31:44-57. doi:10.1016/j.ensm.2020.05.028

Every reasonable effort has been made to acknowledge the owners of copyright material. I would be pleased to hear from any copyright owner who has been omitted or incorrectly acknowledged.

Chapter 2 Literature review

2.1 Introduction

Significant increase in electricity consumption and generation continues to draw attention worldwide. Conventional electricity generation that relies on the combustion of unrenovable fossil fuels poses a low efficiency of converting energy from the chemical energy in the fuels to electricity.^{1,2} Its negative effects on the environment, e.g., greenhouse gas emissions, has also attracted attentions for seeking alternative electricity via more sustainable pathways.^{3,4} Renewable power source, e.g., solar, wind, tidal and hydroelectric, would become the fastest-growing energy sources with an international projection to 2050.⁵ However, the supply of these renewable energies is fluctuated along with time, seasons and other natural circumstances. At the same time, electricity demand may also vary. The mismatch of the power generation and consumption from renewable resources poses great challenges for the power grid.^{6,7} As illustrated in **Figure 2.1a**, electricity power storage systems that can buffer this fluctuation and mismatch between the electricity supply and consumption are required. Advanced large-scale electrochemical energy storage systems are promising techniques which have advantages including high efficiency and low energy loss.

Among the different energy storage techniques, rechargeable lithium-ion (Li-ion) battery is a commercially mature technique which has decent energy density and high energy efficiency.⁸ Rechargeable Li-ion battery has already become the most practical electricity storage component, especially, for a variety of portable applications, electric vehicles and electric drones.^{9,10} However, due to the increasing price of Li and the concerns of the safety issues due to the flammable organic electrolytes,¹¹ Li-ion battery may not be the best candidate for large-scale electricity storage (**Figure 2.1b**).¹² Derived from the Li-ion battery, other alkaline metal ions battery (e.g., sodium-ion battery and potassium-ion battery) have been receiving interests due to the natural abundance and low cost of the sodium (Na) and potassium (K) compared to Li.^{13,14} However, due to the worse kinetics of the reactions involved in the batteries and the inferior cycling stability than state-of-the-art Li-ion batteries, Na-ion and K-ion batteries with an organic electrolyte may still have a long way to practical application.

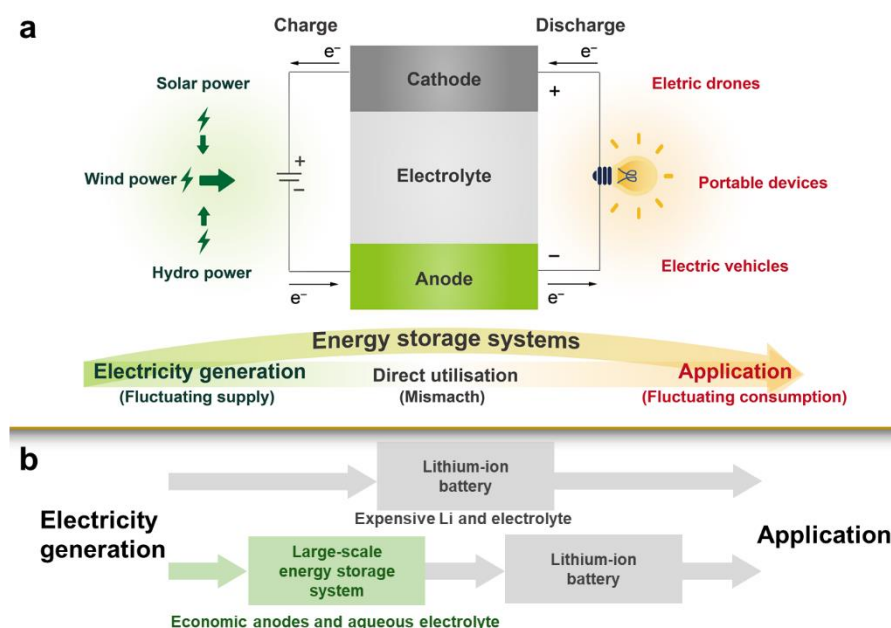


Figure 2.1 Illustration of a) the important role of energy storage systems for buffering the mismatching electricity generation and consumption and b) potential applications of Zn-based batteries as a large-scale energy storage system.

Batteries based on aqueous electrolytes demonstrate better safety due to the intrinsic nonflammability, and usually higher ionic conductivity of the aqueous electrolytes compared to organic electrolytes.^{15,16} Compared to metal compounds, metallic materials can provide much higher energy density. Therefore, utilizing metallic anodes in aqueous batteries is more favorable. Metallic Li, Na and K are highly active in aqueous electrolyte due to their low reduction potentials, thereby may not be suitable for direct use as the anode in the electrolyte.¹⁶ Metallic Zn poses many advantages including decent energy density (1218 W h kg^{-1}), abundant resources, low cost and higher reduction potential compared to other metal anodes (e.g., Zn, Mg, Al, Fe).^{6,17-19} The aqueous battery based on a metallic Zn anode is called aqueous Zn-based battery.

Some of the representative Zn-based batteries have already achieved commercialization, e.g., primary Zn-MnO₂ alkaline batteries and primary Zn-air batteries.^{20,21} In recent decades, intensive efforts have been made to improve the rechargeability of the Zn-based battery, including Zn-ion batteries, Zn-transition metal compound batteries, Zn-air batteries, hybrid Zn-battery and Zn-based flow batteries.^{17, 21-25} Despite the above advantages for aqueous electrolyte and Zn anode,

most Zn-based batteries still face many challenges, e.g., lower output voltages than Li-ion batteries and relatively inferior cycling stability.^{26, 27} As demonstrated in **Figure 2.1b**, Zn-based batteries could be a promising supplementary large-scale energy storage devices between the electricity generation units and the end-user high-performance batteries, which serves as a buffer for a more reliable power grid or as a main power storage station in some remote and isolated places.

In the development of different types of Zn-based batteries, functional transition metal compounds (e.g., oxides, sulfides, nitrides, phosphides) play important roles.^{28, 29} Multiple types of redox reactions (e.g., reduction and oxidation of metal cations, oxygen reduction reaction (ORR), oxygen evolution reaction (OER)) can take place or be facilitated on the transition metal compounds.³⁰ Developing low-cost, eco-friendly functional transition metal compounds and composite materials for Zn-based batteries are important for lowering the overpotentials, improving energy density, enlarging energy efficiency and enhancing the cycling stability, which will facilitate the practical applications of the Zn-based rechargeable batteries.³¹

In this chapter, the fundamentals of some representative types of Zn-based batteries will be briefly described. The recent development of functional transition metal compounds for Zn-based batteries will be summarized.

2.2 Concept and fundamentals of Zn-based batteries

Aqueous Zn-based battery is a battery category based on utilizing Zn (usually metallic Zn) as the anode. A typical Zn-based battery consists of a cathode (positive electrode), a Zn anode (negative electrode), an electrolyte and a separator between the cathode and anode (**Figure 2.2a**).

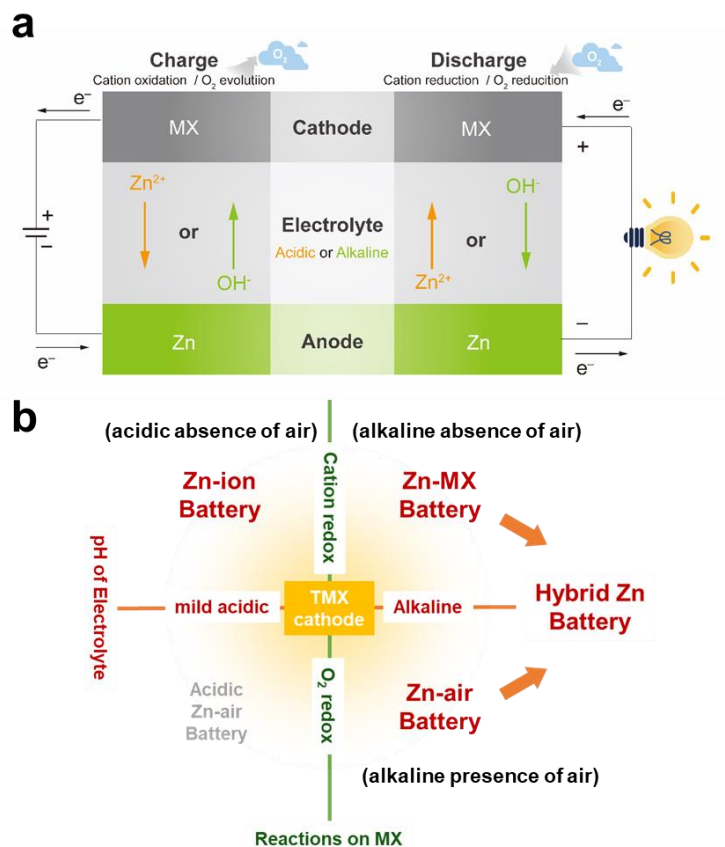


Figure 2.2 a) Role of transition metal compounds (MX) in Zn-based batteries and two different major redox couples on the MX cathodes of rechargeable Zn-based batteries, b) Relationship of different types of Zn-based batteries with neutral/mild acidic or alkaline aqueous electrolyte.

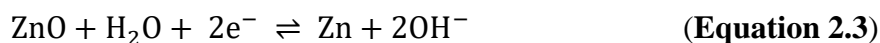
The pH value of the electrolyte and the redox reactions involved in the cathode are two important parameters to differentiate the types of Zn-based batteries.³² The pH value of the electrolyte will have a great impact on the redox process involved in the Zn anode and the charge carrier in the electrolyte. As presented in **Figure 2.2a**, in a neutral/acidic electrolyte, Zn^{2+} acts as the charge carrier. The redox of Zn anode follows the reaction:³³



While in an alkaline electrolyte, OH^{-} serves as the charge carrier. The redox of Zn anode follows:^{23,34}



or



The different pH values and different charge carriers will also influence the reactions involved on the cathode. Two main types of redox couples are presented: 1) the cation redox within the transition metal compounds and 2) the oxygen redox on the surface of the transition metal compounds (**Figure 2.2a**).

It is noted that many other types of redox reactions could also be promising options, e.g., $I^{3-} + 2e^{-} \rightleftharpoons 3I^{-}$ on a Zn-I flow battery cathode.³⁵ This review focuses on the above two main redox couples, and will not extend the summary of recent development of Zn-based flow batteries.³⁶

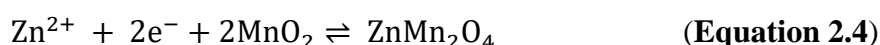
The most studied Zn-based battery can be specifically categorized base on the combination of the above two parameters, as presented in **Figure 2.2b**. For example, a Zn-ion battery performs based on a neutral/mild acidic electrolyte in the absence of air, where cation redox happens between the transition metal compounds (e.g., MnO_2 , V_2O_5) and Zn^{2+}/H^{+} .³⁷ A Zn-transition metal compound (Zn-MX) battery runs based on an alkaline electrolyte without air, where cation redox occurs between the transition metal compounds (e.g., Co_3O_4 , $NiOOH$) and OH^{-} .²³ A Zn-air battery performs based on the exposure of air with an alkaline electrolyte, where oxygen redox takes place on the surface of the transition metal compounds.^{38,39}

Zn-based batteries are one of the hot topics in research for electrochemical energy storage. Despite the successful commercial application of primary Zn-based batteries, the practical utility of aqueous rechargeable Zn-based batteries is still a long way to go. There is no simple answer justifying which type of Zn-based battery is better than the others. For example, Zn-air battery usually has a higher energy density compared to the alkaline Zn-MX battery. However, alkaline Zn-MX battery may provide a higher voltage output and higher power density.²⁴ For another example, alkaline electrolyte usually provides a higher ionic conductivity than acidic neutral/mild acidic electrolyte.³⁰ However, at the same time, corrosion and dendrite formation of the Zn anode are more severe in the alkaline electrolyte, resulting in poor cycling stability.³³ In the following sections, the challenges and recent development of each type of Zn-based batteries will be summarized.

2.3 Zn-ion batteries with neutral or mild acidic aqueous electrolyte

2.3.1 Fundamentals of Zn-ion battery

The concept of the “Zn-ion batteries” and its fundamental working mechanism was first proposed in 2011 by Xu et.al.⁴⁰ They constructed the battery with an α -MnO₂ cathode. Based on this concept, Zn²⁺ is the charge carrier in the mild acidic electrolyte. The reaction on the Zn anode is the same as **Equation 2.1**. The redox of the α -MnO₂ cathode follows the reaction:



As presented in **Figure 2.3**, in the discharging process, the Zn²⁺ ions move toward the cathode and react with the active material (MnO₂). The cation (Mn⁴⁺) in the transition metal compound (MnO₂) is reduced (Mn³⁺) in the discharge process. In the reverse process, the cation is re-oxidized and Zn²⁺ ions move toward the anode. This first reported Zn-ion battery presented a similar open circuit voltage (1.5 V), a higher capacity (210 mAh g⁻¹), and much-improved cycling stability to those of a primary alkaline Zn-MnO₂ battery.⁴⁰ After this report, the Zn-ion battery has received intensive interests.

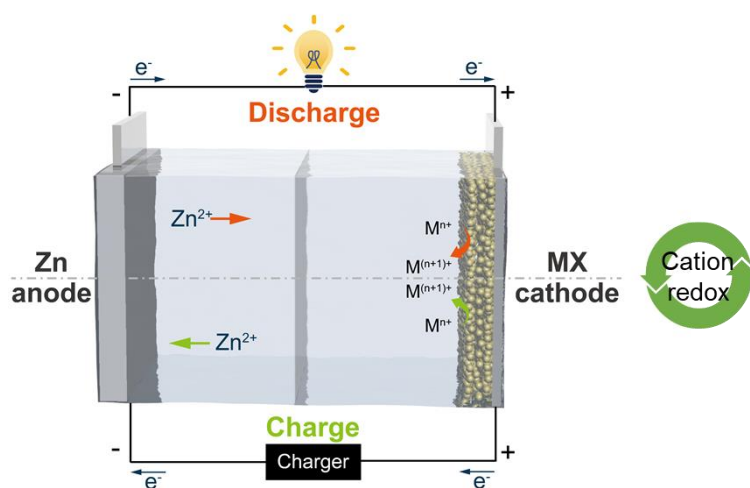


Figure 2.3 Fundamental working mechanism of a Zn-ion battery with a neutral/mild acidic aqueous electrolyte.

2.3.2 Cathode materials for Zn-ion batteries

Cathode materials demonstrate the most vital impact on the performance of the Zn-ion battery, although the investigations in the composition of the electrolyte and the modification of Zn anode have also promoted the advances in this research field.⁴¹ During the recent 10 years, efforts are mainly made on the development and optimization of the cathode materials (e.g., Mn-based oxides^{29,42-47}, V-based oxides⁴⁸⁻⁵¹, Mo/W-based oxide^{50,52}, transition metal sulfides⁵³⁻⁵⁵).

Most of the reactions involved in the MX cathode of Zn-ion battery are based on the cation redox (e.g., $\text{Mn}^{4+}/\text{Mn}^{3+}$, $\text{V}^{4+}/\text{V}^{3+}$).^{56,57} However, such cation redox is presented as different reaction mechanisms. They can be categorized into two different types: intercalation-deintercalation and conversion reactions. Usually, transition metal compounds with a wide interlayer distance or a wide tunnel-like phase structure (e.g., $\gamma\text{-MnO}_2$ ⁵⁸, $\text{Na}_x\text{V}_2\text{O}_5$ ⁵⁹) exhibit reversible Zn^{2+} intercalation-deintercalation during the recharging cycling. Also, co-intercalation of H^+ along with the Zn^{2+} is also observed for some cathode materials.⁶⁰ For some other materials, phase conversions between oxide and hydroxides (or oxyhydroxides) could occur during the redox of transition metal compounds.²⁹ Note that the intercalation-deintercalation and conversion reactions may also coexist in a cathode.⁴⁶

The most studied category is Mn-based oxide materials, which are usually derived from the studies on the conventional alkaline Zn-MnO₂ batteries. Mn-based oxides present multiple advantages including satisfactory theoretical capacity, high discharging voltage, low cost and low toxicity.⁴² MnO₂ materials with different crystal structures, e.g., $\alpha\text{-MnO}_2$ ^{29,61}, $\beta\text{-MnO}_2$ ^{46,62}, $\gamma\text{-MnO}_2$ ^{58,63} and $\delta\text{-MnO}_2$ ^{42,64} have been investigated as the cathode materials. Besides MnO₂, other Mn-based materials, e.g., ZnMn_2O_4 ^{65,66}, Mn_3O_4 ^{67,68}, are also promising cathodes. Most of these oxides undergo a significant phase transformation during the electrochemical performance. A study of the structural transformation of $\gamma\text{-MnO}_2$ cathode proposed by Alfuruqi et al. revealed that the $\gamma\text{-MnO}_2$ transformed into multiple co-existed phases during the Zn-insertion process.⁵⁸

Despite the advantages, Mn-based oxides face a great challenge of capacity deterioration due to the notorious cathode dissolution. The origin of the dissolution of the Mn-based compound is the disproportionation of Mn^{3+} in the Mn-based cathode, which generates soluble Mn^{2+} .^{57,69} This problem is observed for most of the

Mn-based oxide cathodes, regardless of their crystal structure. Attempts have been made to resolve this problem. For example, Zhang et al. proposed that the utilization of a highly concentrated 3 M $\text{Zn}(\text{CF}_3\text{SO}_3)_2$ electrolyte presented alleviation of the dissolution of Mn from the ZnMn_2O_4 cathode.⁶⁶ Another strategy is introducing additional Mn^{2+} in the electrolyte. For example, Pan et al. demonstrated Zn-ion batteries with $\alpha\text{-MnO}_2$ nanofiber (**Figure 2.4a**) as cathode working in an electrolyte with 0.1 M MnSO_4 additive.²⁹ As presented in **Figure 2.4b**, much-improved cycling stability was obtained compared to the battery without the MnSO_4 additive. This strategy has been widely adopted in most of the following study in Mn-based cathodes.^{16,46,61,70}

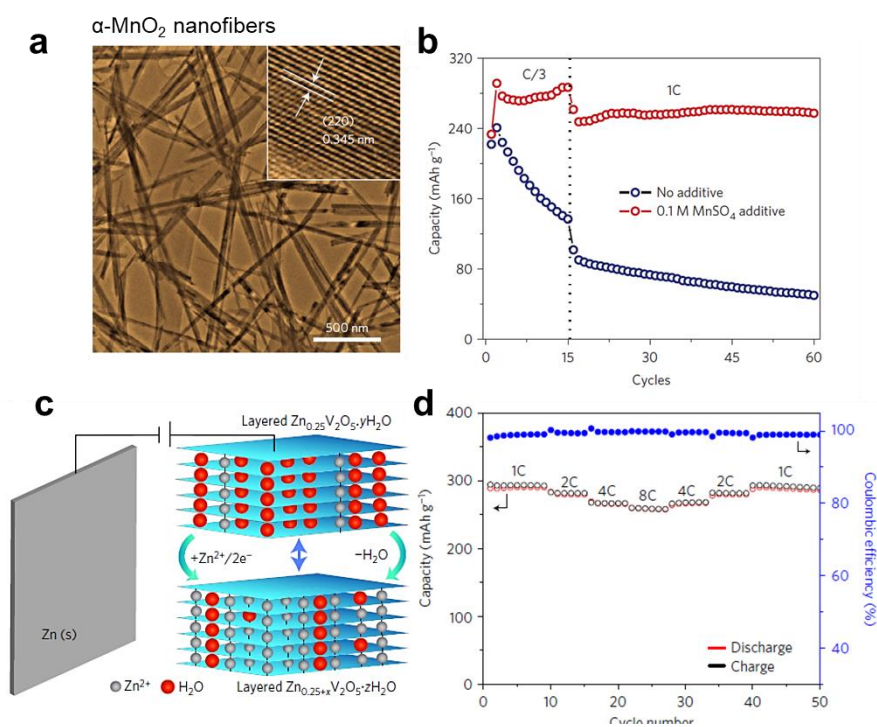


Figure 2.4 a) TEM image of $\alpha\text{-MnO}_2$ nanofibers, b) cycling stability of MnO_2 electrodes in batteries with/without the 0.1 M MnSO_4 additive for electrolyte; c) Illustration of the Zn-ion battery with a $\text{Zn}_{0.25}\text{V}_2\text{O}_5 \cdot \text{H}_2\text{O}$ cathode and d) the rate performance and corresponding Coulombic efficiencies of the $\text{Zn}_{0.25}\text{V}_2\text{O}_5 \cdot \text{H}_2\text{O}$ cathode. Reprinted with permission from a&b)²⁹ Copyright 2016, Springer Nature, c&d)⁵¹ Copyright 2016, Springer Nature.

Vanadium(V)-based materials are another promising category, which usually provide higher capacity and better high-rate performance than Mn oxides. However, the discharging voltage of the V-based materials is lower than most of the Mn-based oxides. Most of the vanadium oxide materials (V_2O_5 ^{71,72}, VO_2 ⁷³⁻⁷⁵, $M_xV_2O_5$ ⁷⁶, $M_xV_3O_7$ ⁷⁷, $M_xV_3O_8$ ^{78,79}, $M_xV_2O_7$ ⁸⁰; M=Zn, H, Li, Na, Ca) and vanadium sulfide (e.g., VS_2 ^{55,81}) materials developed as cathode for Zn-ion battery have an open tunnel-like or layered structure, which provide a fast ionic diffusion channel for the Zn^{2+} . Therefore, most of these V-based materials follow the Zn^{2+} intercalation-deintercalation mechanism. Research in V-based cathodes is focused on the design of an electrochemically stable structure for reversible Zn^{2+} intercalation and for improved ionic diffusion within the cathode.⁸²⁻⁸⁴ For example, Kundu et al. developed a $Zn_{0.25}V_2O_5 \cdot H_2O$ cathode material with excellent high-rate performance (**Figure 2.4d**) and long cycling stability.⁵¹ The remarkable high-rate performance benefits from the structural water molecules which play a key role of allowing Zn^{2+} ingress/egress (**Figure 2.4c**). In addition, the indigenous Zn ions in the interlayers ensure good structural stability during cycling.

Besides the above Mn-based and V-based cathode materials, other materials are also demonstrated promising performance, e.g., Ni/Co-based compounds⁸⁵⁻⁸⁷, zinc hexacyanoferrate^{88,89}, polyanion compounds,⁹⁰ and organic materials^{91,92}.

2.4 Alkaline Zn-MX batteries

2.4.1 Fundamentals of alkaline Zn-MX batteries

In alkaline aqueous electrolyte, redox couples of the transition metal compounds also provide decent capacity for energy storage.⁹³ The redox reaction on the Zn anode follows the **Equation 2.2**.²³ As presented in **Figure 2.5a**, OH^- acts as the charge carrier. During the charging process, OH^- moves toward the cathode and oxidizes the transition metal (e.g., Ag, Cu) or transition metal compounds (e.g., NiO, Co_3O_4). In the subsequent discharging, reduction of the cathode occurs and the OH^- move toward the Zn anode. The reaction process varies from the different types of cathode materials, including Zn-Mn battery^{94,95}, Zn-Ni battery^{96,97}, Zn-Co battery⁹⁸, Zn-Ag battery^{99,100} and Zn-Cu battery¹⁰¹.

Zn-based batteries with alkaline electrolytes

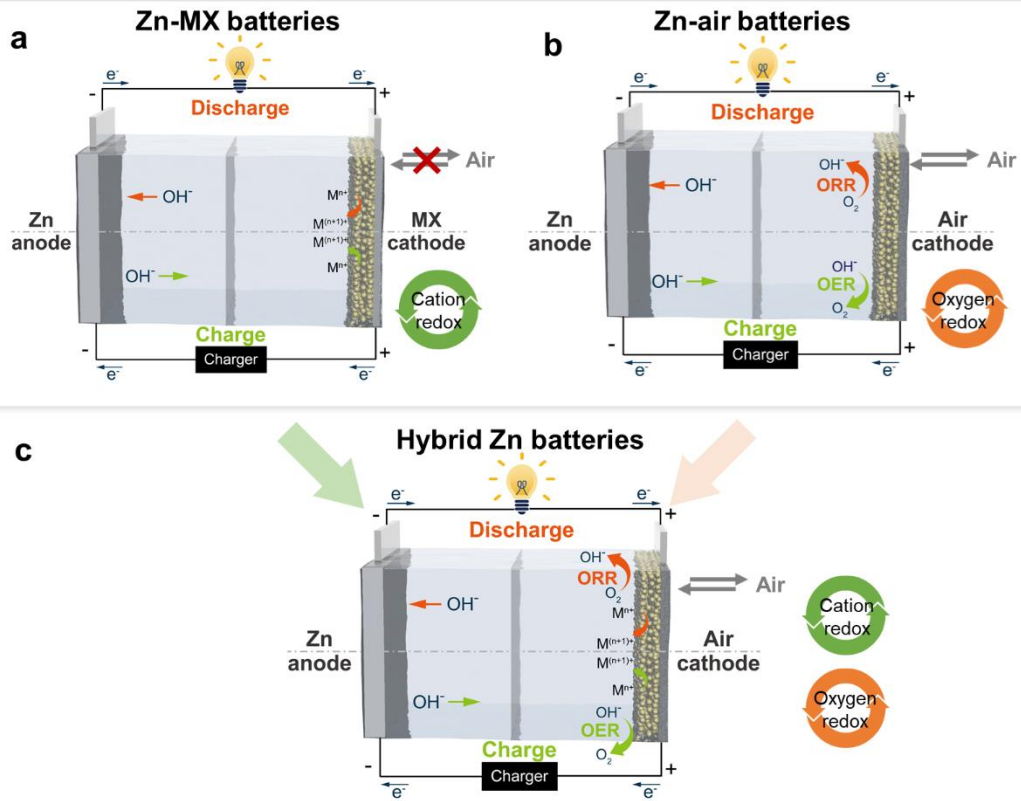


Figure 2.5 Fundamental working mechanisms of three promising alkaline aqueous Zn-based batteries: a) Zn-MX batteries, b) Zn-air batteries and c) hybrid Zn batteries.

2.4.2 Cathode materials for alkaline Zn-MX batteries

Despite the high capacity of alkaline Zn-Mn battery (617 mAh g^{-1}), for a long period, Zn-Mn battery is not a promising rechargeable battery. Usually, MnO_2 is utilized as the cathode material for the alkaline Zn-Mn battery. In the discharging process, the MnO_2 is reduced to MnOOH , then further reduced to Mn(OH)_2 and Mn_3O_4 which are relatively electrochemically inert.^{41,102} Recent studies indicate that the rechargeability of the Zn-Mn battery can be facilitated by introducing suitable dopants (e.g., Bi, Cu) or decoration species (e.g., Ni(OH)_2).¹⁰³⁻¹⁰⁵ Ni-based compounds (e.g., NiOOH , Ni(OH)_2 , NiO , Ni_3S_2) for the Zn-Ni battery are more promising candidates owing to the high discharge voltage and decent rechargeability.^{96,97} Typically, the capacity of the Ni-based cathode is originated from the $\text{Ni}^{3+}/\text{Ni}^{2+}$ redox couple, with the reversible conversion between NiOOH and $\text{Ni(OH)}_2/\text{NiO}$.¹⁰⁶ Recent development of the Ni-based cathode has been focused on the design of cathode material and construction of

highly conductive matrix for smooth electronic transfer.^{106,107} For Zn-Co battery, the most studied cathode material is Co_3O_4 .^{98,108} During the charging process, Co_3O_4 is first oxidized to CoOOH , and further oxidized to CoO_2 .¹⁰⁸ A recent report also proposed cobalt sulfide (i.e., Co_3S_4) as the cathode.¹⁰⁹ Rechargeable Zn-Ag battery is based on the redox reaction of Ag, which follows a two-step oxidation process, producing Ag_2O and AgO , respectively.¹¹⁰ Recent research is focused on improving the reactivity of the oxidized Ag species through the integration of the metallic silver or silver oxide into the highly electronic conductive matrix.¹¹¹ Recently, alkaline Zn-Cu battery was proposed by Zhu et al.¹⁰¹ Reversible two-electron process between the Cu and $\text{Cu}(\text{OH})_2/\text{CuO}$ in an alkaline electrolyte was achieved by tuning the solubility of Cu^{2+} , providing a high theoretical capacity of 844 mAh g^{-1} .

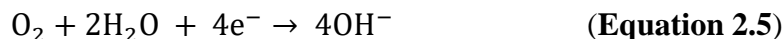
Though most of the transition metals and compounds have high theoretical capacities, the capacity presented in most of the previous works is still far from the theoretical value. Rational design for facilitating the charge and ionic transfers are important for obtaining higher capacities and higher rate performance.^{109,112} For example, Liu et al. incorporated flexible N-doped carbon fiber arrays with NiO nanoflakes to establish an electronic pathway throughout the cathode.¹⁰⁶ At the same time, the well-designed highly porous cathode structure and the ultrathin nanoflake morphology are beneficial to the fast ionic transfers. As a result, superior power and energy density was achieved for the alkaline Zn-Ni battery.

2.5 Zn-air batteries

2.5.1 Fundamentals of Zn-air batteries

The energy density of an alkaline Zn-MX battery highly depends on the capacity of cathode materials. By exposing the cathode in an air atmosphere, an air cathode that operates based on the oxygen redox is established. Theoretically, the energy density of the metal-air batteries only depends on the metallic anode.^{113,114} Due to the high concentration of oxygen (~21%) in the air atmosphere on the earth, metal-air batteries can continuously work in ambient air.¹¹⁵⁻¹¹⁷ As presented in **Figure 2.5b**, The configuration of a Zn-air battery is similar to that of an alkaline Zn-MX battery, except that the cathode is exposed to air via an additional gas diffusion layer which is usually highly hydrophobic carbon. The layer is important for evenly distributing the gas on the air cathode and preventing the leakage of electrolyte.¹¹⁸ In a primary Zn-air battery,

only ORR is involved in the air cathode. During discharge, oxygen is reduced to OH⁻ following a four-electron reaction pathway:¹¹⁹



At the same time, oxidization of the Zn anode follows **Equation 2.3**. Overall, the full reaction equation of a primary Zn-air battery follows:^{39,120}



For a rechargeable Zn-air battery, OER is involved in the cathode in the subsequent recharging process, where OH⁻ is oxidized into oxygen and exhausted into the air atmosphere. It follows the reverse reaction of **Equation 2.5**.

The performance of the Zn-air battery can be evaluated based on some important parameters, including open-circuit voltage (OCV), peak power density (PPD), discharging voltage, charging voltage, voltage gap between the discharging voltage and charging voltage ($\Delta V_{\text{Zn-air}}$) and round-trip efficiency. Specifically, OCV, PPD and discharging voltage in a galvanostatic process with a constant current density are representative parameters for evaluating the performance of the electricity output, which is highly associated with the ORR process. At the same time, charging voltage in a galvanostatic process with a constant current density is highly associated with the OER process. The $\Delta V_{\text{Zn-air}}$ is a vital parameter for evaluating the overall performance of the rechargeable Zn-air battery. The round-trip efficiency, usually determined by the ratio of the discharging voltage to the charging voltage, reflects the energy efficiency of the Zn-air battery. The objectives for the development of advanced rechargeable Zn-air batteries are seeking higher OCV, PPD, discharging voltage, round-trip efficiency along with lower charging voltage and $\Delta V_{\text{Zn-air}}$. In addition, the cycling stability of the battery is also an important objective, but still, no parameter is widely utilized as the standard for evaluation of the cycling stability. A simplified evaluation of the cycling stability is to compare the total cycling duration (hour) for the galvanostatic discharging-charging cycling.

Bifunctional oxygen catalysts for the air cathode are important for the achievement of the above objectives for high-performance and durable Zn-air batteries.^{121,122} Though the ORR is a spontaneous process, the sluggish kinetics usually results in large over-potentials, which lowers the discharging voltages and PPDs without ORR catalysts in the air cathode.¹⁷ At the same time, the even more sluggish OER process will lead to high charging voltages and low round-trip efficiency in a rechargeable Zn-air battery without OER catalysts in the air cathode.^{122,123} Except for the high catalytic

activity for ORR and OER, other requirements are also important for ideal bifunctional oxygen catalysts. For example, during the discharging process, a two-electron reaction pathway is competitive to the four-electron pathway as described in **Equation 2.5**, which generates unfavorable superoxide (HO_2^-) side product.¹¹⁹ Therefore high selectivity of OH^- production versus the HO_2^- is important for the catalyst. Furthermore, the catalysts should also have good chemical and electrochemical stability, especially in a strong alkaline electrolyte and with highly reducing and oxidizing environments during the discharging and charging processes.

2.5.2 Cathode materials for Zn-air batteries

In the past decades, intensive efforts have been made to develop new ORR and OER catalysts, including precious metals, metal-free carbons, metal or alloys loaded nitrogen-doped carbon materials (M-N-C), and non-precious transition metal compounds (**Figure 2.6a**).^{124,125} Noble metals (e.g., Pt, Pd, Ir, Ru) and their oxides demonstrate excellent oxygen catalysis in aqueous electrolytes in a wide range of pH values.¹²⁶⁻¹²⁸ Therefore, the precious metal catalysts are well-recognized commercial benchmarks for the oxygen catalysts (e.g., 20 wt% Pt/C as an ORR benchmark, IrO_2 or RuO_2 as an OER benchmark).¹²⁹ However, the high cost of the precious metal catalysts restricts their large-scale utility. Functional carbon materials with heteroatom doping (e.g., nitrogen) demonstrate decent activity for ORR.^{130,131} M-N-C materials featuring metal/alloy nanoparticles or single metal atoms usually demonstrate excellent ORR catalysis. In some reports, the partial oxidization of the surface of the metal also results in a decent OER catalyst.^{132,133} However, within a strong alkaline electrolyte, corrosion of the carbon material may occur during the recharging (oxidization) process of the Zn-air battery, weakening the stability of these carbon materials and carbon-based composites.¹³⁴

Non-precious transition metal compounds, including oxides¹³⁵, hydroxides¹³⁶, sulfides¹³⁷, and nitrides,^{138,139} are promising economic alternatives that can not only provide a good activity for ORR and OER, but also demonstrate decent stability. Oxide materials demonstrate the best potential for large-scale utility. One of the most significant advantages of the oxide materials is that their composition and crystal structure can be facilely tuned to obtain optimized materials with targeted properties and functions. In addition, most oxide materials can be synthesized under ambient air atmosphere, which lowers the cost for synthesis and mass production.

Among the binary oxide materials, Co_3O_4 ¹⁴⁰⁻¹⁴² and MnO_2 ¹⁴³⁻¹⁴⁵ are most studied materials for Zn-air batteries. Usually, Co_3O_4 is more favorable for OER, while MnO_2 is more favorable for ORR.¹⁴⁶ Other Mn-based (e.g., Mn_3O_4 ¹⁴⁷), Co-based (e.g., CoO ^{148,149}) binary oxides were also reported. Some other transition metal elements, e.g., Ni, Fe, Zn, Cu usually have low activity of their binary oxides. These elements and their compounds are usually utilized as dopants or decoration species for the bulk transition metal compounds to boost their bifunctional catalysis.^{150,151} Complex oxide materials, e.g., bimetallic spinel oxide and perovskite oxide are also investigated. These complex oxides provide a better flexibility for designing different compositions and structures. A variety of spinel oxides (e.g. CoMn_2O_4 ^{147,152}, NiCo_2O_4 ^{153,154}, Co_2FeO_4 ¹⁵⁵, CuCo_2O_4 ¹⁵⁶) and perovskite oxides (e.g. $\text{La}_{0.5}\text{Sr}_{0.5}\text{Co}_{0.8}\text{Fe}_{0.2}\text{O}_3$ ¹⁵⁷, $(\text{PrBa}_{0.5}\text{Sr}_{0.5})_{0.95}\text{Co}_{1.5}\text{Fe}_{0.5}\text{O}_{5+\delta}$ ¹⁵⁸, $\text{Sr}(\text{Co}_{0.8}\text{Fe}_{0.2})_{0.95}\text{P}_{0.05}\text{O}_{3-\delta}$ ¹⁵⁹) have been designed for Zn-air battery cathode.

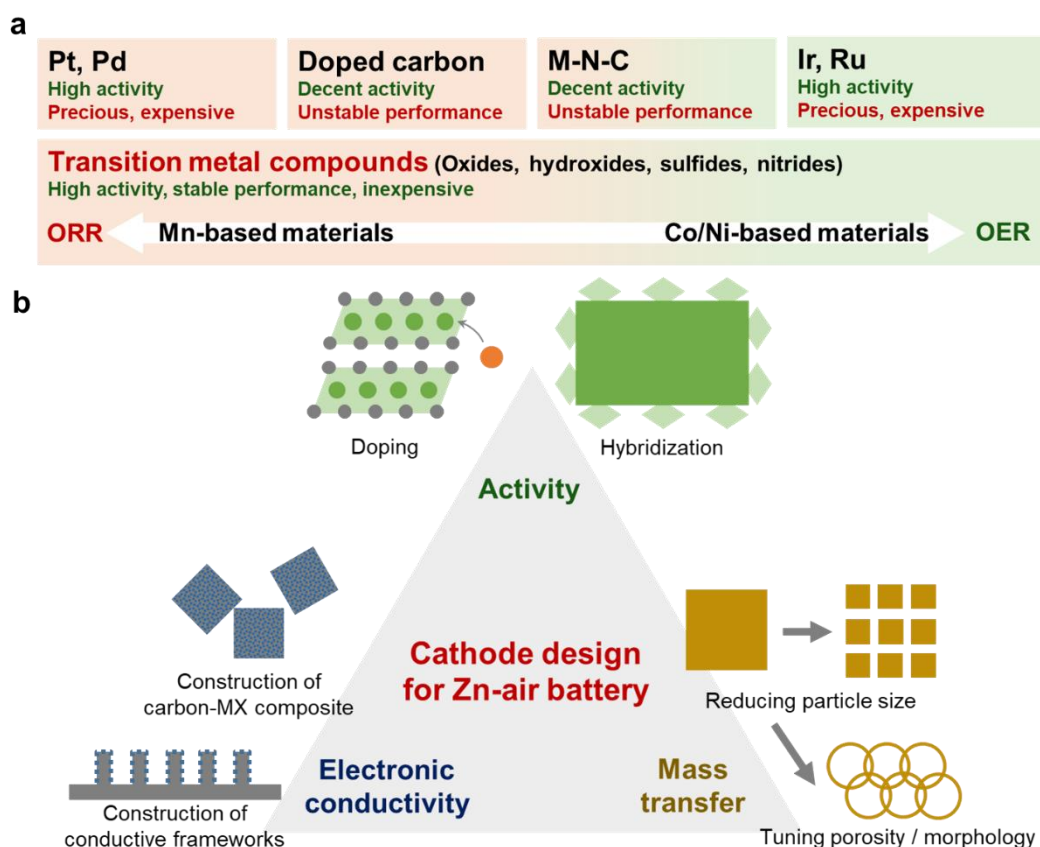


Figure 2.6 a) Comparison of typical catalysts for ORR and OER, b) strategies for the design of cathode materials for Zn-air batteries.

2.5.3 Optimizations of the cathodes

Unlike the research field of electrochemical catalysis that usually focuses on the intrinsic catalytic activity of the materials, research in Zn-air battery cathode usually aims at developing or modifying transition metal compounds that demonstrate good overall catalytic activity and high durability. Additionally, since electronic transfer and gas/ionic transfers on the cathode have significant influences on the performance, optimization of these properties of the transition metal compound cathode is also the main topic of the Zn-air battery research.^{119,160}

As summarized in **Figure 2.6b**, typical design strategies, for example, the increase of the bifunctional catalytic activity, the improvement of electronic conductivity, and the optimization of mass transfers, are presented and discussed as follows.

1) Increasing activity for ORR-OER

Doping of transition metal compounds with one or more elements is reported to promote the activity.^{161,162} Cation doping is widely adopted for tuning the properties of metal oxides. For example, Li et al proposed that the Ni doping on CoO effectively improved the intrinsic activity for ORR.¹⁴⁹ Bian et al. reported that doping Mn in a perovskite oxide (LaNiO₃) boosted the bifunctional ORR-OER catalyst, resulting in a higher PPD, higher discharge voltage and lower charging-discharging voltage gap of the rechargeable Zn-air battery.¹⁶³ Some report also applied anion doping for oxide materials.^{142,164} For example, Yu et al. proposed a N-doped Co₃O₄ which effectively improved the oxygen adsorption strength and the ORR activity of the materials.¹⁴²

Hybridization of two or more catalysts is another strategy for improving the catalytic activity.^{144,159,165,166} For example, to combine the good OER activity of Co₃O₄ and the good ORR activity of MnO₂, Du et al. proposed a Co₃O₄ decorated MnO₂ via a hydrothermal method.¹⁴⁴ In some reports, interactions between the integrated materials further promoted the activity.¹⁶⁷⁻¹⁶⁹ For example, Wang et al. reported that the hybridization of Sr(Co_{0.8}Fe_{0.2})_{0.95}P_{0.05}O_{3-δ} perovskite with Pt/C via a facile ball-milling method produced strong electronic interaction between the oxide and Pt and increased surface vacancies on the oxide, which facilitated the ORR-OER catalysis.¹⁵⁹

2) Improving electronic conductivity

Most of the transition metal compounds, especially, oxide materials, demonstrated low electronic conductivities. Construction of carbon-MX composites has been reported in many previous reports as an effective way to improve the

conductivity.^{155,170-172} For example, Wang et al. proposed a Co_2FeO_4 which is well-anchored on N-doped carbon nanotubes.¹⁵⁵ Compared to the design of carbon-MX composites, construction of conductive frameworks throughout the cathode has also been widely reported.¹⁷³⁻¹⁷⁶ For example, Lee et al. proposed a Co_3O_4 nanowire array deposited directly on a highly electronic conductive stainless steel mesh.¹⁷³ Similar methods that deposited transition metal compounds on the stainless steel, nickel foam and carbon cloth were also reported.¹⁷⁴⁻¹⁷⁶

3) Optimizing mass transfers

Reducing the particle size^{158,177}, tuning porosity^{178,179} and morphologies^{174,180} of the oxide materials are effective strategies for improving the mass transfers.^{158,181,182} Taking Co_3O_4 as an example, a three-dimensional Co_3O_4 with a highly ordered mesoporous morphology demonstrated better performance and stability than the bulk Co_3O_4 .¹⁷⁸ In another report, ultrathin mesoporous Co_3O_4 with good contact with carbon fibers was developed.¹⁷⁷ Compared to the commercial Co_3O_4 with a large particle size loaded on the carbon fibers, the ultrathin and mesoporous morphologies provide a significant improvement on the ORR-OER activity. In addition, the good contact between the ultrathin Co_3O_4 and the carbon fibers also prevented the aggregation of the Co_3O_4 , thus high physical stability and good cycling stability of the Zn-air battery were achieved.

4) Rational design of activity, electronic conductivity, and mass transfers

It is noted that most of the above examples applied not only one design strategy. Rational design of the cathode material and electrode structure via the combination of multiple optimization methods are widely adopted to achieve a comprehensive improvement of the battery performance. For example, Li et al. proposed a hybrid material composed of a CoO incorporated nitrogen-doped carbon nanotubes (CoO/N-CNT) and a Ni-Fe-layered double hydroxide (NiFe-LDH), demonstrating excellent ORR and OER catalysis (**Figure 2.7a**), respectively.²⁸ The CNT support constructs an interconnected framework for ensuing good electronic transfers. The battery presented decent galvanostatic cycling performance and stability (**Figure 2.7b&c**). For another example, metal-organic frameworks (MOFs) were utilized as the precursors for the preparation of metal-oxide via calcination in inert atmosphere.¹⁸³⁻¹⁸⁵ The resulting composite not only has good electronic conductivity but also derived special properties

(e.g., high porosity, and special morphologies) from the MOFs precursor, which is beneficial for obtaining high activity, good charge transfer and mass transfers.

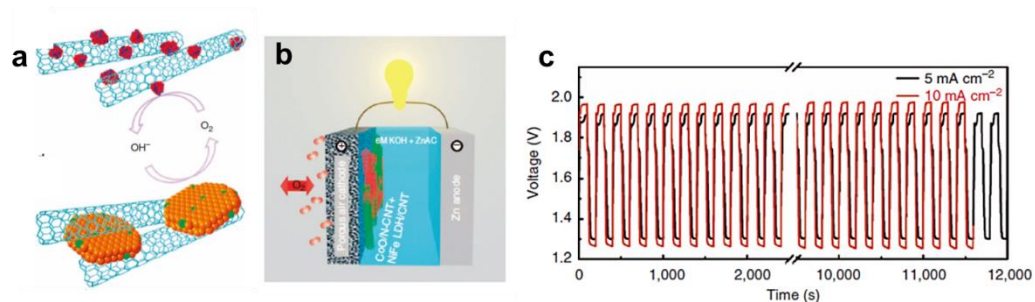


Figure 2.7 a) Illustration of the different functions for the CoO/N-CNT ORR catalyst and the NiFe-LDH/CNT OER catalyst, b) hybridization of the two catalysts in the air cathode for Zn-air battery and c) galvanostatic cycling profiles of the Zn-air battery with the hybrid catalyst. Reprinted with permission from ²⁸ Copyright 2013, Springer Nature.

2.6 Hybrid Zn batteries

2.6.1 Fundamentals of hybrid Zn batteries

Both Zn-MX battery and Zn-air battery have significant advantages and drawbacks. Zn-MX battery usually demonstrate higher discharging voltages, power density and higher energy efficiency than Zn-air battery. However, the energy density of the Zn-MX battery is inferior to the Zn-air battery. Considering some of the transition metal compounds can serve as the active materials for Zn-MX battery and as oxygen catalyst for Zn-air battery, a battery that integrates this two battery functions at the cell level is called hybrid Zn battery.^{24,186}

As presented in **Figure 2.5c**, a hybrid Zn battery derives the configuration of the Zn-air battery. During discharge, both cation reduction and oxygen reduction are involved in the cathode. Owing to the swift kinetics, Faradaic cation reduction occurs first in the discharging, usually producing a higher discharging voltage. Subsequently, the ORR occurs with the catalysis of the reduced metal compounds, producing a lower discharging voltage. At the same time, the Zn anode undergoes oxidization following **Equation 2.2 & 2.3**. In the charging process, oxidization reversibly occurs in the cathode, with the sequence of the cation oxidation and then OER.

2.6.2 Cathode materials for hybrid Zn batteries

As a newly developed research area, only a few cathode materials have been applied to the hybrid Zn-battery cathodes. The first reported hybrid Zn battery with NiO/Ni(OH)₂ nanoflakes as cathode material was proposed by Lee et al. in 2016.¹⁸⁶ With swift kinetic of Faradaic redox of NiO/Ni(OH)₂ and ORR, the hybrid Zn battery demonstrated high power density and energy density at the same time. Following their work, Tan et al. also proposed a hybrid Zn battery with high-rate capability using carbon nanotubes incorporated NiO/Ni(OH)₂ cathode.¹⁸⁷ Attempt to integrate the Zn-Ni and Zn-air hybrid battery in a flow electrolyte system was also made to achieve better cycling stability by Cheng et al.¹⁸⁸

Compared to Ni-based materials, more works have been conducted in Co-based materials, especially, Co₃O₄. Ma et al. proposed an oxygen vacancy-rich Co₃O₄ cathode and applied the hybrid Zn electrochemistry in both aqueous batteries and flexible gel-polymer batteries.¹⁸⁹ A variety of other Co₃O₄ materials prepared via different methods were also proposed in recent three years.¹⁹⁰⁻¹⁹³ By incorporating Ni- and Co-based material into a binary oxide, Li et al, proposed a Ni foam supported NiCo₂O₄.¹⁵⁴ As presented in **Figure 2.8a**, the redox of Ni, Co and O were integrated into the cathode. The Ni foam support provided an efficient electronic transfer pathway. Two well-defined peaks in the CV scans (**Figure 2.8b**) and the additional voltage plateaus in the galvanostatic charging and discharging profile (**Figure 2.8c**) of the hybrid battery indicate the redox couples of the Ni and Co, which provided a higher discharging voltage compared to that of a conventional Zn-air battery. Moreover, the battery demonstrated excellent cycling stability over 2600 h. Very recently, Wu et al proposed a similar electrode with a sandwich-structure with Ni and Co oxides, which also presented a good cycling stability.¹⁹⁴

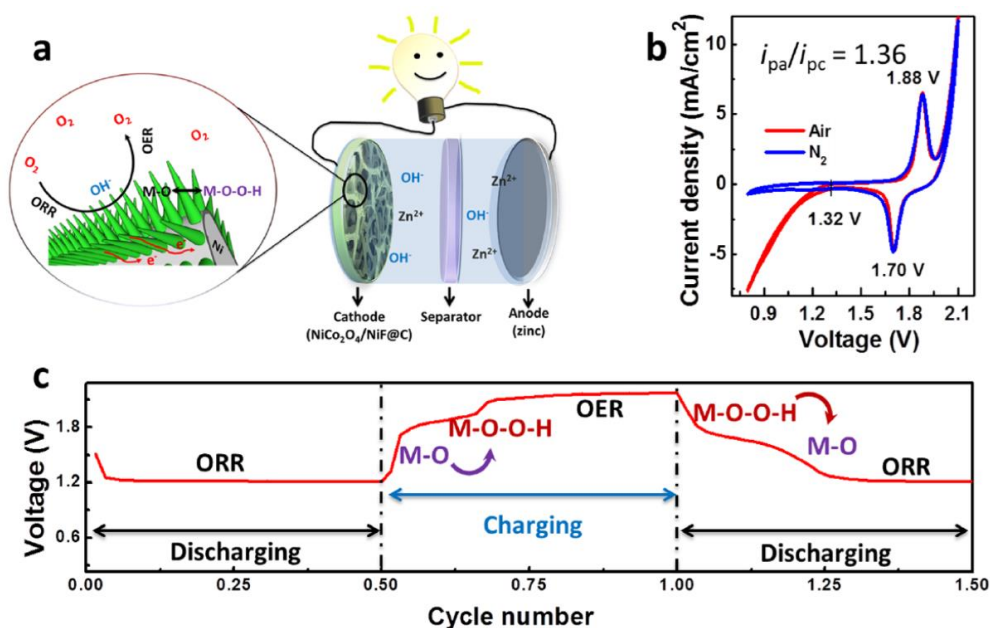


Figure 2.8 a) Illustration of a hybrid Zn battery with a NiCo₂O₄/NiF@C cathode, b) CV profile of the battery working in different atmospheres, c) initial galvanostatic discharging and charging profiles. Reprinted with permission from ¹⁵⁴ Copyright 2017, American Chemical Society.

Besides the above Ni-based and Co-based oxides, Ag^{195,196} was also presented with promising capability as the cathode for hybrid Zn battery. For example, Tan et al. proposed a Zn-Ag and Zn-air hybrid battery which demonstrated two-step oxidation of metallic Ag to Ag₂O and then AgO in the charging process.¹⁹⁵ In each discharging process three discharging voltage plateaus could be observed, which were associated with the stepwise reduction of AgO to Ag and the ORR. In recent studies since 2019, Co/Ni sulfides, e.g., Ni₃S₂¹⁹⁷, NiCo₂S₄¹⁹⁸, have also been developed as cathodes for hybrid Zn batteries.

References

1. Cho J, Jeong S, Kim Y. Commercial and research battery technologies for electrical energy storage applications. *Prog Energy Combust Sci.* 2015;48:84-101. doi:10.1016/j.pecs.2015.01.002
2. Gür TM. Critical review of carbon conversion in "carbon fuel cells". *Chem Rev.* 2013;113(8):6179-206. doi:10.1021/cr400072b

3. D'Alessandro DM, Smit B, Long JR. Carbon dioxide capture: Prospects for new materials. *Angew Chem Int Ed.* 2010;49(35):6058-82. doi:10.1002/anie.201000431
4. Winter M, Brodd RJ. What are batteries, fuel cells, and supercapacitors? *Chem Rev.* 2004;104(10):4245-70. doi:10.1021/cr020730k
5. United States Department of Energy. International Energy Outlook 2019 with projections to 2050. Washington (United States): United States Department of Energy; 2019 [cited 2020 August 29]. Report No.: #IEO2019. Available from <https://www.eia.gov/outlooks/ieo/>
6. Yang Z, Zhang J, Kintner-Meyer MCW, Lu X, Choi D, Lemmon JP, et al. Electrochemical Energy Storage for Green Grid. *Chem Rev.* 2011;111(5):3577-613. doi:10.1021/cr100290v
7. Gür TM. Review of electrical energy storage technologies, materials and systems: Challenges and prospects for large-scale grid storage. *Energy Environ Sci.* 2018;11(10):2696-767. doi:10.1039/C8EE01419A
8. Tarascon J-M, Armand M. Issues and challenges facing rechargeable lithium batteries. *Nature.* 2001;414(6861):359-67. doi:10.1038/35104644
9. Chu S, Cui Y, Liu N. The path towards sustainable energy. *Nat Mater.* 2017;16(1):16-22. doi:10.1038/nmat4834
10. Park C-M, Kim J-H, Kim H, Sohn H-J. Li-alloy based anode materials for Li secondary batteries. *Chem Soc Rev.* 2010;39(8):3115-41. doi:10.1039/B919877F
11. Manthiram A, Yu X, Wang S. Lithium battery chemistries enabled by solid-state electrolytes. *Nat Rev Mater.* 2017;2:16103. doi:10.1038/natrevmats.2016.103
12. Lu J, Wu T, Amine K. State-of-the-art characterization techniques for advanced lithium-ion batteries. *Nature Energy.* 2017;2:17011. doi:10.1038/nenergy.2017.11
13. Yabuuchi N, Kubota K, Dahbi M, Komaba S. Research development on sodium-ion batteries. *Chem Rev.* 2014;114(23):11636-82. doi:10.1021/cr500192f
14. Rajagopalan R, Tang Y, Ji X, Jia C, Wang H. Advancements and challenges in potassium ion batteries: A comprehensive review. *Adv Funct Mater.* 2020;30(12):1909486. doi:10.1002/adfm.201909486

15. Luo J-Y, Cui W-J, He P, Xia Y-Y. Raising the cycling stability of aqueous lithium-ion batteries by eliminating oxygen in the electrolyte. *Nat Chem.* 2010;2(9):760-5. doi:10.1038/nchem.763
16. Huang J, Guo Z, Ma Y, Bin D, Wang Y, Xia Y. Recent progress of rechargeable batteries using mild aqueous electrolytes. *Small Methods.* 2019;3(1):1800272. doi:10.1002/smt.201800272
17. Fu J, Cano ZP, Park MG, Yu A, Fowler M, Chen Z. Electrically rechargeable zinc-air batteries: Progress, challenges, and perspectives. *Adv Mater.* 2017;29(7):1604685. doi:10.1002/adma.201604685
18. Li Y, Lu J. Metal air batteries: Will they be the future electrochemical energy storage device of choice? *ACS Energy Lett.* 2017;2(6):1370-7. doi:10.1021/acseenergylett.7b00119
19. Wang H-F, Xu Q. Materials design for rechargeable metal-air batteries. *Matter.* 2019;1(3):565-95. doi:10.1016/j.matt.2019.05.008
20. Mainar AR, Iruin E, Colmenares LC, Kvasha A, de Meatza I, Bengoechea M, et al. An overview of progress in electrolytes for secondary zinc-air batteries and other storage systems based on zinc. *J Energy Storage.* 2018;15:304-28. doi:10.1016/j.est.2017.12.004
21. Arenas LF, Loh A, Trudgeon DP, Li X, Ponce de León C, Walsh FC. The characteristics and performance of hybrid redox flow batteries with zinc negative electrodes for energy storage. *Renewable Sustainable Energy Rev.* 2018;90:992-1016. doi:10.1016/j.rser.2018.03.016
22. Konarov A, Voronina N, Jo JH, Bakenov Z, Sun Y-K, Myung S-T. Present and future perspective on electrode materials for rechargeable zinc-ion batteries. *ACS Energy Lett.* 2018;3(10):2620-40. doi:10.1021/acseenergylett.8b01552
23. Shang W, Yu W, Liu Y, Li R, Dai Y, Cheng C, et al. Rechargeable alkaline zinc batteries: Progress and challenges. *Energy Storage Mater.* 2020;31:44-57. doi:10.1016/j.ensm.2020.05.028
24. Shang W, Yu W, Tan P, Chen B, Wu Z, Xu H, et al. Achieving high energy density and efficiency through integration: Progress in hybrid zinc batteries. *J Mater Chem A.* 2019;7(26):15564-74. doi:10.1039/C9TA04710G
25. Wu K, Zhang L, Yuan Y, Zhong L, Chen Z, Chi X, et al. An iron-decorated carbon aerogel for rechargeable flow and flexible Zn-air batteries. *Adv Mater.* 2020;32(32):2002292. doi:10.1002/adma.202002292

26. Ming J, Guo J, Xia C, Wang W, Alshareef HN. Zinc-ion batteries: Materials, mechanisms, and applications. *Mater Sci Eng, R.* 2019;135:58-84. doi:10.1016/j.mser.2018.10.002
27. Yi J, Liang P, Liu X, Wu K, Liu Y, Wang Y, et al. Challenges, mitigation strategies and perspectives in development of zinc-electrode materials and fabrication for rechargeable zinc-air batteries. *Energy Environ Sci.* 2018;11(11):3075-95. doi:10.1039/C8EE01991F
28. Li Y, Gong M, Liang Y, Feng J, Kim J-E, Wang H, et al. Advanced zinc-air batteries based on high-performance hybrid electrocatalysts. *Nat Commun.* 2013;4:1805. doi:10.1038/ncomms2812
29. Pan H, Shao Y, Yan P, Cheng Y, Han KS, Nie Z, et al. Reversible aqueous zinc/manganese oxide energy storage from conversion reactions. *Nat Energy.* 2016;1:16039. doi:10.1038/nenergy.2016.39
30. Li H, Ma L, Han C, Wang Z, Liu Z, Tang Z, et al. Advanced rechargeable zinc-based batteries: Recent progress and future perspectives. *Nano Energy.* 2019;62:550-87. doi:10.1016/j.nanoen.2019.05.059
31. Deng Y-P, Liang R, Jiang G, Jiang Y, Yu A, Chen Z. The current state of aqueous Zn-based rechargeable batteries. *ACS Energy Lett.* 2020;5(5):1665-75. doi:10.1021/acsenergylett.0c00502
32. Zeng X, Hao J, Wang Z, Mao J, Guo Z. Recent progress and perspectives on aqueous Zn-based rechargeable batteries with mild aqueous electrolytes. *Energy Storage Mater.* 2019;20:410-37. doi:10.1016/j.ensm.2019.04.022
33. Fang G, Zhou J, Pan A, Liang S. Recent advances in aqueous zinc-ion batteries. *ACS Energy Lett.* 2018;3(10):2480-501. doi:10.1021/acsenergylett.8b01426
34. Zhong Y, Xu X, Wang W, Shao Z. Recent advances in metal-organic framework derivatives as oxygen catalysts for zinc-air batteries. *Batteries Supercaps.* 2019;2(4):272-89. doi:10.1002/batt.201800093
35. Li B, Nie Z, Vijayakumar M, Li G, Liu J, Sprenkle V, et al. Ambipolar zinc-polyiodide electrolyte for a high-energy density aqueous redox flow battery. *Nat Commun.* 2015;6:6303. doi:10.1038/ncomms7303
36. Han X, Li X, White J, Zhong C, Deng Y, Hu W, et al. Metal-air batteries: From static to flow system. *Adv Energy Mater.* 2018;8(27):1801396. doi:10.1002/aenm.201801396

37. Blanc LE, Kundu D, Nazar LF. Scientific challenges for the implementation of Zn-ion batteries. *Joule*. 2020;4(4):771-99. doi:10.1016/j.joule.2020.03.002
38. Yu J, Ran R, Zhong Y, Zhou W, Ni M, Shao Z. Advances in porous perovskites: Synthesis and electrocatalytic performance in fuel cells and metal–air batteries. *Energy Environ Mater*. 2020;3(2):121-45. doi:10.1002/eem2.12064
39. Li Y, Dai H. Recent advances in zinc-air batteries. *Chem Soc Rev*. 2014;43(15):5257-75. doi:10.1039/C4CS00015C
40. Xu C, Li B, Du H, Kang F. Energetic zinc ion chemistry: The rechargeable zinc ion battery. *Angew Chem Int Ed*. 2012;51(4):933-5. doi:10.1002/anie.201106307
41. Cheng FY, Chen J, Gou XL, Shen PW. High-power alkaline Zn–MnO₂ batteries using γ -MnO₂ nanowires/nanotubes and electrolytic zinc powder. *Adv Mater*. 2005;17(22):2753-6. doi:10.1002/adma.200500663
42. Wang D, Wang L, Liang G, Li H, Liu Z, Tang Z, et al. A superior δ -MnO₂ cathode and a self-healing Zn- δ -MnO₂ battery. *ACS Nano*. 2019;13(9):10643-52. doi:10.1021/acsnano.9b04916
43. Chao D, Zhou W, Ye C, Zhang Q, Chen Y, Gu L, et al. An electrolytic Zn–MnO₂ battery for high-voltage and scalable energy storage. *Angew Chem Int Ed*. 2019;58(23):7823-8. doi:10.1002/anie.201904174
44. Li Y, Wang S, Salvador JR, Wu J, Liu B, Yang W, et al. Reaction mechanisms for long-life rechargeable Zn/MnO₂ batteries. *Chem Mater*. 2019;31(6):2036-47. doi:10.1021/acs.chemmater.8b05093
45. Nam KW, Kim H, Choi JH, Choi JW. Crystal water for high performance layered manganese oxide cathodes in aqueous rechargeable zinc batteries. *Energy Environ Sci*. 2019;12(6):1999-2009. doi:10.1039/C9EE00718K
46. Zhang N, Cheng F, Liu J, Wang L, Long X, Liu X, et al. Rechargeable aqueous zinc-manganese dioxide batteries with high energy and power densities. *Nat Commun*. 2017;8:405. doi:10.1038/s41467-017-00467-x
47. Huang J, Wang Z, Hou M, Dong X, Liu Y, Wang Y, et al. Polyaniline-intercalated manganese dioxide nanolayers as a high-performance cathode material for an aqueous zinc-ion battery. *Nat Commun*. 2018;9:2906. doi:10.1038/s41467-018-04949-4

48. Zhang N, Dong Y, Jia M, Bian X, Wang Y, Qiu M, et al. Rechargeable aqueous Zn-V₂O₅ battery with high energy density and long cycle life. *ACS Energy Lett.* 2018;3(6):1366-72. doi:10.1021/acseenergylett.8b00565
49. Liu C, Neale Z, Zheng J, Jia X, Huang J, Yan M, et al. Expanded hydrated vanadate for high-performance aqueous zinc-ion batteries. *Energy Environ Sci.* 2019;12(7):2273-85. doi:10.1039/C9EE00956F
50. Kaveevivitchai W, Manthiram A. High-capacity zinc-ion storage in an open-tunnel oxide for aqueous and nonaqueous Zn-ion batteries. *J Mater Chem A.* 2016;4(48):18737-41. doi:10.1039/C6TA07747A
51. Kundu D, Adams BD, Duffort V, Vajargah SH, Nazar LF. A high-capacity and long-life aqueous rechargeable zinc battery using a metal oxide intercalation cathode. *Nat Energy.* 2016;1:16119. doi:10.1038/nenergy.2016.119
52. Li H, McRae L, Firby CJ, Elezzabi AY. Rechargeable aqueous electrochromic batteries utilizing Ti-substituted tungsten molybdenum oxide based Zn²⁺ ion intercalation cathodes. *Adv Mater.* 2019;31(15):1807065. doi:10.1002/adma.201807065
53. Xu W, Sun C, Zhao K, Cheng X, Rawal S, Xu Y, et al. Defect engineering activating (boosting) zinc storage capacity of MoS₂. *Energy Storage Mater.* 2019;16:527-34. doi:10.1016/j.ensm.2018.09.009
54. Liang H, Cao Z, Ming F, Zhang W, Anjum DH, Cui Y, et al. aqueous zinc-ion storage in MoS₂ by tuning the intercalation energy. *Nano Lett.* 2019;19(5):3199-206. doi:10.1021/acs.nanolett.9b00697
55. He P, Yan M, Zhang G, Sun R, Chen L, An Q, et al. Layered VS₂ nanosheet-based aqueous Zn ion battery cathode. *Adv Energy Mater.* 2017;7(11):1601920. doi:10.1002/aenm.201601920
56. Liu S, Kang L, Kim JM, Chun YT, Zhang J, Jun SC. Recent advances in vanadium-based aqueous rechargeable zinc-ion batteries. *Adv Energy Mater.* 2020;10(25):2000477. doi:10.1002/aenm.202000477
57. Song M, Tan H, Chao D, Fan HJ. Recent advances in Zn-ion batteries. *Adv Funct Mater.* 28(41):1802564. doi:10.1002/adfm.201802564
58. Alfaruqi MH, Mathew V, Gim J, Kim S, Song J, Baboo JP, et al. Electrochemically induced structural transformation in a γ -MnO₂ cathode of a high capacity zinc-ion battery system. *Chem Mater.* 2015;27(10):3609-20. doi:10.1021/cm504717p

59. He P, Zhang G, Liao X, Yan M, Xu X, An Q, et al. Sodium ion stabilized vanadium oxide nanowire cathode for high-performance zinc-ion batteries. *Adv Energy Mater.* 2018;8(10):1702463. doi:10.1002/aenm.201702463
60. Sun W, Wang F, Hou S, Yang C, Fan X, Ma Z, et al. Zn/MnO₂ battery chemistry with H⁺ and Zn²⁺ coinsertion. *J Am Chem Soc.* 2017;139(29):9775-8. doi:10.1021/jacs.7b04471
61. Wu B, Zhang G, Yan M, Xiong T, He P, He L, et al. Graphene scroll-coated α -MnO₂ nanowires as high-performance cathode materials for aqueous Zn-ion battery. *Small.* 2018;14(13):1703850. doi:10.1002/sml.201703850
62. Liu M, Zhao Q, Liu H, Yang J, Chen X, Yang L, et al. Tuning phase evolution of β -MnO₂ during microwave hydrothermal synthesis for high-performance aqueous Zn ion battery. *Nano Energy.* 2019;64:103942. doi:10.1016/j.nanoen.2019.103942
63. Wang C, Zeng Y, Xiao X, Wu S, Zhong G, Xu K, et al. γ -MnO₂ nanorods/graphene composite as efficient cathode for advanced rechargeable aqueous zinc-ion battery. *J Energy Chem.* 2020;43:182-7. doi:10.1016/j.jechem.2019.08.011
64. Guo C, Liu H, Li J, Hou Z, Liang J, Zhou J, et al. Ultrathin δ -MnO₂ nanosheets as cathode for aqueous rechargeable zinc ion battery. *Electrochim Acta.* 2019;304:370-7. doi:10.1016/j.electacta.2019.03.008
65. Knight JC, Therese S, Manthiram A. Chemical extraction of Zn from ZnMn₂O₄-based spinels. *J Mater Chem A.* 2015;3(42):21077-82. doi:10.1039/C5TA06482A
66. Zhang N, Cheng F, Liu Y, Zhao Q, Lei K, Chen C, et al. Cation-deficient spinel ZnMn₂O₄ cathode in Zn(CF₃SO₃)₂ electrolyte for rechargeable aqueous Zn-ion battery. *J Am Chem Soc.* 2016;138(39):12894-901. doi:10.1021/jacs.6b05958
67. Sun M, Li D-S, Wang Y-F, Liu W-L, Ren M-M, Kong F-G, et al. Mn₃O₄@NC composite nanorods as a cathode for rechargeable aqueous Zn-ion batteries. *ChemElectroChem.* 2019;6(9):2510-6. doi:10.1002/celec.201900376
68. Zhu C, Fang G, Zhou J, Guo J, Wang Z, Wang C, et al. Binder-free stainless steel@Mn₃O₄ nanoflower composite: A high-activity aqueous zinc-ion battery cathode with high-capacity and long-cycle-life. *J Mater Chem A.* 2018;6(20):9677-83. doi:10.1039/C8TA01198B

69. Yu P, Zeng Y, Zhang H, Yu M, Tong Y, Lu X. Flexible Zn-ion batteries: Recent progresses and challenges. *Small*. 2019;15(7):1804760. doi:10.1002/sml.201804760
70. Fang G, Zhu C, Chen M, Zhou J, Tang B, Cao X, et al. Suppressing manganese dissolution in potassium manganate with rich oxygen defects engaged high-energy-density and durable aqueous zinc-ion battery. *Adv Funct Mater*. 2019;29(15):1808375. doi:10.1002/adfm.201808375
71. Hu P, Yan M, Zhu T, Wang X, Wei X, Li J, et al. Zn/V₂O₅ aqueous hybrid-ion battery with high voltage platform and long cycle life. *ACS Appl Mater Interfaces*. 2017;9(49):42717-22. doi:10.1021/acsami.7b13110
72. Yan M, He P, Chen Y, Wang S, Wei Q, Zhao K, et al. Water-lubricated intercalation in V₂O₅·nH₂O for high-capacity and high-rate aqueous rechargeable zinc batteries. *Adv Mater*. 2018;30(1):1703725. doi:10.1002/adma.201703725
73. Dai X, Wan F, Zhang L, Cao H, Niu Z. Freestanding graphene/VO₂ composite films for highly stable aqueous Zn-ion batteries with superior rate performance. *Energy Storage Mater*. 2019;17:143-50. doi:10.1016/j.ensm.2018.07.022
74. Chen L, Ruan Y, Zhang G, Wei Q, Jiang Y, Xiong T, et al. Ultrastable and high-performance Zn/VO₂ battery based on a reversible single-phase reaction. *Chem Mater*. 2019;31(3):699-706. doi:10.1021/acs.chemmater.8b03409
75. Li Z, Ganapathy S, Xu Y, Zhou Z, Sarilar M, Wagemaker M. Mechanistic insight into the electrochemical performance of Zn/VO₂ batteries with an aqueous ZnSO₄ electrolyte. *Adv Energy Mater*. 2019;9(22):1900237. doi:10.1002/aenm.201900237
76. Yang Y, Tang Y, Fang G, Shan L, Guo J, Zhang W, et al. Li⁺ intercalated V₂O₅·nH₂O with enlarged layer spacing and fast ion diffusion as an aqueous zinc-ion battery cathode. *Energy Environ Sci*. 2018;11(11):3157-62. doi:10.1039/C8EE01651H
77. Cai Y, Liu F, Luo Z, Fang G, Zhou J, Pan A, et al. Pilotaxitic Na_{1.1}V₃O_{7.9} nanoribbons/graphene as high-performance sodium ion battery and aqueous zinc ion battery cathode. *Energy Storage Mater*. 2018;13:168-74. doi:10.1016/j.ensm.2018.01.009
78. Pang Q, Sun C, Yu Y, Zhao K, Zhang Z, Voyles PM, et al. H₂V₃O₈ nanowire/graphene electrodes for aqueous rechargeable zinc ion batteries with

- high rate capability and large capacity. *Adv Energy Mater.* 2018;8(19):1800144. doi:10.1002/aenm.201800144
79. Hu F, Xie D, Cui F, Zhang D, Song G. Synthesis and electrochemical performance of NaV_3O_8 nanobelts for Li/Na-ion batteries and aqueous zinc-ion batteries. *RSC Adv.* 2019;9(36):20549-56. doi:10.1039/C9RA04339J
80. Sambandam B, Soundharrajan V, Kim S, Alfaruqi MH, Jo J, Kim S, et al. Aqueous rechargeable Zn-ion batteries: An imperishable and high-energy $\text{Zn}_2\text{V}_2\text{O}_7$ nanowire cathode through intercalation regulation. *J Mater Chem A.* 2018;6(9):3850-6. doi:10.1039/C7TA11237H
81. Jiao T, Yang Q, Wu S, Wang Z, Chen D, Shen D, et al. Binder-free hierarchical VS_2 electrodes for high-performance aqueous Zn ion batteries towards commercial level mass loading. *J Mater Chem A.* 2019;7(27):16330-8. doi:10.1039/C9TA04798K
82. Park J-S, Jo JH, Aniskevich Y, Bakavets A, Ragoisha G, Streltsov E, et al. Open-structured vanadium dioxide as an intercalation host for Zn ions: Investigation by first-principles calculation and experiments. *Chem Mater.* 2018;30(19):6777-87. doi:10.1021/acs.chemmater.8b02679
83. Tang B, Fang G, Zhou J, Wang L, Lei Y, Wang C, et al. Potassium vanadates with stable structure and fast ion diffusion channel as cathode for rechargeable aqueous zinc-ion batteries. *Nano Energy.* 2018;51:579-87. doi:10.1016/j.nanoen.2018.07.014
84. Yang G, Wei T, Wang C. Self-healing lamellar structure boosts highly stable zinc-storage property of bilayered vanadium oxides. *ACS Appl Mat Interfaces.* 2018;10(41):35079-89. doi:10.1021/acsami.8b10849
85. Zeng Y, Lai Z, Han Y, Zhang H, Xie S, Lu X. Oxygen-vacancy and surface modulation of ultrathin nickel cobaltite nanosheets as a high-energy cathode for advanced Zn-ion batteries. *Adv Mater.* 2018;30(33):1802396. doi:10.1002/adma.201802396
86. Chen H, Shen Z, Pan Z, Kou Z, Liu X, Zhang H, et al. Hierarchical micro-nano sheet arrays of nickel-cobalt double hydroxides for high-rate Ni-Zn batteries. *Adv Sci.* 2019;6(8):1802002. doi:10.1002/advs.201802002
87. Ma L, Chen S, Li H, Ruan Z, Tang Z, Liu Z, et al. Initiating a mild aqueous electrolyte $\text{Co}_3\text{O}_4/\text{Zn}$ battery with 2.2 V-high voltage and 5000-cycle lifespan by

- a Co(III) rich-electrode. *Energy Environ Sci.* 2018;11(9):2521-30.
doi:10.1039/C8EE01415A
88. Zhang L, Chen L, Zhou X, Liu Z. Towards high-voltage aqueous metal-ion batteries beyond 1.5 V: The zinc/zinc hexacyanoferrate system. *Adv Energy Mater.* 2015;5(2):1400930. doi:10.1002/aenm.201400930
89. Kasiri G, Glenneberg J, Hashemi AB, Kun R, La Mantia F. Mixed copper-zinc hexacyanoferrates as cathode materials for aqueous zinc-ion batteries. *Energy Storage Mater.* 2019;19:360-9. doi:10.1016/j.ensm.2019.03.006
90. Hu P, Zhu T, Wang X, Zhou X, Wei X, Yao X, et al. Aqueous Zn//Zn(CF₃SO₃)₂//Na₃V₂(PO₄)₃ batteries with simultaneous Zn²⁺/Na⁺ intercalation/de-intercalation. *Nano Energy.* 2019;58:492-8. doi:10.1016/j.nanoen.2019.01.068
91. Wan F, Zhang L, Wang X, Bi S, Niu Z, Chen J. An aqueous rechargeable zinc-organic battery with hybrid mechanism. *Adv Funct Mater.* 2018;28(45):1804975. doi:10.1002/adfm.201804975
92. Kundu D, Oberholzer P, Glaros C, Bouzid A, Tervoort E, Pasquarello A, et al. Organic cathode for aqueous Zn-ion batteries: Taming a unique phase evolution toward stable electrochemical cycling. *Chem Mater.* 2018;30(11):3874-81. doi:10.1021/acs.chemmater.8b01317
93. Huang S, Zhu J, Tian J, Niu Z. Recent progress in the electrolytes of aqueous zinc-ion batteries. *Chem Eur J.* 2019;25(64):14480-94. doi:10.1002/chem.201902660
94. Cheng FY, Chen J, Gou XL, Shen PW. High-power alkaline Zn-MuO₂ batteries using γ -MnO₂ nanowires/nanotubes and electrolytic zinc powder. *Adv Mater.* 2005;17(22):2753-2756. doi:10.1002/adma.200500663
95. Hertzberg BJ, Huang A, Hsieh A, Chamoun M, Davies G, Seo JK, et al. Effect of multiple cation electrolyte mixtures on rechargeable Zn–MnO₂ alkaline battery. *Chem Mater.* 2016;28(13):4536-45. doi:10.1021/acs.chemmater.6b00232
96. Hu P, Wang T, Zhao J, Zhang C, Ma J, Du H, et al. Ultrafast alkaline Ni/Zn battery based on Ni-foam-supported Ni₃S₂ nanosheets. *ACS Appl Mater Interfaces.* 2015;7(48):26396-9. doi:10.1021/acsami.5b09728

97. Li J, Chen C. The novel mesoporous NiO/C microspheres as cathode material for alkaline NiO-Zn battery. *J Porous Mater.* 2020;27:1447-54. doi:10.1007/s10934-020-00921-0
98. Tang Y, Li X, Lv H, Xie D, Wang W, Zhi C, et al. Stabilized Co³⁺/Co⁴⁺ redox pair in in situ produced CoSe_{2-x}-derived cobalt oxides for alkaline Zn batteries with 10 000-cycle lifespan and 1.9-V voltage plateau. *Adv Energy Mater.* 2020;10(25):2000892. doi:10.1002/aenm.202000892
99. Berchmans S, Bandodkar AJ, Jia W, Ramirez J, Meng YS, Wang J. An epidermal alkaline rechargeable Ag-Zn printable tattoo battery for wearable electronics. *J Mater Chem A.* 2014;2(38):15788-95. doi:10.1039/C4TA03256J
100. Huang J, Yang Z. A one-pot method to prepare a ZnO/Ag/polypyrrole composite for zinc alkaline secondary batteries. *RSC Adv.* 2015;5(43):33814-7. doi:10.1039/C5RA01452B
101. Zhu Q, Cheng M, Zhang B, Jin K, Chen S, Ren Z, et al. Realizing a rechargeable high-performance Cu-Zn battery by adjusting the solubility of Cu²⁺. *Adv Funct Mater.* 2019;29(50):1905979. doi:10.1002/adfm.201905979
102. Ingale ND, Gallaway JW, Nyce M, Couzis A, Banerjee S. Rechargeability and economic aspects of alkaline zinc-manganese dioxide cells for electrical storage and load leveling. *J Power Sources.* 2015;276:7-18. doi:10.1016/j.jpowsour.2014.11.010
103. Im D, Manthiram A. Role of bismuth and factors influencing the formation of Mn₃O₄ in rechargeable alkaline batteries based on bismuth-containing manganese oxides. *J Electrochem Soc.* 2002;150(1):A68-73. doi:10.1149/1.1524611
104. Xia X, Zhang C, Guo Z, Liu HK, Walter G. Studies on electrochemical performance of partially reduced MnO₂ used as cathode for MH-MnO₂ rechargeable battery. *J Power Sources.* 2002;109(1):11-6. doi:10.1016/S0378-7753(02)00019-8
105. Yadav GG, Wei X, Huang J, Gallaway JW, Turney DE, Nyce M, et al. A conversion-based highly energy dense Cu²⁺ intercalated Bi-birnessite/Zn alkaline battery. *J Mater Chem A.* 2017;5(30):15845-54. doi:10.1039/C7TA05347A

106. Liu J, Guan C, Zhou C, Fan Z, Ke Q, Zhang G, et al. A flexible quasi-solid-state nickel–zinc battery with high energy and power densities based on 3D electrode design. *Adv Mater.* 2016;28(39):8732-9. doi:10.1002/adma.201603038
107. Fu X-Z, Xu Q-C, Hu R-Z, Pan B-X, Lin J-D, Liao D-W. β -CoOOH coated spherical β -NiOOH as the positive electrode material for alkaline Zn-NiOOH battery. *J Power Sources.* 2007;164(2):916-20. doi:10.1016/j.jpowsour.2006.09.112
108. Wang X, Wang F, Wang L, Li M, Wang Y, Chen B, et al. An aqueous rechargeable Zn//Co₃O₄ battery with high energy density and good cycling behavior. *Adv Mater.* 2016;28(24):4904-11. doi:10.1002/adma.201505370
109. Zhang S-W, Yin B-S, Luo Y-Z, Shen L, Tang B-S, Kou Z, et al. Fabrication and theoretical investigation of cobaltosic sulfide nanosheets for flexible aqueous Zn/Co batteries. *Nano Energy.* 2020;68:104314. doi:10.1016/j.nanoen.2019.104314
110. Le S, Zhang L, Song X, He S, Yuan Z, Liu F, et al. Status of zinc-silver battery. *J Electrochem Soc.* 2019;166(13):A2980-9. Doi:10.1149/2.1001913jes
111. Li C, Zhang Q, Sun J, Li T, E S, Zhu Z, et al. High-performance quasi-solid-state flexible aqueous rechargeable Ag–Zn battery based on metal–organic framework-derived Ag nanowires. *ACS Energy Lett.* 2018;3(11):2761-8. doi:10.1021/acseenergylett.8b01675
112. Ma Y, Xiao X, Yu W, Shang W, Tan P, Wu Z, et al. Mathematical modeling and numerical analysis of the discharge process of an alkaline zinc-cobalt battery. *J Energy Storage.* 2020;30:101432. doi:10.1016/j.est.2020.101432
113. Aurbach D, McCloskey BD, Nazar LF, Bruce PG. Advances in understanding mechanisms underpinning lithium–air batteries. *Nat Energy.* 2016;1:16128. doi:10.1038/nenergy.2016.128
114. Song M-K, Park S, Alamgir FM, Cho J, Liu M. Nanostructured electrodes for lithium-ion and lithium-air batteries: The latest developments, challenges, and perspectives. *Mater Sci Eng, R.* 2011;72(11):203-52. doi:10.1016/j.mser.2011.06.001
115. Cheng F, Chen J. Metal-air batteries: From oxygen reduction electrochemistry to cathode catalysts. *Chem Soc Rev.* 2012;41(6):2172-92. doi:10.1039/C1CS15228A

116. Li L, Chang Z-w, Zhang X-B. Recent progress on the development of metal-air batteries. *Adv Sustainable Syst.* 2017;1(10):1700036.
doi:10.1002/adsu.201700036
117. Geng D, Ding N, Hor TSA, Chien SW, Liu Z, Wu D, et al. From lithium-oxygen to lithium-air batteries: Challenges and opportunities. *Adv Energy Mater.* 2016;6(9):1502164. doi:10.1002/aenm.201502164
118. Chen X, Zhou Z, Karahan HE, Shao Q, Wei L, Chen Y. Recent advances in materials and design of electrochemically rechargeable zinc-air batteries. *Small.* 2018;14(44):1801929. doi:10.1002/sml.201801929
119. Cai X, Lai L, Lin J, Shen Z. Recent advances in air electrodes for Zn-air batteries: Electrocatalysis and structural design. *Mater Horiz.* 2017;4(6):945-76. doi:10.1039/C7MH00358G
120. Tan P, Chen B, Xu H, Zhang H, Cai W, Ni M, et al. Flexible Zn- and Li-air batteries: Recent advances, challenges, and future perspectives. *Energy Environ Sci.* 2017;10(10):2056-80. doi:10.1039/C7EE01913K
121. Pan J, Xu YY, Yang H, Dong Z, Liu H, Xia BY. Advanced architectures and relatives of air electrodes in Zn-air batteries. *Adv Sci.* 2018;5(4):1700691. doi:10.1002/advs.201700691
122. Wang H-F, Tang C, Wang B, Li B-Q, Zhang Q. Bifunctional transition metal hydroxysulfides: Room-temperature sulfurization and their applications in Zn-air batteries. *Adv Mater.* 2017;29(35):1702327. doi:10.1002/adma.201702327
123. Zhang J, Zhao Z, Xia Z, Dai L. A metal-free bifunctional electrocatalyst for oxygen reduction and oxygen evolution reactions. *Nat Nanotechnol.* 2015;10(5):444-52. doi:10.1038/nnano.2015.48
124. Tahir M, Pan L, Idrees F, Zhang X, Wang L, Zou J-J, et al. Electrocatalytic oxygen evolution reaction for energy conversion and storage: A comprehensive review. *Nano Energy.* 2017;37:136-57. doi:10.1016/j.nanoen.2017.05.022
125. Xia W, Mahmood A, Liang Z, Zou R, Guo S. Earth-abundant nanomaterials for oxygen reduction. *Angew Chem Int Ed.* 2016;55(8):2650-76. doi:10.1002/anie.201504830
126. Shao M, Chang Q, Dodelet J-P, Chenitz R. Recent advances in electrocatalysts for oxygen reduction reaction. *Chem Rev.* 2016;116(6):3594-657. doi:10.1021/acs.chemrev.5b00462

127. Qian Y, Khan IA, Zhao D. Electrocatalysts derived from metal-organic frameworks for oxygen reduction and evolution reactions in aqueous media. *Small*. 2017;13(37):1701143. doi:10.1002/sml.201701143
128. Davari E, Ivey DG. Bifunctional electrocatalysts for Zn-air batteries. *Sustainable Energy Fuels*. 2018;2(1):39-67. doi:10.1039/C7SE00413C
129. Deng Y-P, Jiang Y, Liang R, Zhang S-J, Luo D, Hu Y, et al. Dynamic electrocatalyst with current-driven oxyhydroxide shell for rechargeable zinc-air battery. *Nat Commun*. 2020;11:1952. doi:10.1038/s41467-020-15853-1
130. Yang HB, Miao J, Hung S-F, Chen J, Tao HB, Wang X, et al. Identification of catalytic sites for oxygen reduction and oxygen evolution in N-doped graphene materials: Development of highly efficient metal-free bifunctional electrocatalyst. *Sci Adv*. 2016;2(4):e1501122. doi:10.1126/sciadv.1501122
131. Wang D-W, Su D. Heterogeneous nanocarbon materials for oxygen reduction reaction. *Energy Environ Sci*. 2014;7(2):576-91. doi:10.1039/C3EE43463J
132. Wang H-F, Tang C, Zhang Q. A review of precious-metal-free bifunctional oxygen electrocatalysts: Rational design and applications in Zn-air batteries. *Adv Funct Mater*. 2018;28(46):1803329. doi:10.1002/adfm.201803329
133. Fu Y, Yu H-Y, Jiang C, Zhang T-H, Zhan R, Li X, et al. NiCo alloy nanoparticles decorated on N-doped carbon nanofibers as highly active and durable oxygen electrocatalyst. *Adv Funct Mater*. 2018;28(9):1705094. doi:10.1002/adfm.201705094
134. Zhu Y, Zhou W, Shao Z. Perovskite/carbon composites: Applications in oxygen electrocatalysis. *Small*. 2017;13(12):1603793. doi:10.1002/sml.201603793
135. Hong WT, Risch M, Stoerzinger KA, Grimaud A, Suntivich J, Shao-Horn Y. Toward the rational design of non-precious transition metal oxides for oxygen electrocatalysis. *Energy Environ Sci*. 2015;8(5):1404-27. doi:10.1039/C4EE03869J
136. Yin H, Tang Z. Ultrathin two-dimensional layered metal hydroxides: An emerging platform for advanced catalysis, energy conversion and storage. *Chem Soc Rev*. 2016;45(18):4873-91. doi:10.1039/C6CS00343E
137. Fu G, Lee J-M. Ternary metal sulfides for electrocatalytic energy conversion. *J Mater Chem A*. 2019;7(16):9386-405. doi:10.1039/C9TA01438A

138. Xu K, Chen P, Li X, Tong Y, Ding H, Wu X, et al. Metallic nickel nitride nanosheets realizing enhanced electrochemical water oxidation. *J Am Chem Soc.* 2015;137(12):4119-25. doi:10.1021/ja5119495
139. Balogun M-S, Huang Y, Qiu W, Yang H, Ji H, Tong Y. Updates on the development of nanostructured transition metal nitrides for electrochemical energy storage and water splitting. *Mater Today.* 2017;20(8):425-51. doi:10.1016/j.mattod.2017.03.019
140. Li B, Ge X, Goh FWT, Hor TSA, Geng D, Du G, et al. Co_3O_4 nanoparticles decorated carbon nanofiber mat as binder-free air-cathode for high performance rechargeable zinc-air batteries. *Nanoscale.* 2015;7(5):1830-8. doi:10.1039/C4NR05988C
141. Li Y, Zhong C, Liu J, Zeng X, Qu S, Han X, et al. Atomically thin mesoporous Co_3O_4 layers strongly coupled with N-rGO nanosheets as high-performance bifunctional catalysts for 1D knittable zinc-air batteries. *Adv Mater.* 2018;30(4):1703657. doi:10.1002/adma.201703657
142. Yu M, Wang Z, Hou C, Wang Z, Liang C, Zhao C, et al. Nitrogen-doped Co_3O_4 mesoporous nanowire arrays as an additive-free air-cathode for flexible solid-state zinc-air batteries. *Adv Mater.* 2017;29(15):1602868. doi:10.1002/adma.201602868
143. Goh FWT, Liu Z, Ge X, Zong Y, Du G, Hor TSA. Ag nanoparticle-modified MnO_2 nanorods catalyst for use as an air electrode in zinc-air battery. *Electrochim Acta.* 2013;114:598-604. doi:10.1016/j.electacta.2013.10.116
144. Du G, Liu X, Zong Y, Hor TSA, Yu A, Liu Z. Co_3O_4 nanoparticle-modified MnO_2 nanotube bifunctional oxygen cathode catalysts for rechargeable zinc-air batteries. *Nanoscale.* 2013;5(11):4657-61. doi:10.1039/C3NR00300K
145. Chen Z, Yu A, Ahmed R, Wang H, Li H, Chen Z. Manganese dioxide nanotube and nitrogen-doped carbon nanotube based composite bifunctional catalyst for rechargeable zinc-air battery. *Electrochim Acta.* 2012;69:295-300. doi:10.1016/j.electacta.2012.03.001
146. Pan J, Tian XL, Zaman S, Dong Z, Liu H, Park HS, et al. Recent progress on transition metal oxides as bifunctional catalysts for lithium-air and zinc-air batteries. *Batteries Supercaps.* 2019;2(4):336-47. doi:10.1002/batt.201800082
147. Prabu M, Ramakrishnan P, Shanmugam S. CoMn_2O_4 nanoparticles anchored on nitrogen-doped graphene nanosheets as bifunctional electrocatalyst for

- rechargeable zinc-air battery. *Electrochem Commun.* 2014;41:59-63.
doi:10.1016/j.elecom.2014.01.027
148. Lin C, Shinde SS, Jiang Z, Song X, Sun Y, Guo L, et al. In situ directional formation of Co@CoO_x-embedded 1D carbon nanotubes as an efficient oxygen electrocatalyst for ultra-high rate Zn-air batteries. *J Mater Chem A.* 2017;5(27):13994-4002. doi:10.1039/C7TA02215H
149. Li Y-J, Cui L, Da P-F, Qiu K-W, Qin W-J, Hu W-B, et al. Multiscale structural engineering of Ni-doped CoO nanosheets for zinc-air batteries with high power density. *Adv Mater.* 2018;30(46):1804653. doi:10.1002/adma.201804653
150. Yin J, Li Y, Lv F, Fan Q, Zhao Y-Q, Zhang Q, et al. NiO/CoN porous nanowires as efficient bifunctional catalysts for Zn-air batteries. *ACS Nano.* 2017;11(2):2275-83. doi:10.1021/acsnano.7b00417
151. Wang P, Lin Y, Wan L, Wang B. Construction of a Janus MnO₂-NiFe electrode via selective electrodeposition strategy as a high-performance bifunctional electrocatalyst for rechargeable zinc-air batteries. *ACS Appl Mater Interfaces.* 2019;11(41):37701-7. doi:10.1021/acscami.9b12232
152. Prabu M, Ramakrishnan P, Nara H, Momma T, Osaka T, Shanmugam S. Zinc-air battery: Understanding the structure and morphology changes of graphene-supported CoMn₂O₄ bifunctional catalysts under practical rechargeable conditions. *ACS Appl Mater Interfaces.* 2014;6(19):16545-55. doi:10.1021/am5047476
153. Guo X, Zheng T, Ji G, Hu N, Xu C, Zhang Y. Core/shell design of efficient electrocatalysts based on NiCo₂O₄ nanowires and NiMn LDH nanosheets for rechargeable zinc-air batteries. *J Mater Chem A.* 2018;6(22):10243-52. doi:10.1039/C8TA02608D
154. Li B, Ruan J, Loh A, Chai J, Chen Y, Tan C, et al. A robust hybrid Zn-battery with ultralong cycle life. *Nano Lett.* 2017;17(1):156-63. doi:10.1021/acs.nanolett.6b03691
155. Wang X-T, Ouyang T, Wang L, Zhong J-H, Ma T, Liu Z-Q. Redox-inert Fe³⁺ ions in octahedral sites of Co-Fe spinel oxides with enhanced oxygen catalytic activity for rechargeable zinc-air batteries. *Angew Chem Int Ed.* 2019;58(38):13291-6. doi:10.1002/anie.201907595
156. Wang X, Li Y, Jin T, Meng J, Jiao L, Zhu M, et al. Electrospun thin-walled CuCo₂O₄@C nanotubes as bifunctional oxygen electrocatalysts for rechargeable

- Zn-air batteries. *Nano Lett.* 2017;17(12):7989-94.
doi:10.1021/acs.nanolett.7b04502
157. Park HW, Lee DU, Zamani P, Seo MH, Nazar LF, Chen Z. Electrospun porous nanorod perovskite oxide/nitrogen-doped graphene composite as a bi-functional catalyst for metal air batteries. *Nano Energy.* 2014;10:192-200.
doi:10.1016/j.nanoen.2014.09.009
158. Bu Y, Gwon O, Nam G, Jang H, Kim S, Zhong Q, et al. A highly efficient and robust cation ordered perovskite oxide as a bifunctional catalyst for rechargeable zinc-air batteries. *ACS Nano.* 2017;11(11):11594-601.
doi:10.1021/acsnano.7b06595
159. Wang X, Sunarso J, Lu Q, Zhou Z, Dai J, Guan D, et al. High-performance platinum-perovskite composite bifunctional oxygen electrocatalyst for rechargeable Zn-air battery. *Adv Energy Mater.* 2020;10(5):1903271.
doi:10.1002/aenm.201903271
160. Zhou T, Zhang N, Wu C, Xie Y. Surface/interface nanoengineering for rechargeable Zn-air batteries. *Energy Environ Sci.* 2020;13(4):1132-53.
doi:10.1039/C9EE03634B
161. Jung K-N, Jung J-H, Im WB, Yoon S, Shin K-H, Lee J-W. Doped lanthanum nickelates with a layered perovskite structure as bifunctional cathode catalysts for rechargeable metal-air batteries. *ACS Appl Mater Interfaces.* 2013;5(20):9902-7. doi:10.1021/am403244k
162. Ni S, Zhang H, Zhao Y, Li X, Sun Y, Qian J, et al. Single atomic Ag enhances the bifunctional activity and cycling stability of MnO₂. *Chem Eng J.* 2019;366:631-8. doi:10.1016/j.cej.2019.02.084
163. Bian J, Su R, Yao Y, Wang J, Zhou J, Li F, et al. Mg doped perovskite LaNiO₃ nanofibers as an efficient bifunctional catalyst for rechargeable zinc-air batteries. *ACS Appl Energy Mater.* 2019;2(1):923-31. doi:10.1021/acsaem.8b02183
164. Qian J, Bai X, Xi S, Xiao W, Gao D, Wang J. Bifunctional electrocatalytic activity of nitrogen-doped NiO nanosheets for rechargeable zinc-air batteries. *ACS Appl Mater Interfaces.* 2019;11(34):30865-71.
doi:10.1021/acsaem.9b08647
165. Xu N, Liu Y, Zhang X, Li X, Li A, Qiao J, et al. Self-assembly formation of Bi-functional Co₃O₄/MnO₂-CNTs hybrid catalysts for achieving both high

- energy/power density and cyclic ability of rechargeable zinc-air battery. *Sci Rep.* 2016;6:33590. doi:10.1038/srep33590
166. Ma H, Wang B. A bifunctional electrocatalyst α -MnO₂-LaNiO₃/carbon nanotube composite for rechargeable zinc-air batteries. *Rsc Advances.* 2014;4(86):46084-92. doi:10.1039/C4RA07401G
167. Kim J, Gwon O, Kwon O, Mahmood J, Kim C, Yang Y, et al. Synergistic coupling derived cobalt oxide with nitrogenated holey two-dimensional matrix as an efficient bifunctional catalyst for metal-air batteries. *ACS Nano.* 2019;13(5):5502-12. doi:10.1021/acsnano.9b00320
168. Zhou T, Xu W, Zhang N, Du Z, Zhong C, Yan W, et al. Ultrathin cobalt oxide layers as electrocatalysts for high-performance flexible Zn-air batteries. *Adv Mater.* 2019;31(15):1807468. doi:10.1002/adma.201807468
169. Lu XF, Chen Y, Wang S, Gao S, Lou XW. Interfacing manganese oxide and cobalt in porous graphitic carbon polyhedrons boosts oxygen electrocatalysis for Zn-air batteries. *Adv Mater.* 2019;31(39):1902339. doi:10.1002/adma.201902339
170. Jiang Y, Deng Y-P, Fu J, Lee DU, Liang R, Cano ZP, et al. Interpenetrating triphase cobalt-based nanocomposites as efficient bifunctional oxygen electrocatalysts for long-lasting rechargeable Zn-air batteries. *Adv Energy Mater.* 2018;8(15):1702900. doi:10.1002/aenm.201702900
171. Lu Q, Yu J, Zou X, Liao K, Tan P, Zhou W, et al. Self-catalyzed growth of Co, N-codoped CNTs on carbon-encased CoS_x surface: A noble-metal-free bifunctional oxygen electrocatalyst for flexible solid Zn-air batteries. *Adv Funct Mater.* 2019;29(38):1904481. doi:10.1002/adfm.201904481
172. Wei L, Karahan HE, Zhai S, Liu H, Chen X, Zhou Z, et al. Amorphous bimetallic oxide-graphene hybrids as bifunctional oxygen electrocatalysts for rechargeable Zn-air batteries. *Adv Mater.* 2017;29(38):1701410. doi:10.1002/adma.201701410
173. Lee DU, Choi J-Y, Feng K, Park HW, Chen Z. Advanced extremely durable 3D bifunctional air electrodes for rechargeable zinc-air batteries. *Adv Energy Mater.* 2014;4(6):1301389. doi:10.1002/aenm.201301389
174. Fu J, Hassan FM, Li J, Lee DU, Ghannoum AR, Lui G, et al. Flexible rechargeable zinc-air batteries through morphological emulation of human hair array. *Adv Mater.* 2016;28(30):6421-8. doi:10.1002/adma.201600762

175. Ren J-T, Yuan G-G, Weng C-C, Yuan Z-Y. Rationally designed Co_3O_4 -C nanowire arrays on Ni foam derived from metal organic framework as reversible oxygen evolution electrodes with enhanced performance for Zn-air batteries. *ACS Sustainable Chem Eng.* 2018;6(1):707-18. doi:10.1021/acssuschemeng.7b03034
176. Sumboja A, Lubke M, Wang Y, An T, Zong Y, Liu Z. All-solid-state, foldable, and rechargeable Zn-air batteries based on manganese oxide grown on graphene-coated carbon cloth air cathode. *Adv Energy Mater.* 2017;7(20):1700927. doi:10.1002/aenm.201700927
177. Chen X, Liu B, Zhong C, Liu Z, Liu J, Ma L, et al. Ultrathin Co_3O_4 layers with large contact area on carbon fibers as high-performance electrode for flexible zinc-air battery integrated with flexible display. *Adv Energy Mater.* 2017;7(18):1700779. doi:10.1002/aenm.201700779
178. Park MG, Lee DU, Seo MH, Cano ZP, Chen Z. 3D ordered mesoporous bifunctional oxygen catalyst for electrically rechargeable zinc-air batteries. *Small.* 2016;12(20):2707-14. doi:10.1002/smll.201600051
179. Ishihara T, Guo LM, Miyano T, Inoishi Y, Kaneko K, Ida S. Mesoporous $\text{La}_{0.6}\text{Ca}_{0.4}\text{CoO}_3$ perovskites with large surface areas as stable air electrodes for rechargeable Zn-air batteries. *J Mater Chem A.* 2018;6(17):7686-92. doi:10.1039/C8TA00426A
180. Lee DU, Scott J, Park HW, Abureden S, Choi J-Y, Chen Z. Morphologically controlled Co_3O_4 nanodisks as practical bi-functional catalyst for rechargeable zinc-air battery applications. *Electrochem Commun.* 2014;43:109-12. doi:10.1016/j.elecom.2014.03.020
181. Prabu M, Ketpang K, Shanmugam S. Hierarchical nanostructured NiCo_2O_4 as an efficient bifunctional non-precious metal catalyst for rechargeable zinc-air batteries. *Nanoscale.* 2014;6(6):3173-81. doi:10.1039/C3NR05835B
182. Singh SK, Dhavale VM, Kurungot S. Surface-tuned Co_3O_4 nanoparticles dispersed on nitrogen-doped graphene as an efficient cathode electrocatalyst for mechanical rechargeable zinc-air battery application. *ACS Appl Mater Interfaces.* 2015;7(38):21138-49. doi:10.1021/acsami.5b04865
183. Lee J-S, Nam G, Sun J, Higashi S, Lee H-W, Lee S, et al. Composites of a Prussian blue analogue and gelatin-derived nitrogen-doped carbon-supported

- porous spinel oxides as electrocatalysts for a Zn-air battery. *Adv Energy Mater.* 2016;6(22):1601052. doi:10.1002/aenm.201601052
184. Arafat Y, Azhar MR, Zhong Y, Xu X, Tadé MO, Shao Z. A porous nano-micro-composite as a high-performance bi-functional air electrode with remarkable stability for rechargeable zinc-air batteries. *Nano-Micro Lett.* 2020;12:130. doi:10.1007/s40820-020-00468-4
185. Wang X, Ge L, Lu Q, Dai J, Guan D, Ran R, et al. High-performance metal-organic framework-perovskite hybrid as an important component of the air-electrode for rechargeable Zn-Air battery. *J Power Sources.* 2020;468:228377. doi:10.1016/j.jpowsour.2020.228377
186. Lee DU, Fu J, Park MG, Liu H, Ghorbani Kashkooli A, Chen Z. Self-assembled NiO/Ni(OH)₂ nanoflakes as active material for high-power and high-energy hybrid rechargeable battery. *Nano Lett.* 2016;16(3):1794-802. doi:10.1021/acs.nanolett.5b04788
187. Tan P, Chen B, Xu H, Cai W, Liu M, Shao Z, et al. Nanoporous NiO/Ni(OH)₂ plates incorporated with carbon nanotubes as active materials of rechargeable hybrid zinc batteries for improved energy efficiency and high-rate capability. *J Electrochem Soc.* 2018;165(10):A2119-26. doi:10.1149/2.0481810jes
188. Cheng Y, Zhang N, Wang Q, Guo Y, Tao S, Liao Z, et al. A long-life hybrid zinc flow battery achieved by dual redox couples at cathode. *Nano Energy.* 2019;63:103822. doi:10.1016/j.nanoen.2019.06.018
189. Ma L, Chen S, Pei Z, Li H, Wang Z, Liu Z, et al. Flexible waterproof rechargeable hybrid zinc batteries initiated by multifunctional oxygen vacancies-rich cobalt oxide. *ACS Nano.* 2018;12(8):8597-605. doi:10.1021/acsnano.8b04317
190. Tan P, Chen B, Xu H, Cai W, He W, Liu M, et al. Co₃O₄ nanosheets as active material for hybrid Zn batteries. *Small.* 2018;14(21):1800225. doi:10.1002/smll.201800225
191. Tan P, Chen B, Xu H, Cai W, He W, Ni M. In-situ growth of Co₃O₄ nanowire-assembled clusters on nickel foam for aqueous rechargeable Zn-Co₃O₄ and Zn-air batteries. *Appl Catal, B.* 2019;241:104-12. doi:10.1016/j.apcatb.2018.09.017
192. Liu S, Zhao L, Cui B, Liu X, Han W, Zhang J, et al. A long life and high efficient rechargeable hybrid zinc-air/Co₃O₄ battery with stable high working voltage. *Ionics.* 2020;26(2):767-75. doi:10.1007/s11581-019-03226-8

193. Xu D, Wu S, Xu X, Wang Q. Hybrid Zn battery with coordination-polymer-derived, oxygen-vacancy-rich Co_3O_4 as a cathode material. *ACS Sustainable Chem Eng.* 2020;8(11):4384-91. doi:10.1021/acssuschemeng.9b06715
194. Wu M, Zhang G, Chen N, Chen W, Qiao J, Sun S. A self-supported electrode as a high-performance binder- and carbon-free cathode for rechargeable hybrid zinc batteries. *Energy Storage Mater.* 2020;24:272-80. doi:10.1016/j.ensm.2019.08.009
195. Tan P, Chen B, Xu H, Cai W, He W, Zhang H, et al. Integration of Zn–Ag and Zn–Air batteries: A hybrid battery with the advantages of both. *ACS Appl. Mater. Interfaces.* 2018;10(43):36873-81. doi:10.1021/acsaami.8b10778
196. Chang C-C, Lee Y-C, Liao H-J, Kao Y-T, An J-Y, Wang D-Y. Flexible hybrid Zn–Ag/Air battery with long cycle life. *ACS Sustainable Chem Eng.* 2019;7(2):2860-6. doi:10.1021/acssuschemeng.8b06328
197. Huang Z, Li X, Yang Q, Ma L, Mo F, Liang G, et al. $\text{Ni}_3\text{S}_2/\text{Ni}$ nanosheet arrays for high-performance flexible zinc hybrid batteries with evident two-stage charge and discharge processes. *J Mater Chem A.* 2019;7(32):18915-24. doi:10.1039/C9TA06337D
198. Wang X, Xu X, Chen J, Wang Q. Combination of Zn- NiCo_2S_4 and Zn-Air batteries at the cell level: A hybrid battery makes the best of both worlds. *ACS Sustainable Chem Eng.* 2019;7(14):12331-9. doi:10.1021/acssuschemeng.9b01707

Every reasonable effort has been made to acknowledge the owners of copyright material. I would be pleased to hear from any copyright owner who has been omitted or incorrectly acknowledged.

Chapter 3 Self-recovery chemistry on cobalt-modified δ - MnO_2 nanosheets as high-performance and durable aqueous zinc-ion battery cathodes §

Abstract

Rechargeable Zn-ion batteries working with manganese oxide cathodes and mild aqueous electrolytes suffer from notorious cathode dissolution during galvanostatic cycling. Herein, for the first time we demonstrate the dynamic self-recovery chemistry of manganese compound during charge/discharge processes, which strongly determines the battery performance. A cobalt-modified δ - MnO_2 with a redox-active surface shows superior self-recovery capability as a cathode. The cobalt-containing species in the cathode enable the efficient self-recovery by continuously catalyzing the electrochemical deposition of active Mn compound, which is confirmed by characterizations of both practical coin-type batteries and a new-designed electrolyzer system. Under optimized condition, a high specific capacity over 500 mAh g^{-1} is achieved, together with a decent cycling performance with a retention rate of 63% over 5000 cycles. With this cobalt-facilitated deposition effect, the battery with low concentration (0.02 M) of additive Mn^{2+} in the electrolyte (only 12 at% to the overall Mn) maintains decent capacity retention.

§ Reprinted (adapted) from (Zhong Y, Xu X, Veder J-P, Shao Z. Self-recovery chemistry and cobalt-catalyzed electrochemical deposition of cathode for boosting performance of aqueous zinc-ion batteries. *iScience*. 2020;23(3):100943. doi:10.1016/j.isci.2020.100943). Copyrights (2020) the authors, under a Creative Commons license.

3.1 Introduction

Zn-ion batteries have attracted increasing attention owing to the abundance of Zn resource and the relatively high electrochemical potential of Zn metal in neutral or mildly acidic aqueous electrolytes, which is beneficial to the stable performance.¹⁻³ In recent years, intensive efforts have been made to the investigation of the composition of aqueous electrolytes, the preparation and protection of Zn anodes, and the development of high-performance and stable cathode materials.³⁻⁵ Compared to metallic Zn anode, the capacity of the cathode is usually much lower, which becomes one of the bottlenecks for the commercialization of aqueous Zn-ion batteries. Till now, most of the research activities on Zn-ion batteries have been focused on the development and modification of the cathode.

Zn/MnO₂ battery is one of the earliest systems for primary Zn-ion batteries, which is achieved commercialization many years ago.⁶ Due to the fast kinetics of the Mn redox, Mn compounds (e.g., MnO₂) show promising capability as high-performance cathodes for rechargeable Zn-ion batteries.⁷⁻⁹ In recent years, a variety of modification strategies (e.g., pre-intercalation, heteroatom doping, and defect engineering) have been proposed for improving the performance of the Mn-based cathodes.¹⁰⁻¹³ For example, pre-intercalation of ions or molecules (e.g., Na⁺, Zn²⁺, polyaniline or water) in the layered MnO₂ can boost the redox kinetics by facilitating the charge storage.^{10,14,15} Doping cathode materials with cobalt or nickel is beneficial to improve the energy density of the cathode by increasing the discharge voltage or improving the electronic conductivity.^{11,16,17}

Despite significant advantages (e.g., high theoretical capacity, low cost, low toxicity), the notorious instability of the Mn-based cathodes during recharging cycles severely impedes their use in practical Zn-ion batteries.^{13,18} The instability could be mainly associated with the disproportionation of Mn(III), generating Mn(IV) and highly soluble Mn(II).^{2,19} It is important to note that for MnO₂, regardless of its initial phase structure (e.g., α -MnO₂, β -MnO₂, γ -MnO₂ or δ -MnO₂), this charge disproportionation is very likely to happen, leading to the same result of the dissolution and loss of active Mn compound and consequently deterioration of the capacity. To address this issue, additional Mn²⁺ at high concentrations (usually 0.1-0.5 M) was proposed to be introduced into the electrolyte to suppress the disproportionation reaction.^{5,8,13,14,20-22} The cycling stability of Mn-based cathodes have been greatly

enhanced by adopting this strategy. However, this enhancement is at the expense of reduced mass energy density of the battery, given that the large proportion of the extra Mn^{2+} occupies additional weight but might not provide decent capacity.

To date, mechanisms behind the enhanced stability of Zn-ion batteries with Mn^{2+} -containing electrolytes are still unclear. Recent reports have provided some clues that Mn^{2+} in the electrolyte can be oxidized, inducing the deposition of active Mn compound on the cathode surface.^{23,24} This suggests that the deposition of Mn compound from the Mn^{2+} -containing electrolytes is also an important phenomenon that deserves more research attention. Such a self-recovery phenomenon resulting from the deposition of Mn compound on the cathode may have a significant effect on the capacity and stability of Zn-ion batteries. However, most of the previous reports evaluated the capacity only based on the weight of the Mn-based cathode. In addition, only the Mn^{2+} concentration in the electrolyte was given while the information about the volume of the electrolyte and the Mn ratio (atomic/weight) of the solid Mn-based cathode to the aqueous Mn^{2+} in the electrolyte is lacking. This could lead to an unreliable comparison of the results across different publications. Due to the potential contribution of Mn^{2+} in electrolyte to the capacity, retention rates of the cathode much higher than 100% were observed in some literature reports where the capacity was calculated just based on the active material at the cathode.^{15,20,25,26}

All these facts emphasize the motivation of this work, i.e., to study self-recovery chemistry in the cathode of Zn-ion batteries, including the influencing parameters for the process and their interactions, and the mechanism behind the electrochemical deposition of Mn compound during the battery cycling. Based on the understanding of the self-recovery chemistry in the cathode, we further propose a cobalt-modified δ - MnO_2 as a cathode material with a redox-active surface for fast deposition of Mn compound. To emphasize the importance of the deposition rate of the Mn active compounds for the self-recovery cycling capacity, an equation that describes the dynamic capacity of the Mn-based cathode is also demonstrated. The cobalt-induced facilitating of deposition is confirmed by the electrochemical and chemical characterizations of both practical coin-type batteries and a new-designed electrolyzer system. Insights into the catalysis routes of the Mn compound deposition are also revealed. This work provides guidance of the utility of the Mn^{2+} -containing electrolyte for the development of Zn-ion batteries and may provide inspiration for the materials

engineering for future functionalized cathodes, especially for other conversion-type battery cathodes which have similar dissolution issues.

3.2 Experimental sections

Synthesis of δ -MnO₂ nanosheets and α -MnO₂ nanowires

A molten-salt assisted synthesis procedure reported by Hu et al.²⁷ was adjusted in this work for a 10-minute fast synthesis of δ -MnO₂ nanosheets. Typically, 15 g of NaNO₃ and 0.6 g of MnSO₄·H₂O were mixed and ground with mortar to obtain a light pink fine powder. The powder was placed in a 150-mL crucible and heated at 350 °C for 10 min with a heating rate of 10 °C min⁻¹. After the synthesis, the crucible was immediately removed from the furnace at 350 °C and rapidly cooled down to room temperature. 100 mL of deionized (DI) water was added into the crucible and the liquid mixture was continuously stirred for 30 min at room temperature to dissolve the sintered NaNO₃ salt, then the mixture was filtrated. This washing procedure was repeated several times to completely remove the residual salt. After drying in an oven at 60 °C, the δ -MnO₂ product was obtained.

α -MnO₂ nanowires were synthesized via a hydrothermal method.⁸ Herein, 0.51 g of MnSO₄·H₂O was dissolved in 90 mL of DI water, then 54.3 μ L of 98% sulfuric acid was added into the solution. After that, another solution containing 0.32 g of KMnO₄ and 20 mL of DI water was mixed with the as-prepared acidic MnSO₄ solution. The mixture was then stirred in a beaker for 1 h and then put into an ultrasonic bath for another 30 min. The mixture was transferred to two 100-mL Teflon lined hydrothermal autoclaves and was heated at 120 °C for 16 h. After the hydrothermal autoclaves were cooled to room temperature, the obtained mixture was vacuum filtered and washed with DI water several times. After drying in an oven at 60 °C, the α -MnO₂ was obtained.

Synthesis of cobalt-modified δ -MnO₂

Typically, 0.2 g of as-prepared δ -MnO₂ powder was mixed with a 20 mL of 1 M CoCl₂ aqueous solution by constant stirring for 8 h at room temperature. The mixture was filtrated, and the as-obtained powder was further stirred with a new 20 mL of 1 M CoCl₂ for another 16 h. Then the mixture was filtrated and washed by DI water three times to remove the residual CoCl₂. After drying in an oven at 60 °C, cobalt-modified δ -MnO₂ powder was obtained.

Material characterizations

Chemical composition of the materials was qualitatively observed by energy-dispersive X-ray spectroscopy (EDS, Titan G2) and was further quantitatively evaluated with inductively coupled plasma-optical emission spectrometry (ICP-OES). Morphologies of the materials were observed using scanning electron microscopy (SEM) and transmission electron microscopy (TEM, Titan G2). Crystal phase structures of the materials were characterized with a combined analysis of X-ray diffraction (XRD, Bruker D8 Advance, Cu K α radiation), high-resolution TEM (HR-TEM, Titan G2) and selected area electron diffraction (SAED, Titan G2). The thickness of the cobalt-modified δ -MnO₂ nanosheets was evaluated by TEM and confirmed by atomic force microscopy (AFM, Bruker Dimension Icon, platinum tip). Porosity and pore structure information was obtained with nitrogen adsorption/desorption (Micromeritics TriStar) at 77 K. Specific surface areas (S_{BET}) were evaluated using the Brunauer–Emmett–Teller (BET) theory. Total pore volumes were calculated with nitrogen uptake at $p/p^0 = 0.99$. Pore size distributions were calculated using Quenched Solid-State Functional Theory (QSDFT). Surface chemical states of the materials were analyzed with X-ray photoelectron spectroscopy (XPS, Kratos AXIS Ultra DLD, Al K α radiation) and near-edge X-ray absorption fine-structure spectroscopy (NEXAFS, Australian Synchrotron).

Electrochemical tests

Free-standing cathode film composed of cathode materials, conductive carbon (acetylene black) and polytetrafluoroethylene (PTFE) with a weight ratio of 7:2:1 were prepared for electrochemical performance tests. Typically, 0.07 g of MnO₂, 0.02 g of acetylene black, 1.67 g of 0.6 wt% PTFE (in ethanol solution) and 5 mL of absolute ethanol were mixed in a 30-mL bottle for 1 h using an ultrasonic bath. After drying the mixture at 60 °C in an oven, the dry powder was collected and wetted with ~500 μ L of absolute ethanol, forming a soft black gum. The gum was ground with a glass bar and then peeled off and dried at 60 °C in a vacuum oven for ~12 h. Dried film disks with a diameter of ϕ 8 mm (area: 0.5 cm², areal loading of MnO₂: ~2.0 mg cm⁻²) were cut using a hole puncher. Batteries were assembled as the order of a CR2032 positive case, a ϕ 16 mm stainless steel, a cathode film, a Whatman GF/D glass fiber, electrolyte, a 10x10 mm Zn plate, a ϕ 16 mm stainless steel, a stainless-steel shrapnel and a CR2032 negative case. Aqueous electrolyte for the Zn-ion batteries and for

electrochemical deposition experiment on stainless steel was 2 M ZnSO₄ and 0.2 M MnSO₄ in DI water unless otherwise specified. Electrolyte volume used in each battery was 200 μL unless otherwise specified. Galvanostatic discharge-charge profile of the batteries was recorded using LANHE CT2001A battery test system (5 V, 10 mA). The specific current densities and specific capacities were calculated based on the weight of MnO₂ in the cathodes unless otherwise specified. Cyclic voltammetry (CV) profiles of the batteries and linear sweep voltammetry (LSV) of the electrochemical deposition of active Mn compound were obtained using a Biologic VSP potentiostat system.

3.3 Results and discussions

3.3.1 Self-recovery chemistry in MnO₂ electrodes of Zn-ion batteries

Figure 3.1a presents the galvanostatic cycling stability of aqueous Zn-ion batteries working with several different MnO₂-based cathodes. Here, the capacity was calculated based on the mass of the initial weight of solid MnO₂ on the cathode. For fair comparison, parameters including 1) the mass loading of cathode (area: 0.5 cm², areal loading of MnO₂: ~2.0 mg cm⁻²), 2) the concentration of MnSO₄ additive (0.2 M), and 3) the volume of electrolyte (200 μL for each battery) were well-controlled for all batteries. The δ-MnO₂ cathode synthesized via a molten-salt assisted method showed an initial discharge capacity of 252 mAh g⁻¹, and reached 317 mAh g⁻¹ after a 5-cycle activation process (**Figure 3.1a**). Unlike most of the previously reported works, it is interesting that the discharge capacity of the δ-MnO₂ cathode kept increasing during subsequent cycling at a current density of 300 mA g⁻¹, and reached a discharge capacity of 403 mAh g⁻¹ after 100 cycles. α-MnO₂, another cathode material widely utilized in Zn-ion batteries, was also evaluated for its cycling stability. Although showing better discharge capacities in the first 5 cycles (1st discharge: 325 mAh g⁻¹ and 5th discharge: 339 mAh g⁻¹), the α-MnO₂ cathode exhibited inferior capacity retention to that of the δ-MnO₂ cathode. It suggests that different cathodes delivered different electrochemical behaviors in Zn-ion batteries.

The different capacity variation tendencies of these two cathodes point to a fact that is seldom noticed: The capacity of Zn-ion battery cathodes may not be simply determined, as previously reported, by the capability of suppressing Mn-based cathode dissolution. The intrinsic property of the cathode (e.g., the specific surface area, the valent state of Mn cations and Mn-site defects) may result in the change of parameters

that were not given sufficient attention, i.e., the oxidation of the Mn^{2+} ion in the electrolyte that can lead to the deposition of active Mn compound on the cathode. Considering the abundant defects in the $\delta\text{-MnO}_2$ cathode material as synthesized under an unstable, highly oxidizing atmosphere generated by the molten sodium nitrate salt,²⁷ modification of $\delta\text{-MnO}_2$ was conducted using a facile method where the oxide was stirred in 1 M CoCl_2 at room temperature. Compared with the original $\delta\text{-MnO}_2$, the resulting cobalt-modified $\delta\text{-MnO}_2$ showed an even more pronounced capacity enhancement (**Figure 3.1a**), increasing from the initial discharge capacity of 196 mAh g^{-1} to 258 mAh g^{-1} after 5 cycles and further to 435 mAh g^{-1} at the 100th discharge. This capacity is surprisingly high when compared to the previously reported values ($\sim 300 \text{mAh g}^{-1}$ in the 100th discharge).^{5,8,14}

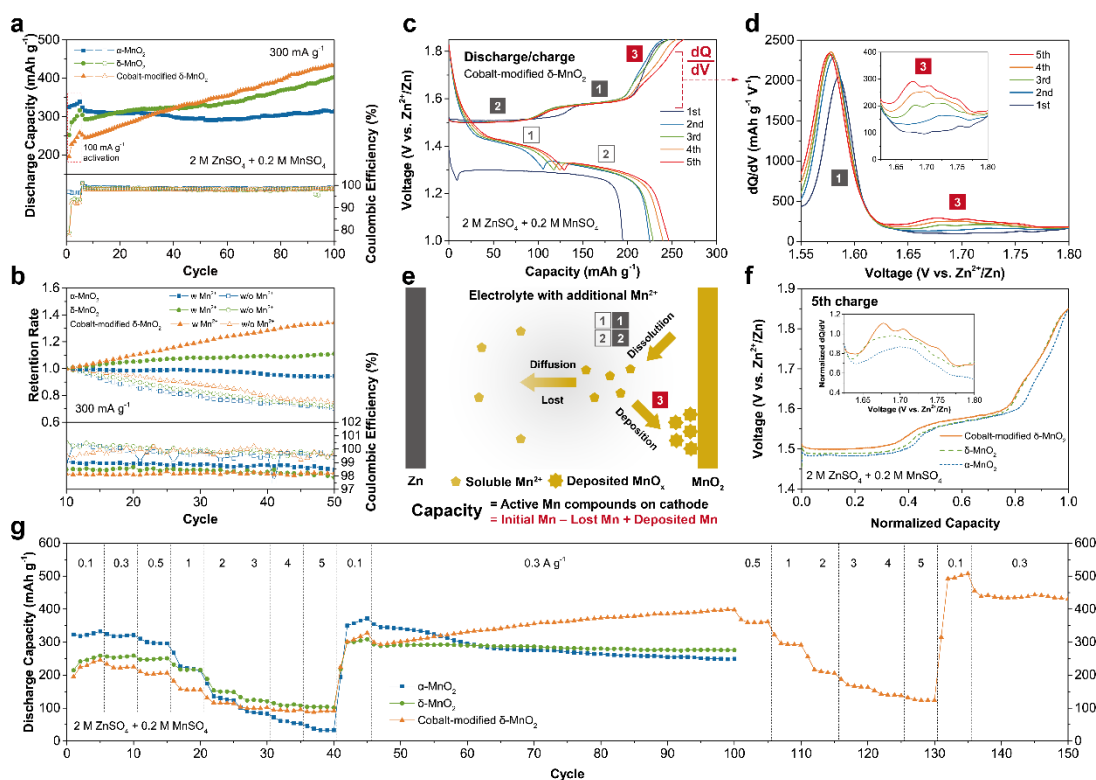


Figure 3.1 Comparison of performance and the self-recovery chemistry in a MnO_2 cathode. a) Comparison of cycling performance of $\alpha\text{-MnO}_2$, $\delta\text{-MnO}_2$ and cobalt-modified $\delta\text{-MnO}_2$ cathodes with a 2 M ZnSO_4 electrolyte containing 0.2 M MnSO_4 , b) Comparison of retention rates and Coulombic efficiencies of the MnO_2 cathodes with or without 0.2 M MnSO_4 in the electrolyte (the calculation of retention rate is based on the 10th discharging of the cathodes). c) First five galvanostatic discharging and charging profiles of a cobalt-modified $\delta\text{-MnO}_2$ cathode and d) the corresponding dQ/dV profiles from 1.55 to 1.80 V. e) A schematic and an equation for describing the

dynamic capacity retention of a Mn-based cathode. f) Comparison of the 5th charging of the MnO₂ cathodes; inset shows their corresponding dQ/dV profiles from 1.62 to 1.80 V. g) Comparison of the rate performance.

The increment of the capacity could be highly associated with the oxidation of Mn²⁺ in the electrolyte, which was evidenced by the analysis of Coulombic efficiency and the differential capacity (dQ/dV). While all the cathodes showed high Coulombic efficiency close to 100%, the cobalt-modified δ -MnO₂ showed slightly lower Coulombic efficiencies during the recharging cycles (**Figure 3.1b**). Without the MnSO₄ additive, the Coulombic efficiency of all samples is similar and near 100% (**Figure 3.1b**). This indicates that the additional Mn²⁺ in the electrolyte was actually involved in the redox process on the cathode. To further investigate this issue, the first five discharge-charge profiles of the cobalt-modified δ -MnO₂ cathode are presented in **Figure 3.1c**. Two conventional plateaus at the potential of 1.4 and 1.3 V vs Zn/Zn²⁺ reflect the H⁺ intercalation process and the Zn²⁺ intercalation process, respectively.¹⁴ In each subsequent charging process, an additional plateau/slope was observed at potential around 1.6-1.8 V, besides the two conventional plateaus that represent the reverse process of Zn²⁺ and H⁺ intercalation. In **Figure 3.1d**, differential capacity (dQ/dV) analysis more clearly shows this additional oxidation process happening at a voltage range of 1.62-1.80 V. This could be ascribed to the oxidation of Mn²⁺ to Mn³⁺, as will be discussed in the following sections. In a mild aqueous electrolyte environment, subsequent hydrolysis of Mn³⁺ could result in the deposition of Mn compound on the cathode.²³ These compounds were involved in the subsequent discharge, thus providing additional capacity.

Figure 3.1e gives a schematic and an equation that describe the dynamic capacity of a Mn-based cathode. Based on the fact that no matter what phase structures of the Mn-based cathode (e.g., α -MnO₂, δ -MnO₂), the discharge capacity of the cathode is mainly originated from the redox of Mn species between different valent states (from +4 to +3 or even to +2). Therefore, the discharge capacity of a Mn-based cathode on a specific cycle is determined by three essential parameters and their interaction (**Figure 3.1e**): (1) the initial amount and valence of Mn in the solid Mn-based cathode before cycling, (2) the dissolution amount of the active Mn compound during each discharge/charge cycle and (3) the deposition amount of active Mn compound during each charge. In these parameters, the initial valent state of the Mn element is

determined by the cathode material itself, which has a significant influence on the first discharge capacity. On the subsequent cycling, the dissolution rate and deposition rate will negatively or positively, respectively, influence the amount of Mn on the cathode, thereby playing a more important role in the capacity retention. Based on this equation, developing a cathode with a low dissolution rate and a high deposition rate is crucial to the stable operation of Zn-ion batteries.

The synthesis of δ -MnO₂ and its further modification by cobalt were illustrated in **Figure 3.2a** (details are provided in the Supplemental Information).²⁷ of the As indicated by the qualitative analysis of the Mn L-edge near-edge X-ray absorption fine-structure (NEXAFS) spectra^{28,29} (**Figure 3.2d**), cobalt-modified δ -MnO₂ showed the lowest Mn valency among the three different MnO₂-based cathodes. Therefore an expected lower initial capacity was observed for cobalt-modified δ -MnO₂. For the batteries without any additional MnSO₄ in the electrolyte, the dissolution rate is reflective of the capacity retention. As shown in **Figure 3.1b**, the dissolution rate of cobalt-modified δ -MnO₂ is only slightly lower than the other two cathodes. Based on these results, the significant capacity increment of cobalt-modified δ -MnO₂ during cycling could be attributed to its superior deposition rate of Mn compound. A comparison of the dQ/dV profile of the fifth charging (**Figure 3.1f**) also indicates that the this additional oxidation process on a δ -MnO₂ cathode with cobalt-modification is more significant than that without cobalt-modification. Furthermore, the cobalt-modified δ -MnO₂ cathode shows excellent rate performance and rate retention (over 500 mAh g⁻¹ at 0.1 mA g⁻¹ and ~125 mAh g⁻¹ at 5 mA g⁻¹) after 100 cycles of cathode recovery (**Figure 3.1g**). In the following sections, we analyze the property of the material and design a first-reported home-made electrolyzer system to offer more insights into the role of the cobalt-containing species on the mechanism behind the unique performance.

The existence of the cobalt element and its chemical state is crucial to the deposition rate of the cobalt-modified δ -MnO₂ cathode material. The presence of the Co was revealed by Co 2p peaks (2p_{3/2} at 795.5 eV and 2p_{1/2} at 780.7 eV) in the spectra of X-ray photoelectron spectroscopy (XPS) (**Figure 3.2b**). The quantity of cobalt element was further evaluated with inductively coupled plasma-optical emission spectrometry (ICP-OES), which gave a Co/Mn atomic ratio of 0.063:1 after cobalt-modification (**Table 3.1**). A similar result of Co/Mn ratio (0.052:1) was also obtained by the compositional analysis of the XPS survey spectra (**Table 3.2**). These results from both

bulk-sensitive ICP and surface-sensitive XPS indicate that Co element is evenly decorated on the δ -MnO₂. Evidence from the Co L-edge NEXAFS spectra (**Figure 3.2e**) suggests that Co species on the cobalt-modified δ -MnO₂ has a valent state between +2 and +3. This indicates that during the modification process, Co²⁺ in the CoCl₂ solution was partially oxidized by the high-valent-state (+4) Mn cations in the δ -MnO₂. Meanwhile, the valent state of Mn cation was decreased, as evidenced by the Mn L-edge NEXAFS spectra (**Figure 3.2d**). Due to the presence of Mn-site defects, cobalt-containing species (e.g., Co(II) and Co(III)) can be incorporated in δ -MnO₂ nanosheets (as illustrated in **Figure 3.2a**).³⁰ In addition, X-ray diffraction (XRD, **Figure 3.3**) and selected area electron diffraction (SAED, **Figure 3.4c**) patterns of the material show no other well-defined crystalline phase. Detailed observation of the TEM and HR-TEM images did not reveal the existence of any amorphous phase other than the layer-structured manganese oxide. Energy-dispersive X-ray (EDS) mapping in **Figure 3.4f** indicates that cobalt element is well dispersed on the cobalt-modified δ -MnO₂ with no significant agglomeration. In short, after cobalt-modification, cobalt cations with valent states of +2 and +3 in the form of cobalt-containing species is incorporated in the highly defective δ -MnO₂ nanosheets. A similar conclusion was also drawn by Wang et al. based on analysis of the quick extended X-ray absorption fine structure data.³⁰

Table 3.1 ICP-OES analysis of δ -MnO₂ and cobalt-modified δ -MnO₂.

Sample	Na:Mn (at:at)	Co:Mn (at:at)
δ -MnO ₂	0.074	/
Cobalt-modified δ -MnO ₂	0.024	0.063

Note: all ratio results are averaged values based on three repeated samples with the same synthesis procedure.

Table 3.2 XPS analysis of δ -MnO₂ and cobalt-modified δ -MnO₂.

Sample	Na	Co	Mn	O	Na:Mn	Co:Mn
	(at%)	(at%)	(at%)	(at%)	(at:at)	(at:at)
δ -MnO ₂	1.01	/	26.90	72.08	0.038	/
Cobalt-modified δ -MnO ₂	0.31	1.38	26.65	71.66	0.012	0.052

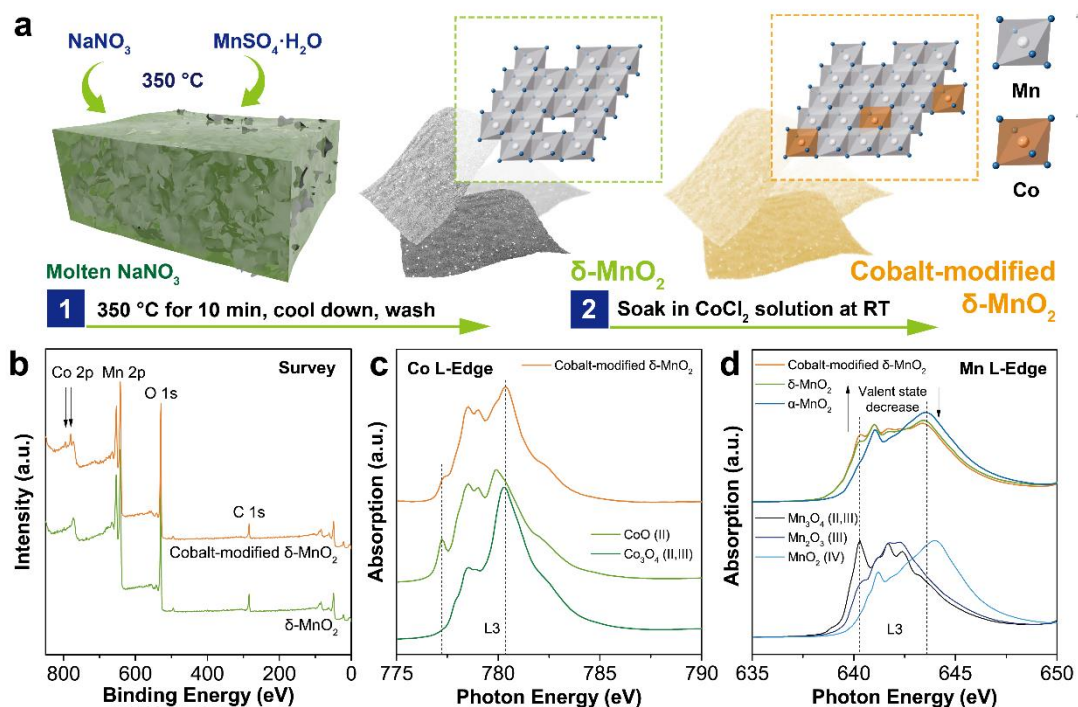


Figure 3.2 Synthesis and characterization of cobalt-modified δ -MnO₂. a) Illustration of the synthesis procedure of cobalt-modified δ -MnO₂ and schematic demonstration of incorporating positions of the Co species on the layered δ -MnO₂; b) XPS survey profiles of δ -MnO₂ and cobalt-modified δ -MnO₂; c) Co L-edge NEXAFS spectra (TEY mode) of Cobalt-modified δ -MnO₂ and d) Mn L-edge NEXAFS spectra (TEY mode) of the three MnO₂ materials.

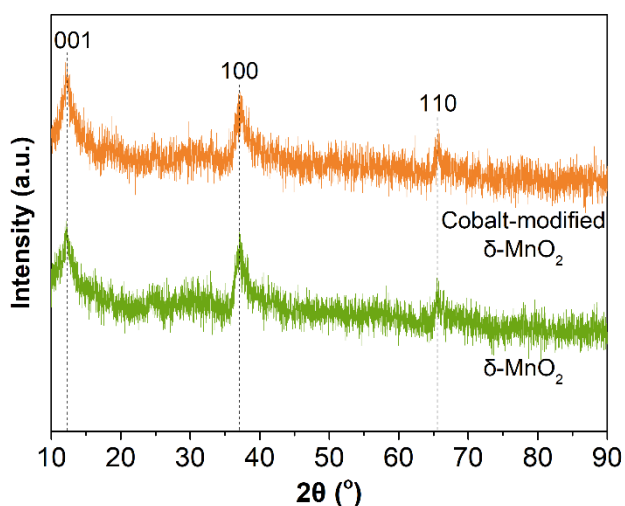


Figure 3.3 XRD patterns of δ -MnO₂ before and after cobalt-modification.

Resulting from the removal of the salts after the molten-salt synthesis, the δ -MnO₂ nanosheets formed loose-packed particles with a size of several micrometers (**Figure 3.5**). The loose packing morphology results in abundant secondary pores, which demonstrates a high specific surface area (139 m² g⁻¹) and a large total pore volume (0.50 cm³ g⁻¹), as presented in **Figure 3.6**. Due to the mild condition utilized for the cobalt-modification, the resulting material shows a flower-like morphology (**Figure 3.4a**), exhibiting similar surface area (161 m² g⁻¹) and porosity (0.48 cm³ g⁻¹) (**Figure 3.6**). The thickness of the cobalt-modified δ -MnO₂ nanosheets is approximately 3-5 nm, which is evaluated by linear analysis of the 2D height sensor signals using atomic force microscopy (AFM, **Figure 3.7**). High-resolution TEM (HR-TEM) in **Figure 3.4d&e** demonstrates the [001] view direction of the cobalt-modified δ -MnO₂ nanosheet, which clearly shows the (010), (100) and (110) planes with a lattice distance of 2.4, 2.4 and 1.4 Å, respectively. This result is also confirmed by the SAED (**Figure 3.4**) and XRD (**Figure 3.3**) patterns.

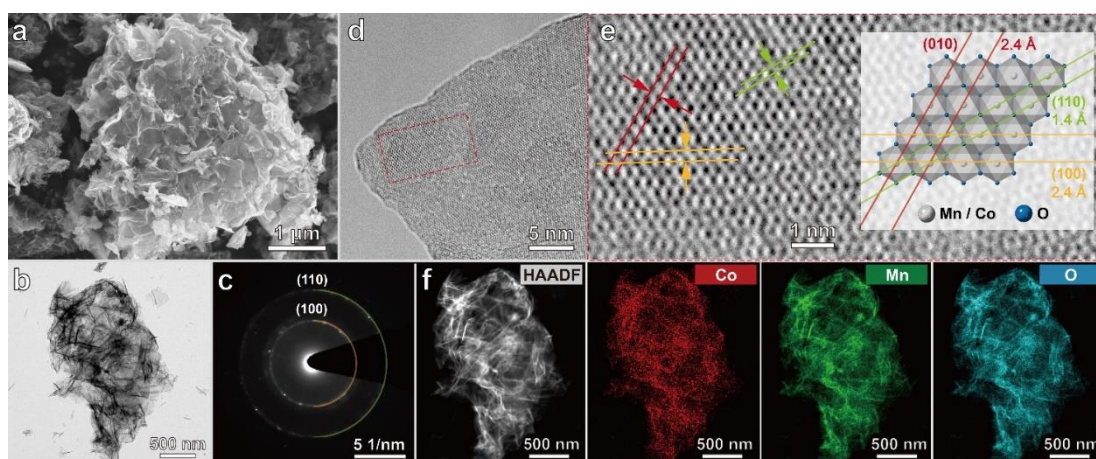


Figure 3.4 Microscopic characterization of cobalt-modified δ -MnO₂. a) SEM, b) TEM, c) SAED pattern, d,e) HR-TEM and f) EDS mapping of cobalt-modified δ -MnO₂.

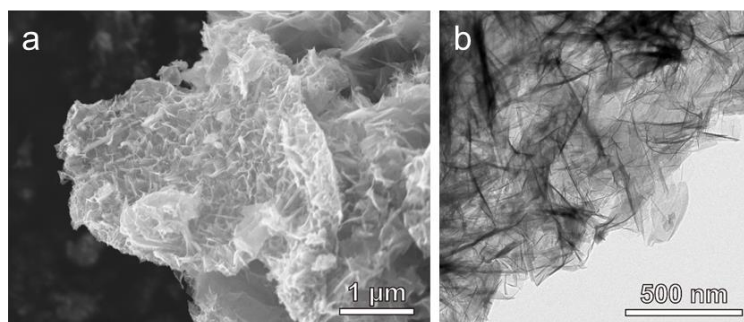


Figure 3.5 a) SEM and b) TEM images of δ -MnO₂ prepared using a molten-salt method.

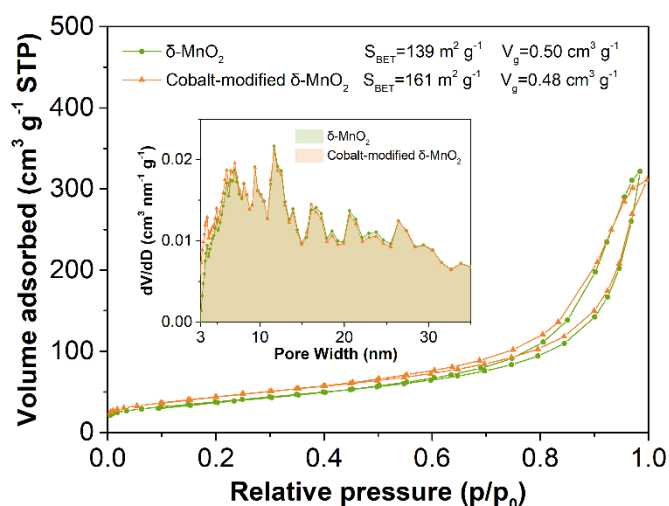


Figure 3.6 N_2 adsorption-desorption isotherms and corresponding pore size distributions of the materials calculated by a QSDFT method.

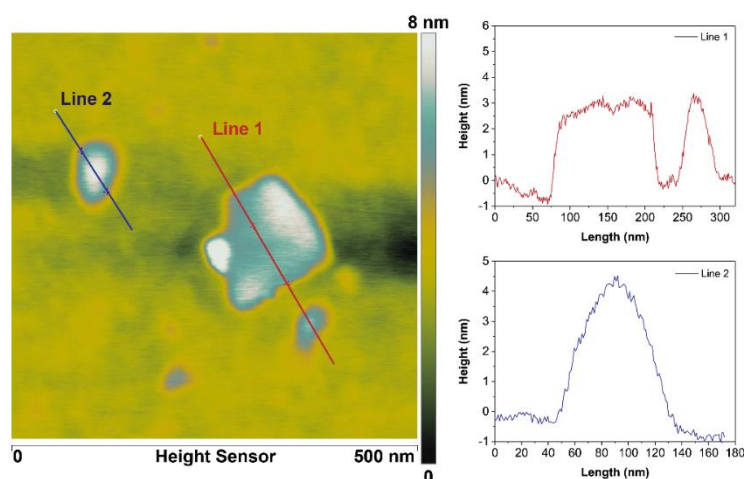


Figure 3.7 AFM images of cobalt-modified $\delta\text{-MnO}_2$ and linear analysis of height profiles.

3.3.2 The catalytic effect of cobalt components in the deposition process of active Mn compound

In this section, the role of cobalt components in the deposition of active Mn compound is further discussed using cyclic voltammetry (CV) and linear sweep voltammetry (LSV) for a practical battery configuration and a home-made electrolyzer cell. Compared to the galvanostatic charging process where the time duration in the range of 1.6-1.8 V for each charging is very short (causing a fast voltage build-up due to the full charge of the cathode), the CV and LSV methods allow equal time at every

voltage step. Therefore, well-defined peaks could be identified from a CV or an LSV curve, as compared to the dQ/dV profile extracted from a galvanostatic charging profile.

Using a conventional Zn|electrolyte|MnO₂ coin-type battery configuration, a oxidation peak at around 1.65 V was observed, indicative of the oxidation of Mn²⁺. It is no surprise that without introducing MnSO₄ into the electrolyte, the oxidation of Mn²⁺ is much less significant (**Figure 3.8**). Also, in the same electrolyte composition, the oxidation peaks at 1.65 V of the cobalt-modified δ -MnO₂ cathode were more noticeable than those of the δ -MnO₂ cathode, as presented in **Figure 3.9a**.

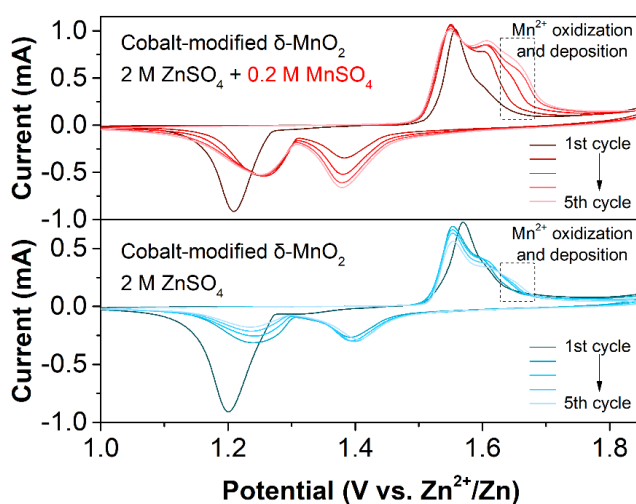


Figure 3.8 Comparison of CVs of coin-type batteries using Cobalt-modified δ -MnO₂ cathode in the electrolyte with or without additive MnSO₄.

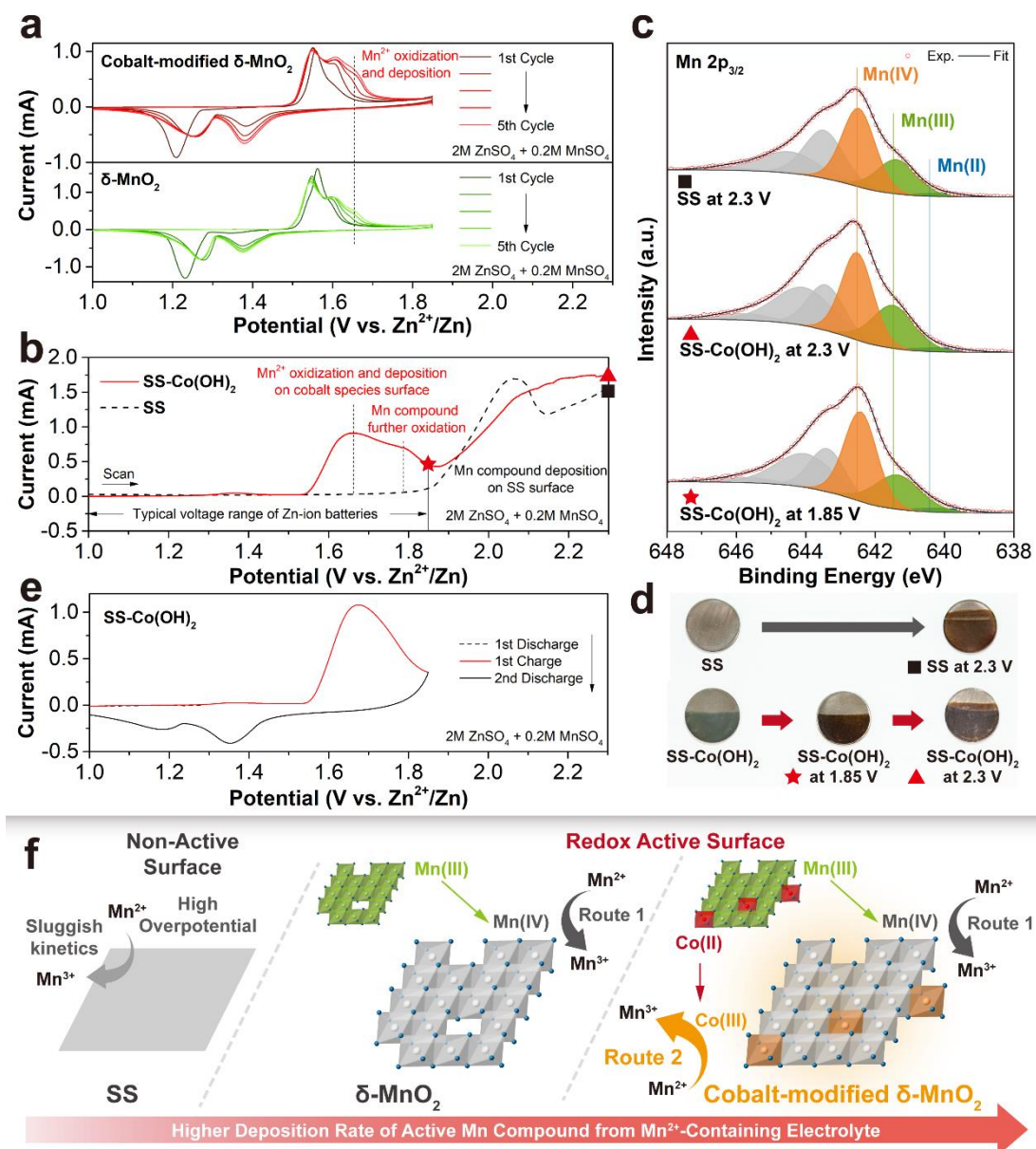


Figure 3.9 Catalytic effect of cobalt components in the deposition process of active Mn compound. a) Comparison of CVs (0.1 mV s⁻¹) of coin-type batteries using δ -MnO₂ cathodes with or without cobalt-modification; b) Comparison of LSV profiles (positive sweep, 1 mV s⁻¹) of a stainless steel (SS) and a SS covered with pre-electrodeposited Co(OH)₂; c) Mn 2p_{3/2} XPS profiles and d) digital photographs of the samples after the LSV positive sweep to specific potentials; e) first two CV cycles (1 mV s⁻¹) of SS with pre-electrodeposited Zn Co(OH)₂; f) Illustration of mechanism of the catalysis effect via a Mn self-catalysis (Route 1) and via a cobalt-induced catalysis (Route 2). Note that results in (b-e) are obtained based on a home-made electrochemical cell. Detail of preparation of the cell is described in **Figure 3.10a**.

To further reveal the role of cobalt components, a home-made electrolyzer cell with a two-electrode configuration was designed (**Figure 3.10a**). A stainless steel (SS) electrode or a Co(OH)_2 coated SS electrode (denoted as SS- Co(OH)_2) was used as the working electrode. A Zn plate was used as both the reference and the counter electrode. A larger quantity (10 mL) of the electrolyte with the same composition (2 M ZnSO_4 + 0.2 M MnSO_4) were used. An LSV scan from 1.0 to 2.3 V (oxidizing process) was applied to the SS electrode and SS- Co(OH)_2 electrode.

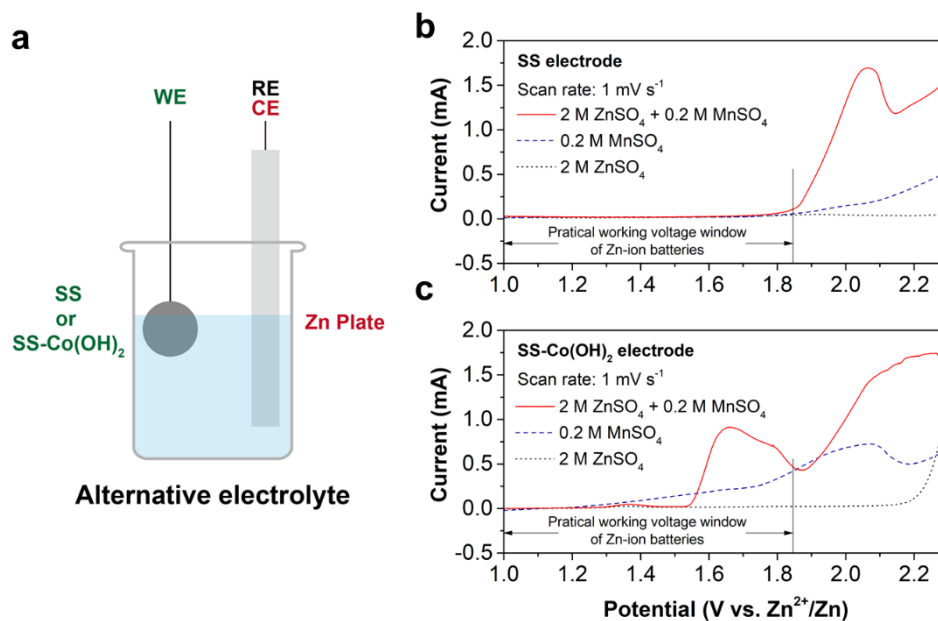


Figure 3.10 a) Illustration of the configuration of the home-made electrolyzer; Comparison of LSV profiles (positive sweep, 1 mV s^{-1}) of b) the SS electrode and c) the SS- Co(OH)_2 electrode in different electrolytes. Alternative electrolytes were utilized for evaluating the function of components in the electrolyte. The electrolyte used in this work included: 2 M ZnSO_4 , 0.2 M MnSO_4 , and 2 M ZnSO_4 + 0.2 M MnSO_4 .

For SS electrode, with the onset voltage at $\sim 1.85 \text{ V}$, an oxidation peak centered at $\sim 2.05 \text{ V}$ was observed (**Figure 3.9b**). Without any Mn compound on the original electrode, this process can be attributed to the oxidation of the Mn^{2+} in the electrolyte. After scanned to 2.3 V, the electrode (denoted as ■ in **Figure 3.9b-d**) was collected and characterized with XPS. The Mn $2p_{3/2}$ profile of the sample indicates the deposited Mn compound was mainly in high valent states of +3 and +4 (**Figure 3.9c**). For the SS- Co(OH)_2 electrode, two additional peaks centered at $\sim 1.65 \text{ V}$ and $\sim 1.80 \text{ V}$ were identified, which could be ascribed to the oxidation of Mn^{2+} in the electrolyte and the further oxidation of Mn compound (e.g., from +3 to +4) on the solid electrode (**Figure**

3.9b). The Mn 2p_{3/2} profile (**Figure 3.9c**) of the SS-Co(OH)₂ electrode after scanned to 1.85 V (denoted as ★) shows that the chemical state of the deposited Mn compound was very similar to those of SS and SS-Co(OH)₂ after scanned to 2.3 V (denoted as ■ and ▲). XRD profiles of the SS-Co(OH)₂ after scanned to 1.85 and 2.3 V (denoted as ★ and ▲) indicate that their phase structures are similar to the layered δ -MnO₂ and cobalt-modified δ -MnO₂ (**Figure 3.11**). As presented in the digital photographs (**Figure 3.9d**), the major colour and texture changes of the SS electrode and SS-Co(OH)₂ electrode before and after the LSV scan to a certain voltage also provide visual support that indicates the deposition of the Mn compound.

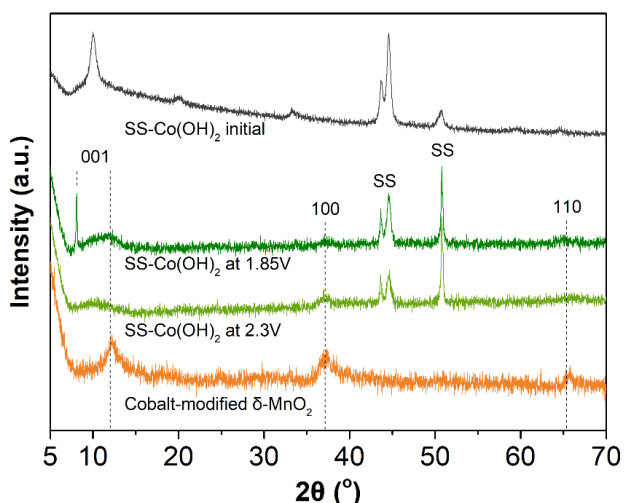


Figure 3.11 XRD profiles of the SS-Co(OH)₂ electrode at the initial state and after the LSV scan to 1.85 V and 2.3 V. Noted that to obtain a greater amount of the materials for identical XRD signal, the pre-deposition time of the Co(OH)₂ was tripled (180 s), and slower LSV scan rate was utilized (0.2 mV s⁻¹). The XRD profile of the cobalt-modified δ -MnO₂ powder sample is also presented for comparison.

The high valent state of the Mn compound of the SS-Co(OH)₂ sample after scanned to 1.85 V (★) indicates the readiness to be reduced and to provide capacity in a subsequent discharge process. In **Figure 3.9e**, the SS-Co(OH)₂ electrode was CV scanned (1 mV s⁻¹). No reduction peak was found at the first negative scan from open circuit voltage (OCV) (~1.28 V) to 1.0 V, indicating that no significant discharging capacity was provided from SS-Co(OH)₂. The following positive (oxidation) scan from 1.0 to 1.85 V shows the oxidation of Mn²⁺ and further oxidation as mentioned

earlier, after which the subsequent negative scan shows two well-defined peaks at ~ 1.4 and ~ 1.2 V (**Figure 3.9e**), matching well with the reduction peaks observed from the cobalt-modified δ -MnO₂ cathode in a typical Zn-ion battery (**Figure 3.9a**).

It is important to note that cobalt element in the state of unbound Co²⁺ in the electrolyte did not facilitate the deposition of active Mn compound. As presented in **Figure 3.12**, LSV of SS in the electrolyte with and without additional 0.01 M CoSO₄ demonstrated similar onset potentials of ~ 1.9 V, indicating no beneficial effect on facilitating the Mn compound deposition. Therefore, the promoted deposition of active Mn compound would be ascribed to the cobalt hydroxides and cobalt-containing species that bound on the solid cathode. This result is vital for the analysis of the following section.

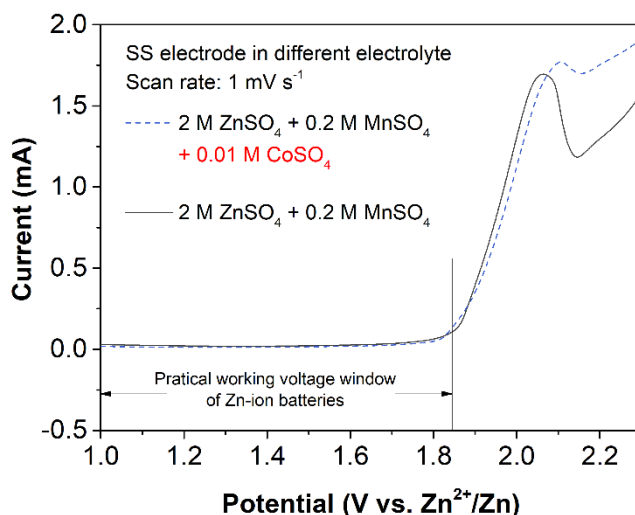
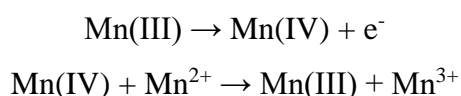


Figure 3.12 Comparison of LSV profiles (positive sweep, 1 mV s^{-1}) of a stainless steel (SS) in $2\text{M ZnSO}_4 + 0.2\text{M MnSO}_4$ electrolytes with or without additional 0.01M CoSO_4 . With a similar onset potential of ~ 1.9 V, this result indicates that the Co element in the state of unbound Co²⁺ in the electrolyte does not facilitate the deposition of active Mn compound.

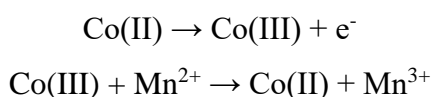
The mechanism behind the facilitated deposition of active Mn compound could be ascribed to dual-catalysis effects from Mn(IV) species and Co(III) species on the cathode. Usually, Mn²⁺ in the electrolyte is more stable than most of the Mn cations due to the high tendency of Mn³⁺ disproportionation.²³ A recent research reported by Qiao's group indicated that the deposition of MnO₂ on a carbon fiber using a Mn²⁺-containing electrolyte took place at a high potential of 2.2 V vs Zn²⁺/Zn in a

chronoamperometry charge process.³¹ The sluggish kinetics of the direct oxidation of Mn^{2+} could result in a large overpotential. Our LSV scan for the SS electrode in the Mn^{2+} -containing electrolyte (**Figure 3.9b**) also indicates a similar result where an onset potential of deposition of the active Mn compound was higher than 1.85 V vs Zn^{2+}/Zn , which is beyond the voltage window for a typical Zn-ion battery. The unique facilitated deposition observed in this work within the voltage range below 1.85 V could be ascribed to two different catalysis routes (**Figure 3.9f**):

Mn self-catalysis (Route 1): where oxidation of Mn^{2+} was achieved by the comproportionation of Mn(IV) and Mn^{2+}



Co-induced catalysis (Route 2): where oxidation of Mn^{2+} was enhanced by cobalt-facilitated charge-transfer



After the oxidation process, the generated Mn^{3+} is then hydrolyzed and deposited as solid Mn(III) compounds on the cathode.²³

For cobalt-modified $\delta\text{-MnO}_2$ cathode, both catalysis routes contribute to the deposition process. Of importance, the well dispersed cobalt-containing species could serve as preferred active sites through providing enhanced charge-transfer capability, thereby demonstrating a much superior deposition rate. On the contrary, the deposition of active Mn compound was still observed but less significant (**Figure 3.9a**) for the cathode without cobalt-modification, since the catalysis could only rely on the Mn self-catalysis route.

3.3.3 The dynamic movement of cobalt components for self-recovery of the Mn-based cathode

As shown previously in **Figure 3.1a**, the cobalt-modified $\delta\text{-MnO}_2$ cathode exhibits a superior rate towards the deposition of active Mn compound during the entire cycling test. This result indicates the continuous influence of cobalt components on facilitating the recovery of the Mn-based cathode. The authors once considered that the cobalt components could be only confined on the initial $\delta\text{-MnO}_2$ cathode. In other words, the newly deposited Mn compound (**Figure 3.13a&b**) on the surface might not contain

cobalt components. Interestingly, however, after 10 and 100 cycles, identical cobalt signals were still observed both in bulk sensitive EDS spectra (**Figure 3.13c** & **Figure 3.14**) and in surface-sensitive Co 2p XPS profiles (**Figure 3.13d**), though both signals were decreased as expected. This could be attributed to a dynamic movement of cobalt components, similar to the dissolution-deposition process of the MnO₂ cathode.

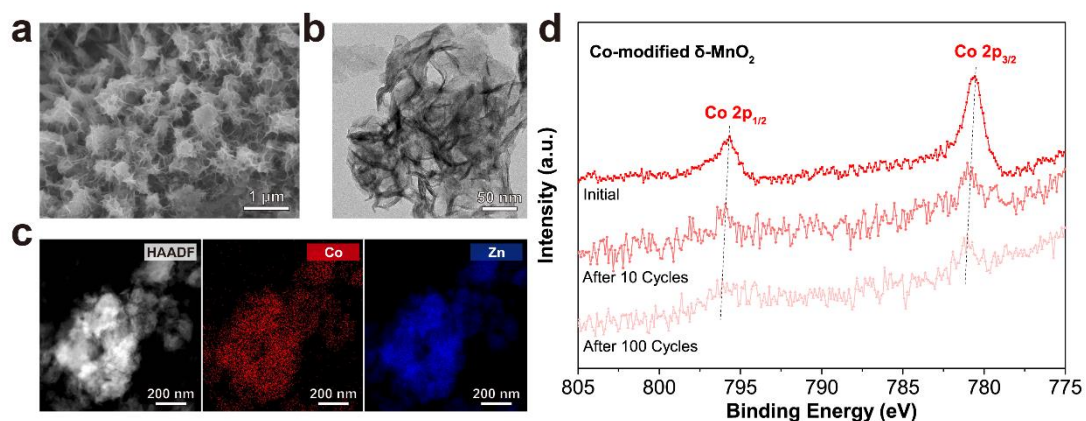


Figure 3.13 Investigation of the cobalt component before and after cycling. a) SEM, b) TEM, c) EDS mapping images of cobalt-modified δ -MnO₂ cathode after 100 cycles; d) Co 2p XPS profiles of cobalt-modified δ -MnO₂ cathode at OCV before cycling and charged state after 10 and 100 cycles.

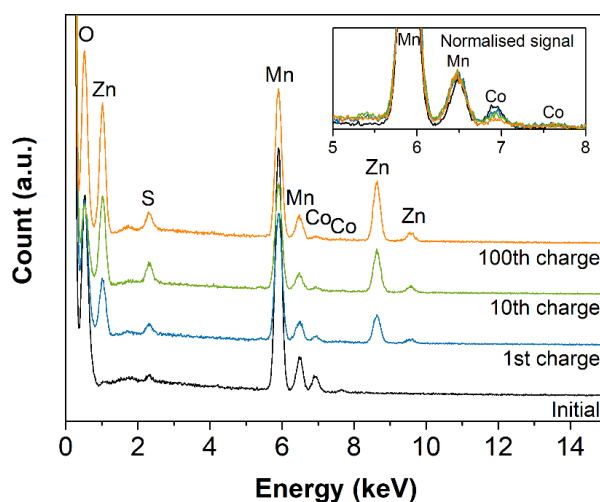


Figure 3.14 EDS profiles of the surface of cobalt-modified δ -MnO₂ cathode before cycling and after specific cycles at fully charged state (1.85 V). The inset shows the normalized signals where the Mn peak values at 5.9 keV were referred to as the maximum and the baselines as the minimum.

It is important to note that the pH value of the electrolyte could be one of the important parameters that may cause the dissolution and redeposition of cobalt components. The pH value of the electrolyte (2 M ZnSO₄ + 0.2 M MnSO₄) is ~5,³² a mild acidic environment under which the cobalt components (e.g., Co(OH)₂) could be unstable.³³ As indicated in previous reports, the electrolyte pH of Zn-ion batteries may vary due to the intercalation/de-intercalation of H⁺. In a system with a large volume of electrolyte (e.g., 10 mL, experiment shown in **Figure 3.10**), the intercalation/de-intercalation of H⁺ is not significant enough to largely influence the pH value. Decomposition of Co(OH)₂ was observed only after 5 CV cycles (1.0-1.85 V, **Figure 3.15**). However, in a coin-type battery with a small amount of electrolyte (200 μL in each of our battery), the pH value of the electrolyte could be significantly increased after fully discharged.³⁴ The pH increase after the 1st discharge to 1.0 V was evidenced by the formation of zinc hydroxide sulphate hydrate (which only forms in high pH environment) on the cathode surface, as confirmed by XRD analysis (**Figure 3.16**).^{8,14}

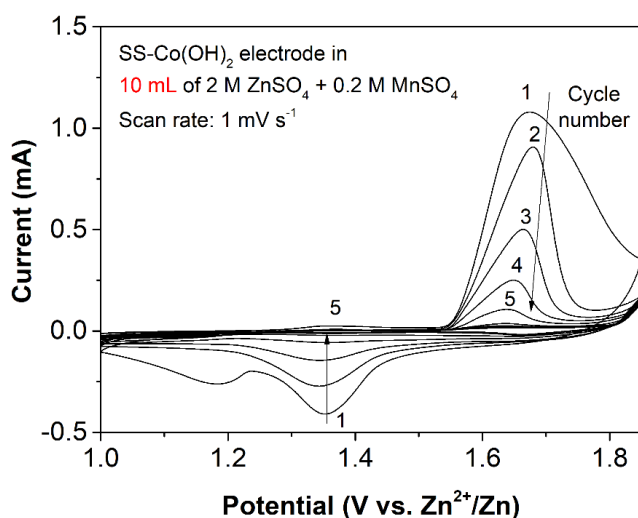


Figure 3.15 The first 10 CV cycles (1 mV s⁻¹) of SS with pre-electrodeposited Co(OH)₂. With a large volume (10 mL) of electrolyte, the Co(OH)₂ is gradually dissolved. The unbound Co²⁺ in the electrolyte does not facilitate the deposition of active Mn compound.

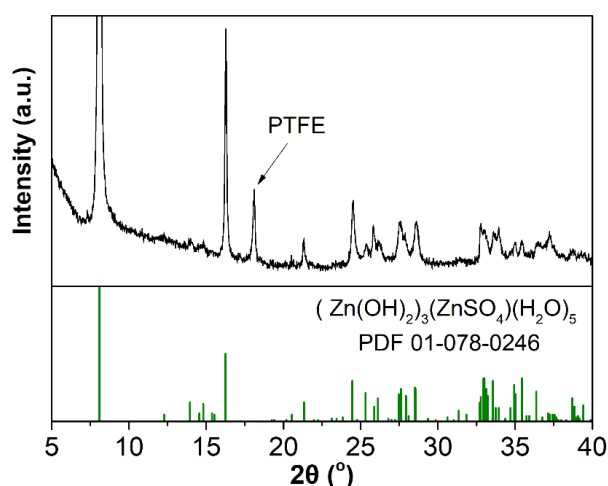


Figure 3.16 XRD profile of the cobalt-modified δ -MnO₂ cathode after first discharge to 1.0 V.

In **Figure 3.17**, a bigger picture of the role of cobalt components in facilitating the recovery of the cathode and their dynamic movement is demonstrated. During the cycling, cathode reconstruction occurs in the battery, involving the dissolution and deposition of both Mn and Co components. Deposition of the Mn-based cathode is driven by an electrochemical charge process, which is further facilitated by cobalt components bound on the Mn compound. At the same time, the deposition/dissolution of the Co component is a pH-sensitive process. Due to the weak acidic environment, a small fraction of cobalt component was dissolved in the electrolyte. During battery discharging, H⁺ was inserted in the Mn-based cathode,³² resulting in the increase of pH value and consequently the re-deposition of cobalt component on the reconstructed cathode surface. During each charge process, H⁺ was reversibly released, causing the re-dissolution of cobalt components to some extent. This dynamic movement of the cobalt component in the solid electrode and liquid electrolyte is important for the persistent facilitation of cathode recovery.

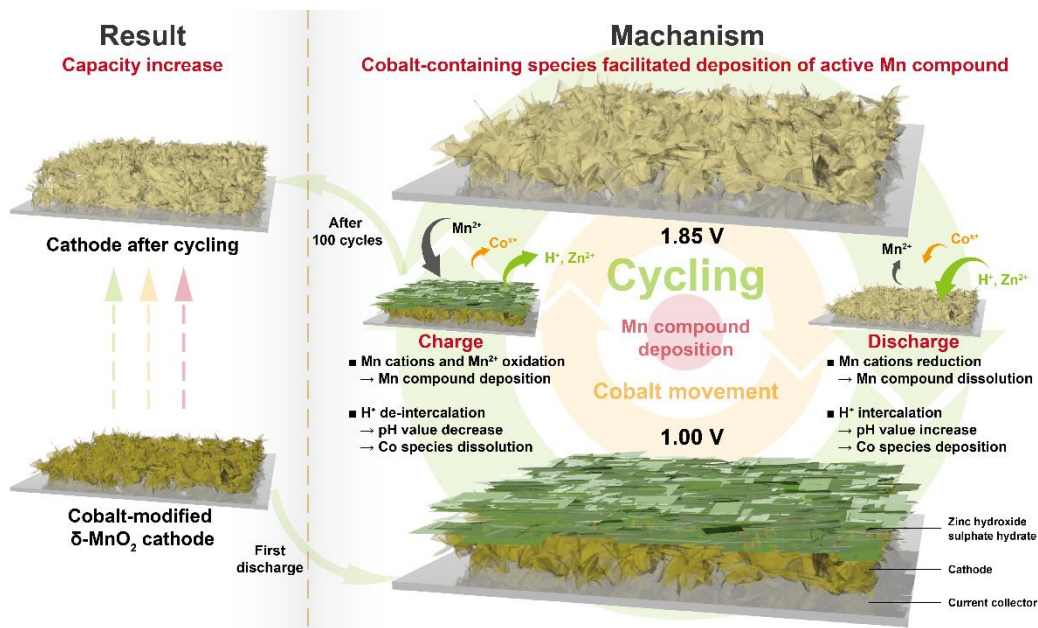


Figure 3.17 Schematic illustration of the whole picture of this work: the dynamic movement of cobalt components during discharge and charge of the batteries and its influence on facilitating deposition of active Mn compound.

It is worth mentioning that apart from the facilitating effect from cobalt components, the overall capacity recovery rate of the Mn-based cathode is also limited by many other factors, e.g., 1) limited conductive cathode surface, 2) decreased Mn^{2+} concentration in the electrolyte after many discharging-charging cycles, 3) The ionic conductivity and pH of the electrolyte, and 4) deterioration of the Zn anode^{9,35}. From the consideration of the first factor, the increment of the capacity for a battery with the cobalt-modified $\delta\text{-MnO}_2$ cathode (as shown in **Figure 3.1g**) gradually slowed down during the 50-100 cycles. In addition, a comparison of the morphologies of cathode surface before cycling and after 100th charge provides clear evidence that most of the conductive surface (e.g., current collector and conductive carbon) was heavily covered with dense, newly deposited active Mn compound (**Figure 3.18c&e**). The deterioration of the charge-transfer situation of cathode surface could further limit the redeposition of active Mn compound.

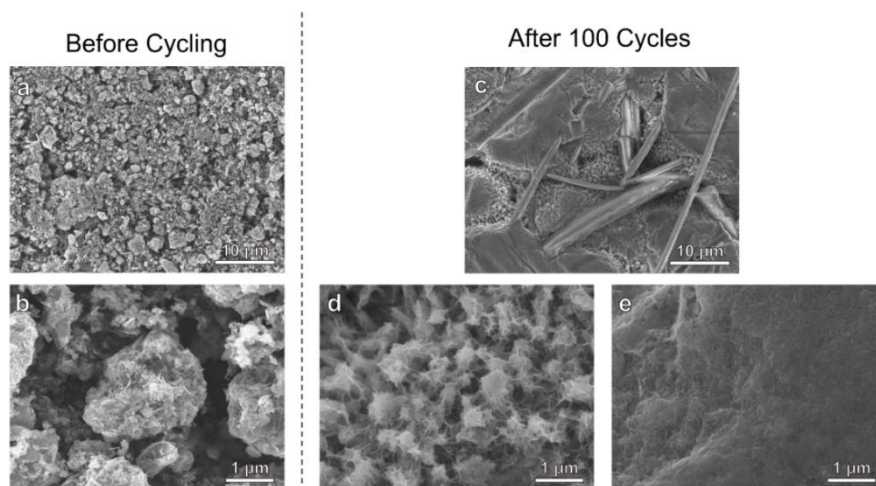


Figure 3.18 Morphology evolution observed with SEM images of cobalt-modified δ -MnO₂ cathode (conductive carbon and binder contained) a-b) before cycling and c-e) after 100 cycles.

3.3.4 Cycling performance and more practical battery configurations

The practical viability of the cobalt-modified δ -MnO₂ cathode was further demonstrated with a prolonged cycling test based on a higher current density of 2 A g⁻¹ in a 200 μ L electrolyte of 2 M ZnSO₄ and 0.2 M MnSO₄ (**Figure 3.19a**). A commercially applicable battery cycle life (80% of capacity retention) of 2000 discharge-charge cycle is presented. Even after 5000 cycles, the battery still shows decent capacity retention of approximately 63% (compared to the 10th discharge capacity). As mentioned in the introduction section, since the Mn²⁺ additive is also active during cycling, it should also be considered for the evaluation of the overall capacity of the cathode. From the practical utility aspect, the final objective is to stabilize the battery performance with minimum additional Mn²⁺. Using a smaller electrolyte volume of 70 μ L, we then investigate the capacity retention of batteries in 2 M ZnSO₄ with five different concentrations of MnSO₄ additives (from 0 to 0.2 M as demonstrated in **Figure 3.19b**) based on the total Mn compound mass (i.e., MnO₂ in the solid cathode and MnSO₄·H₂O added in the electrolyte). As indicated in **Figure 3.19c**, due to its good cathode recovery capability, the cobalt-modified δ -MnO₂ cathode enabled a more stable operation of rechargeable aqueous Zn-ion batteries. With a low MnSO₄ additive concentration of only 0.02 M (corresponding to an atomic percentage of 12% of the Mn additive in the electrolyte), an average capacity fading

rate of 0.23% per cycle was achieved between 7th and 100th cycles, much lower than that without MnSO₄ additive (0.35% per cycle, 1.5 times faster fading).

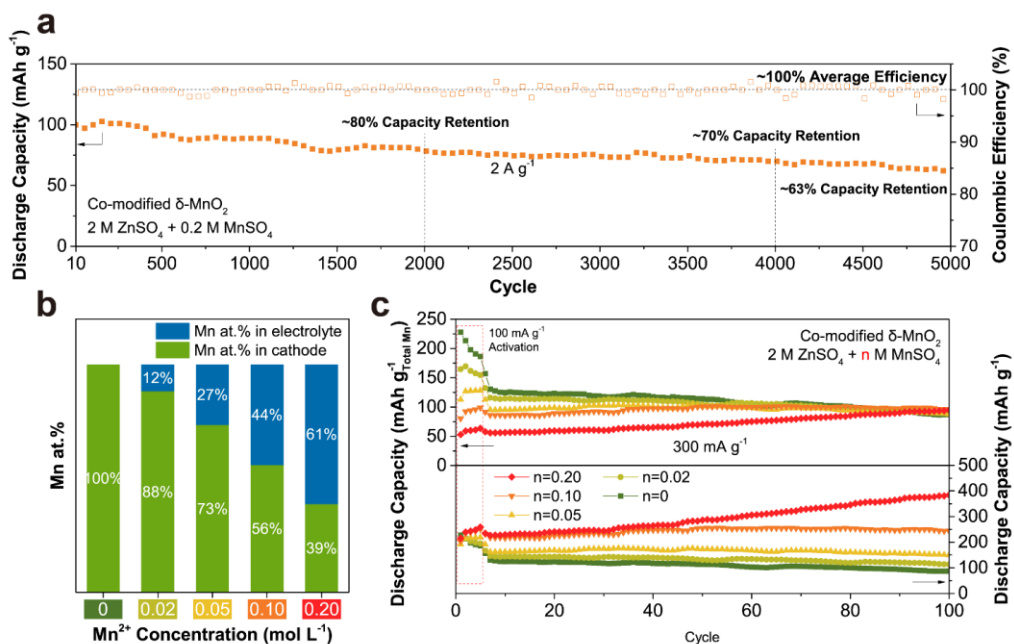


Figure 3.19 Investigation of long cycling performance and the electrolyte compositions. a) Cycle life and corresponding Coulombic efficiency over 5000 cycles at 2 A g⁻¹ of the batteries with cobalt-modified δ -MnO₂ cathode and 200 μ L of electrolyte; b) Comparison of atomic contents of Mn element in electrolyte and cathode; c) Comparison of cycling performance for the batteries with 70 μ L of aqueous electrolyte containing 2 M ZnSO₄ and MnSO₄ additives at different concentrations.

3.4 Conclusion

In conclusion, stable performance of Zn-ion batteries was realized through a first reported cobalt-catalyzed recovery strategy which was achieved by facilitating the deposition of active Mn compound in the cathode. The discharge capacity of a Mn-based cathode was determined by (1) the initial amount and valence of Mn in the solid Mn-based cathode before cycling, (2) the dissolution amount of the Mn cathode, and (3) most importantly, the deposition amount of active Mn compound. The facilitating of the redeposition is achieved by utilizing a facile cobalt-modification strategy that integrated the well dispersed, cobalt-containing species into the defective δ -MnO₂ nanosheets. Verified by both practical coin-type batteries and a newly-designed home-made electrolyzer system, the deposition of active Mn compound was confirmed to be significantly facilitated with cobalt-based compounds (e.g., Co(OH)₂) and the bound

cobalt-containing species (e.g., Co(II) and Co(III)) in the cobalt-modified δ -MnO₂ cathode, while the unbound Co²⁺ in the electrolyte showed no significant impact on the redeposition process. In addition, the concentration of Mn²⁺ additives and the volume of the electrolyte are also vital parameters for capacity recovery of the cathode. For a fair performance comparison, these two parameters should be well controlled and clearly indicated in future publications of Mn-based cathode for Zn-ion batteries. Overall, this work provides a deeper insight into the redeposition behaviors of the active cathode material and its significant influence on the stable performance of aqueous Zn-ion batteries. This work could also provide inspiration for the materials engineering for future functionalized cathodes, especially for other conversion-type battery cathodes which suffer from the similar dissolution issue, for example, manganese-based cathodes for Li-ion and Na-ion batteries and sulfur cathodes for Li-S and Na-S batteries.

References

1. Konarov A, Voronina N, Jo JH, Bakenov Z, Sun Y-K, Myung S-T. Present and future perspective on electrode materials for rechargeable zinc-ion batteries. *ACS Energy Lett.* 2018;3(10):2620-40. doi:10.1021/acseenergylett.8b01552
2. Song M, Tan H, Chao D, Fan HJ. Recent advances in Zn-ion batteries. *Adv Funct Mater.* 28(41):1802564. doi:10.1002/adfm.201802564
3. Zeng X, Hao J, Wang Z, Mao J, Guo Z. Recent progress and perspectives on aqueous Zn-based rechargeable batteries with mild aqueous electrolytes. *Energy Storage Mater.* 2019;20:410-37. doi:10.1016/j.ensm.2019.04.022
4. Yang Q, Bang G, Guo Y, Liu Z, Yon B, Wang D, et al. Do zinc dendrites exist in neutral zinc batteries: A developed electrohealing strategy to in situ rescue in-service batteries. *Adv Mater.* 2019;31(43):1903778. doi:10.1002/adma.201903778
5. Zhang N, Cheng F, Liu J, Wang L, Long X, Liu X, et al. Rechargeable aqueous zinc-manganese dioxide batteries with high energy and power densities. *Nat Commun.* 2017;8:405. doi:10.1038/s41467-017-00467-x
6. Li H, Ma L, Han C, Wang Z, Liu Z, Tang Z, et al. Advanced rechargeable zinc-based batteries: Recent progress and future perspectives. *Nano Energy.* 2019;62:550-87. doi:10.1016/j.nanoen.2019.05.059

7. Cheng FY, Chen J, Gou XL, Shen PW. High-power alkaline Zn–MnO₂ batteries using γ -MnO₂ nanowires/nanotubes and electrolytic zinc powder. *Adv Mater.* 2005;17(22):2753-6. doi:10.1002/adma.200500663
8. Pan H, Shao Y, Yan P, Cheng Y, Han KS, Nie Z, et al. Reversible aqueous zinc/manganese oxide energy storage from conversion reactions. *Nat Energy.* 2016;1:16039. doi:10.1038/nenergy.2016.39
9. Ha S, Lee KT. Batteries: Converting to long stability. *Nat Energy.* 2016;1:16057. doi:10.1038/nenergy.2016.57
10. Wang D, Wang L, Liang G, Li H, Liu Z, Tang Z, et al. A superior δ -MnO₂ cathode and a self-healing Zn- δ -MnO₂ battery. *ACS Nano.* 2019;13(9):10643-52. doi:10.1021/acsnano.9b04916
11. Long J, Gu J, Yang Z, Mao J, Hao J, Chen Z, et al. Highly porous, low band-gap Ni_xMn_{3-x}O₄ (0.55 \leq x \leq 1.2) spinel nanoparticles with in situ coated carbon as advanced cathode materials for zinc-ion batteries. *J Mater Chem A.* 2019;7(30):17854-66. doi:10.1039/C9TA05101E
12. Xiong T, Yu ZG, Wu H, Du Y, Xie Q, Chen J, et al. Defect engineering of oxygen-deficient manganese oxide to achieve high-performing aqueous zinc ion battery. *Adv Energy Mater.* 2019;9(14):1803815. doi:10.1002/aenm.201803815
13. Fang G, Zhu C, Chen M, Zhou J, Tang B, Cao X, et al. Suppressing manganese dissolution in potassium manganate with rich oxygen defects engaged high-energy-density and durable aqueous zinc-ion battery. *Adv Funct Mater.* 2019;29(15):1808375. doi:10.1002/adfm.201808375
14. Huang J, Wang Z, Hou M, Dong X, Liu Y, Wang Y, et al. Polyaniline-intercalated manganese dioxide nanolayers as a high-performance cathode material for an aqueous zinc-ion battery. *Nat Commun.* 2018;9:2906. doi:10.1038/s41467-018-04949-4
15. Wang J, Wang J-G, Liu H, Wei C, Kang F. Zinc ion stabilized MnO₂ nanospheres for high capacity and long lifespan aqueous zinc-ion batteries. *J Mater Chem A.* 2019;7(22):13727-35. doi:10.1039/C9TA03541A
16. Pan C, Zhang R, Nuzzo RG, Gewirth AA. ZnNi_xMn_xCO_{2-2x}O₄ spinel as a high-voltage and high-capacity cathode material for nonaqueous Zn-ion batteries. *Adv Energy Mater.* 2018;8(22):1800589. doi:10.1002/aenm.201800589

17. Ma L, Li N, Long C, Dong B, Fang D, Liu Z, et al. Achieving both high voltage and high capacity in aqueous zinc-ion battery for record high energy density. *Adv Funct Mater.* 2019;29(46):1906142. doi:10.1002/adfm.201906142
18. Nam KW, Kim H, Choi JH, Choi JW. Crystal water for high performance layered manganese oxide cathodes in aqueous rechargeable zinc batteries. *Energy Environ Sci.* 2019;12(6):1999-2009. doi:10.1039/C9EE00718K
19. Yu P, Zeng Y, Zhang H, Yu M, Tong Y, Lu X. Flexible Zn-ion batteries: Recent progresses and challenges. *Small.* 2019;15(7):1804760. doi:10.1002/sml.201804760
20. Wu B, Zhang G, Yan M, Xiong T, He P, He L, et al. Graphene scroll-coated α -MnO₂ nanowires as high-performance cathode materials for aqueous Zn-ion battery. *Small.* 2018;14(13):1703850. doi:10.1002/sml.201703850
21. Huang J, Guo Z, Ma Y, Bin D, Wang Y, Xia Y. Recent progress of rechargeable batteries using mild aqueous electrolytes. *Small Methods.* 2019;3(1):1800272. doi:10.1002/smt.201800272
22. Huang Y, Mou J, Liu W, Wang X, Dong L, Kang F, et al. Novel insights into energy storage mechanism of aqueous rechargeable Zn/MnO₂ batteries with participation of Mn²⁺. *Nano-Micro Lett.* 2019;11:49. doi:10.1007/s40820-019-0278-9
23. Gibson AJ, Johannessen B, Beyad Y, Allen J, Donne SW. Dynamic electrodeposition of manganese dioxide: Temporal variation in the electrodeposition mechanism. *J Electrochem. Soc.* 2016;163(5):H305-H12. doi:10.1149/2.0721605jes
24. Li Y, Wang S, Salvador JR, Wu J, Liu B, Yang W, et al. Reaction mechanisms for long-life rechargeable Zn/MnO₂ batteries. *Chem Mater.* 2019;31(6):2036-47. doi:10.1021/acs.chemmater.8b05093
25. Fu Y, Wei Q, Zhang G, Wang X, Zhang J, Hu Y, et al. High-performance reversible aqueous Zn-ion battery based on porous MnO_x nanorods coated by MOF-derived N-doped carbon. *Adv Energy Mater.* 2018;8(26):1801445. doi:10.1002/aenm.201801445
26. Zhu C, Fang G, Zhou J, Guo J, Wang Z, Wang C, et al. Binder-free stainless steel@Mn₃O₄ nanoflower composite: A high-activity aqueous zinc-ion battery cathode with high-capacity and long-cycle-life. *J Mater Chem A.* 2018;6(20):9677-83. doi:10.1039/C8TA01198B

27. Hu Z, Xiao X, Jin H, Li T, Chen M, Liang Z, et al. Rapid mass production of two-dimensional metal oxides and hydroxides via the molten salts method. *Nat Commun.* 2017;8:15630. doi:10.1038/ncomms15630
28. Cowie BCC, Tadich A, Thomsen L. The current performance of the wide range (90–2500 eV) soft X-ray beamline at the Australian Synchrotron. *AIP Conf Proc.* 2010;1234(1):307-10. doi:10.1063/1.3463197
29. Gann E, McNeill CR, Tadich A, Cowie BCC, Thomsen L. Quick AS NEXAFS Tool (QANT): A program for NEXAFS loading and analysis developed at the Australian Synchrotron. *J Synchrotron Radiat.* 2016;23(1):374-80. doi:10.1107/S1600577515018688
30. Wang Y, Benkaddour S, Marafatto FF, Peña J. Diffusion- and pH-dependent reactivity of layer-type MnO₂: Reactions at particle edges versus vacancy sites. *Environ Sci Technol.* 2018;52(6):3476-85. doi:10.1021/acs.est.7b05820
31. Chao D, Zhou W, Ye C, Zhang Q, Chen Y, Gu L, et al. An electrolytic Zn–MnO₂ battery for high-voltage and scalable energy storage. *Angew Chem Int Ed.* 2019;58(23):7823-8. doi:10.1002/anie.201904174
32. Sun W, Wang F, Hou S, Yang C, Fan X, Ma Z, et al. Zn/MnO₂ battery chemistry with H⁺ and Zn²⁺ coininsertion. *J Am Chem Soc.* 2017;139(29):9775-8. doi:10.1021/jacs.7b04471
33. Gayer KH, Garrett AB. The solubility of cobalt hydroxide, Co(OH)₂, in solutions of hydrochloric acid and sodium hydroxide at 25°. *J Am Chem Soc.* 1950;72(9):3921-3. doi:10.1021/ja01165a024
34. Lee B, Seo HR, Lee HR, Yoon CS, Kim JH, Chung KY, et al. Critical role of pH evolution of electrolyte in the reaction mechanism for rechargeable zinc batteries. *Chemsuschem.* 2016;9(20):2948-56. doi:10.1002/cssc.201600702
35. Selvakumaran D, Pan A, Liang S, Cao G. A review on recent developments and challenges of cathode materials for rechargeable aqueous Zn-ion batteries. *J Mater Chem A.* 2019;7(31):18209-36. doi:10.1039/C9TA05053A

Every reasonable effort has been made to acknowledge the owners of copyright material. I would be pleased to hear from any copyright owner who has been omitted or incorrectly acknowledged.

Chapter 4 Cobalt-modified MnO₂ as an oxygen catalyst for zinc-air battery cathode §

Abstract

Bifunctional oxygen catalyst is an important component in the cathode for rechargeable Zn-air batteries. MnO₂ catalysts have aroused intense interests owing to their promising activity for oxygen reduction reaction (ORR), which, however, is still not comparable to precious metal catalysts. To improve the ORR catalysis and meet the requirement for a bifunctional oxygen catalyst, MnO₂ nanosheets are modified with Co, Ni or Fe via a facile solution-based method. Among the modified samples, Co-MnO₂ presents improved catalysis for both ORR and oxygen evolution reaction (OER). The modification introduces additional active sites for OER and induced more oxygen defects to further facilitate the ORR. Zn-air batteries with the Co-MnO₂ air cathode showed a higher peak power density of 167 mW cm⁻², a lower potential gap of 0.75 V and a higher round-trip efficiency of 63% (5 mA cm⁻²) compared to MnO₂ without modification. Good cycling stability of the battery is also achieved. The proper amount of cobalt species in the MnO₂ is vital for achieving a balance between high performance and durable cycling.

§ Reprinted (adapted) from (Zhong Y, Dai J, Xu X, Su C, Shao Z. Facilitating oxygen redox on manganese oxide nanosheets by tuning active species and oxygen defects for zinc-air batteries. ChemElectroChem. 2020;7(24):4949-55. doi:10.1002/celec.202001419). Copyrights (2020) Wiley-VCH GmbH.

4.1 Introduction

Among non-precious metal-based alternatives, manganese oxides have shown promise as the oxygen catalysts for Zn-air batteries due to their good activity for ORR.¹⁻⁴ Some manganese oxides have also demonstrated good catalytic activity toward the OER, indicating their capability as bifunctional oxygen catalysts.^{5,6} However, the activity of manganese oxides is usually inferior to that of precious metals. To improve the OER activity of manganese oxides, doping/co-doping other transition metal elements (e.g., Co, Ni, Fe)^{7,8} and integration of other non-previous transition metal compounds (e.g., Co_3O_4)^{9,10} were effective strategies. Since the flexibility of the doping integrating species and the tunable amounts of the modifications, intense research on seeking better OER activity had been conducted based on these two most studied strategies.¹¹ For further improving the ORR activity of manganese oxides, previous works indicated that introduce oxygen defects (or oxygen vacancies) in the crystal lattice of manganese oxides is an effective pathway for generating highly active, unsaturated Mn atoms as reactive sites.^{12,13} Multiple strategies were proposed to induce oxygen defects on manganese oxides.¹⁴ For example, some researchers induced oxygen defects without modification with other additives, e.g., heating manganese oxides under different temperatures and atmospheres,^{15,16} and proton irradiation¹⁷, while some others created oxygen defects by electrochemical extraction of pre-inserted cations from a Mn-based crystal structure.² In addition, oxygen defects can also be introduced by doping.^{18,19} In light of improving its ORR catalysis and meeting the requirement for a bifunctional oxygen catalyst, a facile modification method that not only introduces a highly active species for OER catalysis but also induces proper oxygen defects for facilitating the ORR catalysis is required.

In **Chapter 3** about mild acidic Zn-ion batteries, highly Mn-site defective MnO_2 nanosheets were synthesized using the molten-salt method.²⁰ By simply mixing the resulting highly defective MnO_2 nanosheets with CoCl_2 aqueous solution in ambient condition, Co species were integrated on the ultrathin MnO_2 structure with good dispersion. The small amount of Co species demonstrated decent catalysis for the Mn redox during the discharging/charging in the Zn-ion battery cathode. In fact, such a well-dispersed decoration of the Co species may also serve as highly active sites for OER in alkaline electrolytes. At the same time, the introduction of Co species may

induce more oxygen defects on the modified compound, which could further improve the ORR activity.

In this chapter, the facile solution-based method was applied to modify MnO₂ nanosheets with Co species, which was further extended to modification by other transition metal species (e.g., Ni and Fe). The cobalt-modified samples (Co-MnO₂) with the proper amount of oxygen defects demonstrated the best ORR-OER bifunctional catalysis, comparable to the benchmark Pt/C + IrO₂ catalyst. The Co-MnO₂ also demonstrated good capability as an efficient oxygen catalyst in the air cathode for Zn-air batteries, showing a good open-circuit voltage (OCV), a high peak power density (PPD), a good voltage gap between charging and discharging and decent cycling stability.

4.2 Experimental Sections

Synthesis of modified MnO₂

δ -MnO₂ nanosheets (denoted as MnO₂) were synthesized using a molten salt method (detail procedure described in **Chapter 3**). Modification of the MnO₂ with cobalt (Co-MnO₂), nickel (Ni-MnO₂) and iron (Fe-MnO₂) was conducted using a solution-based method. Take the modification with Co as an example, 0.2 g of MnO₂ and 20 mL of 1 M CoCl₂ aqueous solution was mixed continually with a magnetic stirrer for 8 h at room temperature. After filtering the sample, the powder was then mixed with a new 20 mL of 1 M CoCl₂ for 16 h. After filtering and washing with deionized water for three times, the powder was dried at 60 °C. For the synthesis of Ni-MnO₂, 1 M NiCl₂ aqueous solution was used. Due to the highly reductive character of Fe²⁺, mixing MnO₂ with a 1 M FeCl₂ solution resulted in the full dissolution of MnO₂. Therefore, the Fe-MnO₂ reported in this work was synthesized using a 1 M FeCl₃ aqueous solution.

Material characterizations

The elemental compositions of the MnO₂ materials before and after modification were characterized using EDS equipped on a SEM (Zeiss) and ICP-OES. Crystal structures of the materials were analyzed using XRD (Bruker D8 Advance, Cu K α radiation). The chemical states of the materials were characterized using XPS (Al K α radiation), Raman spectroscopy (HORIBA LabRAM HR Evolution, 532 nm laser excitation) and NEXAFS (Australian Synchrotron)^{21,22}.

Electrochemical tests

The ORR and OER catalysis was evaluated with a RDE in a three-electrode system. A Pt wire and a Ag/AgCl (4 M KCl) was employed as the counter and reference electrode, respectively. A freshly prepared 0.1 M KOH solution was used as the electrolyte. The catalyst dispersions were prepared by mixing 10 mg of oxide catalyst and 10 mg of conductive carbon (Super P Li) with 1 mL of absolute ethanol and 100 μ L of Nafion®117 solution (5 wt%) and then ultrasonicated for 1 h. 5 μ L of the dispersions was coated on the RDE (0.196 cm²), achieving a catalyst mass loading of \sim 0.232 mg cm⁻². For the Pt/C + IrO₂ sample, commercial products of 20% Pt/C and IrO₂ were used with a mass ratio of Pt/C:IrO₂ = 1:1. Oxygen gas was purged into the electrolyte before and during the RDE test. A potentiostat (CHI760E) was used for recording the RDE test. The linear sweep voltammetry (LSV, 5 mV s⁻¹) was conducted at 1600 rpm. For the ORR and OER evaluation, a negative scan (0.2 to -0.6 V vs. Ag/AgCl) and a positive scan (0.2 to 1.0 V vs. Ag/AgCl) was used, respectively. The potentials in the RDE test results are converted to the RHE scale converted using the following equation: $E(\text{RHE}) = E(\text{Ag/AgCl}) + 0.199 + 0.0591 \times \text{pH}$. Ohmic voltage drop was compensated for by taking into consideration of the effect from solution resistance (\sim 45 Ω , as measured by electrochemical impedance spectroscopy).

A rotating ring-disk electrode (RRDE) technique was utilized to determine the electron transfer number (n) and percentage of HO₂⁻ during the ORR evaluation. The working electrode (AFE7R9GCPT, Pine Instruments, Collection efficiency (N): 37%.) consisted of a glassy carbon disk (5.61 mm diameter) and a Pt ring (inner diameter: 6.25 mm; outer diameter: 7.92 mm). The working electrode was negatively linear scanned (5 mV s⁻¹) from 0.2 to -0.6 V (vs Ag/AgCl). Ring potential was set at 0.5 V (vs Ag/AgCl). The n and X are calculated by the equations:

$$n = 4 \times \frac{I_d}{I_d + I_r/N}$$
$$X (\%) = 200 \times \frac{I_r/N}{I_d + I_r/N}$$

Where I_d , I_r and N refer to the disk current, ring current and current collection efficiency.

Assembling and evaluation of rechargeable Zn-air batteries

The catalyst dispersions for RDE tests were also used for the preparation of air cathode. 165 μL of the dispersion (with 1.5 mg of catalyst) was drop-cast on an 8 mm circular area (0.5 cm^2) on the center of a 15×15 mm gas diffusion layer (AVCarb P75T). The air cathode was dried on a hot plate at $60\text{ }^\circ\text{C}$. The mass loading of the catalyst on an air cathode was 3 mg cm^{-2} unless otherwise specified. A Zn-air battery was assembled with the as-prepared air cathode, a Zn plate anode and ~ 2 mL of 6 M KOH + 0.2 M Zn(Ac)₂ electrolyte in a home-made test model. Galvanostatic charging and discharging performance was evaluated using a battery test system (LANHE CT2001A). Other electrochemical evaluations of the Zn-air batteries were performed using a potentiostat (Biologic VSP).

4.3 Results and Discussions

4.3.1 Characterization of modified MnO₂ samples

MnO₂ nanosheets were prepared using a molten salt assisted method. The modification of the as-synthesized MnO₂ with Co, Ni or Fe was performed using a facile solution-based approach proposed in **Chapter 3**.²⁰ Herein, three different transition metal species were respectively integrated into the MnO₂ nanosheet, which were denoted as Co-MnO₂, Ni-MnO₂ and Fe-MnO₂.

As seen from the scanning electron microscopy (SEM) images presented in **Figure 4.1a-d**, the modified samples maintained the sheet-like morphology derived from the MnO₂ nanosheet. Such loose-packed nanosheet morphology could be beneficial for providing sufficient surface for the oxygen redox reactions and channels for the gas/ionic diffusion in a cathode for Zn-air battery. Energy-dispersive X-ray spectroscopy (EDS) profiles (**Figure 4.1e**) and X-ray photoelectron spectroscopy (XPS) profiles (**Figure 4.2**) of the samples confirmed the existence of Co, Ni or Fe element after the modification. Further evaluation with inductively coupled plasma-optical emission spectrometry (ICP-OES) provided the atomic ratio of the Co, Ni or Fe versus the Mn in the modified samples (**Table 4.1**). X-ray diffraction (XRD) analysis of MnO₂ and the modified MnO₂ samples (**Figure 4.3**) confirmed that they share the same layered crystal structure. The broad XRD peaks reflect the weak

crystallization degree, which is not unexpected for the materials with a thin nanosheet morphology and is in accordance with the SEM observation (**Figure 4.1a-d**).

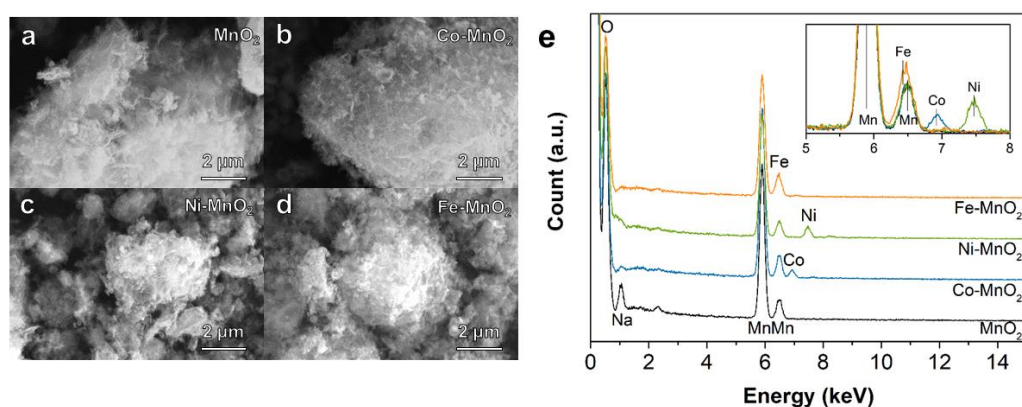


Figure 4.1 SEM-EDS characterization of the MnO₂ and modified MnO₂ samples. a-d) SEM of a) MnO₂, b) Co-MnO₂, c) Ni-MnO₂, d) Fe-MnO₂; e) EDS spectra.

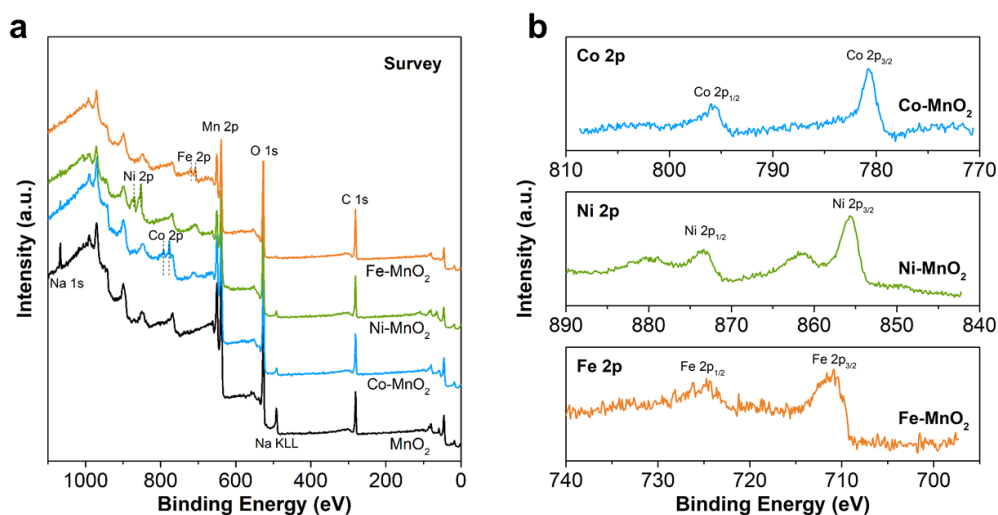


Figure 4.2 a) XPS survey spectra of the MnO₂ and modified MnO₂ samples and b) high-resolution Co 2p spectrum of Co-MnO₂, Ni 2p spectrum of Ni-MnO₂ and Fe 2p spectrum of Fe-MnO₂.

Table 4.1 Compositional analysis from ICP-OES for the modified MnO₂ samples.

Sample	Co:Mn (at:at)	Ni:Mn (at:at)	Fe:Mn (at:at)
Co-MnO ₂	0.063	/	/
Ni-MnO ₂	/	0.111	/
Fe-MnO ₂	/	/	0.076

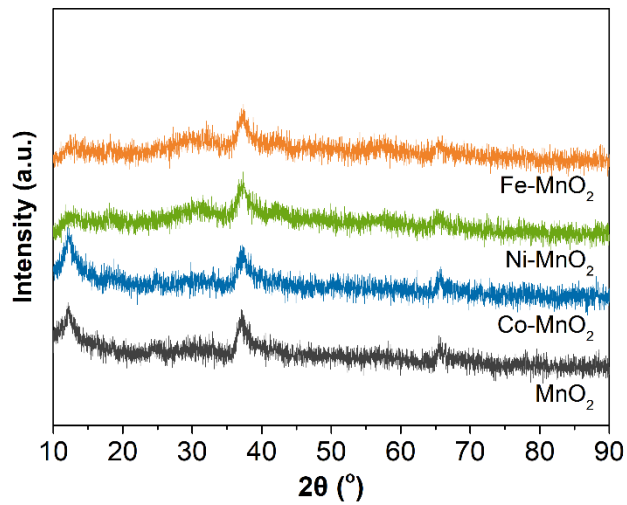


Figure 4.3 XRD profiles of the MnO₂ and modified MnO₂ samples.

4.3.2 Bifunctional catalytic activity for ORR and OER

The bifunctional catalysis of the MnO₂ samples was evaluated using a rotating disk electrode (RDE)-based system in a 0.1 M KOH electrolyte. As presented in **Figure 4.4a**, the Co-MnO₂ demonstrated improved catalysis for ORR while the Ni-MnO₂ and Fe-MnO₂ showed a negative influence on the ORR. This could be associated with the proper amount of oxygen defects induced by the cobalt modification, which will be discussed later. The Co-MnO₂ also presented an electron transfer number (n) of 3.96, which is close to 4 (**Figure 4.5**). This result indicates that most of the oxygen undergoes a four-electron reduction process, which leads to a high selectivity for the OH⁻ production.²³⁻²⁵ In **Figure 4.4b**, Co-MnO₂ and Ni-MnO₂ presented improved OER catalysis, which could be highly associated with the introduced Co and Ni and the oxygen defects. The combination of the polarization curves of ORR and OER (**Figure 4.4c**) presented the bifunctional catalysis of the samples. The activity of oxygen catalysis was evaluated by two indicative parameters, i.e., half-wave potential ($E_{1/2}$, V vs iR -corrected reversible hydrogen electrode (RHE)) for ORR and potential at the current density of 10 mA cm⁻² ($E_{j=10}$, V vs iR -corrected RHE) for OER. The $E_{1/2}$ and $E_{j=10}$ and their differences (ΔE) for the samples were extracted from **Figure 4.4c** and summarized in **Figure 4.4d**. Co-MnO₂ demonstrated an $E_{1/2}$ of 0.76 V and $E_{j=10}$ of 1.71 V, corresponding to a ΔE of 0.95 V, which is superior to the MnO₂ without

modification (1.00 V), Ni-MnO₂ (1.01 V), Fe-MnO₂ (1.12 V), and is only inferior to Pt/C + IrO₂ (0.88 V) by 0.07 V.

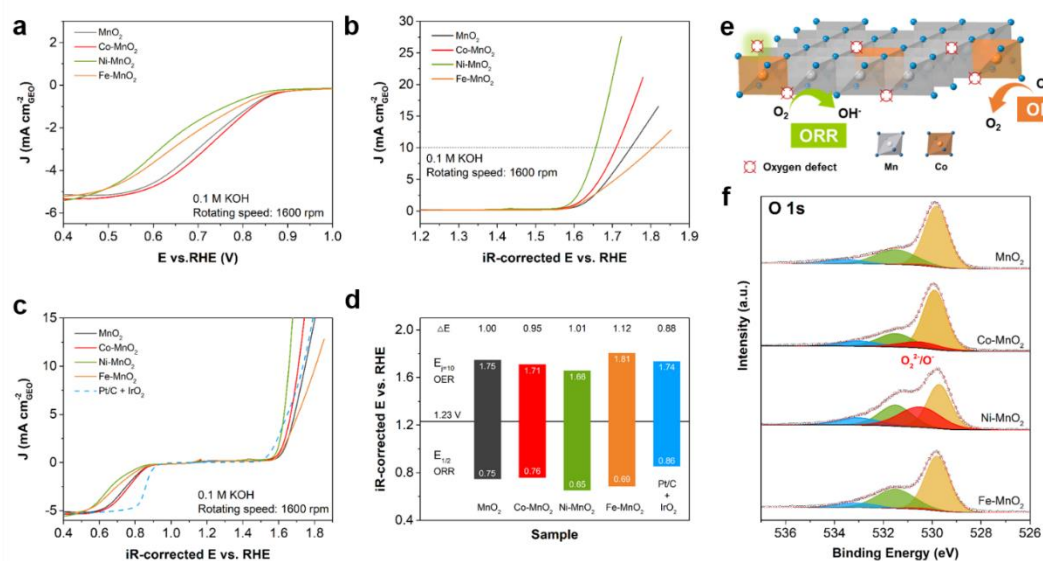


Figure 4.4 Bifunctional oxygen catalytic activity of MnO₂ and modified MnO₂ materials. a) ORR, b) OER, c) ORR-OER polarization curves in a 0.1 M KOH electrolyte, d) comparison of the corresponding ΔE , e) Illustration of boosted ORR and OER resulting from the integrated Co cation and oxygen defects, f) XPS O 1s of MnO₂, Co-MnO₂, Ni-MnO₂ and Fe-MnO₂.

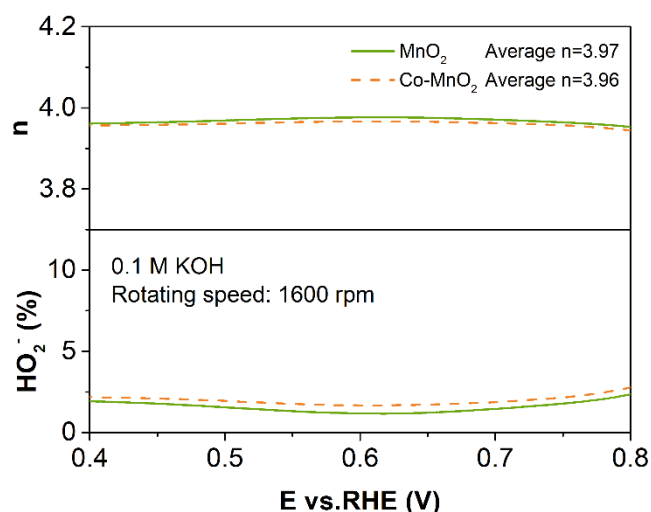


Figure 4.5 The electron transfer number (n) and HO₂⁻ yield percentage based on the data from RRDE.

The improved catalysis for OER and ORR of the Co-MnO₂ could be associated with the induced Co species and oxygen defects that induced by the cobalt modification (**Figure 4.4e**). On the one hand, as evidenced by EDS, XPS and ICP-OES results, MnO₂ after modification induced a small amount of Co which could act as the active species for OER.⁸ On the other hand, as previously reported in other publications, proper oxygen defects in the oxide materials are beneficial for both ORR and OER.^{12, 13} In our previous study of the MnO₂ and Co-MnO₂ materials for mild acidic Zn-ion battery, we focused on the analysis of the interaction of Mn and Co in the Co-MnO₂ and valence changes of the Mn before and after the cobalt modification by XPS and near-edge X-ray absorption fine-structure spectroscopy (NEXAFS).²⁰ A recent review article on the defect engineering of manganese oxide materials by Xiong et al.²⁶ indicated that oxygen vacancy (oxygen defect) is another type of defect that may influence the electrochemical performance. To evaluate the effect of oxygen defect on the oxygen catalysis in detail in this chapter, we reconducted the XPS characterization and analysis of the O1s spectra for the samples. The spectra (**Figure 4.4f**) of the four samples presented different ratios of the highly oxidative oxygen species (O₂²⁻/O⁻), which were closely associated with oxygen defects.²⁷⁻²⁹ The increase of oxygen defects is observed for Co-MnO₂ compared to MnO₂ without modification. The increase of oxygen defect is also evidenced by the comparison of Raman spectra and NEXAFS O K-edge spectra of MnO₂ and Co-MnO₂. The Raman spectra (**Figure 4.6a**) showed a decreased Mn-O vibration peak centered at ~650 cm⁻¹ for Co-MnO₂, indicating the fewer Mn-O bonds owing to more oxygen defects.³⁰ Also, the NEXAFS O K-edge spectra (**Figure 4.6b**) showed a lower intensity of the O K-pre edge peak centered at ~529 eV for Co-MnO₂, which could also be ascribed to the larger number of oxygen defects.³¹ As discussed in **Chapter 3**, after modifying MnO₂ in Co²⁺-containing solutions, MnO₂ is partially reduced while the cobalt species anchored on the MnO₂ is oxidized.²⁰ This could result in the rearrangement of the oxygen atoms, which leads to the increase of oxygen defects in the MnO₂. The unsaturated Mn atoms could serve as a more active site for ORR.^{12, 13} In the case of Ni-MnO₂, as expected, the more Ni species (as evidenced by ICP-OES, **Table 4.1**) improved the OER catalysis. At the same time, more oxygen defects are induced in the MnO₂ (**Figure 4.4f**). However, it seems that the much higher oxygen defects brings a negative result on the ORR catalysis.³² It is noted that due to the highly reductive nature of Fe²⁺, mixing Fe²⁺ (1 M concentration) and MnO₂ resulted in the entire dissolution of MnO₂. Therefore, the Fe-

MnO₂ was synthesized from the modification with Fe³⁺ instead. As expected, due to the lack of reduction capability of the Fe³⁺, no significant increase of oxygen defects was observed in the resultant Fe-MnO₂ (**Figure 4.4f**). According to the previous report, Fe-based catalysts without the integration of Ni/Co-based compounds usually do not present high activity for OER.³³ As a result, the Fe-MnO₂ demonstrated poor catalysis for ORR and OER.

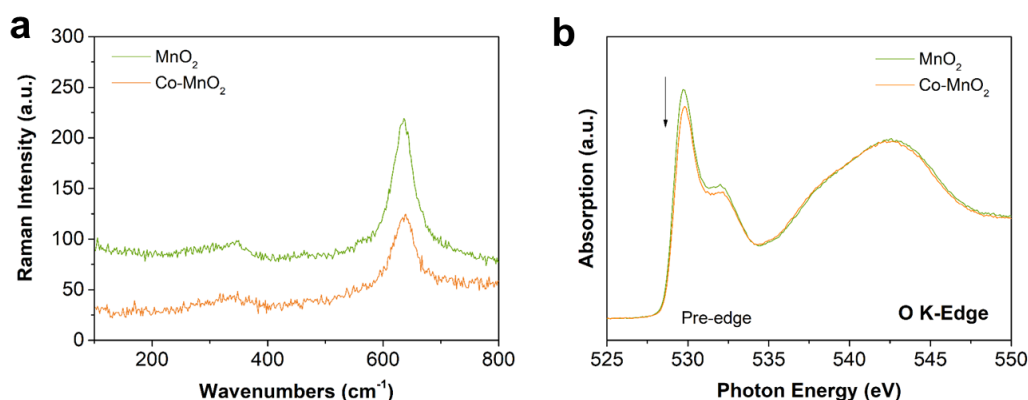


Figure 4.6 a) Raman spectra and, b) NEXAFS O K-edge of MnO₂ and Co-MnO₂.

4.3.3 Performance of the Zn-air batteries

As illustrated in **Figure 4.7a**, rechargeable Zn-air batteries with MnO₂, Co-MnO₂ or Pt/C + IrO₂ as catalyst (3 mg cm⁻²) for the air cathode, respectively, and a Zn plate as anode and an alkaline electrolyte were evaluated. During the charging process, OER occurs on the air cathode while during the discharging, ORR happens on the air cathode. Due to the improved ORR-OER catalysis, battery with Co-MnO₂ presented a higher current response at a wide voltage range, as presented in **Figure 4.8** showing the CV scans of the Zn-air battery. This result is in accordance with the LSV profiles from the RDE test. As presented in **Figure 4.7b**, Co-MnO₂ demonstrated a higher open-circuit voltage (OCV, 1.44 V) and a higher peak power density (PPD, 167 mW cm⁻²), compared to those of MnO₂ without modification (OCV: 1.41 V, PPD: 151 mW cm⁻²). The voltage gap (ΔV) between the charging voltage (V_C) and discharging voltage (V_D), and the round-trip efficiency (voltage efficiency, V_D/V_C) are important indicators for evaluating the rechargeable performance. The V_C and V_D reported in this work were evaluated by the voltages observed at the middle (2.5 min, as shown in **Figure 4.7c**) of the the corresponding charging and discharging process (i.e. median voltage). Due to the improved ORR-OER catalysis, Co-MnO₂ presented a ΔV of 0.75 V and a round-

trip efficiency of 63% (**Figure 4.7c**), which are also superior to MnO_2 without modification ($\Delta V = 0.86$ V, round-trip efficiency = 59%). The performance of the Zn-air batteries with different areal weight loadings of the Co- MnO_2 catalyst was also evaluated. As compared in **Figure 4.9**, an increase in the air cathode with catalyst loading from 1 to 2 mg cm^{-2} resulted in a lower ΔV (0.81 V vs 0.75 V). Better stability of charging voltage was also observed. Further increase of loading to 3 mg cm^{-2} did not present a significant improvement in performance and stability. The performance and stability were also compared with Pt/C + IrO_2 catalyst (both 3 mg cm^{-2}). Though the Pt/C + IrO_2 catalyst demonstrated better PPD (224 mW cm^{-2}) (**Figure 4.7b**) and lower ΔV (0.72 V) than Co- MnO_2 (**Figure 4.7c**), it presented inferior cycling stability (**Figure 4.7d**), which was also reflected by other previous reports.^{34,35} As displayed in **Figure 4.7e**, Co- MnO_2 also showed decent high-rate performance with ΔV of ~ 0.6 and ~ 1.0 V at 1 and 30 mA cm^{-2} , respectively. The lower charging voltages of Co- MnO_2 than MnO_2 without modification indicated the improved OER activity.

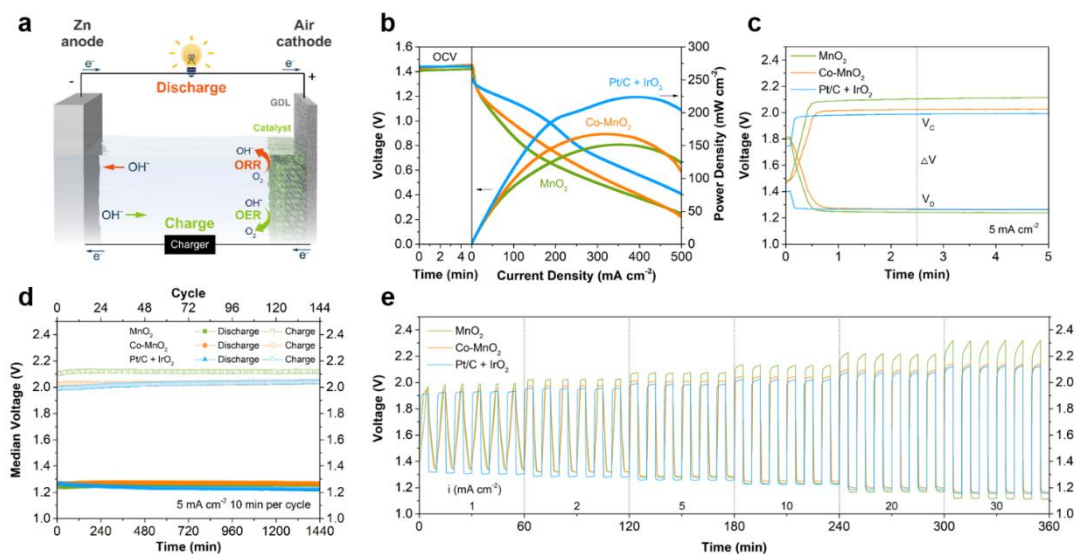


Figure 4.7 Performance of Zn-air batteries with MnO_2 , Co- MnO_2 or Pt/C + IrO_2 as the cathode catalyst. a) Illustration of a rechargeable Zn-air battery with an alkaline electrolyte, b) OCV, current density-voltage-power density (I - V - P) profiles, c) second galvanostatic charge-discharge profile, d) cycling stability, e) rate performance. Note that results in c-e) were evaluated by 5-minute galvanostatic charging and 5-minute galvanostatic discharging.

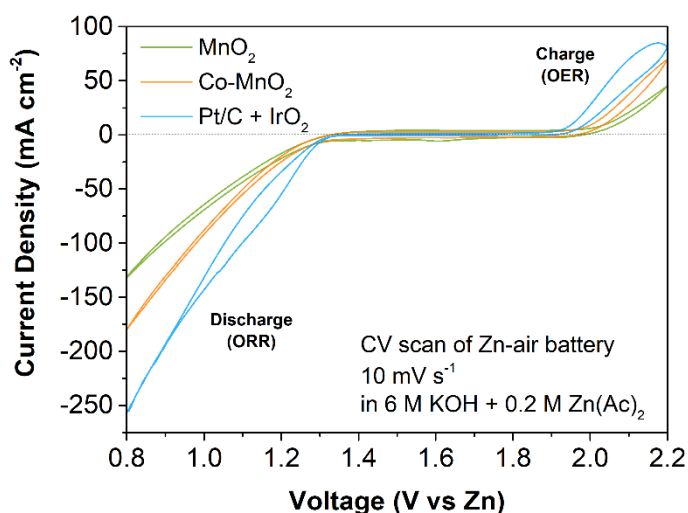


Figure 4.8 CV profiles of Zn-air batteries with MnO₂, Co-MnO₂ and Pt/C + IrO₂ as oxygen catalysts.

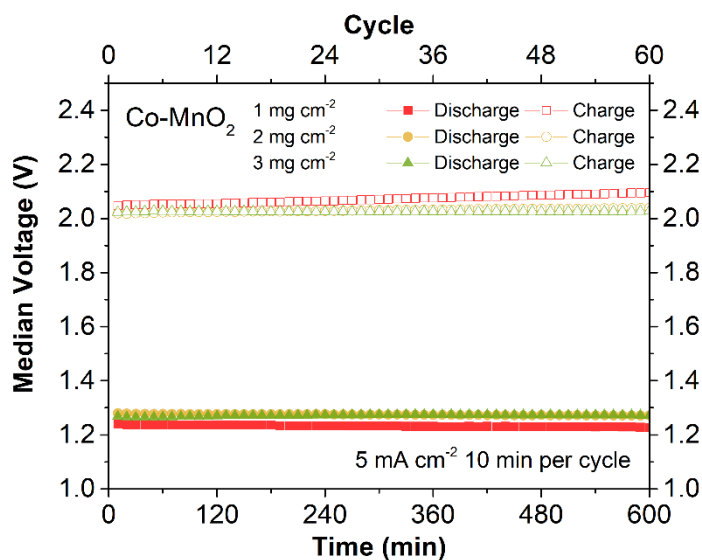


Figure 4.9 Comparison of galvanostatic charging-discharging performance of Zn-air batteries with different areal weight loadings of Co-MnO₂.

It is noted that the atomic ratio of Co:Mn for Co-MnO₂ is only 0.063 (**Table 4.2**). Increasing the amount of Co may induce more active sites for OER. By utilizing a higher temperature (80 °C) in the solution-based modification process, the Co:Mn ratio significantly increased to 0.378 (**Table 4.2**, sample denoted as Co-MnO₂-HT). The morphology of Co-MnO₂-HT maintained well after the higher temperature modification process (**Figure 4.10**), which is similar to Co-MnO₂. As expected, a higher $E_{1/2}$ for ORR of 0.78 V and a lower $E_{j=10}$ for OER of 1.64 V were achieved

(**Figure 4.11a**), corresponding to a ΔE of 0.86 V, which is slightly better compared to Pt/C + IrO₂ ($\Delta E = 0.88$ V). The improved catalysis was also confirmed in the performance of the battery with Co-MnO₂-HT, based on the higher response current density in the CV scan (**Figure 4.11b**). Cycling Zn-air battery performance with Co-MnO₂-HT also demonstrated decreased V_C (**Figure 4.11c**), indicating better catalysis for OER. However, the stability of the V_D of the battery with Co-MnO₂-HT was worse than that with Co-MnO₂. This could be associated with the lower Mn amount in Co-MnO₂-HT. At the same time, a higher Co amount might induce more oxygen defects on the MnO₂, As indicated in some previous works, too many oxygen defects may bring an adverse effect on the structural stability of the MnO₂.^{32,36} This result suggests that the proper amount of Co modification could be vital for achieving a balance between high performance and durable cycling of the Zn-air batteries.

Table 4.2 Compositional analysis from ICP-OES for Co-modified MnO₂.

Sample	Co:Mn (at:at)
Co-MnO ₂	0.063
Co-MnO ₂ -HT	0.378

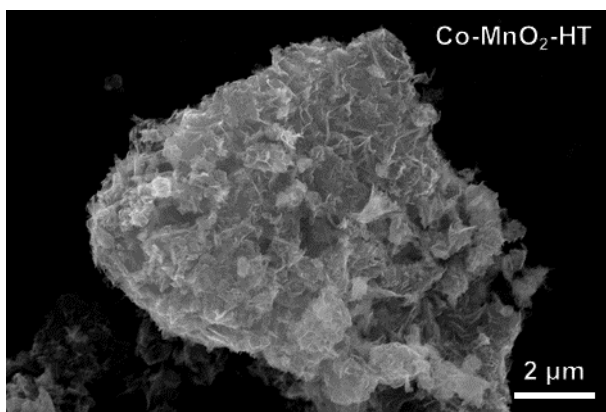


Figure 4.10 SEM image of Co-MnO₂-HT.

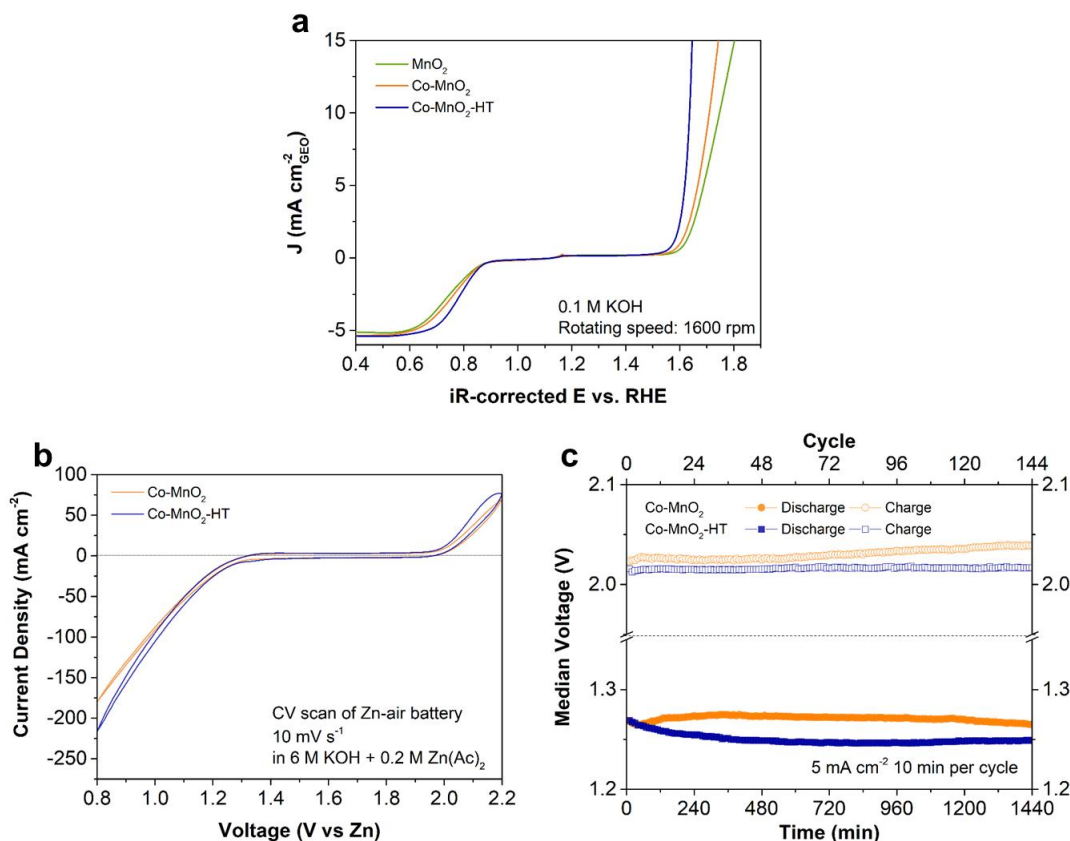


Figure 4.11 Optimization of Co-MnO₂ for improved oxygen catalysis and Zn-air battery performance. a) ORR-OER polarization curves from the RDE test, b) CV profiles and c) cycling stability at 5 mA cm⁻² of Zn-air batteries.

4.4 Conclusion

In conclusion, MnO₂ nanosheets were modified with Co, Ni or Fe via a facile solution-based method. Among the modified samples, Co-MnO₂ demonstrated improved bifunctional ORR-OER catalysis. The modification introduces an additional active site for OER and induced the proper amount of oxygen defects on the MnO₂ to further promote the ORR. As a result, Zn-air batteries with the Co-MnO₂ air cathode demonstrated lower potential gap, higher round-trip efficiency and better high-rate performance compared to the pristine MnO₂ without modification. Decent cycling stability was also achieved. By increasing the number of Co species incorporated, the bifunctional activity of Co-MnO₂ could be further improved, approaching that of the commercial benchmark catalysts. Our work provides a new avenue for developing non-precious metal-based catalysts for Zn-air batteries.

References

1. Du G, Liu X, Zong Y, Hor TSA, Yu A, Liu Z. Co₃O₄ nanoparticle-modified MnO₂ nanotube bifunctional oxygen cathode catalysts for rechargeable zinc-air batteries. *Nanoscale*. 2013;5(11):4657-61. doi:10.1039/C3NR00300K
2. Lee S, Nam G, Sun J, Lee J-S, Lee H-W, Chen W, et al. Enhanced intrinsic catalytic activity of λ -MnO₂ by electrochemical tuning and oxygen vacancy generation. *Angew Chem Int Ed*. 2016;55(30):8599-604. doi:10.1002/anie.201602851
3. Yu Q, Xu J, Wu C, Zhang J, Guan L. MnO₂ nanofilms on nitrogen-doped hollow graphene spheres as a high-performance electrocatalyst for oxygen reduction reaction. *ACS Appl Mater Interfaces*. 2016;8(51):35264-9. doi:10.1021/acsami.6b11870
4. Xue Q, Pei Z, Huang Y, Zhu M, Tang Z, Li H, et al. Mn₃O₄ nanoparticles on layer-structured Ti₃C₂ MXene towards the oxygen reduction reaction and zinc-air batteries. *J Mater Chem A*. 2017;5(39):20818-23. doi:10.1039/C7TA04532H
5. Yan G, Lian Y, Gu Y, Yang C, Sun H, Mu Q, et al. Phase and morphology transformation of MnO₂ induced by ionic liquids toward efficient water oxidation. *ACS Catal*. 2018;8(11):10137-47. doi:10.1021/acscatal.8b02203
6. Kim J, Kim JS, Baik H, Kang K, Lee K. Porous beta-MnO₂ nanoplates derived from MnCO₃ nanoplates as highly efficient electrocatalysts toward oxygen evolution reaction. *RSC Adv*. 2016;6(32):26535-9. doi:10.1039/C6RA01091A
7. Ye Z, Li T, Ma G, Dong Y, Zhou X. Metal-ion (Fe, V, Co, and Ni)-doped MnO₂ ultrathin nanosheets supported on carbon fiber paper for the oxygen evolution reaction. *Adv Funct Mater*. 2017;27(44):1704083. doi: 10.1002/adfm.201704083
8. Thenuwara AC, Shumlas SL, Attanayake NH, Aulin YV, McKendry IG, Qiao Q, et al. Intercalation of cobalt into the interlayer of birnessite improves oxygen evolution catalysis. *ACS Catal*. 2016;6(11):7739-43. doi:10.1021/acscatal.6b01980
9. Kim G-P, Sun H-H, Manthiram A. Design of a sectionalized MnO₂-Co₃O₄ electrode via selective electrodeposition of metal ions in hydrogel for enhanced electrocatalytic activity in metal-air batteries. *Nano Energy*. 2016;30:130-7. doi:10.1016/j.nanoen.2016.10.003

10. Fang M, Han D, Xu W-B, Shen Y, Lu Y, Cao P, et al. Surface-guided formation of amorphous mixed-metal oxyhydroxides on ultrathin MnO₂ nanosheet arrays for efficient electrocatalytic oxygen evolution. *Adv Energy Mater.* 2020;10(27):2001059. doi:10.1002/aenm.202001059
11. Tang Y, Zheng S, Cao S, Xue H, Pang H. Advances in the application of manganese dioxide and its composites as electrocatalysts for the oxygen evolution reaction. *J Mater Chem A.* 2020;8(36):18492-514. doi:10.1039/D0TA05985D
12. Jiang M, Fu C, Yang J, Liu Q, Zhang J, Sun B. Defect-engineered MnO₂ enhancing oxygen reduction reaction for high performance Al-air batteries. *Energy Storage Mater.* 2019;18:34-42. doi:10.1016/j.ensm.2018.09.026
13. Zhu Y, Zhou W, Yu J, Chen Y, Liu M, Shao Z. Enhancing electrocatalytic activity of perovskite oxides by tuning cation deficiency for oxygen reduction and evolution reactions. *Chem Mater.* 2016;28(6):1691-7. doi:10.1021/acs.chemmater.5b04457
14. Zeng K, Zheng X, Li C, Yan J, Tian J-H, Jin C, et al. Recent advances in non-noble bifunctional oxygen electrocatalysts toward large-scale production. *Adv Funct Mater.* 2020;30(27):2000503. doi:10.1002/adfm.202000503
15. Cheng F, Zhang T, Zhang Y, Du J, Han X, Chen J. Enhancing electrocatalytic oxygen reduction on MnO₂ with vacancies. *Angew Chem Int Ed.* 2013;52(9):2474-7. doi:10.1002/anie.201208582
16. Shi X, Zheng H, Kannan AM, Perez-Salcedo K, Escobar B. Effect of thermally induced oxygen vacancy of α -MnO₂ nanorods toward oxygen reduction reaction. *Inorg Chem.* 2019;58(8):5335-44. doi:10.1021/acs.inorgchem.9b00492
17. Choi Y, Lim D, Oh E, Lim C, Baeck S-H. Effect of proton irradiation on electrocatalytic properties of MnO₂ for oxygen reduction reaction. *J Mater Chem A.* 2019;7(19):11659-64. doi:10.1039/C9TA03879E
18. Chu K, Liu Y-p, Cheng Y-h, Li Q-q. Synergistic boron-dopants and boron-induced oxygen vacancies in MnO₂ nanosheets to promote electrocatalytic nitrogen reduction. *J Mater Chem A.* 2020;8(10):5200-8. doi:10.1039/D0TA00220H
19. Zhao Y, Zhang J, Wu W, Guo X, Xiong P, Liu H, et al. Cobalt-doped MnO₂ ultrathin nanosheets with abundant oxygen vacancies supported on

- functionalized carbon nanofibers for efficient oxygen evolution. *Nano Energy*. 2018;54:129-37. doi:10.1016/j.nanoen.2018.10.008
20. Zhong Y, Xu X, Veder J-P, Shao Z. Self-recovery chemistry and cobalt-catalyzed electrochemical deposition of cathode for boosting performance of aqueous zinc-ion batteries. *iScience*. 2020;23(3):100943. doi:10.1016/j.isci.2020.100943
 21. Cowie BCC, Tadich A, Thomsen L. The current performance of the wide range (90–2500 eV) soft X-ray beamline at the Australian Synchrotron. *AIP Conf Proc*. 2010;1234(1):307-10. doi:10.1063/1.3463197
 22. Gann E, McNeill CR, Tadich A, Cowie BCC, Thomsen L. Quick AS NEXAFS Tool (QANT): A program for NEXAFS loading and analysis developed at the Australian Synchrotron. *J Synchrotron Radiat*. 2016;23(1):374-80. doi:10.1107/S1600577515018688
 23. Niu W, Li Z, Marcus K, Zhou L, Li Y, Ye R, et al. Surface-modified porous carbon nitride composites as highly efficient electrocatalyst for Zn-air batteries. *Adv Energy Mater*. 2018;8(1):1701642. doi:10.1002/aenm.201701642
 24. Ma L, Chen S, Pei Z, Huang Y, Liang G, Mo F, et al. Single-site active iron-based bifunctional oxygen catalyst for a compressible and rechargeable zinc–air battery. *ACS Nano*. 2018;12(2):1949-58. doi:10.1021/acsnano.7b09064
 25. Arafat Y, Azhar MR, Zhong Y, Xu X, Tadé MO, Shao Z. A porous nano-micro-composite as a high-performance bi-functional air electrode with remarkable stability for rechargeable zinc–air batteries. *Nano-Micro Lett*. 2020;12:130. doi:10.1007/s40820-020-00468-4
 26. Xiong T, Zhang Y, Lee WSV, Xue J. Defect engineering in manganese-based oxides for aqueous rechargeable zinc-ion batteries: A review. *Adv Energy Mater*. 2020;10(34): 2001769. doi:10.1002/aenm.202001769
 27. Zhu Y, Zhou W, Zhong Y, Bu Y, Chen X, Zhong Q, et al. A perovskite nanorod as bifunctional electrocatalyst for overall water splitting. *Adv Energy Mater*. 2017;7(8):1602122. doi:10.1002/aenm.201602122
 28. Merino NA, Barbero BP, Eloy P, Cadús LE. $\text{La}_{1-x}\text{Ca}_x\text{CoO}_3$ perovskite-type oxides: Identification of the surface oxygen species by XPS. *Appl Surf Sci*. 2006;253(3):1489-93. doi:10.1016/j.apsusc.2006.02.035
 29. Cheng G, Kou T, Zhang J, Si C, Gao H, Zhang Z. $\text{O}_2^{2-}/\text{O}^-$ functionalized oxygen-deficient Co_3O_4 nanorods as high performance supercapacitor electrodes

- and electrocatalysts towards water splitting. *Nano Energy*. 2017;38:155-66. doi:10.1016/j.nanoen.2017.05.043
30. Han M, Huang J, Liang S, Shan L, Xie X, Yi Z, et al. Oxygen defects in β -MnO₂ enabling high-performance rechargeable aqueous zinc/manganese dioxide battery. *iScience*. 2020;23(1):100797. doi:10.1016/j.isci.2019.100797
 31. Guo E-J, Liu Y, Sohn C, Desautels RD, Herklotz A, Liao Z, et al. Oxygen diode formed in nickelate heterostructures by chemical potential mismatch. *Adv Mater*. 2018;30(15):1705904. doi:10.1002/adma.201705904
 32. Li L, Feng X, Nie Y, Chen S, Shi F, Xiong K, et al. Insight into the effect of oxygen vacancy concentration on the catalytic performance of MnO₂. *ACS Catal*. 2015;5(8):4825-32. doi:10.1021/acscatal.5b00320
 33. Han L, Dong S, Wang E. Transition-metal (Co, Ni, and Fe)-based electrocatalysts for the water oxidation reaction. *Adv Mater*. 2016;28(42):9266-91. doi:10.1002/adma.201602270
 34. Wei L, Karahan HE, Zhai S, Liu H, Chen X, Zhou Z, et al. Amorphous bimetallic oxide-graphene hybrids as bifunctional oxygen electrocatalysts for rechargeable Zn-air batteries. *Adv Mater*. 2017;29(38):1701410. doi:10.1002/adma.201701410
 35. Wang X, Sunarso J, Lu Q, Zhou Z, Dai J, Guan D, et al. High-performance platinum-perovskite composite bifunctional oxygen electrocatalyst for rechargeable Zn-air battery. *Adv Energy Mater*. 2020;10(5):1903271. doi:10.1002/aenm.201903271
 36. Ji Q, Bi L, Zhang J, Cao H, Zhao XS. The role of oxygen vacancies of ABO₃ perovskite oxides in the oxygen reduction reaction. *Energy Environ Sci*. 2020;13(5):1408-28. doi:10.1039/D0EE00092B

Every reasonable effort has been made to acknowledge the owners of copyright material. I would be pleased to hear from any copyright owner who has been omitted or incorrectly acknowledged.

Chapter 5 A function-separated MnS-Ni_xCo_{1-x}S₂ electrode for realizing high-performance hybrid zinc batteries §

Abstract

Rechargeable hybrid Zn battery is developed for reaching high power density and high energy density simultaneously by introducing an additional alkaline Zn-transition metal compound (Zn-MX) battery function into rechargeable Zn-air battery. However, the conventional single-layer electrode design is impossible to satisfy the requirements of both a hydrophilic interface for facilitating ionic transfer to maximize the Zn-MX battery function and a hydrophobic interface for promoting gas diffusion to maximize the Zn-air battery function. To tackle this dilemma, here we propose a function-separated design which allocates the two battery functions to the two faces of the cathode. The electrode is composed of a hydrophobic MnS layer decorated with Ni-Co-S nanoclusters that allows for smooth gas diffusion and efficient oxygen electrocatalysis and a hydrophilic Ni_xCo_{1-x}S₂ layer that favors fast ionic transfer and superior performance for energy storage. The hybrid Zn battery operating with the function-separated electrode shows a high short-term discharge voltage of ~1.7 V, an excellent high-rate galvanostatic discharge-charge with a power density up to 153 mW cm⁻² at 100 mA cm⁻², a good round-trip efficiency of 75% at 5 mA cm⁻², and a robust cycling stability for 330 h with an excellent voltage gap of ~0.7 V at 5 mA cm⁻².

§ Reprinted (adapted) from (Zhong Y, Xu X, Liu P, Ran R, Jiang SP, Wu H, Shao Z. A function-separated design of electrode for realizing high-performance hybrid zinc battery. *Adv Energy Mater.* 2020;10(47):2002992. doi:10.1002/aenm.202002992). Copyrights (2020) Wiley-VCH GmbH.

5.1 Introduction

The relatively poor rate capability and low round-trip efficiency are two major drawbacks of Zn-air batteries show. By introducing the function of a Zn-MX battery into the air electrode of a Zn-air battery, a hybrid Zn battery was proposed, which may show both high power density and excellent energy density.^{1,2} The cathode, where both cation redox and oxygen redox occur, can have a great impact on the overall performance.²⁻⁴ During the past, most of the efforts on hybrid Zn-based batteries were made on the electrochemical evaluation of the hybrid features and the development of multifunctional cathode materials (e.g., Co_3O_4 ⁴⁻⁶, NiO/Ni(OH)_2 ^{2,7,8}, NiCo_2O_4 ^{3,9}, NiCo_2S_4 ^{10,11}, Ag ^{12,13}) with favorable cation redox capability and decent bifunctional catalysis towards both oxygen reduction reaction (ORR) and oxygen evolution reaction (OER).¹⁴⁻¹⁶ Most hybrid batteries in these works presented single-layer electrodes with even dispersion of all functional components (catalyst/active material, conductive carbon and binder). The rational design of the electrode structure for improving the mass transfer on a hybrid Zn battery cathode may also have a considerable influence on the battery performance, which remains largely underexplored.

In some reports, cathode with optimized liquid-solid interfaces¹⁷ and optimized gas-liquid-solid interfaces^{18,19} has been demonstrated to enhance the overall performance of Zn-MX batteries and Zn-air batteries, respectively. The construction of a porous electrode with suitable pore size and pore distribution is a widely adopted strategy in Zn-air batteries and Zn-MX batteries, which can improve the mass transfer to some extent.²⁰⁻²⁴ Another effective strategy for achieving fast mass transfer is through tuning the wettability (i.e., hydrophilicity or hydrophobicity) of the cathode.^{17,25,26} The Faradaic cation redox in a Zn-MX battery cathode requires improved electrolyte accessibility for better ionic transfer²³ while the oxygen redox in a Zn-air battery cathode requires improved gas accessibility for accelerated gas diffusion²⁷. The conventional single layer electrode design, however, can only meet one of the two requirements, i.e., establishing either a hydrophilic interface for facilitating ionic transfer or a hydrophobic interface for providing better gas diffusion. This contradiction leads to an inevitable sacrifice of the performance of one function in order to satisfy the other.

A separation of the two battery functions based on the above specific requirements, in the electrode scale, may resolve this contradiction. To achieve this separation, a double-face (Janus-type) electrode design with different properties on each face would be a promising method. In other electrochemical applications (e.g., electrochemical H₂O₂ production, fuel cells, electrocatalysis, and conventional rechargeable Zn-air batteries), Janus-type electrodes with an asymmetric double-layered structure have demonstrated some unique improvement on the mass transfers and stability.^{18,28-32} Some previous reports for oxygen electrocatalysis developed the Janus-type electrode with asymmetric wettabilities to facilitate the mass transfer for oxygen redox,^{18,30} while some others proposed Janus-type electrodes with asymmetric compositions (e.g., MnO₂-NiFe layered double hydroxides) to improve the cycling stability of Zn-air batteries.^{31,32} However, the above asymmetric designs for other applications only focus on specific reactions (e.g., ORR & OER) which may not achieve an effective improvement of both battery function of the hybrid Zn battery, especially for the Zn-MX battery function.

In this work, we propose a new function-separated design which allocates the two battery functions to the two faces of the electrode, respectively. The electrode perfectly tackles the dilemma between electrolyte accessibility and gas accessibility in a single-layer electrode and facilitates both oxygen redox and Faradaic cation redox at the same time. Specifically, a hydrophobic polytetrafluoroethylene (PTFE)-incorporated MnS layer with modification of Ni-Co-S nanoclusters provides outstanding electrocatalytic activity for ORR and OER as an air electrode for Zn-air battery and a Ni_xCo_{1-x}S₂ layer with a hydrophilic surface acts as the cathode of Zn-MX battery. Such an exquisitely designed electrode was fabricated based on a facile two-step process. Hybrid Zn batteries with the function-separation design of the electrode demonstrated advantageous features of high power density, excellent round trip efficiency and good stability.

5.2 Experimental Sections

Preparation of MnO₂-CNT-PTFE film

The MnO₂-CNT-PTFE (with a mass ratio of 6:2:2) film was prepared by ultrasonic mixing 0.06 g MnO₂ (detailed synthesis see Supporting Information), 0.02 g CNT, 3.33 g 0.6 wt% PTFE solution (containing 0.02 g of PTFE) and 10 mL of ethanol. The

mixed dispersion was dried at 60°C and wetted with a small amount of ethanol again to form a gum-like mixture. The gum was pressed into a thin film and dried at 60 °C, resulting in a dry film with an areal MnO₂ loading amount of ~2 to 3 mg cm⁻². Small round disks with a diameter of 8 mm and an area of 0.5 cm² were cut using a hole puncher.

Preparation of function-separated MnS-Ni_xCo_{1-x}S₂ electrode

The electrode was prepared with a two-step procedure. First step is the electrodeposition of NiCo-LDH on the MnO₂-CNT-PTFE film. Typically, MnO₂-CNT-PTFE film was cold pressed on one side of a stainless-steel mesh current collector. The MnO₂-CNT-PTFE electrode and a graphite electrode were soaked in a 0.05 M Co(NO₃)₂ + 0.05 M Ni(NO₃)₂ aqueous solution to establish a two-electrode system. A constant reduction current (10 mA) was applied on the working electrode with a duration time of 60-300 s. The double-layer electrode after deposition (NiCo-LDH on MnO₂-CNT-PTFE) was removed from the solution and flushed with deionized water and then dried at ambient atmosphere. The second step is the sulfurization of the double layered electrode. The electrode was put in one end of a 3x6 cm alumina boat while 0.1 g of sulfur powder was put on the other end. The boat was covered by another empty alumina boat and then placed into a quartz tube in a tube furnace. A heating treatment of 350 °C for 0.5 h with a fast heating rate of 10 °C min⁻¹ and with a nitrogen gas flow was applied. During the treatment, sulfur powder was vaporized and reacted with the electrode. The residual sulfur in the boat was removed along with the nitrogen gas flow. The residual area of the stainless-steel mesh current collector was removed by the hole puncher with a diameter of 8 mm. Due to the similar molar mass of MnO₂ and MnS, the resulting areal MnS loading amount is same to that of MnO₂ (~2-3 mg cm⁻²). The areal loading amount of the Ni_xCo_{1-x}S₂ was evaluated based on the weight differences before and after the electrodeposition of NiCo-LDH and on the molar weight relationship between NiCo-LDH and Ni_xCo_{1-x}S₂. For a 300s deposition, areal loading amount of the resulting Ni_xCo_{1-x}S₂ was ~0.8 mg cm⁻². For comparison purpose, a single layer electrode with Pt/C + IrO₂ (4 mg cm⁻² with a mass ratio of Pt/C:IrO₂ = 1:1), CNT and PTFE (with a mass ratio of catalyst:CNT:PTFE = 6:2:2) was also prepared following procedures similar to those for the MnO₂-CNT-PTFE film.

Characterizations

Phase structure of the samples was analyzed with XRD (Bruker D8 Advance, Cu K α radiation) and HR-TEM (Titan G2). The hydrophilicity and hydrophobicity of the electrodes were evaluated using the contact angle test with the Zn-based battery electrolyte (6 M KOH + 0.2 M Zn(Ac)₂). The texture, morphology and elemental dispersion of the double-layer electrode was analyzed with a SEM (Zeiss) equipped with an EDS function. High-resolution elemental dispersion on the electrode layers was further analyzed with the EDS mapping function equipped on the Titan G2.

Evaluation of oxygen catalytic activity

Electrochemical measurements for the ORR and OER activity of the MnS, Ni_xCo_{1-x}S₂ and MnS-Ni_xCo_{1-x}S₂ powder samples and the benchmark Pt/C + IrO₂ sample were conducted using the same methods and conditions as described in **Chapter 4** (See **4.2 Experimental sections**).

Assembling and evaluation of hybrid Zn batteries

The as-prepared function-separated electrodes (diameter of 8 mm) was put in the center of a carbon gas diffusion layer (GDL, AVCarb P75T, 1.5×1.5 cm) and then put on a stainless-steel mesh (1.5×1.5 cm), then cold pressed with a 4 MPa pressure. A home-made Zn-air battery model was utilized for the electrochemical evaluation of the hybrid Zn battery with a Zn plate as anode and an 6 M KOH + 0.2 M Zn(Ac)₂ as electrolyte. Cyclic voltammetry (CV) scans of the hybrid Zn batteries were recorded using a Biologic VSP potentiostat. Galvanostatic charging and discharging profiles and cycling stability of the batteries were recorded using a LANHE CT2001A battery test system.

Synthesis of MnO₂ powder and MnS powder

The MnO₂ was synthesized using a molten salt assisted method. Typically, 0.6 g of MnSO₄·H₂O was mixed with 15 g of NaNO₃ in a mortar. The mixture powder was transferred to a crucible and heated at 350 °C for 10 min. After cooled to room temperature, the solid mixture was dissolved in deionized water and filtered for three times to remove the residual salts. The powder was dried at 60 °C before use. For synthesis of the MnS, similar sulfurization process as the function-separated electrode was applied. Typically, 0.05 g of the as-synthesized MnO₂ powder and 0.2 g of sulfur powder was used for the sulfurization. Given the greater amount of MnO₂, a longer

heating time of 1 h was applied. The as-obtained MnS powder is used for RDE tests and for preparation of the single-layer electrodes.

Synthesis of NiCo-LDH powder and Ni_xCo_{1-x}S₂ powder

The NiCo-LDH was electrochemically deposited on a stainless-steel mesh in 0.05 M Co(NO₃)₂ + 0.05 M Ni(NO₃)₂ aqueous solution with a constant reduction current of 50 mA for 10 min. The attached NiCo-LDH was separated using an ultrasonic bath and further filtration and water washing was applied. The resulting powder was dried under ambient condition. The Ni_xCo_{1-x}S₂ powder was synthesized using the same condition to that of the MnS. The as-obtained Ni_xCo_{1-x}S₂ powder is used for RDE tests and for preparation of the single-layer electrodes.

Preparation of conventional single layer MnS-Ni_xCo_{1-x}S₂ electrode

The electrode slurry was prepared by mixing 6 or 8 mg of MnS powder, 1.6 mg of Ni_xCo_{1-x}S₂ powder, 2 mg of CNT, binder solution (with a total binder amount of 2 mg; PTFE, Nafion and their 1:1 (wt:wt) mixture were used as three different binders and wettability tuning agents). Proper amount of ethanol was added into the mixture until the volume reached 1 mL. The mixture was ultrasonic for 1 h to form a slurry. A stainless-steel mesh disk with a diameter of 0.5 cm² was put in the center of a GDL (1.5×1.5 cm) and then put on another stainless-steel mesh (1.5×1.5 cm), then cold pressed with a 4 MPa pressure. 250 μL of the slurry was drop-cast within the area of the stainless-steel mesh with a diameter of 8 mm (area: 0.5 cm²). After the electrode was dried at 100 °C, the entire electrode with powders, GDL and current collectors was cold pressed with a 4 MPa pressure. The resulting areal amount of MnS and Ni_xCo_{1-x}S₂ were 3 or 4 mg cm⁻² and 0.8 mg cm⁻², respectively.

5.3 Results and Discussions

5.3.1 Preparation and characterization of the function-separated electrode

Compared to the conventional single-layer electrodes (**Figure 5.1a&b**), the new function-separated design allocates the electrode layer face to the electrolyte for the Zn-MX battery function and the layer face to air for the Zn-air battery function. The achievement of the function-separated design includes two different aspects, i.e., asymmetric wettability and asymmetric composition. Based on the rational design of the composition which facilitates kinetics of the redox reactions and the design of the

wettability which facilitate the specific mass transfers (**Figure 5.1c**), both battery functions could be optimized. Noted that such function-separation focuses on the optimization at the electrode scale, and it does not conflict with the concept of the “hybrid Zn battery” where battery functions are still hybridized at the battery scale with only one Zn anode and one electrolyte, aiming at achieving both high power density and energy density in a single battery.

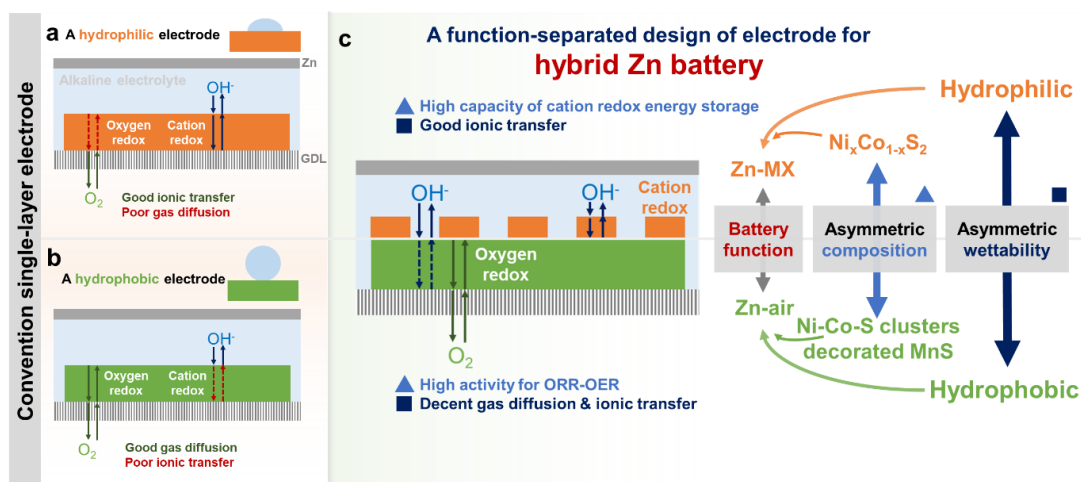


Figure 5.1 Schematic illustrations of the function-separated design of electrode for hybrid Zn battery. a,b) conventional single-layer electrodes with a) a hydrophilic surface and b) a hydrophobic surface; c) the advantages for facilitating redox reactions and mass transfers in different layers of a function-separated MnS-Ni_xCo_{1-x}S₂ electrode, respectively.

The fabrication procedure of such a function-separated electrode is schematically shown in **Figure 5.2a-c**. A layer consisting of MnO₂ nanosheets, carbon nanotube (CNT) and polytetrafluoroethylene (PTFE) with a mass ratio of 6:2:2 was first prepared (**Figure 5.2a**). Nickel-cobalt bimetallic layered double hydroxide (NiCo-LDH) was integrated to the MnO₂-CNT-PTFE layer by electrodeposition at a reduction current of 10 mA in a 0.05 M Co(NO₃)₂ + 0.05 M Ni(NO₃)₂ aqueous solution. During the electrodeposition process, NO₃⁻ was reduced while at the same time OH⁻ was generated and reacted with the Co²⁺ and Ni²⁺ to form NiCo-LDH that deposited within the pores of MnO₂-CNT-PTFE layer or on its surface.^{33,34} It is important to note that the PTFE in the MnO₂-CNT-PTFE layer served not only as a binder, but also as a wettability tuning agent. The hydrophobic nature of the MnO₂-CNT-PTFE layer effectively suppressed accessibility of the Co(NO₃)₂ + 0.05 M Ni(NO₃)₂ solution during the electrodeposition process. As a result, only a small amount of NiCo-LDH

was deposited inside the MnO₂-CNT-PTFE layer while the majority of the NiCo-LDH was deposited on the layer surface (**Figure 5.2b**). This design of distribution of Ni, Co species could provide two beneficial effects on the hybrid Zn batteries. On the one hand, sufficient pores were preserved for smooth gas diffusion and ionic transfer. On the other hand, the proper amount of NiCo-LDH deposition inside the layer could enhance the bifunctionality for oxygen electrocatalysis, which will be discussed in more detail later. It was reported that the electronic conductivity of manganese sulfide (e.g., α -MnS: $\sim 1 \times 10^{-1} \text{ S cm}^{-1}$)³⁵ is ~ 5 orders of magnitude higher than manganese oxide (e.g., δ -MnO₂: $\sim 2 \times 10^{-6} \text{ S cm}^{-1}$)³⁶ at room temperature. To achieve a higher electronic conductivity of the electrode material for better charge transfer, the resulting dual-layer electrode was further sulfurized using a facile thermal treatment with sulfur vapour at 350 °C (**Figure 5.2c**), where MnO₂ was converted into MnS and NiCo-LDH was converted into Ni_xCo_{1-x}S₂.

According to the results in **Figure 5.2d&e**, the different hydrophilic/hydrophobic properties of the different layers in the electrode were confirmed by contact angle analysis with the liquid electrolyte for the hybrid Zn batteries. For the Ni_xCo_{1-x}S₂ layer, a contact angle of 82° was observed suggesting its hydrophilic character. As to the MnS layer, however, a much larger contact angle of 148° was observed, suggesting its hydrophobic nature, as expected. **Figure 5.2f&g** gives the surface morphology and element mapping of the sulfurized electrode based on the analysis from scanning electron microscope and energy-dispersive X-ray spectroscopy (SME-EDS). The dual-layer feature with Ni-, Co-rich hydrophilic layer and a Mn-rich hydrophobic layer was revealed according to the Ni, Co and Mn dispersion within the electrode. Cracks with a width around tens of micrometers were observed on the top Ni_xCo_{1-x}S₂ layer. Such cracks may form during the drying process of the deposited LDH (**Figure 5.3a**), likely due to the mismatched shrinkage of the bottom layer and the loose and porous hydrophilic layer (**Figure 5.3d** & inset image of **Figure 5.2f**). It is worth noting that firm attachment of the top Ni_xCo_{1-x}S₂ layer onto the bottom layer was realized owing to the presence of strong interaction between the Ni, Co species and the surface CNT and PTFE (**Figure 5.3b&c**). The thickness of the hydrophilic layer and the hydrophobic layer are ~ 15 and $\sim 60 \mu\text{m}$, respectively, as observed with a SEM of the cross-section of the electrode (**Figure 5.2h**). The cross-layer linear scan EDS profile of the electrode cross-section (**Figure 5.2i**) provided further supportive evidence of the dispersion of Mn and Co-Ni compounds (**Figure 5.2g**).

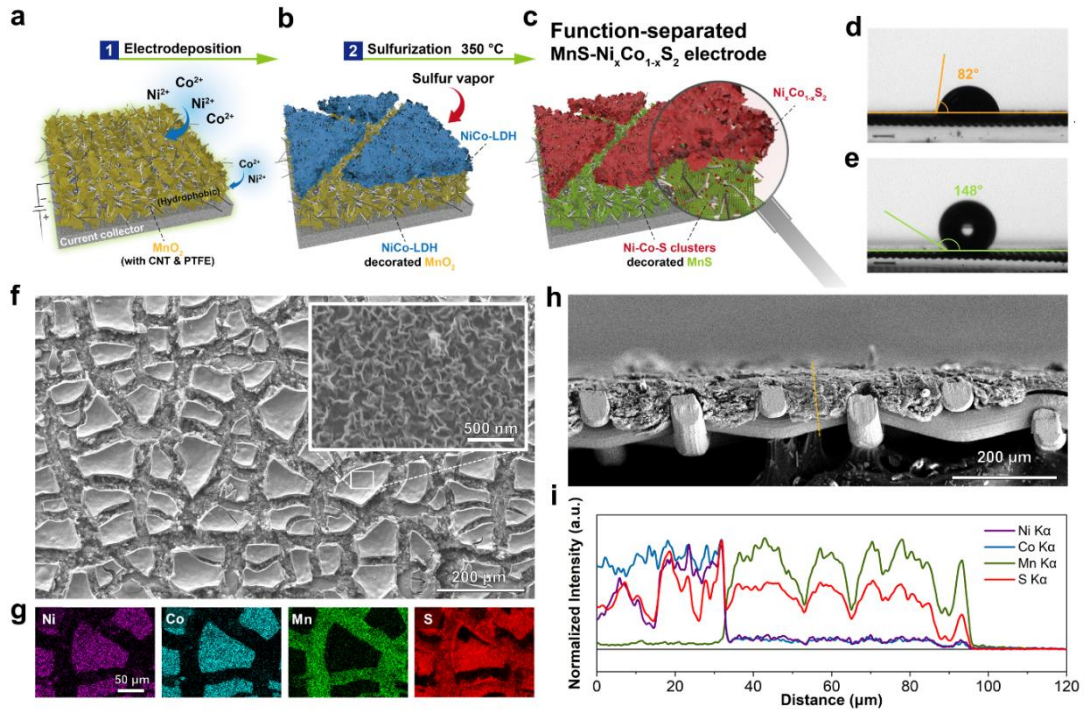


Figure 5.2 Preparation and characterization of the function-separated $\text{MnS-Ni}_x\text{Co}_{1-x}\text{S}_2$ electrode. a-c) Illustration of the preparing process; d-e) Wettability characteristics evaluated by the contact angles analysis with the hybrid battery electrolyte on d) hydrophilic $\text{Ni}_x\text{Co}_{1-x}\text{S}_2$ layer and e) hydrophobic MnS layer; f) SEM of the function-separated $\text{MnS-Ni}_x\text{Co}_{1-x}\text{S}_2$ electrode (inset image shows the porous structure of the hydrophilic $\text{Ni}_x\text{Co}_{1-x}\text{S}_2$ layer) and g) EDS element mapping; h) SEM of the cross-section of the function-separated $\text{MnS-Ni}_x\text{Co}_{1-x}\text{S}_2$ electrode and i) EDS linear scan analysis across the layers.

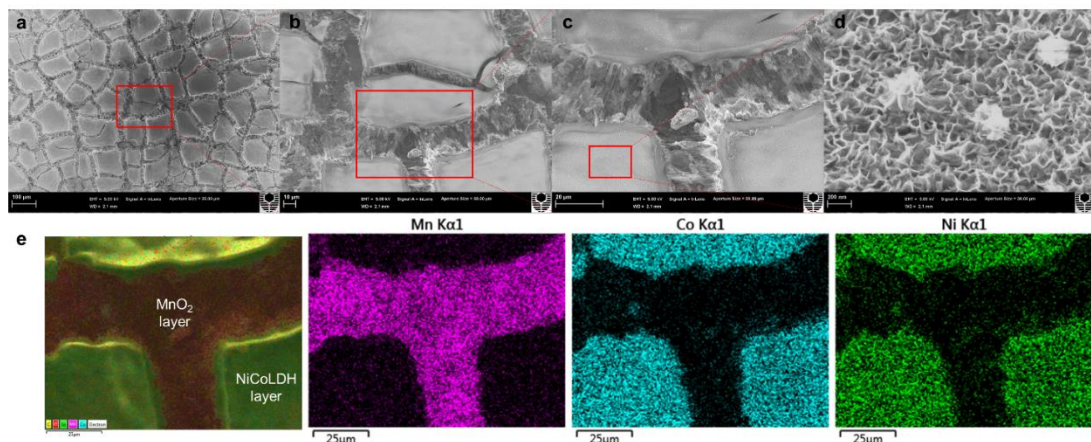


Figure 5.3 SEM and corresponding EDS mapping of the electrodeposited double-layer $\text{MnO}_2\text{-NiCo-LDH}$ electrode.

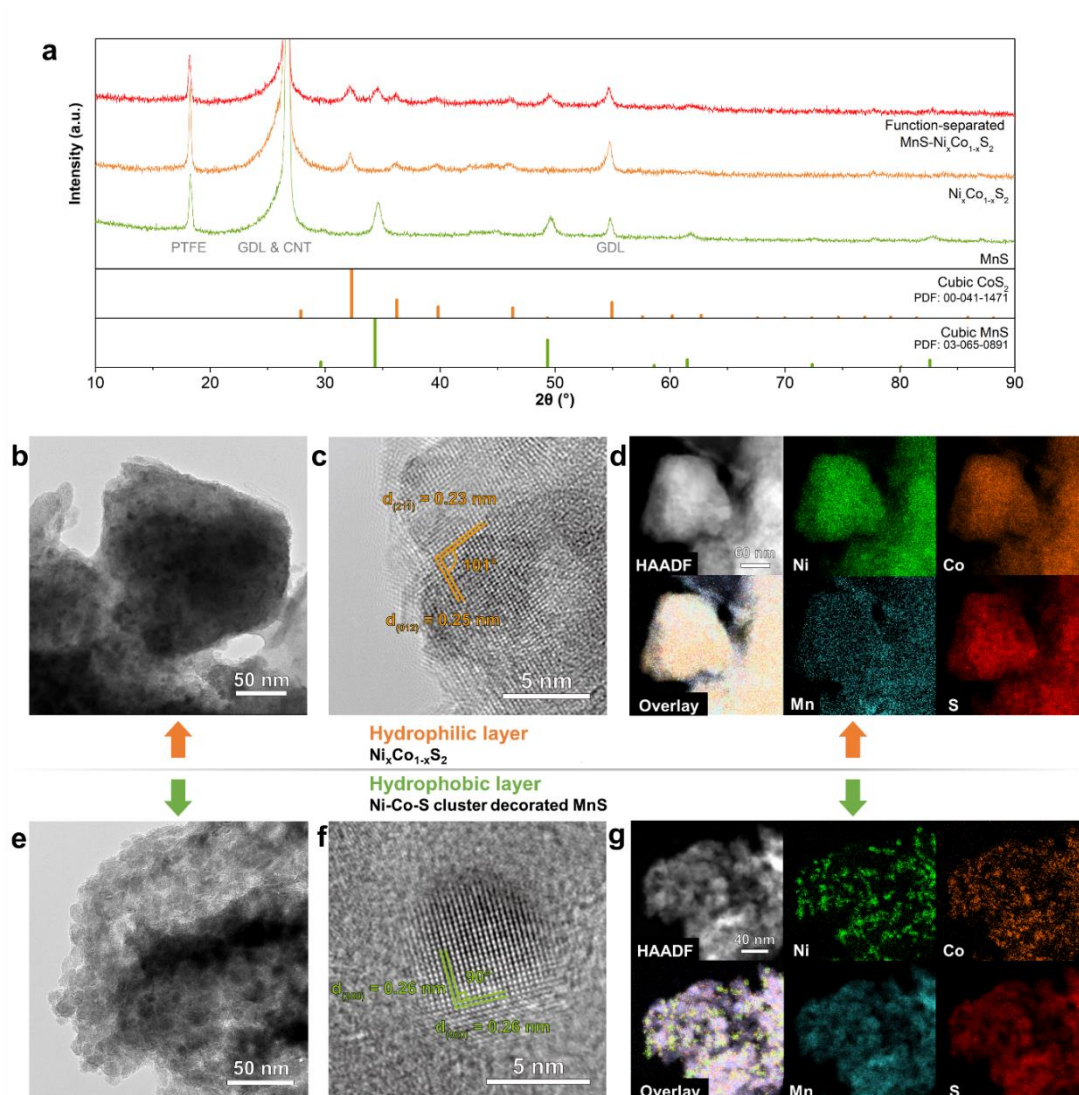


Figure 5.4 Structural and compositional characterization of the function-separated $\text{MnS-Ni}_x\text{Co}_{1-x}\text{S}_2$ electrode. a) XRD profiles of function-separated $\text{MnS-Ni}_x\text{Co}_{1-x}\text{S}_2$ electrode compared with two electrodes with only MnS or $\text{Ni}_x\text{Co}_{1-x}\text{S}_2$; b) TEM and c) HR-TEM observation and d) TEM-EDS elemental mapping of the hydrophilic layer; e) TEM and f) HR-TEM observation and g) TEM-EDS elemental mapping of the hydrophobic layer.

The phase composition of the electrode was first characterized by X-ray diffraction (XRD, **Figure 5.4a**). A cubic phase with an $Fm\bar{3}m$ space group was observed for the hydrophobic layer, which matched well with the standard powder diffraction file (PDF, code 03-065-0891) of MnS, while a cubic phase with a $Pa\bar{3}$ space group was observed for the hydrophilic layer, which is well assigned to a phase similar to cubic CoS_2 (PDF code 00-041-1471). The phase composition of the two different electrode layers was

further investigated by high-resolution transmission electron microscopy (HR-TEM) presented in **Figure 5.4b,c,e,f**. Crystalline phase with lattice distances of 0.23 and 0.25 nm was observed in the hydrophilic layer, which can be assigned to the (21 $\bar{1}$) and (012) lattice planes of Ni_xCo_{1-x}S₂ phase. As to the hydrophobic layer, crystalline phase with lattice distance of 0.26 and 0.26 nm was observed, which matched well with (200) and (020) planes of MnS. Both XRD and HR-TEM results confirmed the different compositions of the two layers in the electrode. The TEM-EDS elemental mapping provided more details about the materials composition (**Figure 5.4d&g**). As expected, a minor amount of Ni-Co-S nanoclusters was deposited on the MnS nanoparticles and well dispersed within the hydrophobic layer (**Figure 5.4g**). It should be mentioned that owing to the strong background signal from MnS, the phase structure of the Ni-Co-S nanoclusters within the hydrophobic layer was difficult to be determined.

5.3.2 Bifunctional catalytic activity for ORR-OER and performance of the Zn-air battery function

Both the intrinsic catalytic activity of the electrocatalyst and the gas diffusion properties of the electrode determine the performance of the air electrode in a Zn-air battery.^{26,27,37,38} The intrinsic catalytic activity of MnS and Ni_xCo_{1-x}S₂ for ORR and OER was assessed using a rotating disk electrode (RDE, 1600 rpm) based setup with a 0.1 M KOH electrolyte (See detailed preparation procedures and characterizations in experimental section and **Figure 5.5**). According to **Figure 5.7a**, MnS shows favourable catalytic activity of ORR with a half-wave potential ($E_{1/2}$) of 0.851 V (iR-corrected, vs RHE), which is comparable to that of the commercial Pt/C + IrO₂ catalyst ($E_{1/2} = 0.854$ V). An electron transfer number of 3.97 between 0.4 and 0.8 V vs RHE was presented for the ORR of the MnS (**Figure 5.6**). The transfer number of ~4 indicates the predominant 4-electron transfer process for OH⁻ yielding.³⁹⁻⁴¹ MnS also shows a fair OER activity with a potential of 1.813 V at 10 mA cm⁻² ($E_{j=10}$). While the ORR activity of Ni_xCo_{1-x}S₂ ($E_{1/2} = 0.710$ V) is inferior to MnS, Ni_xCo_{1-x}S₂ material shows a more favourable OER activity indicated by an $E_{j=10}$ of 1.610 V. It suggests that the introduction of Ni_xCo_{1-x}S₂ into the MnS will realize a significant improvement of the OER activity. The voltage gap (ΔE) between $E_{j=10}$ for ORR and $E_{1/2}$ for OER indicates the bifunctionality of the oxygen catalysts. Indeed, the MnS-Ni_xCo_{1-x}S₂ mixtures (physically mixed) with a wide range of weight ratio from 4:1 to 1:2

demonstrated smaller ΔE from 867 to 813 mV (**Figure 5.7b**), which are all better than single component MnS ($\Delta E = 962$ mV), $\text{Ni}_x\text{Co}_{1-x}\text{S}_2$ ($\Delta E = 900$ mV) and a mixture of benchmark commercial Pt/C + IrO_2 catalysts ($\Delta E = 882$ mV), demonstrating the superiority of MnS- $\text{Ni}_x\text{Co}_{1-x}\text{S}_2$ as a bifunctional electrocatalyst for Zn-air batteries. This result indicates that even a small amount of $\text{Ni}_x\text{Co}_{1-x}\text{S}_2$ decoration on the MnS could lead to a significantly improved bifunctionality for oxygen catalysis. It is noted that the above results were achieved by physical mixing of MnS and $\text{Ni}_x\text{Co}_{1-x}\text{S}_2$ powders. Improved activity of oxygen catalysis for the function-separated electrode is expected considering that better dispersion of Ni-Co-S nanoclusters on the MnS was achieved by the wettability-selective electrodeposition as discussed.

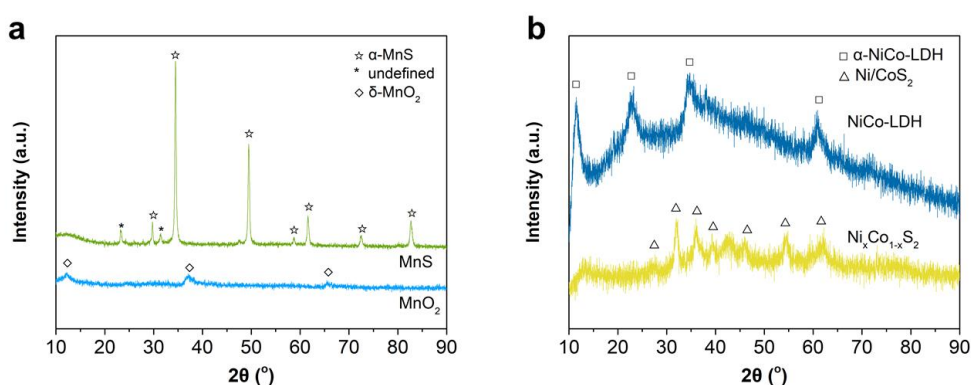


Figure 5.5 XRD profiles of a) MnS powder and its precursor MnO_2 , and b) $\text{Ni}_x\text{Co}_{1-x}\text{S}_2$ powder and its precursor NiCo-LDH.

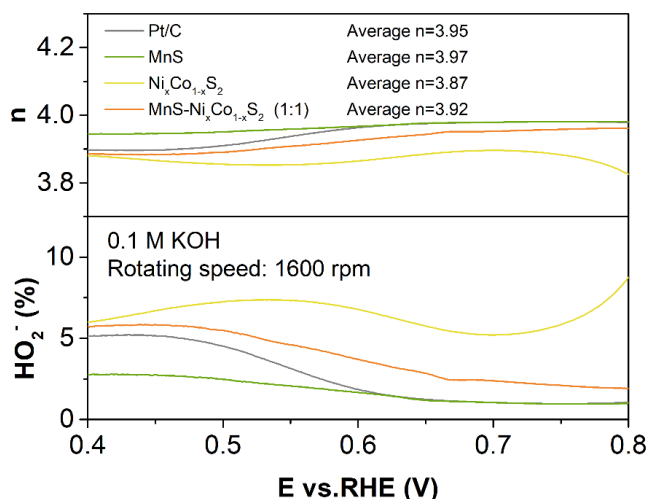


Figure 5.6 Comparison of electron transfer number (n) and yield percentage of HO_2^- for MnS, $\text{Ni}_x\text{Co}_{1-x}\text{S}_2$, MnS- $\text{Ni}_x\text{Co}_{1-x}\text{S}_2$ (1:1, wt:wt) and commercial 20 wt.% Pt/C based on the data from RRDE with a rotating speed of 1600 rpm in 0.1 M KOH.

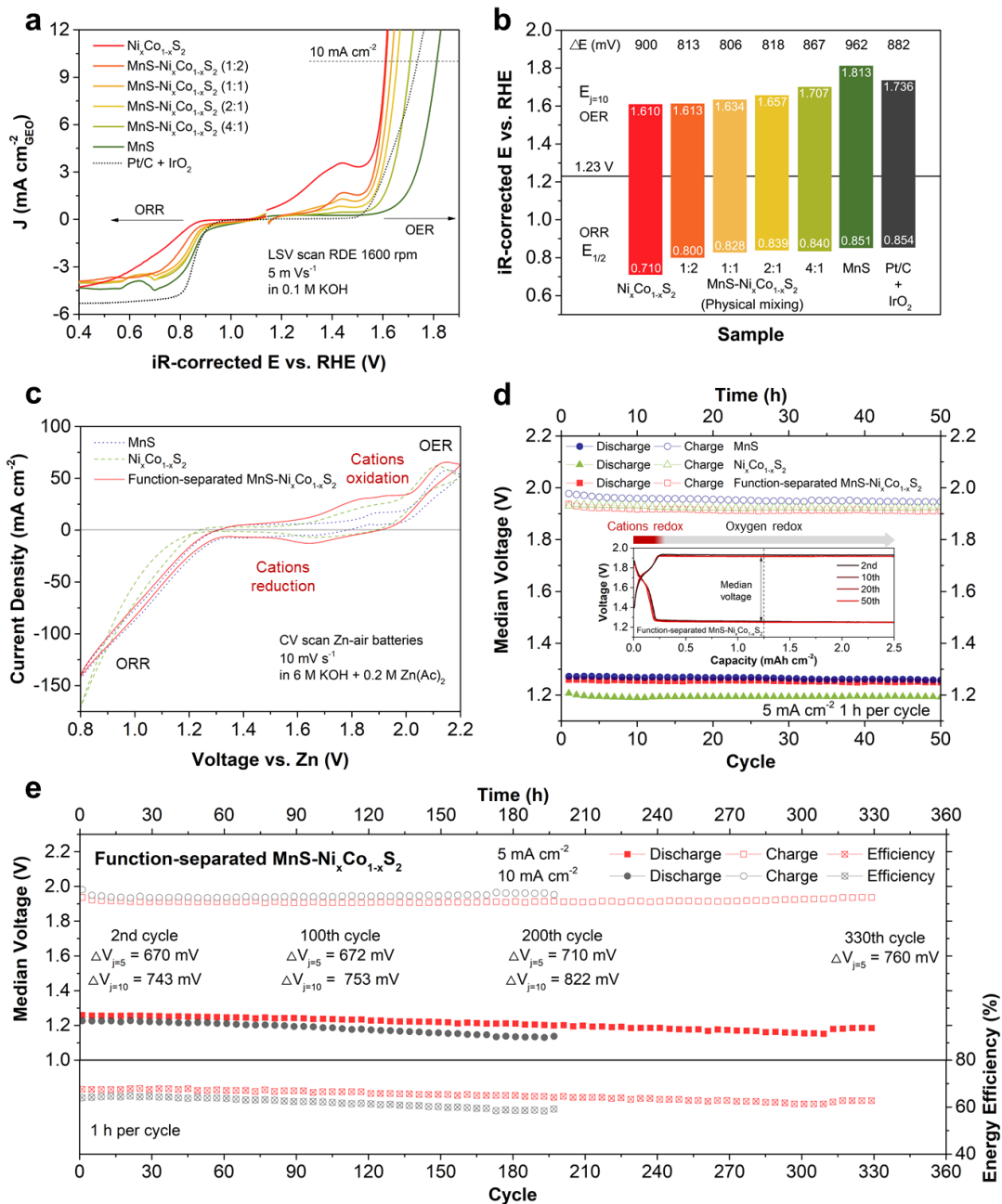


Figure 5.7 Bifunctional catalytic activity of MnS and $\text{Ni}_x\text{Co}_{1-x}\text{S}_2$ materials and performance of the Zn-air battery function of the function-separated $\text{MnS-Ni}_x\text{Co}_{1-x}\text{S}_2$ electrode. a) ORR and OER polarization curves of MnS, $\text{Ni}_x\text{Co}_{1-x}\text{S}_2$ materials and their physical mixture compared with commercial Pt/C + IrO_2 , b) the corresponding potential gaps (ΔE) between potential at 10 mA cm^{-2} ($E_{j=10}$) for OER and the half-wave potential ($E_{1/2}$) for ORR; c) CV scan profiles of the hybrid Zn battery with function-separated $\text{MnS-Ni}_x\text{Co}_{1-x}\text{S}_2$ electrode compared with electrodes with only MnS or $\text{Ni}_x\text{Co}_{1-x}\text{S}_2$; d) variation of the median discharge and charge voltages over 50 cycles of the batteries at 5 mA cm^{-2} ; e) cycling stabilities at 5 and 10 mA cm^{-2} .

The performance of the function-separated electrode in real Zn-air battery was then evaluated using a home-constructed Zn-air battery model with an alkaline electrolyte and a metallic Zn anode. For comparison, a similar MnS electrode without the electrodeposition of $\text{Ni}_x\text{Co}_{1-x}\text{S}_2$ was also investigated. In cyclic Voltammetry (CV) scans as shown in **Figure 5.7c**, the function-separated MnS- $\text{Ni}_x\text{Co}_{1-x}\text{S}_2$ electrode demonstrated a similar ORR (discharging) onset voltage to the MnS electrode. However, a much-increased current response for OER (charging) was demonstrated for the function-separated MnS- $\text{Ni}_x\text{Co}_{1-x}\text{S}_2$ electrode. Considering the possible overlap of the current response of the cations redox and of the OER in the CV scans, galvanostatic (5 mA cm^{-2}) charging (30 min)-discharging (30 min) technique was applied to avoid the interfere from cation redox. As shown in inset image in **Figure 5.7d**, in every galvanostatic charging and discharging, Zn-MX battery function contributed by the cation redox happens first and presents a lower charging voltage and a higher discharge voltage. Once the cation redox is completed, the subsequent voltage profile represents the actual working voltages of Zn-air battery function. The median charging voltage (V_C) and the median discharging voltage (V_D) located after the completion of cation redox provide a better evaluation of the actual performance of the Zn-air battery function. The battery with the function-separated MnS- $\text{Ni}_x\text{Co}_{1-x}\text{S}_2$ electrode (with a MnS and $\text{Ni}_x\text{Co}_{1-x}\text{S}_2$ loading of ~ 2 and $\sim 0.8 \text{ mg cm}^{-2}$, respectively) showed a high V_D of 1.930 V and a low V_C of 1.260 V in the 2nd cycle (**Figure 5.7d**), corresponding to a voltage gap ($\Delta V_{\text{Zn-air}} = V_C - V_D$) of only 670 mV. For comparison, similar electrode with only MnS or only $\text{Ni}_x\text{Co}_{1-x}\text{S}_2$ prepared by a similar method showed an inferior $\Delta V_{\text{Zn-air}}$ of 702 mV and 737 mV in the 2nd cycle, respectively. The lower $\Delta V_{\text{Zn-air}}$ of the MnS- $\text{Ni}_x\text{Co}_{1-x}\text{S}_2$ than the single material (MnS or $\text{Ni}_x\text{Co}_{1-x}\text{S}_2$) electrodes further confirmed the beneficial effect from the Ni-Co-S nanocluster deposited within the hydrophobic MnS layer for facilitating OER. A prolonged cycling test of the battery at 5 mA cm^{-2} was presented in **Figure 5.7e**. In the first 100 cycles, the $\Delta V_{\text{Zn-air}}$ kept almost unchanged (672 mV in 100th cycle, 670 mV in 2nd cycle). A very good $\Delta V_{\text{Zn-air}}$ of 760 mV still remained at the 330th cycle. (**Figure 5.7e**). The battery also showed good $\Delta V_{\text{Zn-air}}$ of 743 mV and good cycling stability for 200 h at a higher current density of 10 mA cm^{-2} .

5.3.3 Performance of the Zn-MX battery function and optimization of the function-separated electrode

The electrochemical character of Zn-MX battery function for the function-separated electrode was evaluated by CV scans at a wide voltage window of 0.8-2.2V vs Zn. As shown in **Figure 5.7c**, a broad peak couple was presented within the voltage window from ~1.4 to ~2.0 V, which could be mainly attributed to the redox couples of Ni²⁺/Ni³⁺ and Co²⁺/Co³⁺ in Ni_xCo_{1-x}S₂.⁴²⁻⁴⁵ The reversible discharge/charge reaction of Ni_xCo_{1-x}S₂ may follow the reactions:



The function-separated electrodes with higher Ni_xCo_{1-x}S₂ loadings (achieved by controlling the deposition time of NiCo-LDH) demonstrated significantly larger capacity at higher potential range (300 s deposition, ~0.15 mA cm⁻² at voltage >1.5 V) than the electrode with less (60 s deposition, ~0.10 mA cm⁻²) or no Ni_xCo_{1-x}S₂ deposition (**Figure 5.8a&b**). It is noted that MnS also presented the partial contribution to the capacity, while its contribution was not as significant as Ni_xCo_{1-x}S₂ and such capacity is presented at lower voltage range.^{46,47} Indeed, increasing the loading of MnS from 0 to 3 mg did not significantly improve the capacity at the high voltage range (**Figure 5.8c**). Since the power density and energy density of the Zn-MX battery is highly associated with the working voltage which is related to the electrode material, the higher discharge potential of Ni_xCo_{1-x}S₂ is thus more favourable compared with the MnS.

The above performance results of the Zn-air battery function and Zn-MX battery function with the function-separated MnS-Ni_xCo_{1-x}S₂ electrode confirms our hypothesis on the asymmetric compositional design. Based on this understanding, the electrode was further optimized by varying the loading of MnS and Ni_xCo_{1-x}S₂. With an optimized MnS loading of 3 mg cm⁻² and NiCo-LDH deposition time of 300 s (**Figure 5.9**), a $\Delta V_{\text{Zn-air}}$ of 659 mV (**Figure 5.8b**) and a capacity of Zn-MX battery ($C_{\text{Zn-MX}}$, approximately determined by the intersection of the two tangent lines on the deep-slope side representing the Zn-MX battery function and the flat side at ~1.3 V representing the Zn-air battery function in the galvanostatic discharge profiles) reached ~0.27 mAh cm⁻² (**Figure 5.8c**) in the 2nd cycle, with round-trip efficiency (energy efficiency) of 69% (**Figure 5.8b**).

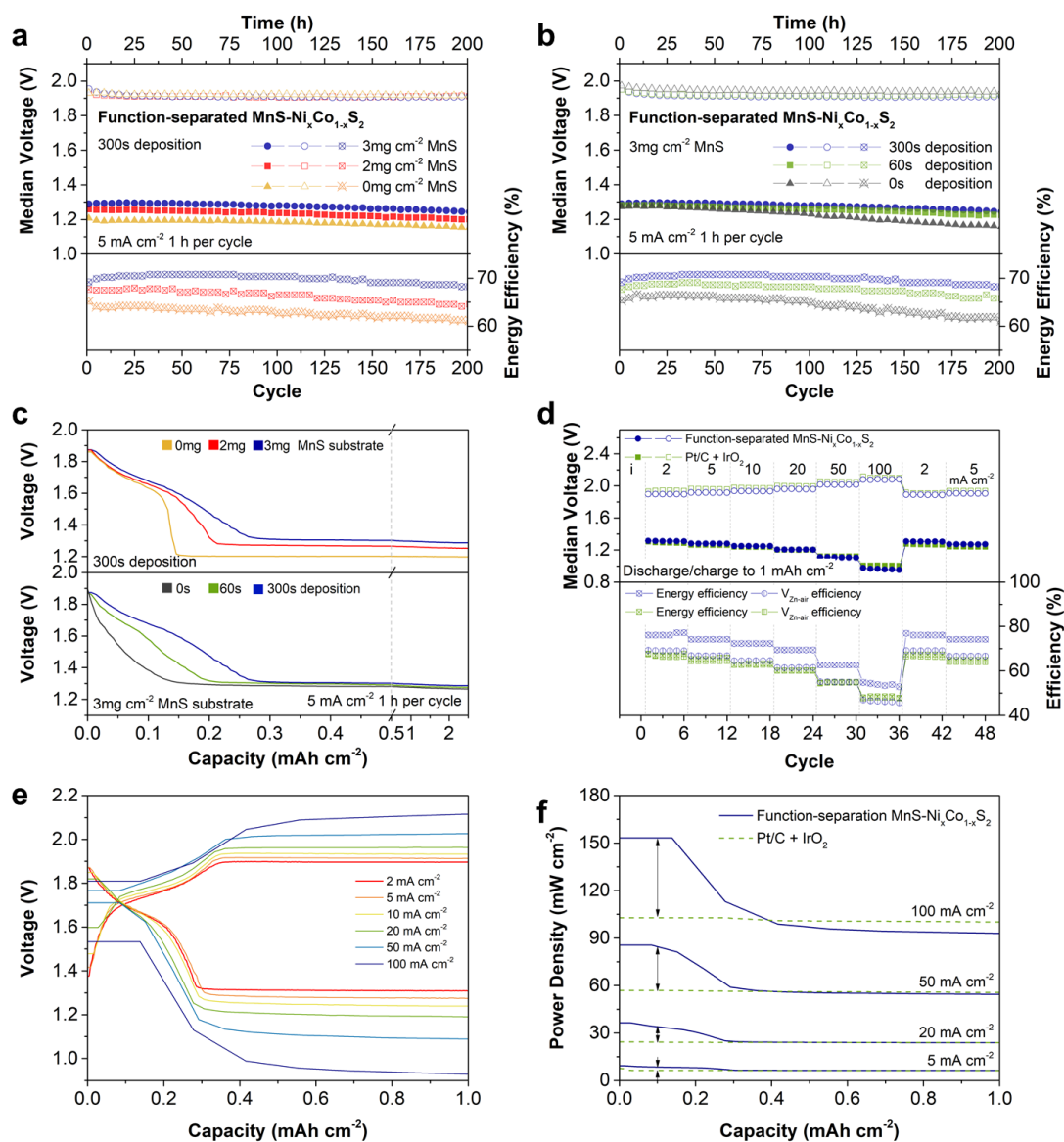


Figure 5.8 Performance of the Zn-MX battery function and optimization of the function-separated MnS-Ni_xCo_{1-x}S₂ electrode. a) Comparison of cycling performance of cathodes with different mass loading of MnS and b) with different amount of Ni_xCo_{1-x}S₂ by applying different deposition time. c) Comparison of capacities of the Zn-MX battery function of cathodes with different MnS and Ni_xCo_{1-x}S₂ loading. d) Variation of median discharge and charge voltages for the optimized electrode at current densities ranging from 2 to 100 mA cm⁻², e) the corresponding single cycle charge-discharge profiles and f) variation of power densities along with the capacity evaluated at different constant current densities.

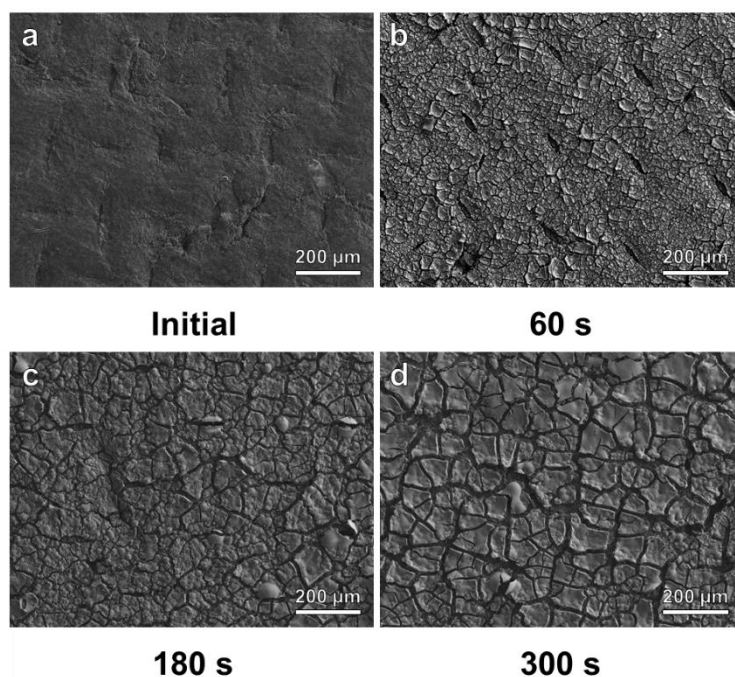


Figure 5.9 Comparison of the pristine MnO_2 layer and double-layer MnO_2 -NiCo-LDH electrode prepared with different electrodeposition durations (60-300s).

The optimized electrode also demonstrated excellent high-rate-performance for both battery functions. A lower cut-off-capacity (1 mAh cm^{-2}) was then set for the high-rate-performance test to highlight the improvement of round-trip efficiency resulted from the Zn-MX battery function. As presented in **Figure 5.8d**, $\Delta V_{\text{Zn-air}}$ of 586, 635, 687, 757 and 906 mV for the Zn-air battery function were achieved at 2, 5, 10, 20, 50 mA cm^{-2} , respectively. Even at a very high current density of 100 mA cm^{-2} , a fair $\Delta V_{\text{Zn-air}}$ of 1101 mV was presented. Good rate retention with a $\Delta V_{\text{Zn-air}}$ of 585 mV was also achieved when the current density decreased back to 2 mA cm^{-2} . The round-trip efficiency of the hybrid battery reaches 76% and 74% at 2 and 5 mA cm^{-2} , respectively. For comparison, the round-trip efficiency of the Zn-air battery function only ($V_{\text{Zn-air}}$ efficiency, evaluated by the median discharge/charge voltages, **Figure 5.8d**) is 67% at 5 mA cm^{-2} . As compared in **Figure 5.8d**, although a Pt/C + IrO_2 electrode demonstrated similar $\Delta V_{\text{Zn-air}}$ and $V_{\text{Zn-air}}$ efficiency to the function-separated $\text{MnS-Ni}_x\text{Co}_{1-x}\text{S}_2$ electrode, the energy efficiency of the Pt/C + IrO_2 electrode (66%) is much inferior. Although increased overpotentials of the Zn-MX battery function were observed when the current density was higher than 10 mA cm^{-2} (**Figure 5.8e**), the increase was much insignificant than those of the Zn-air battery function. This result suggests the benefits from the integration of the Zn-MX battery function for improving

power density, especially at high current densities. The direct comparison of power densities profiles of the two electrodes at different constant discharging current (5-100 mA cm⁻²) are presented in **Figure 5.8f**. In a short-term discharging situation (e.g., discharge energy < 0.1 mAh cm⁻²), the hybrid battery with the function-separated electrode provide ~50% higher power density (153 mW cm⁻²) than that with a conventional Pt/C + IrO₂ electrode (103 mW cm⁻²) at 100 mA cm⁻². As discussed in the Introduction section, Zn-based battery is a promising technique designed for buffering the unpredictable fluctuating electricity supply from renewable energy resources and unstable electricity consumption. Such a short-term sensitive, high-power-density, high-energy-efficiency and highly reversible performance of the function-separated electrode is exactly suitable for this purpose.

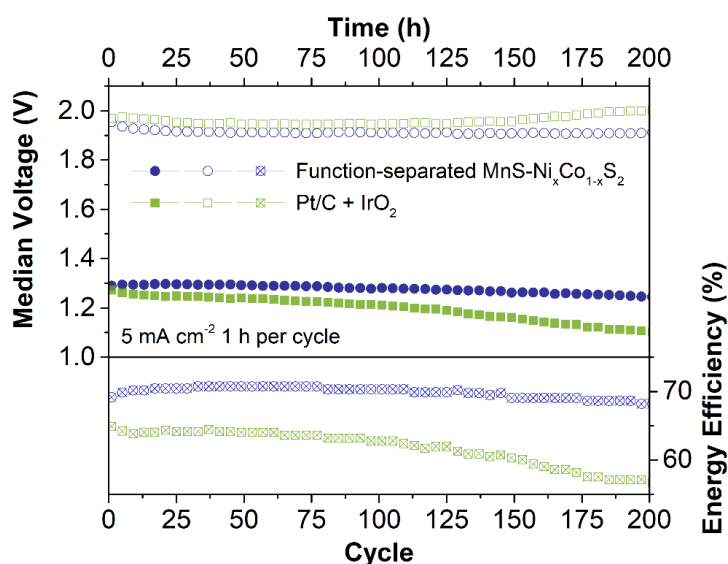


Figure 5.10. Comparison of cycling stability of the function-separated MnS-Ni_xCo_{1-x}S₂ electrode and the electrode with Pt/C + IrO₂ catalyst.

Moreover, the optimized electrode presented a favorable stability over 200 h (**Figure 5.8b**), which was more stable than the Pt/C + IrO₂ electrode (**Figure 5.10**). It is interesting that the increased loading of Ni_xCo_{1-x}S₂ also had a positive impact on the stability of the battery performance as presented in **Figure 5.8b**. This could be ascribed to the alleviation of the loss of Mn compounds by Ni_xCo_{1-x}S₂. During the discharging process, MnS could partially dissolve in the strong alkaline electrolyte,^{48,49} which could result in the deterioration of discharge overpotentials. On the one hand, the partial coverage of Ni_xCo_{1-x}S₂ on the MnS surface provided physical blockage for

alleviating the diffusion of the dissolved Mn species. On the other hand, the $\text{Ni}_x\text{Co}_{1-x}\text{S}_2$ may provide a redox-active surface for facilitating the re-deposition of the dissolved Mn species.⁵⁰

5.3.4 Important role of the asymmetric wettability design in the function-separated electrode

To verify the beneficial effect for both gas diffusion and ionic transfer from the function-separated design as illustrated in **Figure 5.1**, performance of hybrid Zn battery with the function-separated electrode was further compared with the conventional single-layer electrodes with similar MnS and $\text{Ni}_x\text{Co}_{1-x}\text{S}_2$ loading. The wettability of the single-layer electrodes was modified by using different binders (hydrophilic Nafion and hydrophobic PTFE, **Figure 5.11b**) and their combination (1:1 wt:wt). A more hydrophilic electrode (e.g., electrode with Nafion) presented a higher $C_{\text{Zn-MX}}$, at the same time, however, a larger $\Delta V_{\text{Zn-air}}$ (**Figure 5.11a**). This result provides clear evidence that the inevitable contradiction of wettability design if a conventional single-layer design is applied. The as-designed optimized function-separated MnS- $\text{Ni}_x\text{Co}_{1-x}\text{S}_2$ electrode demonstrated both a higher $C_{\text{Zn-MX}}$ (0.27 mAh cm^{-2}) and a significantly smaller $\Delta V_{\text{Zn-air}}$ (659 mV) (**Figure 5.11c**), compared to a single layer electrode with a balanced performance (Nafion+PTFE: 0.15 mAh cm^{-2} and 692 mV). As a result, the energy efficiency of the function-separated electrode (69%) was higher than all the tested single-layer electrodes (PTFE: 66%, Nafion:66%, PTFE+Nafion: 67%).

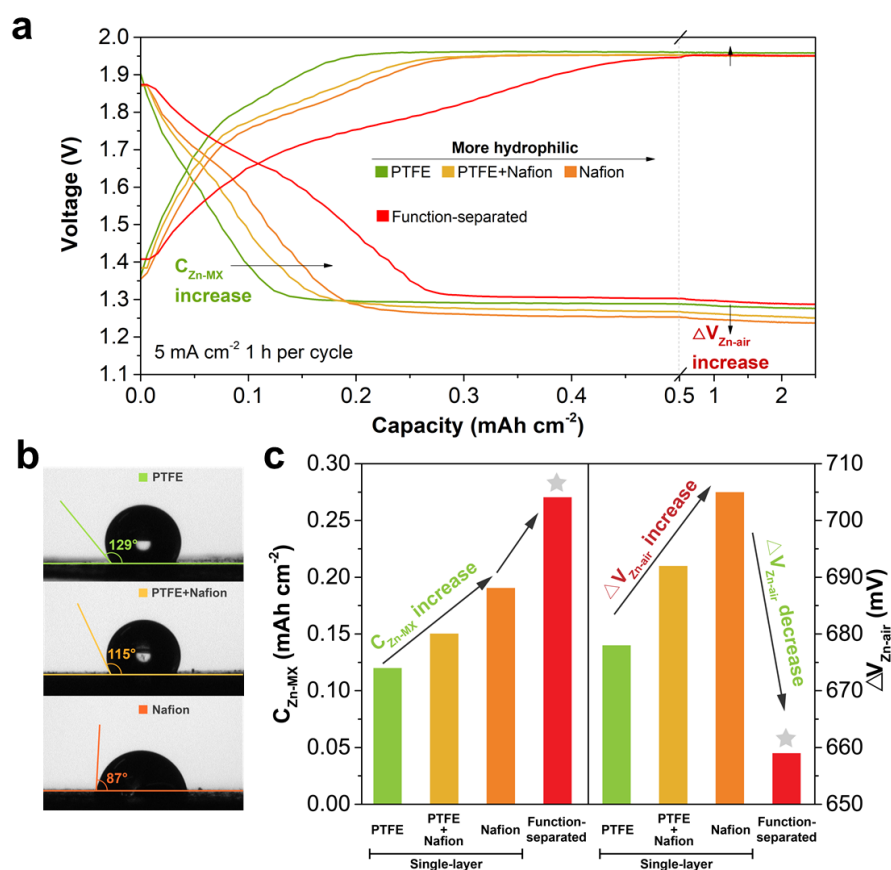


Figure 5.11. Verification of the important role of the asymmetric wettability design of the function-separation MnS-Ni_xCo_{1-x}S₂ electrode. a) Second charge-discharge profiles of three hybrid Zn-based batteries with conventional single-layer MnS-Ni_xCo_{1-x}S₂ electrode with different wettability and the function-separated MnS-Ni_xCo_{1-x}S₂ electrode. b) contact angles analysis on the electrode with different wettability tuning agents with the hybrid Zn battery electrolyte. c) Comparison of hybrid Zn-based batteries performance based on the two essential parameters, i.e., capacity of the Zn-MX battery function (C_{Zn-MX} , mAh cm⁻²) and charge-discharge voltage gap of the Zn-air battery function (ΔV_{Zn-air} , mV vs. Zn).

5.4 Conclusion

In summary, a function-separated design of electrode with unique compositional distribution and distinguishing wettability on the two different layers was proposed for realizing high-performance hybrid Zn batteries. The electrode design perfectly tackles the dilemma between electrolyte accessibility and gas accessibility in a conventional single-layer electrode and facilitates both cation redox and oxygen redox. As a result,

both functions of Zn-air battery and Zn-MX battery were optimized simultaneously, demonstrating advantageous features of high power density, excellent round trip efficiency and superior cycling stability. The concept of function-separated electrode design also provides opportunities for further optimizing redox reactions and multiple mass transfers in cathodes with other advanced active materials and catalysts (e.g., Ag/AgO_x, simple or complex Mn/Co/Ni-based metal hydroxides/oxides/sulfides) for hybrid Zn batteries. The design could also provide inspiration for the development of other electrodes with complicated ionic and gas transfer situations, e.g., proton-exchange membrane fuel cells and metal-air batteries.

References

1. Shang W, Yu W, Tan P, Chen B, Wu Z, Xu H, et al. Achieving high energy density and efficiency through integration: Progress in hybrid zinc batteries. *J. Mater Chem A* 2019;7(26):15564-74. doi:10.1039/C9TA04710G
2. Lee DU, Fu J, Park MG, Liu H, Ghorbani Kashkooli A, Chen Z. Self-assembled NiO/Ni(OH)₂ nanoflakes as active material for high-power and high-energy hybrid rechargeable battery. *Nano Lett.* 2016;16(3):1794-802. doi:10.1021/acs.nanolett.5b04788
3. Li B, Ruan J, Loh A, Chai J, Chen Y, Tan C, et al. A robust hybrid zn-battery with ultralong cycle life. *Nano Lett.* 2017;17(1):156-63. doi:10.1021/acs.nanolett.6b03691
4. Ma L, Chen S, Pei Z, Li H, Wang Z, Liu Z, et al. Flexible waterproof rechargeable hybrid zinc batteries initiated by multifunctional oxygen vacancies-rich cobalt oxide. *ACS Nano.* 2018;12(8):8597-605. doi:10.1021/acsnano.8b04317
5. Tan P, Chen B, Xu H, Cai W, He W, Liu M, et al. Co₃O₄ nanosheets as active material for hybrid Zn batteries. *Small.* 2018;14(21):1800225. doi:10.1002/sml.201800225
6. Xu D, Wu S, Xu X, Wang Q. Hybrid Zn battery with coordination-polymer-derived, oxygen-vacancy-rich Co₃O₄ as a cathode material. *ACS Sustainable Chem Eng.* 2020;8(11):4384-91. doi:10.1021/acssuschemeng.9b06715

7. Cheng Y, Zhang N, Wang Q, Guo Y, Tao S, Liao Z, et al. A long-life hybrid zinc flow battery achieved by dual redox couples at cathode. *Nano Energy*. 2019;63:103822. doi:10.1016/j.nanoen.2019.06.018
8. Tan P, Chen B, Xu H, Cai W, Liu M, Shao Z, et al. Nanoporous NiO/Ni(OH)₂ plates incorporated with carbon nanotubes as active materials of rechargeable hybrid zinc batteries for improved energy efficiency and high-rate capability. *J Electrochem Soc*. 2018;165(10):A2119-A26. doi:10.1149/2.0481810jes
9. Wu M, Zhang G, Chen N, Chen W, Qiao J, Sun S. A self-supported electrode as a high-performance binder- and carbon-free cathode for rechargeable hybrid zinc batteries. *Energy Storage Mater*. 2020;24:272-80. doi:10.1016/j.ensm.2019.08.009
10. Wang X, Xu X, Chen J, Wang Q. Combination of Zn-NiCo₂S₄ and Zn-air batteries at the cell level: A hybrid battery makes the best of both worlds. *ACS Sustainable Chem Eng*. 2019;7(14):12331-9. doi:10.1021/acssuschemeng.9b01707
11. Sarawutanukul S, Tomon C, Duangdangchote S, Phattharasupakun N, Sawangphruk M. Rechargeable photoactive Zn-air batteries using NiCo₂S₄ as an efficient bifunctional photocatalyst towards OER/ORR at the cathode. *Batteries Supercaps*. 2020;3(6):541-7. doi:10.1002/batt.201900205
12. Chang C-C, Lee Y-C, Liao H-J, Kao Y-T, An J-Y, Wang D-Y. Flexible hybrid Zn-Ag/air battery with long cycle life. *ACS Sustainable Chem Eng*. 2019;7(2):2860-6. doi:10.1021/acssuschemeng.8b06328
13. Tan P, Chen B, Xu H, Cai W, He W, Zhang H, et al. Integration of Zn-Ag and Zn-air batteries: A hybrid battery with the advantages of both. *ACS Appl Mater Interfaces*. 2018;10(43):36873-81. doi:10.1021/acscami.8b10778
14. Huang Z, Li X, Yang Q, Ma L, Mo F, Liang G, et al. Ni₃S₂/Ni nanosheet arrays for high-performance flexible zinc hybrid batteries with evident two-stage charge and discharge processes. *J Mater Chem A*. 2019;7(32):18915-24. doi:10.1039/C9TA06337D
15. Khaja Hussain S, Su Yu J. Cobalt-doped zinc manganese oxide porous nanocubes with controlled morphology as positive electrode for hybrid supercapacitors. *Chem Eng J*. 2019;361:1030-42. doi:10.1016/j.cej.2018.12.152
16. Qaseem A, Chen F, Qiu C, Mahmoudi A, Wu X, Wang X, et al. Reduced graphene oxide decorated with manganese cobalt oxide as multifunctional

- material for mechanically rechargeable and hybrid zinc–air batteries. Part Part Syst Char. 2017;34(10):1700097. doi:10.1002/ppsc.201700097
17. Meng L, Lin D, Wang J, Zeng Y, Liu Y, Lu X. Electrochemically activated nickel–carbon composite as ultrastable cathodes for rechargeable nickel–zinc batteries. ACS Appl Mater Interfaces. 2019;11(16):14854-61. doi:10.1021/acsami.9b04006
 18. Yu J, Li B-Q, Zhao C-X, Liu J-N, Zhang Q Asymmetric air cathode design for enhanced interfacial electrocatalytic reactions in high-performance zinc–air batteries. Adv Mater. 2020;32(12):1908488. doi:10.1002/adma.201908488
 19. Zhou T, Zhang N, Wu C, Xie Y. Surface/interface nanoengineering for rechargeable Zn-air batteries. Energy Environ Sci. 2020;13(4):1132-53. doi:10.1039/C9EE03634B
 20. Lin C, Shinde SS, Jiang Z, Song X, Sun Y, Guo L, et al. In situ directional formation of Co@CoO_x-embedded 1D carbon nanotubes as an efficient oxygen electrocatalyst for ultra-high rate Zn-air batteries. J Mater Chem A. 2017;5(27):13994-4002. doi:10.1039/C7TA02215H
 21. Song X, Guo L, Liao X, Liu J, Sun J, Li X. Hollow carbon nanopolyhedra for enhanced electrocatalysis via confined hierarchical porosity. Small. 2017;13(23):1700238. doi:10.1002/sml.201700238
 22. Li Z, Jiang G, Deng Y-P, Liu G, Ren D, Zhang Z, et al. Deep-breathing honeycomb-like Co-N_x-C nanopolyhedron bifunctional oxygen electrocatalysts for rechargeable Zn-air batteries. iScience. 2020;23(8):101404. doi:10.1016/j.isci.2020.101404
 23. Shang W, Yu W, Liu Y, Li R, Dai Y, Cheng C, et al. Rechargeable alkaline zinc batteries: Progress and challenges. Energy Storage Mater. 2020;31:44-57. doi:10.1016/j.ensm.2020.05.028
 24. Lu Y, Wang J, Zeng S, Zhou L, Xu W, Zheng D, et al. An ultrathin defect-rich Co₃O₄ nanosheet cathode for high-energy and durable aqueous zinc ion batteries. J Mater Chem A. 2019;7(38):21678-83. doi:10.1039/C9TA08625K
 25. Tian W, Li H, Qin B, Xu Y, Hao Y, Li Y, et al. Tuning the wettability of carbon nanotube arrays for efficient bifunctional catalysts and Zn-air batteries. J Mater Chem A. 2017;5(15):7103-10. doi:10.1039/C6TA10505J

26. Pan J, Xu YY, Yang H, Dong Z, Liu H, Xia BY. Advanced architectures and relatives of air electrodes in Zn-air batteries. *Adv Sci.* 2018;5(4):1700691. doi:10.1002/advs.201700691
27. Cai X, Lai L, Lin J, Shen Z. Recent advances in air electrodes for Zn-air batteries: Electrocatalysis and structural design. *Mater Horiz.* 2017;4(6):945-76. doi:10.1039/C7MH00358G
28. Zhang H, Zhao Y, Li Y, Li G, Li J, Zhang F. Janus electrode of asymmetric wettability for H₂O₂ production with highly efficient O₂ utilization. *ACS Appl Energy Mater.* 2020;3(1):705-14. doi:10.1021/acsaem.9b01908
29. Meng X, Deng X, Zhou L, Hu B, Tan W, Zhou W, et al. A highly ordered hydrophilic–hydrophobic Janus bi-functional layer with ultralow Pt loading and fast gas/water transport for fuel cells. *Energy Environ Mater.* 2020;4(1):126-133. doi:10.1002/eem2.12105
30. Li Y, Zhang H, Han N, Kuang Y, Liu J, Liu W, et al. Janus electrode with simultaneous management on gas and liquid transport for boosting oxygen reduction reaction. *Nano Res.* 2019;12(1):177-82. doi:10.1007/s12274-018-2199-1
31. Wang P, Lin Y, Wan L, Wang B. Construction of a Janus MnO₂-NiFe electrode via selective electrodeposition strategy as a high-performance bifunctional electrocatalyst for rechargeable zinc–air batteries. *ACS Appl Mater Interfaces.* 2019;11(41):37701-7. doi:10.1021/acsaami.9b12232
32. Wan L, Wang P, Lin Y, Wang B. Janus-typed integrated bifunctional air electrode with MnO_x-NiFe LDH/Ni foam for rechargeable zinc-air batteries. *J Electrochem Soc.* 2019;166(14):A3409-15. doi:10.1149/2.1001914jes
33. Yuan C, Li J, Hou L, Zhang X, Shen L, Lou XW. Ultrathin mesoporous NiCo₂O₄ nanosheets supported on Ni foam as advanced electrodes for supercapacitors. *Adv Funct Mater.* 2012;22(21):4592-7. doi:10.1002/adfm.201200994
34. Huang L, Chen D, Ding Y, Feng S, Wang ZL, Liu M. Nickel–cobalt hydroxide nanosheets coated on NiCo₂O₄ nanowires grown on carbon fiber paper for high-performance pseudocapacitors. *Nano Lett.* 2013;13(7):3135-9. doi:10.1021/nl401086t
35. Heikens HH, Van Bruggen CF, Haas C. Electrical properties of α -MnS. *J Phys Chem Solids.* 1978;39(8):833-40. doi:10.1016/0022-3697(78)90141-5

36. De Guzman RN, Awaluddin A, Shen Y-F, Tian ZR, Suib SL, Ching S, et al. Electrical resistivity measurements on manganese oxides with layer and tunnel structures: Birnessites, todorokites, and cryptomelanes. *Chem Mater*. 1995;7(7):1286-92. doi:10.1021/cm00055a003
37. Xu X, Wang W, Zhou W, Shao Z. Recent advances in novel nanostructuring methods of perovskite electrocatalysts for energy-related applications. *Small Methods*. 2018;2(7):1800071. doi:10.1002/smt.201800071
38. Pei Z, Yuan Z, Wang C, Zhao S, Fei J, Wei L, et al. A flexible rechargeable zinc–air battery with excellent low-temperature adaptability. *Angew Chem Int Ed*. 2020;59(12):4793-9. doi:10.1002/anie.201915836
39. Tang T, Jiang W-J, Liu X-Z, Deng J, Niu S, Wang B, et al. Metastable rock salt oxide-mediated synthesis of high-density dual-protected M@NC for long-life rechargeable zinc–air batteries with record power density. *J Am Chem Soc* 2020;142(15):7116-27. doi:10.1021/jacs.0c01349
40. Arafat Y, Azhar MR, Zhong Y, Xu X, Tadé MO, Shao Z. A porous nano-micro-composite as a high-performance bi-functional air electrode with remarkable stability for rechargeable zinc–air batteries. *Nano-Micro Lett*. 2020;12:130. doi:10.1007/s40820-020-00468-4
41. Lu Q, Zou X, Liao K, Ran R, Zhou W, Ni M, et al. Direct growth of ordered N-doped carbon nanotube arrays on carbon fiber cloth as a free-standing and binder-free air electrode for flexible quasi-solid-state rechargeable Zn-Air batteries. *Carbon Energy*. 2020;2(3):461-471. doi:10.1002/cey2.50
42. Zhang L, Wu HB, Lou XW. Unusual CoS₂ ellipsoids with anisotropic tube-like cavities and their application in supercapacitors. *Chem Commun*. 2012;48(55):6912-4. doi:10.1039/C2CC32750C
43. Jin L, Liu B, Wu Y, Thanneeru S, He J. Synthesis of mesoporous CoS₂ and Ni_xCo_{1-x}S₂ with superior supercapacitive performance using a facile solid-phase sulfurization. *ACS Appl Mater Interfaces*. 2017;9(42):36837-48. doi:10.1021/acsami.7b11453
44. Peng S, Li L, Tan H, Cai R, Shi W, Li C, et al. MS₂ (M = Co and Ni) hollow spheres with tunable interiors for high-performance supercapacitors and photovoltaics. *Adv Funct Mater*. 2014;24(15):2155-62. doi:10.1002/adfm.201303273

45. Ruan Y, Jiang J, Wan H, Ji X, Miao L, Peng L, et al. Rapid self-assembly of porous square rod-like nickel persulfide via a facile solution method for high-performance supercapacitors. *J Power Sources*. 2016;301:122-30.
doi:10.1016/j.jpowsour.2015.09.116
46. Tang YF, Chen T, Yu SX. Morphology controlled synthesis of monodispersed manganese sulfide nanocrystals and their primary application in supercapacitors with high performances. *Chem Commun*. 2015;51(43):9018-21.
doi:10.1039/C5CC01700A
47. Tang YF, Chen T, Yu SX, Qiao YQ, Mu SC, Hu J, et al. Synthesis of graphene oxide anchored porous manganese sulfide nanocrystals via the nanoscale Kirkendall effect for supercapacitors. *J Mater Chem A*. 2015;3(24):12913-9.
doi:10.1039/C5TA02480C
48. Kozawa A, Yeager JF. The cathodic reduction mechanism of electrolytic manganese dioxide in alkaline electrolyte. *J Electrochem Soc*. 1965;112(10):959-63. doi:10.1149/1.2423350
49. Kozawa A, Yeager JF. Cathodic reduction mechanism of MnOOH to Mn(OH)₂ in alkaline electrolyte. *J Electrochem Soc*. 1968;115(10):1003-7.
doi:10.1149/1.2410843
50. Zhong Y, Xu X, Veder J-P, Shao Z. Self-recovery chemistry and cobalt-catalyzed electrochemical deposition of cathode for boosting performance of aqueous zinc-ion batteries. *iScience*. 2020;23(3):100943.
doi:10.1016/j.isci.2020.100943

Every reasonable effort has been made to acknowledge the owners of copyright material. I would be pleased to hear from any copyright owner who has been omitted or incorrectly acknowledged.

Chapter 6 Promoting bifunctional oxygen catalyst activity of perovskite-type cubic nanocrystallites for rechargeable zinc-air batteries

Abstract

Transition metal oxide materials are promising oxygen catalysts that are alternative to the expensive precious metal-containing catalysts. Integration of transition metal oxides that either provide good activity for oxygen reduction reaction (ORR) or good activity for oxygen evolution reaction (OER) is an important pathway for achieving good bifunctionality. Different from the conventional physical mixing or hybridization strategies, perovskite-type oxide provides an ideal structure for the integration of the transition metal element atoms in an atomic scale. Herein, perovskite-type $\text{La}_{1.6}\text{Sr}_{0.4}\text{MnCoO}_6$ nanocrystallites with ultra-small cubic (20-50 nm length) morphology and the high specific surface areas ($25 \text{ m}^2 \text{ g}^{-1}$) were proposed. Multiple design strategies were integrated to promote the ORR-OER catalysis, including introducing oxygen vacancies via A-site cation substitution, further increasing surface oxygen vacancies via integration of small amount of Pt/C and nanosizing of the material via a facile molten-salt method. The batteries with the $\text{La}_{1.6}\text{Sr}_{0.4}\text{MnCoO}_6$ nanocrystallites and a conventional aqueous alkaline electrolyte demonstrate decent discharge-charge voltage gaps of 0.75 and 1.10 at 1 and 30 mA cm^{-2} , respectively, and good cycling stability over 250 h corresponding to a 1500-cycle run. A portable coin-type battery with an alkaline gel-polymer electrolyte also presents a good performance (voltage gap of $\sim 0.8 \text{ V}$ at 5 mA cm^{-2}) for 20 h (120 cycles).

6.1 Introduction

Integration of transition metal oxides that takes advantage of their catalysis for either ORR or OER is an important pathway for achieving bifunctional oxygen catalysis for Zn-air battery cathodes. Conventionally, physical mixing of different oxide material is the simplest strategy.¹ However, this strategy may result in poor interaction between the components. Hybridization of different oxides via a chemical or electrochemical method is another most studied pathway.²⁻⁴ In **Chapter 4** and **Chapter 5**, the catalysts for oxygen redox were designed based on this strategy. However, this strategy usually involves relatively more complicated synthesis processes or conditions, which may hinder practical utility.

Different from the simple oxides, perovskite oxides are a category of cost-effective complex oxide materials that shows promising catalysis in aqueous media.⁵ A typical single perovskite oxide has a chemical formula of ABO_3 , where A and B are usually rare earth metal cations and transition metal cations, respectively.⁶ One of the most significant advantage of perovskite oxide is its flexibility of cation element and composition.⁷ Therefore, perovskite-type oxide provides an ideal structure for the integration of the transition metal element atoms in an atomic scale, which is different from the conventional physical mixing or hybridization strategies. In addition, such integration in perovskite can be easily achieved by facile one-step preparation in an ambient atmosphere, which is promising for practical production. In the previous study, different perovskite oxides (e.g., $LaNiO_3$ ⁸, $La_{0.5}Sr_{0.5}Co_{0.8}Fe_{0.2}O_3$ ⁹, $La_{0.8}Sr_{0.2}Co_{1-x}Mn_xO_3$ ¹⁰, $LaMn_{0.75}Co_{0.25}O_{3-\delta}$ ¹¹, $(PrBa_{0.5}Sr_{0.5})_{0.95}Co_{1.5}Fe_{0.5}O_{5+\delta}$ ¹², $Sr(Co_{0.8}Fe_{0.2})_{0.95}P_{0.05}O_{3-\delta}$ ¹³) have been developed and they showed promising capability for facilitating oxygen redox as catalysts for air cathodes in Zn-air batteries.¹⁴⁻²²

Double perovskite oxide is a sub-catalogue of the perovskite oxide. According to some previous reports, double perovskite demonstrates improved electrochemical stability under catalytic conditions.^{6, 23} Integrating two different B-site cations (e.g., Mn and Co) into the perovskite structure usually leads to a random and disordered arrangement.¹¹ Formation of B-site cation ordering may occur when the atomic ratio of the cations is 1:1.⁶ However, achieving the highly ordered cation arrangement is difficult and a slow growth rate is required.²⁴ At the same time, reducing the particle size of the catalyst can increase the specific area, which is beneficial for improving the activity due to more exposure of active sites. Molten-salt assisted synthesis method

provides an ideal route for achieving the nanosizing of the perovskite material.^{25, 26} Furthermore, the molten salt environment may facilitate ionic diffusion during the synthesis process,²⁷ which is expected to shorten the synthesis duration of the B-site ordered double perovskite.

Herein, we proposed a rationally designed perovskite-type $\text{La}_{1.6}\text{Sr}_{0.4}\text{MnCoO}_6$ nanocrystallites with an ultra-small cubic morphology and a high specific surface area for Zn-air battery cathodes. Design strategies including nanosizing of the material and introducing oxygen vacancies via A-site cation substitution effectively improve the oxygen catalysis. Zn-air battery with the perovskite-type $\text{La}_{1.6}\text{Sr}_{0.4}\text{MnCoO}_6$ nanocrystallites demonstrated good discharge-charge voltage gaps and good cycling stability. By increasing surface oxygen vacancies via integration of a small amount of Pt/C, the bifunctional oxygen catalysis and battery performance are further promoted.

6.2 Experimental sections

Synthesis of perovskite-type oxide nanocrystallites

A fast and low-temperature synthesis of perovskite-type oxide nanocrystallites was achieved using a Na-K mix nitrate molten salts as a highly oxidized media, which was adjusted based on the method reported by Tian et al.²⁶ La, Sr, Mn, Co nitrate salts were utilized as the source of the cations and the amount of each cation was determined according to the stoichiometric number of the target perovskite products. Take the synthesis of 0.005 mol $\text{La}_{1.6}\text{Sr}_{0.4}\text{MnCoO}_6$ as an example, 3.46 g of $\text{La}(\text{NO}_3)_3 \cdot 6\text{H}_2\text{O}$, 0.42 g of $\text{Sr}(\text{NO}_3)_2$, 1.26 g of $\text{Mn}(\text{NO}_3)_2 \cdot 4\text{H}_2\text{O}$, 1.46 g of $\text{Co}(\text{NO}_3)_2 \cdot 6\text{H}_2\text{O}$ (weights calculated based on the stoichiometric ratio of cations in $\text{La}_{1.6}\text{Sr}_{0.4}\text{MnCoO}_6$) were manually dry-mixed in a motor for 5 min. The molar ratio of the above cation element is La:Sr:Mn:Co=0.008:0.002:0.005:0.005, and the total molar amount of the cation was 0.02 mol. After that, pre-mixed salts consisting of 5.67 g of NaNO_3 and 3.37 g of KNO_3 (total molar amount of Na+K was 0.1 mol) were added and further milled for 5 min. The resulting pink colour powder was then transferred into a 100-mL alumina crucible and heated at 550 °C for 3 h with a heating rate of 10 °C min⁻¹. After cooled to room temperature, 80 mL of DI water was added into the crucible and put into an ultrasonic bath for 10 min to dissolve the rigid nitrate salts. The resulting dispersion was vacuum filtered, then repeatedly washed with DI water for another three times. The final product powder was dried at 60 °C.

For comparison, $\text{La}_{1.6}\text{Sr}_{0.4}\text{MnCoO}_6$ bulk particle sample was prepared via a conventional sol-gel method.^{21, 28} Typically, 3.46 g of $\text{La}(\text{NO}_3)_3 \cdot 6\text{H}_2\text{O}$, 0.42 g of $\text{Sr}(\text{NO}_3)_2$, 1.26 g of $\text{Mn}(\text{NO}_3)_2 \cdot 4\text{H}_2\text{O}$, 1.46 g of $\text{Co}(\text{NO}_3)_2 \cdot 6\text{H}_2\text{O}$ were dissolved in 100 mL of deionized water. 5.84 g of ethylenediaminetetraacetic acid (EDTA), 7.68 g of citric acid (CA) and 15.5 mL of ammonia solution were added into the solution. The mixture was heated at 180 °C until a transparent gel was formed. Then the gel was heated at 250 °C for 5 h. The obtained precursor was further calcinated at 700 °C for 5 h.

Material characterizations

Morphologies of the perovskite-type cubic nanocrystallites were observed using microscopic techniques including scanning electron microscopy (SEM, Zeiss Neon) and transmission electron microscopy (TEM, Titan G2). Phase structures of the samples were analyzed using X-ray diffraction (XRD, Bruker D8 Advance, Cu $K\alpha$ radiation) and high-resolution TEM (HR-TEM, Titan G2). Dispersion of the cations was evaluated by energy-dispersive X-ray spectroscopy (EDS) mapping technique equipped on the Titan G2 TEM. The composition ratio of the cations was evaluated by the EDS system (Oxford) equipped on an SEM (Tescan Clara). Porous information of the materials was analyzed using 77 K liquid nitrogen adsorption-desorption technique (Micromeritics TriStar). The chemical state of elements on the perovskite surface was analyzed using X-ray photoelectron spectroscopy (XPS, Al $K\alpha$ radiation).

Evaluation of oxygen catalytic activity

Electrochemical measurements for the ORR and OER activity of the perovskite oxides and commercial samples were conducted using the same methods and conditions as described in **Chapter 4 (See 4.2 Experimental Sections)**.

For the $\text{La}_{1.6}\text{Sr}_{0.4}\text{MnCoO}_6$ catalyst sample with a small amount (2-5 wt.%) of Pt/C, the mass loading of oxide and metallic Pt on the working electrode is same to that without Pt/C ($\sim 0.232 \text{ mg cm}^{-2}$), and the ratio of oxide+Pt to carbon was fixed at 1:1. Take the $\text{La}_{1.6}\text{Sr}_{0.4}\text{MnCoO}_6$ -Pt (95:5) as an example, the electrode dispersion consists of 9.5 mg of oxide, 2.5 mg of commercial 20% Pt/C (containing 0.5 mg of Pt and 2 mg of carbon support), 8 mg of Super P Li, 1 mL of ethanol and 100 μL of Nafion solution (5 wt%). For ensuring the accuracy of weighing, 10 times of above weighting of the oxide, commercial 20% Pt/C and Super P Li were premixed in 10 mL of ethanol

in an ultrasonic bath and dried at 60 °C. Then 1/10 weighting amount of the mixture (20 mg) was used for preparing the dispersion.

Assembling and evaluation of aqueous Zn-air batteries

Same catalyst dispersions for the RDE tests were also applied to prepare the cathodes for aqueous Zn-air batteries. Typically, 55 μL of the dispersion (containing 0.5 mg of oxide) was drop-casted on a 15x15 mm hydrophobic carbon paper (AVCarb P75T) within a $\phi 8$ mm circular coated area ($\sim 0.5 \text{ cm}^2$, oxide loading of 1 mg cm^{-2}). After dried at 100 °C for evaporating the ethanol, the air cathode film was put into the positive side of a home-made Zn-air battery model. A Zn plate was put into the negative side and 2 mL of 6 M KOH + 0.2 M Zn(Ac)₂ electrolyte was injected in the chamber between the positive and negative electrode. Open-circuit-voltages (OCV), current density-voltage-power density (*I-V-P*) profiles, peak powder densities (PPD) of the aqueous Zn-air batteries were recorded using a Biologic VSP potentiostat. Galvanostatic charging and discharging profiles of the aqueous Zn-air batteries were recorded using a LANHE CT2001A battery test system.

Assembling and evaluation of coin-type Zn-air batteries with gel-polymer electrolyte

SiO₂ nanoparticles modified PVA-based gel-polymer electrolyte was prepared using a cast and freeze method.²⁹ Typically, 25 g of DI water and 2.5 g of polyvinyl alcohol (PVA) were mixed at 100 °C, followed by adding 0.83 g of SiO₂ dispersion (containing 0.25 g of nano SiO₂) at 100 °C until a high-viscosity mixture with evenly dispersed SiO₂ nanoparticles was formed. The mixture was cast in a coin-type CR2016 positive battery case. A freezing (-20 °C, 24 h) and unfrozen (room temperature, 2 h) process were repeated for 2 times until the casted mixture eventually formed a flexible and stretchable gel. The gel film was removed from the CR2016 case and soaked in a 1 M KOH + 0.2 M Zn(Ac)₂ solution for 24 h. As presented in Figure 4d, a coin-type quasi-solid-state Zn-air battery was assembled according to the following order: 1) a meshed CR2032 negative case, 2) a $\phi 19$ mm hydrophobic carbon paper as gas diffusion layer, 3) a $\phi 8$ mm catalyst film (perovskite:CNT:PTFE=6:2:2 wt:wt:wt) 4) a gel-polymer electrolyte film, 5) a $\phi 8$ mm Zn plate as an anode, 6) a $\phi 16$ mm stainless steel plate, 7) a stainless steel spring, and 8) a CR2032 negative case.

6.3 Results and discussions

6.3.1 Synthesis and characterization

The perovskite-type cubic nanocrystallites ($\text{La}_2\text{MnCoO}_6$, $\text{La}_{1.6}\text{Sr}_{0.4}\text{MnCoO}_6$) were synthesized using a facile molten-salt method as illustrated in **Figure 6.1a**. Take $\text{La}_{1.6}\text{Sr}_{0.4}\text{MnCoO}_6$ as an example, solid solvent salt powders (Na, K nitrates) and target cation salt powders (i.e., La, Sr, Mn, Co nitrates) were dry mixed then underwent 3-hour heat treatment in an air atmosphere at 550 °C. After washing the residual solvent salts with deionized water, the perovskite-type cubic $\text{La}_{1.6}\text{Sr}_{0.4}\text{MnCoO}_6$ nanocrystallites were obtained.

The nanocrystallites show a cubic morphology with a side length of approximately 20 to 50 nm, as presented in the SEM (**Figure 6.2**) and TEM (**Figure 6.1c**) images. XRD patterns (**Figure 6.1b**) of the $\text{La}_2\text{MnCoO}_6$ and $\text{La}_{1.6}\text{Sr}_{0.4}\text{MnCoO}_6$ show that their phases are well aligned with a B-site (Mn and Co) ordered double perovskite with a symmetry of cubic $Fm-3m$ and a unit-cell parameter $a \approx 7.69 \text{ \AA}$ which doubled that of a cubic single perovskite.³⁰ An illustration of the cubic B-site ordered double-perovskite is presented in the inset image in **Figure 6.1a**. TEM image of a cubic $\text{La}_{1.6}\text{Sr}_{0.4}\text{MnCoO}_6$ nanocrystallite (**Figure 6.1c**) and its corresponding fast Fourier transformed (FFT, **Figure 6.1d**) pattern with zone axis of $[-1\ 1\ 0]$ shows the (002), (220) and (222) planes with lattice distances of 3.88, 2.75 and 2.24 Å, respectively. The pattern confirms the basic cubic structure of the material. The FFT pattern also presents a spot with weaker intensity at the position of half (222) spot. The superstructure spot representing the (111) plane with a lattice distance of 4.48 Å which doubles that of the (222) plane. This provides evidence that the cubic perovskite sub-cell is doubled, indicating the existence of the B-site ordered feature of the $\text{La}_{1.6}\text{Sr}_{0.4}\text{MnCoO}_6$ perovskite, as illustrated in **Figure 6.1d**.³⁰ The high-angle annular dark-field scanning TEM (HAADF-STEM) and EDS mapping images of the $\text{La}_{1.6}\text{Sr}_{0.4}\text{MnCoO}_6$ indicate the homogeneous distribution of the compositional elements (**Figure 6.1f**). Analysis of the N_2 adsorption-desorption isotherms (**Figure 6.3**) indicates that $\text{La}_2\text{MnCoO}_6$ and $\text{La}_{1.6}\text{Sr}_{0.4}\text{MnCoO}_6$ share similar pore structure with specific areas of 22.1 and 25.2 $\text{m}^2 \text{ g}^{-1}$ and total pore volumes (micro and mesopores) of 0.023 and 0.024 $\text{cm}^3 \text{ g}^{-1}$, respectively (**Table 6.1**).

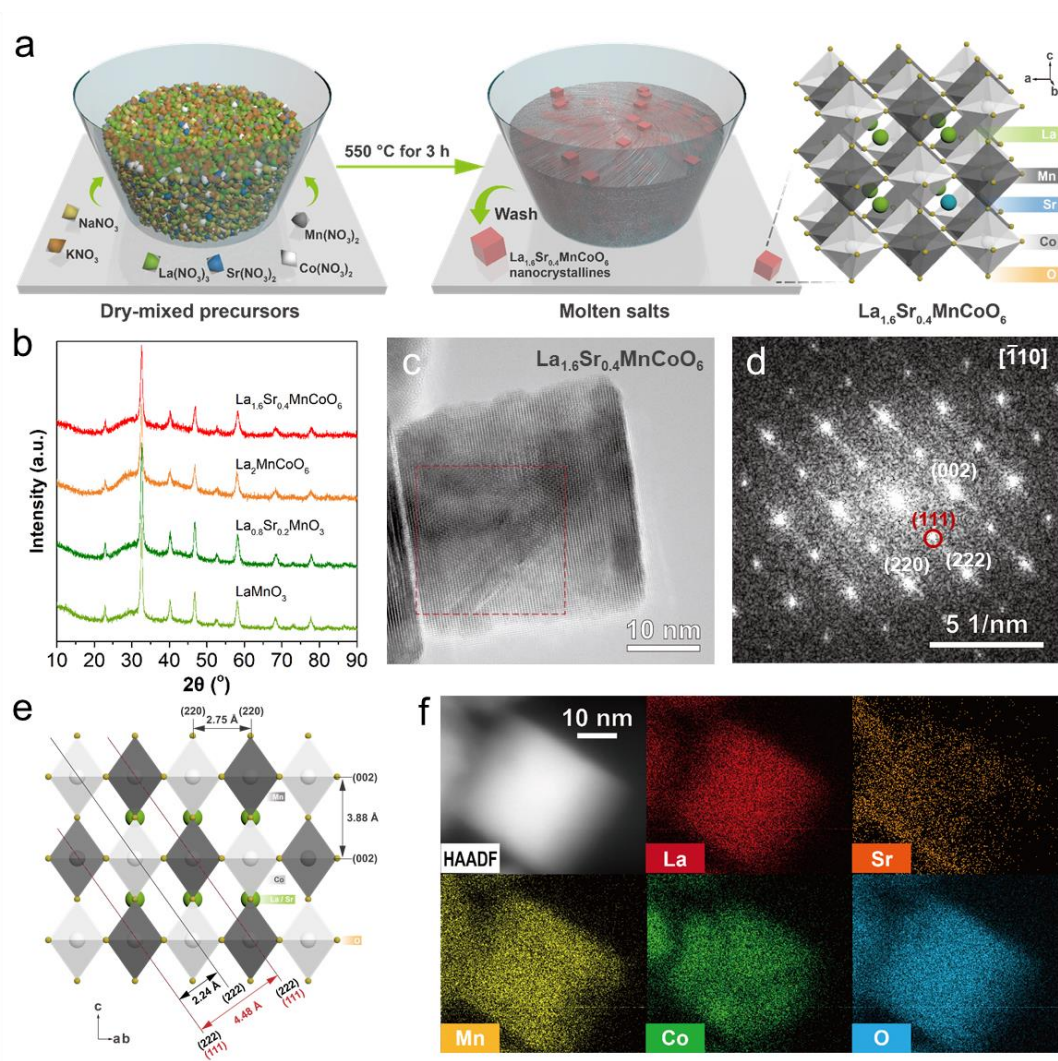


Figure 6.1 Synthesis and characterization of the perovskite-type cubic nanocrystallites. a) Illustrative demonstration of synthesis procedure with the inset showing the atomic arrangements of $\text{La}_{1.6}\text{Sr}_{0.4}\text{MnCoO}_6$; b) XRD patterns, c) TEM image, d) corresponding FFT pattern with zone axis of $[-1\ 1\ 0]$, e) illustrative demonstration of the atomic arrangements viewed along the $[-1\ 1\ 0]$ direction and f) Elemental mapping of a $\text{La}_{1.6}\text{Sr}_{0.4}\text{MnCoO}_6$ nanocrystallite.

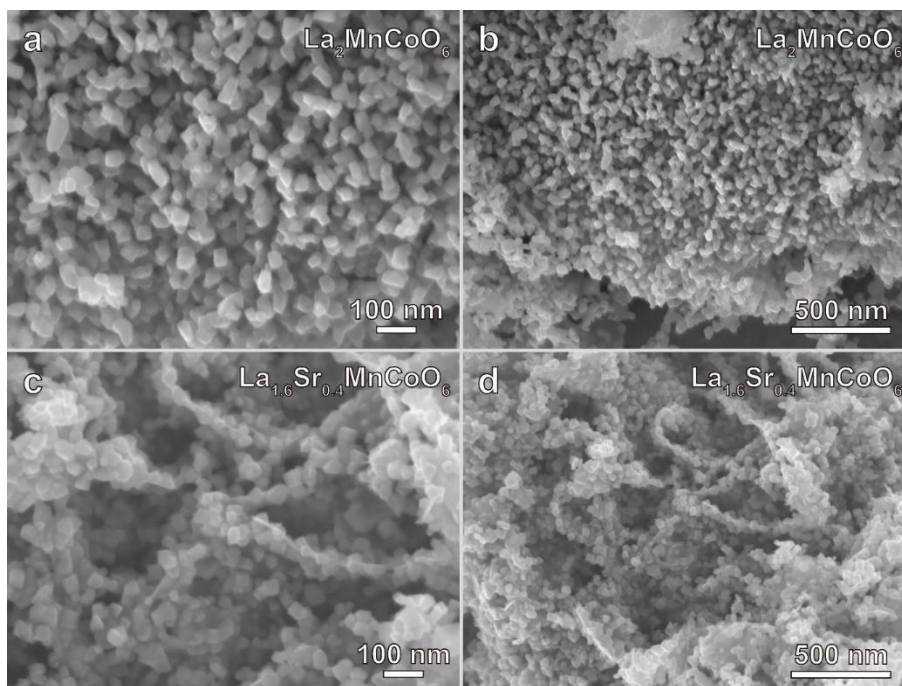


Figure 6.2 SEM images of a), b) $\text{La}_2\text{MnCoO}_6$ and c), d) $\text{La}_{1.6}\text{Sr}_{0.4}\text{MnCoO}_6$ nanocrystallites.

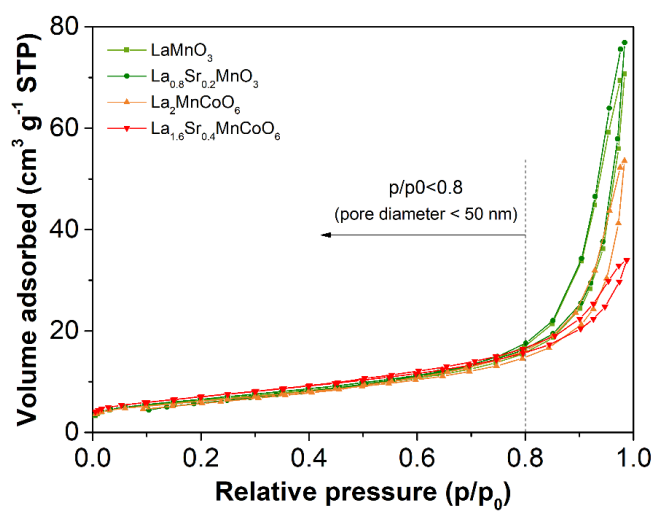


Figure 6.3 N_2 adsorption-desorption isotherms of the perovskite-type nanocrystallites.

Table 6.1 Physical parameters for the perovskite-type nanocrystallites.

Sample	a _{BET} m ² g ⁻¹	V _{total} * cm ³ g ⁻¹
LaMnO ₃	22.8	0.024
La _{0.8} Sr _{0.2} MnO ₃	23.7	0.025
La ₂ MnCoO ₆	22.1	0.023
La _{1.6} Sr _{0.4} MnCoO ₆	25.2	0.024

*p/p⁰=0.8, corresponding to total pore volume of micro- and meso-pores with diameter <50 nm

6.3.2 Bifunctional catalytic activity for ORR and OER

The ORR-OER catalysis was evaluated using an RDE-based three-electrode system with a 0.1 M KOH electrolyte. By integrating both Mn and Co cations into the perovskite-type structure, both La₂MnCoO₆ and La_{1.6}Sr_{0.4}MnCoO₆ demonstrated decent ORR-OER activity (**Figure 6.4a** and **Figure 6.4c**). Without the integration of Co cation, LaMnO₃ and La_{0.8}Sr_{0.2}MnO₃ presented very poor catalysis for OER, which even cannot reach 10 mA cm⁻² at 1.9 V (vs. *iR*-corrected RHE), even though they demonstrated better catalysis for ORR (**Figure 6.4a**). The potential difference (ΔE) of major parameters, i.e., half-wave potential ($E_{1/2}$) for ORR and potential at the current density of 10 mA cm⁻² ($E_{j=10}$) for OER, is an indicator for evaluating the bifunctional catalysis. As compared in **Figure 6.4e**, the $E_{1/2}$ of La_{1.6}Sr_{0.4}MnCoO₆ (0.63 V) was higher than that of La₂MnCoO₆ (0.61 V). At the same time, the $E_{j=10}$ of La_{1.6}Sr_{0.4}MnCoO₆ (1.73 V) was lower than that of La₂MnCoO₆ (1.78 V). As a result, a decent ΔE of 1.10 V was observed for La_{1.6}Sr_{0.4}MnCoO₆. In addition, La_{1.6}Sr_{0.4}MnCoO₆ presented good selectivity of OH⁻ production over the unfavorable HO₂⁻, which is indicated by the ~4 electron transfer number (**Figure 6.4b**).^{31, 32} La_{1.6}Sr_{0.4}MnCoO₆ also demonstrated a Tafel slope of 72 mV dec⁻¹ (**Figure 6.4d**), indicating a good OER kinetics which is comparable to the benchmark commercial IrO₂ (67 mV dec⁻¹).³³

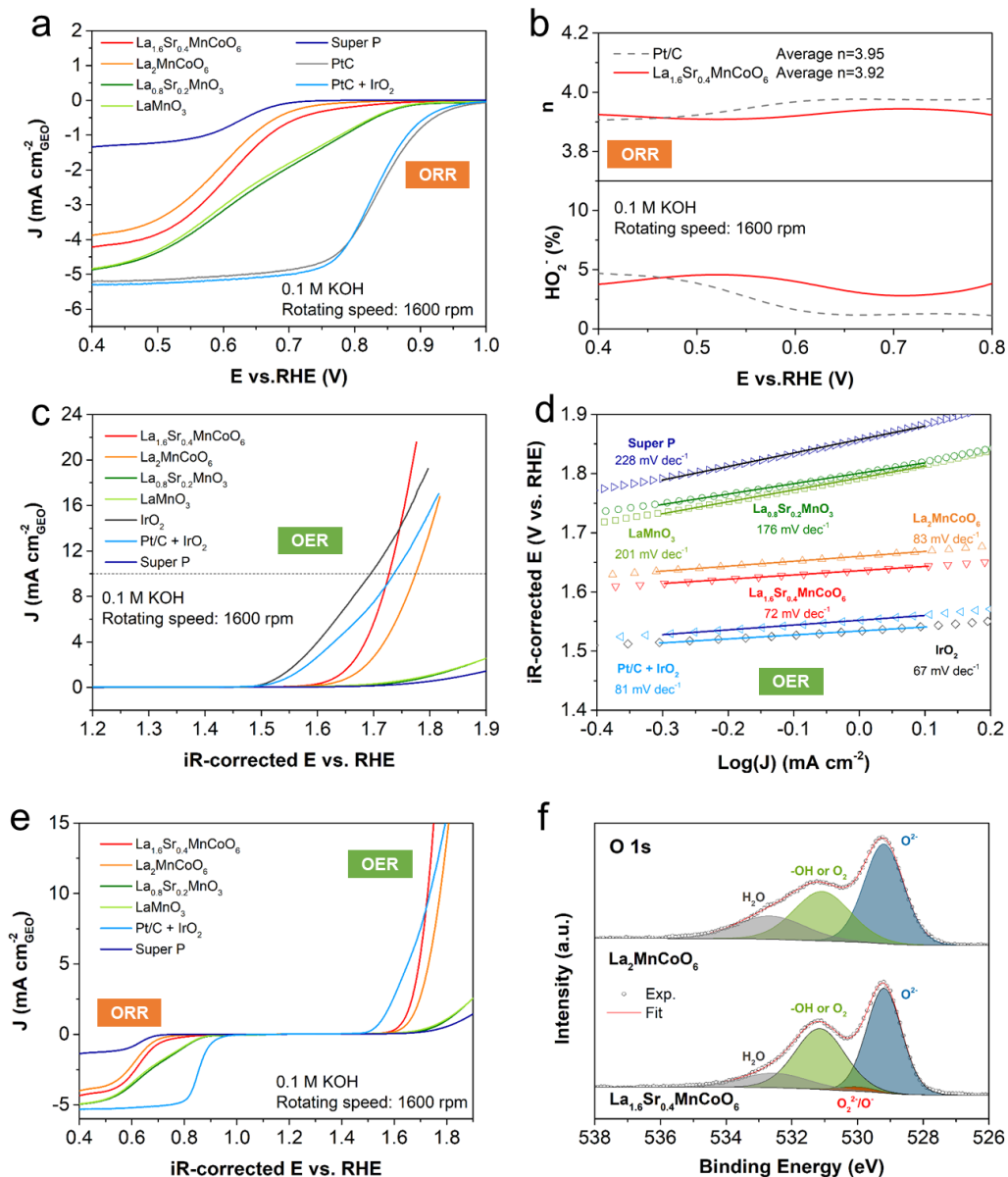


Figure 6.4 Bifunctional oxygen catalytic activity of the perovskite-type cubic nanocrystallites. a) Comparison of ORR polarization curves for perovskite-type oxide nanocrystallites and three different commercial samples, b) The electron transfer number (n) and HO_2^- yield percentage based on the data from RRDE. c) Comparison of OER polarization curves for the perovskite-type materials with commercial samples and d) corresponding Tafel plots. e) Comparison of bifunctional oxygen catalysis activities. f) XPS O 1s profiles of $\text{La}_2\text{MnCoO}_6$ and $\text{La}_{1.6}\text{Sr}_{0.4}\text{MnCoO}_6$ with peak fitting results.

The improved catalytic activity of $\text{La}_{1.6}\text{Sr}_{0.4}\text{MnCoO}_6$ compared to $\text{La}_2\text{MnCoO}_6$ for both ORR and OER could be associated with the appearance of oxygen vacancies in the perovskite-type oxide, which could promote catalysis of ORR and OER according to previous reports.³⁴⁻³⁶ Usually, oxygen vacancies are unlikely to occur in LaMnO_3 .³⁷ The oxygen vacancies in $\text{La}_{1.6}\text{Sr}_{0.4}\text{MnCoO}_6$ could be ascribed to the introduction of Co and the partial substitution of La (+3) with Sr (+2). XPS O 1s spectra presented in **Figure 6.4f** shows three main surface oxygen species: lattice oxygen (O^{2-}), hydroxide or adsorbed oxygen (OH^-/O_2) and adsorbed water (H_2O) in $\text{La}_2\text{MnCoO}_6$.^{38, 39} An additional peak centered at ~ 530.1 eV can be identified for $\text{La}_{1.6}\text{Sr}_{0.4}\text{MnCoO}_6$. The peak could be attributed to the highly oxidative oxygen species ($\text{O}_2^{2-}/\text{O}^-$), which is highly associated with the oxygen vacancies.^{40, 41} The decent catalysis for ORR and OER could also be attributed to the nanosizing of the $\text{La}_{1.6}\text{Sr}_{0.4}\text{MnCoO}_6$, which could increase the surface area and provide more active sites for the oxygen redox. As presented in **Figure 6.5**, the $\text{La}_{1.6}\text{Sr}_{0.4}\text{MnCoO}_6$ nanocrystallites prepared via the molten-salt synthesis method demonstrated better ORR-OER activities than those of a $\text{La}_{1.6}\text{Sr}_{0.4}\text{MnCoO}_6$ sample prepared with a conventional sol-gel method which usually produces particles with a size of several micrometers.

Though decent bifunctional catalytic activity, good selectivity of OH^- generation and fast kinetics of OER were achieved for $\text{La}_{1.6}\text{Sr}_{0.4}\text{MnCoO}_6$, its ΔE (1.10 V) was still not comparable to Pt/C + IrO_2 (0.89 V) at this stage. Further optimization of the $\text{La}_{1.6}\text{Sr}_{0.4}\text{MnCoO}_6$ to improve its catalytic activity is required and will be demonstrated in the last section of this work.

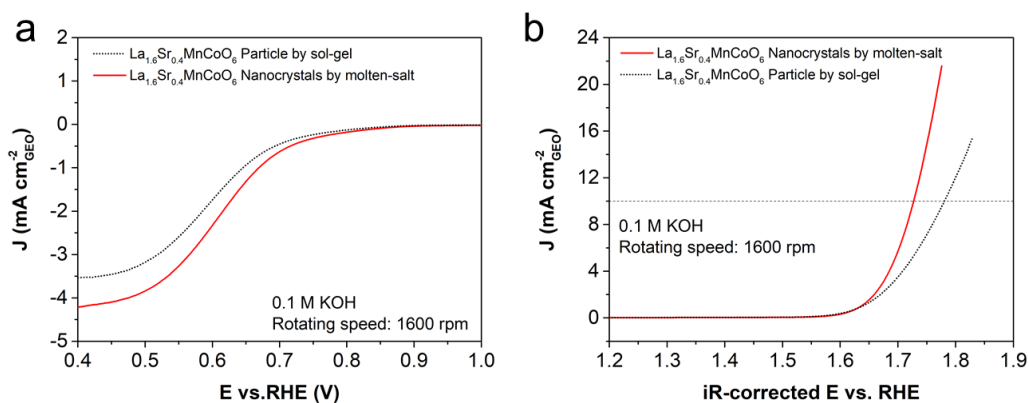


Figure 6.5 Comparison of a) ORR and b) OER polarization curves of $\text{La}_{1.6}\text{Sr}_{0.4}\text{MnCoO}_6$ nanocrystals synthesized via a molten-salt method and $\text{La}_{1.6}\text{Sr}_{0.4}\text{MnCoO}_6$ particle synthesized via a sol-gel method.

6.3.3 Performance of the Zn-air batteries

To testify the validation of the above analysis results, the $\text{La}_{1.6}\text{Sr}_{0.4}\text{MnCoO}_6$ nanocrystalites was applied as a catalyst on air cathodes of aqueous and quasi-solid-state Zn-air batteries. An aqueous Zn-air battery with the catalyst demonstrated a decent OCV of 1.44 V (**Figure 6.6a**), close to that with the Pt/C + IrO_2 catalyst (1.46 V). Discharging performance at different current densities was evaluated with the I-V-P profiles (**Figure 6.6a**). A PPD of 187 mW cm^{-2} was achieved at 419 mA cm^{-2} for $\text{La}_{1.6}\text{Sr}_{0.4}\text{MnCoO}_6$, which is comparable to the Pt/C + IrO_2 (217 mW cm^{-2} at 408 mA cm^{-2}). The rate performance (from 1 to 30 mA cm^{-2}) of the batteries was evaluated with repeating a recharge process of a 5-min galvanostatic charging and a galvanostatic 5-min discharging. The median voltage points of each charging and discharging profile was presented in **Figure 6.6b**. The $\text{La}_{1.6}\text{Sr}_{0.4}\text{MnCoO}_6$ cathode presented a charging and discharging voltages of 2.01 and 1.26 V, respectively, at 1 mA cm^{-2} , indicating a decent charge-discharge voltage gap ($\Delta V_{\text{Zn-air}}$) of 0.75 V corresponding to a round-trip efficiency (i.e., voltage efficiency) of 63%. As the overpotential increased with the rising of current densities, the $\Delta V_{\text{Zn-air}}$ increase to 0.82, 0.90, 0.96, 1.04 and 1.10 at 2, 5, 10, 20 and 30 mA cm^{-2} , respectively. As a comparison, though Pt/C + IrO_2 cathode demonstrated better performance at low current density (e.g., $\Delta V_{\text{Zn-air}}$ of 0.62 V and voltage efficiency of 68% at 1 mA cm^{-2}), the cathode experienced a fast deterioration of working voltage, especially at high current densities. The $\text{La}_{1.6}\text{Sr}_{0.4}\text{MnCoO}_6$ cathode also shows good voltage retention when the current density was reduced back to 1 and 2 mA cm^{-2} , with a $\Delta V_{\text{Zn-air}}$ of 0.73 and 0.81 V, respectively (**Figure 6.6b**).

The battery performance of $\text{La}_{1.6}\text{Sr}_{0.4}\text{MnCoO}_6$ was also compared to $\text{La}_2\text{MnCoO}_6$ without Sr substitution. Benefiting from the higher ORR and OER activity as indicated from the RDE tests presented in **Figure 6.4**, the OCV, PPD (**Figure 6.7**) and rate performance (**Figure 6.8**) of the $\text{La}_{1.6}\text{Sr}_{0.4}\text{MnCoO}_6$ cathode were superior to those of the $\text{La}_2\text{MnCoO}_6$ cathode (OCV: 1.40 V, PPD: 167 mW cm^{-2}).

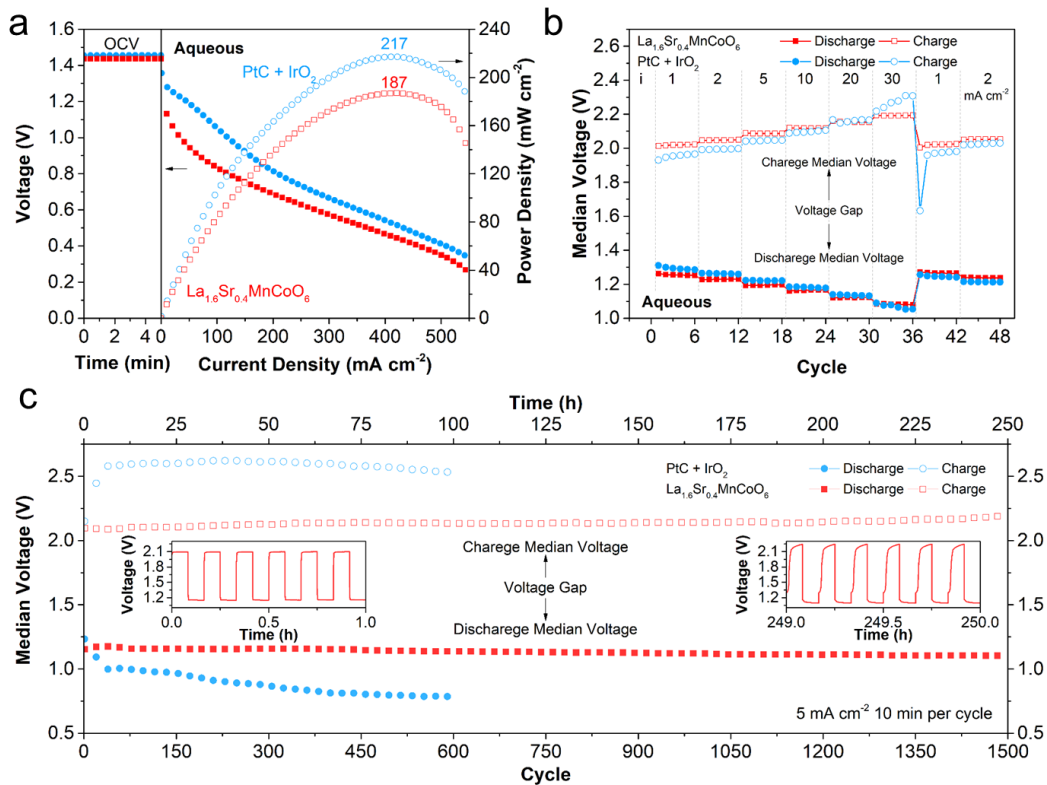


Figure 6.6 Performance of aqueous Zn-air batteries with a $\text{La}_{1.6}\text{Sr}_{0.4}\text{MnCoO}_6$ catalyst in 6 M KOH + 2 M $\text{Zn}(\text{Ac})_2$ electrolyte. a) OCV, I-V-P profiles and PPD, b) rate performance evaluated with 5-minute galvanostatic charging and 5-minute galvanostatic discharging, c) Cycling stability at 5 mA cm⁻², inset shows the specific galvanostatic charge-discharge profiles.

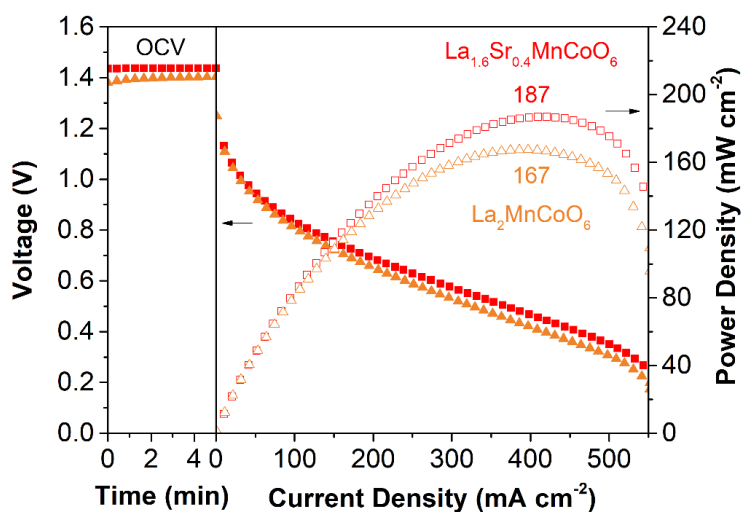


Figure 6.7 Comparison of OCV, I-V-P profiles and PPD for aqueous Zn-air batteries with $\text{La}_2\text{MnCoO}_6$ or $\text{La}_{1.6}\text{Sr}_{0.4}\text{MnCoO}_6$ as the catalyst.

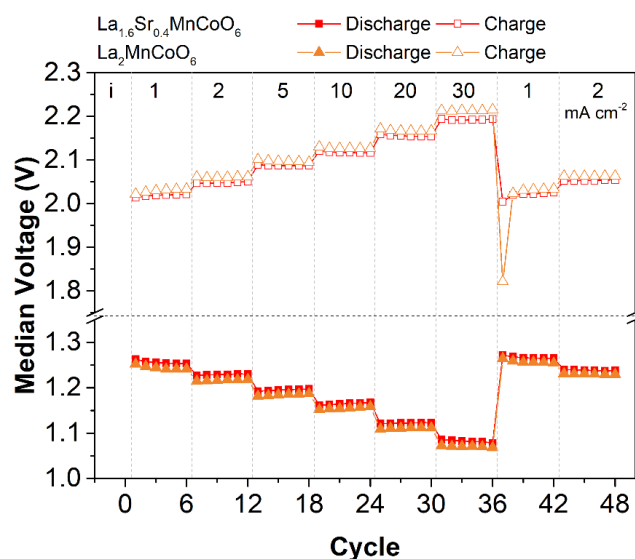


Figure 6.8 Comparison of rate performance for aqueous Zn-air batteries with $\text{La}_2\text{MnCoO}_6$ or $\text{La}_{1.6}\text{Sr}_{0.4}\text{MnCoO}_6$ as air cathode with 10-minute galvanostatic charging-discharging cycles.

As presented in **Figure 6.6c**, the $\text{La}_{1.6}\text{Sr}_{0.4}\text{MnCoO}_6$ cathode also demonstrated superior stability than the commercial Pt/C + IrO_2 catalyst for 1500 recharging cycles (250 h) at 5 mA cm^{-2} . During the cycling performance, the $\text{La}_{1.6}\text{Sr}_{0.4}\text{MnCoO}_6$ cathode showed a gradual increase of $\Delta V_{\text{Zn-air}}$ (inset image in **Figure 6.6c**) from 0.95 V (1st cycle) to 1.09 V (1500th cycle). The stability was much better than the Pt/C + IrO_2 cathode which presented a significant increase of overpotentials only cycling after a few hours. A prolonged cycling of the Zn-air battery over 333 h (1000 cycles) was conducted to evaluate the stability of the $\text{La}_{1.6}\text{Sr}_{0.4}\text{MnCoO}_6$ material and identify the potential reason for the degradation of battery performance. As presented in **Figure 6.9a**, a significant increase of overpotentials for both charging and discharging was observed. The Zn-air battery after cycling for 333 h was disassembled and the $\text{La}_{1.6}\text{Sr}_{0.4}\text{MnCoO}_6$ cathode was characterized by XRD (**Figure 6.9b**), where a cathode before cycling and a cathode after cycling for 50 h were also compared. The characteristic perovskite-type crystal structure remains for the cathode after testing for 50 and 333 h. This indicates the good stability of crystal structure of $\text{La}_{1.6}\text{Sr}_{0.4}\text{MnCoO}_6$, which is beneficial to the stable running of the battery. The fast performance degradation after 250 h could be associated with the precipitation of inert ZnO in the cathode, which could be associated with the over-saturation of zincate ion after

prolonged cycling due to the accumulation of product from the irreversible redox of Zn anode,^{42, 43} which was evidenced by the XRD result presented in **Figure 6.9b**. The accumulation of ZnO deposition could result in the deterioration of gas and ionic transfer pathways.

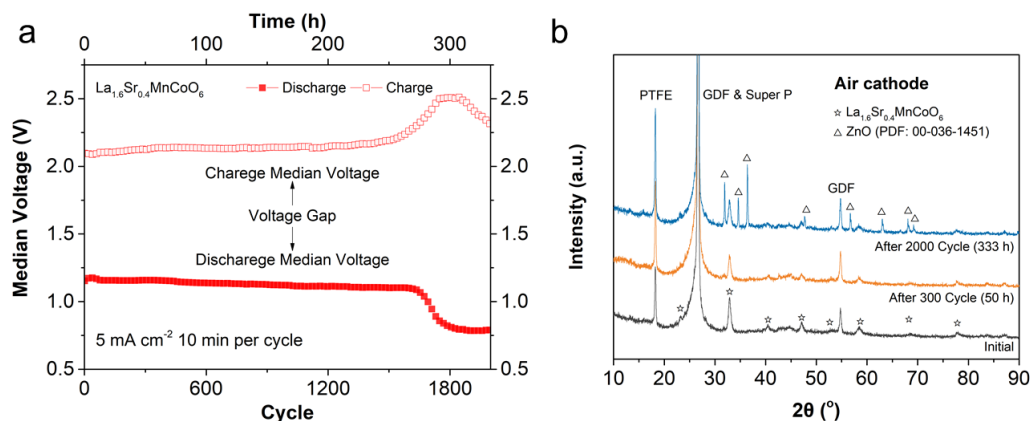


Figure 6.9 a) A prolonged 2000-cycle (~333 h) test until voltage failure of aqueous Zn-air battery with a $\text{La}_{1.6}\text{Sr}_{0.4}\text{MnCoO}_6$ as air cathode; b) XRD profiles of the initial $\text{La}_{1.6}\text{Sr}_{0.4}\text{MnCoO}_6$ as air cathode and after 50 h and 333 h.

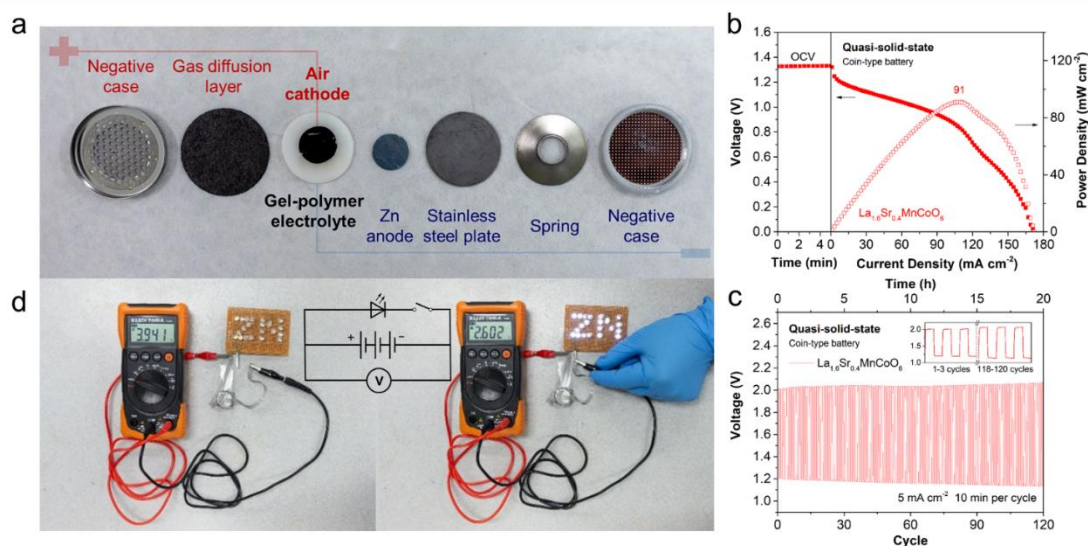


Figure 6.10 Performance of coin-type quasi-solid-state Zn-air battery. a) Configuration of the coin-type quasi-solid-state Zn-air battery, b) OCV and I-V-P profiles, c) cycling stability evaluation at 5 mA cm^{-2} , d) OCV of a 3-series coin-type battery group and working voltage that lightening 21 LED bulbs in parallel.

$\text{La}_{1.6}\text{Sr}_{0.4}\text{MnCoO}_6$ was also evaluated with coin-type batteries with a gel-polymer electrolyte (**Figure 6.10a**). As presented in **Figure 6.10b**, a single coin-type battery presented a decent OCV of 1.33 V and PPD of 91 mW cm^{-2} . The battery also showed

decent cycling stability over 20 h (120 cycles) with a charge-discharge ΔV_{Zn-air} of ~ 0.8 V and a round-trip efficiency of $\sim 55\%$ at 5 mA cm^{-2} (**Figure 6.10c**). A three-series coin-type battery group was also established to verify the practical utility of powering small electronic devices. The battery group presented an OCV of 3.94 V, which was dropped to 2.60 V when 21 LED bulbs were lightened (**Figure 6.10d**). Once after the work loading was removed, the voltage quickly recovers to a level (3.79 V) close to the original OCV within 10 seconds.

6.3.4 Integration of small amount of Pt/C for optimization of oxygen catalysis

The above decent performance and very good stability suggest that the perovskite-type $\text{La}_{1.6}\text{Sr}_{0.4}\text{MnCoO}_6$ is a promising bifunctional oxygen catalyst for practical Zn-air batteries. As discussed in the last few sections, the oxygen vacancies introduced by the Sr doping was the origin of the enhanced catalytic activity (**Figure 6.11d**). The Sr doping is a modification for the entire bulk particles, the oxygen vacancies may disperse both on the particle bulk and surface. Also, the substitution amount of Sr has a limitation which is restricted by the perovskite structure itself. It is worth noting that usually OER and ORR are more likely to happen on the catalyst surface. To further increase surface oxygen vacancies, a facile Pt/C decoration strategy was introduced (**Figure 6.12**). Commercial Pt/C was physically mixed with the $\text{La}_{1.6}\text{Sr}_{0.4}\text{MnCoO}_6$ using an ultrasonic bath. Even though the mass ratio of Pt/C to the perovskite was controlled in a very low value (2 to 5 wt% of Pt to $\text{La}_{1.6}\text{Sr}_{0.4}\text{MnCoO}_6$), the ORR and OER activity was highly boosted. As presented in **Figure 6.11a**, the $\text{La}_{1.6}\text{Sr}_{0.4}\text{MnCoO}_6$ -Pt mixture with a Pt loading of 2% and 5% demonstrated a ΔE (based on RDE test in 0.1 M KOH) of 0.90 and 0.85 V (vs. iR-corrected RHE), which is much superior to that without Pt decoration (1.10 V). Such improvement on the bifunctional catalysis was also reflective by the galvanostatic charging-discharging performance of the Zn-air battery (with 6 M KOH + 0.2 M $\text{Zn}(\text{Ac})_2$). As compared in **Figure 6.11b**, decrease of ΔV_{Zn-air} (0.95, 0.88, 0.85 V vs. Zn) and increase of round-trip efficiency (55%, 58%, 59%) were observed for samples with 0%, 2% and 5% Pt introduction. The XPS O 1s spectra presented in **Figure 6.11c** indicated the increased amount of the $\text{O}_2^{2-}/\text{O}^-$, which is highly related to surface oxygen vacancy for the samples with Pt decoration.⁴⁰ This could be associated with the surface charge transfer from Pt/C to cation elements in the $\text{La}_{1.6}\text{Sr}_{0.4}\text{MnCoO}_6$, which results in more oxygen vacancies on the perovskite surface as compensation (**Figure 6.11e**).¹³

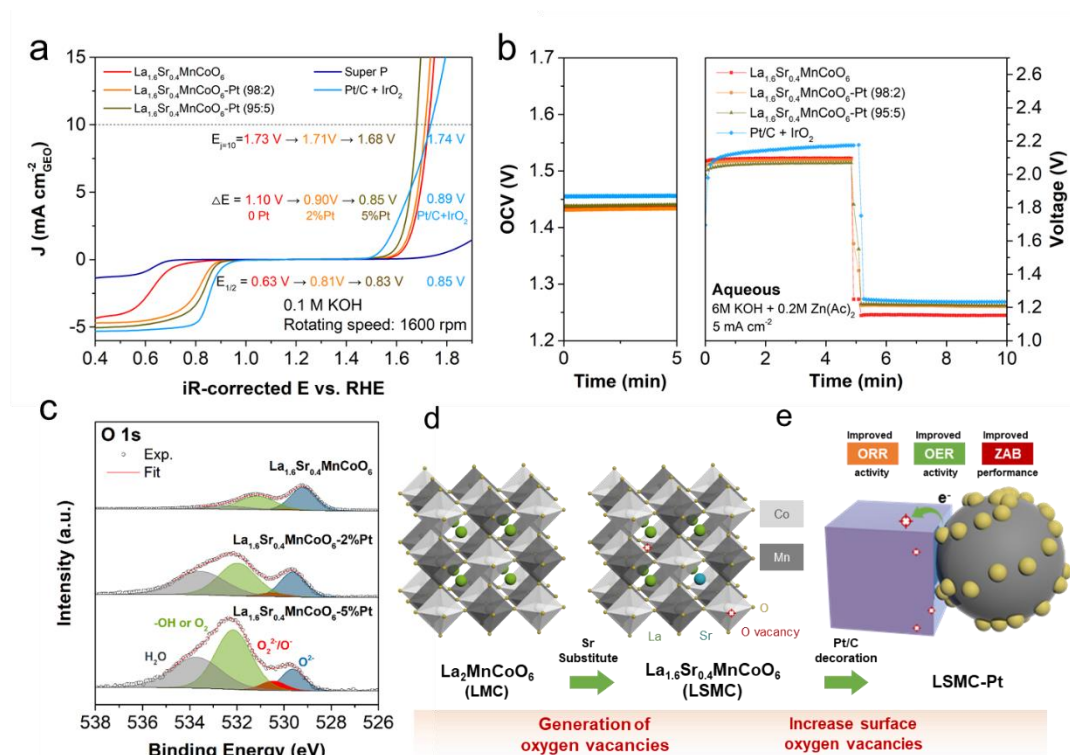


Figure 6.11 Further optimization of the oxygen catalysis. Comparison of a) bifunctional oxygen catalysis activities and b) OCV and first discharge-charge cycle at 5 mA cm^{-2} of Zn-air battery and c) XPS O 1s spectra of $\text{La}_{1.6}\text{Sr}_{0.4}\text{MnCoO}_6$ and Pt/C decorated $\text{La}_{1.6}\text{Sr}_{0.4}\text{MnCoO}_6$ samples. Illustrative demonstration of the improvement of bifunctional oxygen catalysis activity benefited from d) generation of oxygen vacancies via partial Sr substitution in the perovskite structure and from e) increased surface oxygen vacancies induced by facile Pt/C decoration.

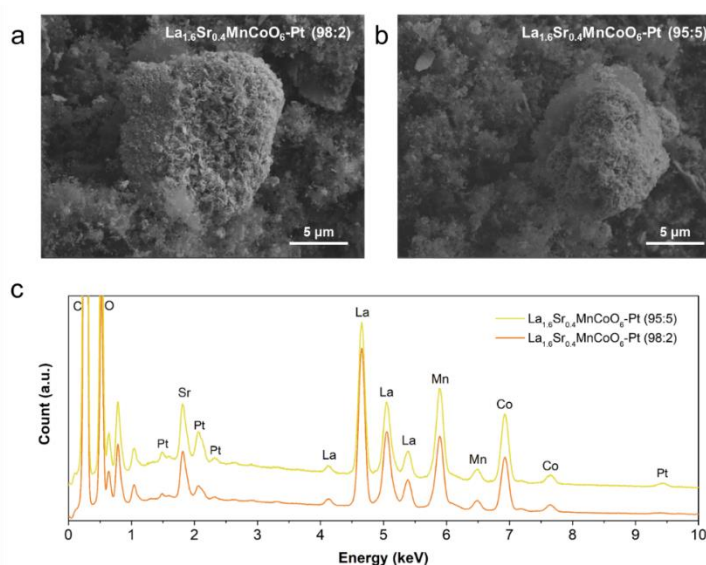


Figure 6.12 SEM images of a) $\text{La}_{1.6}\text{Sr}_{0.4}\text{MnCoO}_6\text{-Pt (98:2)}$ and b) $\text{La}_{1.6}\text{Sr}_{0.4}\text{MnCoO}_6\text{-Pt (95:5)}$ and c) EDS profiles.

6.4 Conclusion

In conclusion, rational designs including introducing and increasing oxygen vacancies and nanosizing of the perovskite were proposed to effectively improve the bifunctional oxygen catalysis. The perovskite-type nanocrystallites with ultra-small cubic (20-50 nm length) morphology and high specific surface areas ($25 \text{ m}^2 \text{ g}^{-1}$) were prepared via a molten-salt method. Due to the introduction of oxygen vacancy by partial substitution of La with Sr, the $\text{La}_{1.6}\text{Sr}_{0.4}\text{MnCoO}_6$ nanocrystallites demonstrated improved catalytic activity for both ORR and OER. Zn-air batteries with the $\text{La}_{1.6}\text{Sr}_{0.4}\text{MnCoO}_6$ as an oxygen catalyst demonstrated decent discharge-charge $\Delta V_{\text{Zn-air}}$ of 0.75 and 1.10 V at 1 and 30 mA cm^{-2} , respectively, and good cycling stability for more than 250 h with a fair $\Delta V_{\text{Zn-air}} \sim 1 \text{ V}$ in an alkaline electrolyte. Crystal structure of the $\text{La}_{1.6}\text{Sr}_{0.4}\text{MnCoO}_6$ nanocrystallites remained stable after hundreds of hours of charge-discharge cycling. Coin-type Zn-air battery with the $\text{La}_{1.6}\text{Sr}_{0.4}\text{MnCoO}_6$ and an alkaline gel-polymer electrolyte also presented good performance and decent stability. Further enhancement of the ORR-OER catalysis and performance of Zn-air battery was achieved by increasing surface oxygen vacancy via integrating a small amount of Pt on the surface of $\text{La}_{1.6}\text{Sr}_{0.4}\text{MnCoO}_6$.

References

- 1 Ma H, Wang B. A bifunctional electrocatalyst $\alpha\text{-MnO}_2\text{-LaNiO}_3$ /carbon nanotube composite for rechargeable zinc-air batteries. *RSC Adv.* 2014;4(86):46084-92. doi:10.1039/C4RA07401G
- 2 Du G, Liu X, Zong Y, Hor TSA, Yu A, Liu Z. Co_3O_4 nanoparticle-modified MnO_2 nanotube bifunctional oxygen cathode catalysts for rechargeable zinc-air batteries. *Nanoscale.* 2013;5(11):4657-61. doi:10.1039/c3nr00300k
- 3 Xu N, Liu Y, Zhang X, Li X, Li A, Qiao J, et al. Self-assembly formation of Bifunctional $\text{Co}_3\text{O}_4/\text{MnO}_2\text{-CNTs}$ hybrid catalysts for achieving both high energy/power density and cyclic ability of rechargeable zinc-air battery. *Sci Rep.* 2016;6:33590. doi:10.1038/srep33590
- 4 Luo Z, Irtem E, Ibanez M, Nafria R, Marti-Sanchez S, Genc A, et al. $\text{Mn}_3\text{O}_4@\text{CoMn}_2\text{O}_4\text{-Co}_x\text{O}_y$ nanoparticles: Partial cation exchange synthesis and electrocatalytic properties toward the oxygen reduction and evolution reactions. *ACS Appl Mater Interfaces.* 2016;8(27):17435-44. doi:10.1021/acsami.6b02786

- 5 Xu X, Wang W, Zhou W, Shao Z. Recent advances in novel nanostructuring methods of perovskite electrocatalysts for energy-related applications. *Small Methods*. 2018;2(7):1800071. doi:10.1002/smt.201800071
- 6 Xu X, Zhong Y, Shao Z. Double perovskites in catalysis, electrocatalysis, and photo(electro)catalysis. *Trends Chem*. 2019;1(4):410-24. doi:10.1016/j.trechm.2019.05.006
- 7 Yu J, Ran R, Zhong Y, Zhou W, Ni M, Shao Z. Advances in porous perovskites: Synthesis and electrocatalytic performance in fuel cells and metal–air batteries. *Energy Environ Mater*. 2020;3(2):121-45. doi:10.1002/eem2.12064
- 8 Chen Z, Yu A, Higgins D, Li H, Wang H, Chen Z. Highly active and durable core-corona structured bifunctional catalyst for rechargeable metal-air battery application. *Nano Lett*. 2012;12(4):1946-52. doi:10.1021/nl2044327
- 9 Park HW, Lee DU, Zamani P, Seo MH, Nazar LF, Chen Z. Electrospun porous nanorod perovskite oxide/nitrogen-doped graphene composite as a bi-functional catalyst for metal air batteries. *Nano Energy*. 2014;10:192-200. doi:10.1016/j.nanoen.2014.09.009
- 10 Wang Q, Xue Y, Sun S, Li S, Miao H, Liu Z. $\text{La}_{0.8}\text{Sr}_{0.2}\text{Co}_{1-x}\text{Mn}_x\text{O}_3$ perovskites as efficient bi-functional cathode catalysts for rechargeable zinc-air batteries. *Electrochim Acta*. 2017;254:14-24. doi:10.1016/j.electacta.2017.09.034
- 11 Bian J, Li Z, Li N, Sun C. Oxygen deficient $\text{LaMn}_{0.75}\text{Co}_{0.25}\text{O}_{3-\delta}$ nanofibers as an efficient electrocatalyst for oxygen evolution reaction and zinc-air batteries. *Inorg Chem*. 2019;58(12):8208-14. doi:10.1021/acs.inorgchem.9b01034
- 12 Bu Y, Gwon O, Nam G, Jang H, Kim S, Zhong Q, et al. A highly efficient and robust cation ordered perovskite oxide as a bifunctional catalyst for rechargeable zinc-air batteries. *ACS Nano*. 2017;11(11):11594-601. doi:10.1021/acsnano.7b06595
- 13 Wang X, Sunarso J, Lu Q, Zhou Z, Dai J, Guan D, et al. High-performance platinum-perovskite composite bifunctional oxygen electrocatalyst for rechargeable Zn-air battery. *Adv Energy Mater*. 2020;10(5). doi:10.1002/aenm.201903271
- 14 Suntivich J, Gasteiger HA, Yabuuchi N, Nakanishi H, Goodenough JB, Shao-Horn Y. Design principles for oxygen-reduction activity on perovskite oxide catalysts for fuel cells and metal-air batteries. *Nat Chem*. 2011;3(7):546-50. doi:10.1038/nchem.1069

- 15 Majee R, Islam QA, Bhattacharyya S. Surface charge modulation of perovskite oxides at the crystalline junction with layered double hydroxide for a durable rechargeable zinc-air battery. *ACS Appl Mater Interfaces*. 2019;11(39):35853-62. doi:10.1021/acsami.9b09299
- 16 Peng S, Han X, Li L, Chou S, Ji D, Huang H, et al. Electronic and defective engineering of electrospun CaMnO_3 nanotubes for enhanced oxygen electrocatalysis in rechargeable zinc-air batteries. *Adv Energy Mater*. 2018;8(22):1800612. doi:10.1002/aenm.201800612
- 17 Ishihara T, Guo LM, Miyano T, Inoishi Y, Kaneko K, Ida S. Mesoporous $\text{La}_{0.6}\text{Ca}_{0.4}\text{CoO}_3$ perovskites with large surface areas as stable air electrodes for rechargeable Zn-air batteries. *J Mater Chem A*. 2018;6(17):7686-92. doi:10.1039/C8TA00426A
- 18 Zhang Y-Q, Tao H-B, Chen Z, Li M, Sun Y-F, Hua B, et al. In situ grown cobalt phosphide (CoP) on perovskite nanofibers as an optimized trifunctional electrocatalyst for Zn-air batteries and overall water splitting. *J Mater Chem A*. 2019;7(46):26607-17. doi:10.1039/C9TA08936E
- 19 Kuai L, Kan E, Cao W, Huttula M, Ollikkala S, Ahopelto T, et al. Mesoporous $\text{LaMnO}_{3+\delta}$ perovskite from spray - pyrolysis with superior performance for oxygen reduction reaction and Zn - air battery. *Nano Energy*. 2018;43:81-90. doi:10.1016/j.nanoen.2017.11.018
- 20 Yan Z, Sun H, Chen X, Fu X, Chen C, Cheng F, et al. Rapid low-temperature synthesis of perovskite/carbon nanocomposites as superior electrocatalysts for oxygen reduction in Zn-air batteries. *Nano Research*. 2018;11(6):3282-93. doi:10.1007/s12274-017-1869-8
- 21 Arafat Y, Azhar MR, Zhong Y, Xu X, Tadé MO, Shao Z. A Porous nano-micro-composite as a high-performance bi-functional air electrode with remarkable stability for rechargeable zinc-air batteries. *Nano-Micro Lett*. 2020;12:130. doi:10.1007/s40820-020-00468-4
- 22 Wang X, Ge L, Lu Q, Dai J, Guan D, Ran R, et al. High-performance metal-organic framework-perovskite hybrid as an important component of the air-electrode for rechargeable Zn-Air battery. *Journal of Power Sources*. 2020;468:228377. doi:10.1016/j.jpowsour.2020.228377

- 23 Grimaud A, May KJ, Carlton CE, Lee Y-L, Risch M, Hong WT, et al. Double perovskites as a family of highly active catalysts for oxygen evolution in alkaline solution. *Nat Commun.* 2013;4:2439. doi:10.1038/ncomms3439
- 24 Kleibeuker JE, Choi E-M, Jones ED, Yu T-M, Sala B, MacLaren BA, et al. Route to achieving perfect B-site ordering in double perovskite thin films. *NPG Asia Mater.* 2017;9(7):e406. doi:10.1038/am.2017.113
- 25 Xue P, Wu H, Lu Y, Zhu X. Recent progress in molten salt synthesis of low-dimensional perovskite oxide nanostructures, structural characterization, properties, and functional applications: A review. *J Mater Sci Technol.* 2018;34(6):914-30. doi:10.1016/j.jmst.2017.10.005
- 26 Tian Y, Chen D, Jiao X. $\text{La}_{1-x}\text{Sr}_x\text{MnO}_3$ ($x = 0, 0.3, 0.5, 0.7$) nanoparticles nearly freestanding in water: Preparation and magnetic properties. *Chem Mater.* 2006;18(26):6088-90. doi:10.1021/cm0622349
- 27 Li LH, Deng JX, Chen J, Xing XR. Topochemical molten salt synthesis for functional perovskite compounds. *Chem Sci.* 2016;7(2):855-65. doi:10.1039/C5SC03521J
- 28 Sun H, Xu X, Hu Z, Tjeng LH, Zhao J, Zhang Q, et al. Boosting the oxygen evolution reaction activity of a perovskite through introducing multi-element synergy and building an ordered structure. *J Mater Chem A.* 2019;7(16):9924-32. doi:10.1039/C9TA01404G
- 29 Zhong Y, Xu X, Veder J-P, Shao Z. Self-recovery chemistry and cobalt-catalyzed electrochemical deposition of cathode for boosting performance of aqueous zinc-ion batteries. *iScience.* 2020;23(3):100943. doi:10.1016/j.isci.2020.100943
- 30 Androulakis J, Katsarakis N, Giapintzakis J, Vouroutzis N, Pavlidou E, Chrissafis K, et al. LaSrMnCoO_6 : A new cubic double perovskite oxide. *J Solid State Chem.* 2003;173(2):350-4. doi:10.1016/S0022-4596(03)00109-9
- 31 Tang T, Jiang W-J, Liu X-Z, Deng J, Niu S, Wang B, et al. Metastable rock salt oxide-mediated synthesis of high-density dual-protected $\text{M}@\text{NC}$ for long-life rechargeable zinc-air batteries with record power density. *J Am Chem Soc.* 2020;142(15):7116-27. doi:10.1021/jacs.0c01349
- 32 Lu Q, Zou X, Liao K, Ran R, Zhou W, Ni M, et al. Direct growth of ordered N-doped carbon nanotube arrays on carbon fiber cloth as a free-standing and

- binder-free air electrode for flexible quasi-solid-state rechargeable Zn-Air batteries. *Carbon Energy*. 2020;2(3):461-71. doi:10.1002/cey2.50
- 33 Pan Y, Xu X, Zhong Y, Ge L, Chen Y, Veder J-PM, et al. Direct evidence of boosted oxygen evolution over perovskite by enhanced lattice oxygen participation. *Nat Commun*. 2020;11:2002. doi:10.1038/s41467-020-15873-x
- 34 Zhu Y, Zhou W, Yu J, Chen Y, Liu M, Shao Z. Enhancing electrocatalytic activity of perovskite oxides by tuning cation deficiency for oxygen reduction and evolution reactions. *Chem of Mater*. 2016;28(6):1691-7. doi:10.1021/acs.chemmater.5b04457
- 35 Chen C-F, King G, Dickerson RM, Papin PA, Gupta S, Kellogg WR, et al. Oxygen-deficient BaTiO_{3-x} perovskite as an efficient bifunctional oxygen electrocatalyst. *Nano Energy*. 2015;13:423-32. doi:10.1016/j.nanoen.2015.03.005
- 36 Bao J, Zhang X, Fan B, Zhang J, Zhou M, Yang W, et al. Ultrathin spinel-structured nanosheets rich in oxygen deficiencies for enhanced electrocatalytic water oxidation. *Angew Chem Int Ed*. 2015;54(25):7399-404. doi:10.1002/anie.201502226
- 37 Ji Q, Bi L, Zhang J, Cao H, Zhao XS. The role of oxygen vacancies of ABO_3 perovskite oxides in the oxygen reduction reaction. *Energy Environ Sci*. 2020;13(5):1408-28. doi:10.1039/D0EE00092B
- 38 She S, Yu J, Tang W, Zhu Y, Chen Y, Sunarso J, et al. Systematic study of oxygen evolution activity and stability on $\text{La}_{1-x}\text{Sr}_x\text{FeO}_{3-\delta}$ perovskite electrocatalysts in alkaline media. *ACS Appl Mater Interfaces*. 2018;10(14):11715-21. doi:10.1021/acsami.8b00682
- 39 Yu J, Sunarso J, Zhu Y, Xu X, Ran R, Zhou W, et al. Activity and stability of Ruddlesden–Popper-type $\text{La}_{n+1}\text{Ni}_n\text{O}_{3n+1}$ ($n=1, 2, 3$, and ∞) electrocatalysts for oxygen reduction and evolution reactions in alkaline media. *Chem Eur J*. 2016;22(8):2719-27. doi:10.1002/chem.201504279
- 40 Zhu Y, Zhou W, Zhong Y, Bu Y, Chen X, Zhong Q, et al. A perovskite nanorod as bifunctional electrocatalyst for overall water splitting. *Adv Energy Mater*. 2017;7(8):1602122. doi:10.1002/aenm.201602122
- 41 Merino NA, Barbero BP, Eloy P, Cadús LE. $\text{La}_{1-x}\text{Ca}_x\text{CoO}_3$ perovskite-type oxides: Identification of the surface oxygen species by XPS. *Appl Surf Sci*. 2006;253(3):1489-93. doi:10.1016/j.apsusc.2006.02.035

- 42 Kim H-I, Kim E-J, Kim S-J, Shin H-C. Influence of ZnO precipitation on the cycling stability of rechargeable Zn–air batteries. *J Appl Electrochem.* 2015;45(4):335-42. doi:10.1007/s10800-015-0793-4
- 43 Lee J-S, Kim ST, Cao R, Choi N-S, Liu M, Lee KT, et al. Metal-air batteries with high energy density: Li-air versus Zn-air. *Adv Energy Mater.* 2011;1(1):34-50. doi:10.1002/aenm.201000010

Every reasonable effort has been made to acknowledge the owners of copyright material. I would be pleased to hear from any copyright owner who has been omitted or incorrectly acknowledged.

Chapter 7 Conclusion and recommendations

7.1 Conclusion

After the intensive research, a series of functional transition metal oxide and sulfide materials have been developed for cathodes of Zn-ion batteries, Zn-air batteries, and hybrid Zn batteries. In different chapters, integration of Mn-based compound and Co-/Ni-based compound to establish a bifunctional or multifunctional material was investigated to take advantage of their corresponding capability for improving Faradaic cation redox or facilitating catalysis for oxygen redox, which promoted the performance of Zn-based batteries. Multiple design strategies including function-oriented composition designs, nanosizing and wettability tuning were investigated. A variety of material characterization techniques combined with electrochemical analysis were utilized to investigate material properties and to provide a better understanding of the mechanisms behind the improved results.

Overall, the aim and five objectives of this research project have been accomplished. Specifically, the advances of cathode materials for different types of Zn-based batteries were summarized as a literature review in **Chapter 2**. The results in **Chapter 3-6** well-addressed the other four objectives of this PhD project, respectively:

In **Chapter 3**, the importance of deposition amount of active Mn compound on the performance and stability of neutral/weak acidic aqueous rechargeable Zn-ion batteries was revealed and investigated. A first reported cobalt-catalyzed recovery strategy was proposed for achieving a stable performance of the Zn-ion batteries. A cobalt-modified δ -MnO₂ nanosheets material was designed and synthesized as active material which showed good performance and improved stability as cathodes for aqueous Zn-ion batteries.

The modification of the δ -MnO₂ nanosheets was extended to other transition metal cations (i.e., Co, Ni, and Fe) in **Chapter 4** for achieving bifunctional oxygen catalysis for alkaline rechargeable Zn-air batteries. Cobalt-modified MnO₂ (Co-MnO₂) demonstrated improved catalytic activity for both ORR and OER. The modification introduced an additional active site for OER and induced proper amount of oxygen defects on the MnO₂ to further promote the ORR. Zn-air batteries with Co-MnO₂ air cathodes demonstrated lower potential gap, higher round-trip efficiency and better high-rate performance compared to those of the MnO₂ without modification.

In **Chapter 5**, a greater amount of Co and Ni species (NiCo-LDH) was introduced into the MnO₂ nanosheets (proposed in **Chapter 3**) using an electrodeposition method to construct a cathode for hybrid Zn-batteries to achieve a higher power density and energy efficiency than conventional Zn-air battery. A function-separated electrode design with asymmetric wettability and asymmetric composition (MnS-Ni_xCo_{1-x}S₂) was proposed. The hydrophobic PTFE-incorporated MnS layer with modification of Ni-Co-S nanoclusters provides outstanding electrocatalytic activity for ORR/OER as an air electrode for Zn-air battery and a Ni_xCo_{1-x}S₂ layer with a hydrophilic surface acts as the cathode of Zn-MX battery. Hybrid Zn batteries with this function-separated MnS-Ni_xCo_{1-x}S₂ electrode demonstrated advantageous features of high power density, excellent round trip efficiency and good stability over 330 h.

In **Chapter 6**, a perovskite-type oxide material (La_{1.6}Sr_{0.4}MnCoO₆) which integrated Mn cation and Co cation with an atomic ordered arrangement was developed. The introduction of oxygen vacancies by partial substitution of La with Sr effectively improved catalytic activity for both ORR and OER. Zn-air batteries with the La_{1.6}Sr_{0.4}MnCoO₆ as an oxygen catalyst demonstrated a decent high-rate performance, and good cycling stability for more than 250 h in an alkaline electrolyte. Coin-type Zn-air battery with the La_{1.6}Sr_{0.4}MnCoO₆ and an alkaline gel-polymer electrolyte also presented good performance and decent stability. Further enhancement of the catalytic activity for ORR and OER and performance of Zn-air battery was achieved by increasing surface oxygen vacancy via integrating a small amount of Pt on the surface of La_{1.6}Sr_{0.4}MnCoO₆.

7.2 Recommendations

Based on the results from the research chapters, the main contributions to the research field of Zn-based batteries include:

1. A cobalt-catalyzed recovery strategy was firstly proposed for achieving a stable performance of the Mn-based cathodes for Zn-ion batteries.
2. A function-separated electrode design for hybrid Zn batteries was firstly proposed. The electrode design perfectly tackles the dilemma between electrolyte accessibility and gas accessibility in a conventional single-layer

electrode and facilitate both oxygen redox and Faradaic cation redox at the same time.

3. Three bifunctional oxygen catalysts with unique physical/chemical properties and good catalysis activity, including 1) a series of (Co-, Ni- or Fe-) modified MnO_2 , 2) a composite containing Ni-Co-S nanoclusters decorated MnS , and 3) a perovskite-type oxide cubic nanocrystallites ($\text{La}_{1.6}\text{Sr}_{0.4}\text{MnCoO}_6$), were designed for the air cathode of Zn-air batteries.

Overall, the new materials and the design strategies proposed in this thesis provide opportunities for the future development of functional transition metal compounds for Zn-based batteries and other electrochemical energy storage and conversion devices. For example, the cobalt-facilitated self-recovery proposed in **Chapter 3** may inspire the future development of novel cathode materials for other conversion-type batteries including Mn-based cathodes for Li-ion and Na-ion batteries and sulfur cathodes for Li-S and Na-S batteries. For another example, the function-separated electrode design proposed in **Chapter 5** may stimulate the development of new electrode designs that target the batteries with complicated ionic and gas transfer situation.

Although the performance and stability of cathodes are vital for Zn-based batteries, the influence of other battery components, e.g., Zn anode and electrolyte, are also important, especially for further promoting the cycling stability. Future research may focus on developing effective strategies for promoting the reversibility and durability of the Zn anode and proposing new electrolyte components/additives for suppressing side reactions, e.g., for avoiding electrochemical water splitting in a closed system (neutral Zn-ion batteries and alkaline Zn-MX batteries) or for alleviating carbon dioxide contamination in open systems (Zn-air batteries and hybrid Zn batteries).

Also, applying multiple computational methods (e.g., first-principles calculations) can obtain better understandings of the reaction process in the cathodes of Zn-based batteries. Process simulation may be helpful for designing cathode compositions and structures for further improving the mass transfer process. In addition, In situ and operando characterizations are expected to provide deeper insights. For example, in Chapter 3, although the catalysis of Mn compounds induced by the cobalt species was observed and analyzed by electrochemical evaluations and ex situ material characterizations, direct evidence of how the cobalt species facilitate the Mn

compound deposition may be obtained by advanced characterization techniques (e.g., operando TEM and NEXAFS).

Last but not the least, while the functional materials developed in this thesis demonstrated promising performance as active materials and catalysts, the particle utility of these materials in a scale-up battery is still a challenging task. Future works that focus on optimizing the electrode parameters (e.g., maximizing the mass loading, tuning the packing density of the materials) would be beneficial to obtain a scale-up battery which is closer to meet the needs of the practical utility requirements.

Appendix 1 Permission of reproduction from the copyright owner

2020/9/7

Rightslink® by Copyright Clearance Center



Home

Help

Email Support

Yijun Zhong ▾

Reversible aqueous zinc/manganese oxide energy storage from conversion reactions

SPRINGER NATURE

Author: Hulin Pan et al
 Publication: Nature Energy
 Publisher: Springer Nature
 Date: Apr 18, 2016

Copyright © 2016, Springer Nature

Order Completed

Thank you for your order.

This Agreement between Curtin University -- Yijun Zhong ("You") and Springer Nature ("Springer Nature") consists of your license details and the terms and conditions provided by Springer Nature and Copyright Clearance Center.

Your confirmation email will contain your order number for future reference.

License Number 4903440179148

[Printable Details](#)

License date Sep 07, 2020

Licensed Content

Licensed Content Publisher Springer Nature
 Licensed Content Publication Nature Energy
 Licensed Content Title Reversible aqueous zinc/manganese oxide energy storage from conversion reactions
 Licensed Content Author Hulin Pan et al
 Licensed Content Date Apr 18, 2016

Order Details

Type of Use Thesis/Dissertation academic/university or research institute
 Requestor type print and electronic
 Format figures/tables/illustrations
 Number of figures/tables/illustrations 2
 High-res required no
 Will you be translating? no
 Circulation/distribution 1 - 29
 Author of this Springer Nature content no

About Your Work

Title Development of Functional Transition Metal Oxide and Sulfide Cathodes for Aqueous Zinc-Based Rechargeable Batteries
 Institution name Curtin University
 Expected presentation date Sep 2020

Additional Data

Portions Figure 1b and Figure 3b.

Requestor Location

Requestor Location Curtin University
 Curtin University, Bentley
 Perth, Western Australia 6102
 Australia
 Attn: Curtin University

Tax Details

Price

Total 0.00 AUD

https://s100.copyright.com/AppDispatchServlet

1/2



RightsLink®



Home



Help



Email Support



Yijun Zhong ▾

A high-capacity and long-life aqueous rechargeable zinc battery using a metal oxide intercalation cathode

Author: Dipan Kundu et al
 Publication: Nature Energy
 Publisher: Springer Nature
 Date: Aug 26, 2016

Copyright © 2016, Springer Nature

Order Completed

Thank you for your order.

This Agreement between Curin University -- Yijun Zhong ("You") and Springer Nature ("Springer Nature") consists of your license details and the terms and conditions provided by Springer Nature and Copyright Clearance Center.

Your confirmation email will contain your order number for future reference.

License Number 4903440333259

[Printable Details](#)

License date Sep 07, 2020

Licensed Content

Licensed Content Publisher Springer Nature
 Licensed Content Publication Nature Energy
 Licensed Content Title A high-capacity and long-life aqueous rechargeable zinc battery using a metal oxide intercalation cathode
 Licensed Content Author Dipan Kundu et al
 Licensed Content Date Aug 26, 2016

Order Details

Type of Use Thesis/Dissertation
 Requestor type academic/university or research institute
 Format print and electronic
 Portion figures/tables/illustrations
 Number of figures/tables/illustrations 2
 High-res required no
 Will you be translating? no
 Circulation/distribution 1 - 29
 Author of this Springer Nature content no

About Your Work

Title Development of Functional Transition Metal Oxide and Sulfide Cathodes for Aqueous Zinc-Based Rechargeable Batteries
 Institution name Curtin University
 Expected presentation date Sep 2020

Additional Data

Portions Figure 1a and Figure 4d

Requestor Location

Curin University
 Curtin University, Bentley
 Requestor Location Perth, Western Australia 6102
 Australia
 Attn: Curtin University

Tax Details

Price

Total 0.00 AUD



RightsLink®



Home



Help



Email Support



Yijun Zhong ▾

Advanced zinc-air batteries based on high-performance hybrid electrocatalysts

Author: Yanguang Li et al
Publication: Nature Communications
Publisher: Springer Nature
Date: May 7, 2013

Copyright © 2013, Springer Nature

Order Completed

Thank you for your order.

This Agreement between Curtin University -- Yijun Zhong ("You") and Springer Nature ("Springer Nature") consists of your license details and the terms and conditions provided by Springer Nature and Copyright Clearance Center.

Your confirmation email will contain your order number for future reference.

License Number 4899381069671

[Printable Details](#)

License date Aug 31, 2020

Licensed Content

Licensed Content Publisher Springer Nature
Licensed Content Publication Nature Communications
Licensed Content Title Advanced zinc-air batteries based on high-performance hybrid electrocatalysts
Licensed Content Author Yanguang Li et al
Licensed Content Date May 7, 2013

Order Details

Type of Use Thesis/Dissertation
Requestor type academic/university or research institute
Format print and electronic
Portion figures/tables/illustrations
Number of figures/tables/illustrations 2
High-res required no
Will you be translating? no
Circulation/distribution 1 - 29
Author of this Springer Nature content no

About Your Work

Title Development of Functional Transition Metal Oxide and Sulfide Cathodes for Aqueous Zinc-Based Rechargeable Batteries
Institution name Curtin University
Expected presentation date Sep 2020

Additional Data

Portions Figure 1 & Figure 4.

Requestor Location

Requestor Location Curtin University
 Curtin University, Bentley
 Perth, Western Australia 6102
 Australia
 Attn: Curtin University

Tax Details

Price

Total 0.00 AUD

RightsLin[®]

Home



Help



Email Support



Yijun Zhong ▾

A Robust Hybrid Zn-Battery with Ultralong Cycle Life

Author: Bing Li, Junye Quan, Adeline Loh, et al

Publication: Nano Letters

Publisher: American Chemical Society

Date: Jan 1, 2017

Copyright © 2017, American Chemical Society

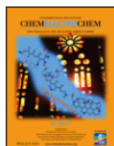
Most Trusted. Most Cited. Most Read.

PERMISSION/LICENSE IS GRANTED FOR YOUR ORDER AT NO CHARGE

This type of permission/license, instead of the standard Terms & Conditions, is sent to you because no fee is being charged for your order. Please note the following:

- Permission is granted for your request in both print and electronic formats, and translations.
- If figures and/or tables were requested, they may be adapted or used in part.
- Please print this page for your records and send a copy of it to your publisher/graduate school.
- Appropriate credit for the requested material should be given as follows: "Reprinted (adapted) with permission from (COMPLETE REFERENCE CITATION). Copyright (YEAR) American Chemical Society." Insert appropriate information in place of the capitalized words.
- One-time permission is granted only for the use specified in your request. No additional uses are granted (such as derivative works or other editions). For any other uses, please submit a new request.
- If credit is given to another source for the material you requested, permission must be obtained from that source.

[BACK](#)[CLOSE WINDOW](#)



Facilitating Oxygen Redox on Manganese Oxide Nanosheets by Tuning Active Species and Oxygen Defects for Zinc-Air Batteries

Author: Zongping Shao, Chao Su, Xiaomin Xu, et al

Publication: ChemElectroChem

Publisher: John Wiley and Sons

Date: Dec 16, 2020

© 2020 Wiley-VCH GmbH

Order Completed

Thank you for your order.

This Agreement between Curtin University -- Yijun Zhong ("You") and John Wiley and Sons ("John Wiley and Sons") consists of your license details and the terms and conditions provided by John Wiley and Sons and Copyright Clearance Center.

Your confirmation email will contain your order number for future reference.

License Number 5003641250958

[Printable Details](#)

License date Feb 07, 2021

Licensed Content

Licensed Content Publisher	John Wiley and Sons
Licensed Content Publication	ChemElectroChem
Licensed Content Title	Facilitating Oxygen Redox on Manganese Oxide Nanosheets by Tuning Active Species and Oxygen Defects for Zinc-Air Batteries
Licensed Content Author	Zongping Shao, Chao Su, Xiaomin Xu, et al
Licensed Content Date	Dec 16, 2020
Licensed Content Volume	7
Licensed Content Issue	24
Licensed Content Pages	7

Order Details

Type of use	Dissertation/Thesis
Requestor type	Author of this Wiley article
Format	Print and electronic
Portion	Full article
Will you be translating?	No

About Your Work

Title	Development of Functional Transition Metal Oxide and Sulfide Cathodes for Aqueous Zinc-Based Rechargeable Batteries
Institution name	Curtin University
Expected presentation date	Sep 2020

Additional Data



A Function-Separated Design of Electrode for Realizing High-Performance Hybrid Zinc Battery

Author: Zongping Shao, Hongwei Wu, San Ping Jiang, et al

Publication: Advanced Energy Materials

Publisher: John Wiley and Sons

Date: Nov 2, 2020

© 2020 Wiley-VCH GmbH

Order Completed

Thank you for your order.

This Agreement between Curtin University -- Yijun Zhong ("You") and John Wiley and Sons ("John Wiley and Sons") consists of your license details and the terms and conditions provided by John Wiley and Sons and Copyright Clearance Center.

Your confirmation email will contain your order number for future reference.

License Number 5003680938814

[Printable Details](#)

License date Feb 07, 2021

Licensed Content

Licensed Content Publisher	John Wiley and Sons
Licensed Content Publication	Advanced Energy Materials
Licensed Content Title	A Function-Separated Design of Electrode for Realizing High-Performance Hybrid Zinc Battery
Licensed Content Author	Zongping Shao, Hongwei Wu, San Ping Jiang, et al
Licensed Content Date	Nov 2, 2020
Licensed Content Volume	10
Licensed Content Issue	47
Licensed Content Pages	11

Order Details

Type of use	Dissertation/Thesis
Requestor type	Author of this Wiley article
Format	Print and electronic
Portion	Full article
Will you be translating?	No

About Your Work

Title	Development of Functional Transition Metal Oxide and Sulfide Cathodes for Aqueous Zinc-Based Rechargeable Batteries
Institution name	Curtin University
Expected presentation date	Sep 2020

Additional Data




Appendix 2 Co-author attribution statement

Chapter 3 is reprinted (adapted) from the below publication. The coauthor attribution statement for this paper is given in the following table.

Publication detail:

Yijun Zhong, Xiaomin Xu, Jean-Pierre Veder, Zongping Shao, Self-recovery chemistry and cobalt-catalyzed electrochemical deposition of cathode for boosting performance of aqueous zinc-ion batteries. *iScience* 2020, 23, 100943. doi:10.1016/j.isci.2020.100943

Co-author attribution statement:


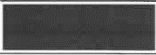


Co-author	Conception and design	Methodology and data acquisition	Data processing and analysis	Interpretation and discussion	Manuscript writing, revision and finalization	Final Approval
Xiaomin Xu				×	×	×
	I acknowledge that these represent my contribution to the above result output.				Signed.	
Jean-Pierre Veder		×	×			×
	I acknowledge that these represent my contribution to the above result output.				Signed.	
Zongping Shao	×			×	×	×
	I acknowledge that these represent my contribution to the above result output.				Signed.	

Chapter 4 is reprinted (adapted) from the below publication. The coauthor attribution statement for this paper is given in the following table.

Publication detail:

Yijun Zhong, Jie Dai, Xiaomin Xu, Chao Su, Zongping Shao, Facilitating oxygen redox on manganese oxide nanosheets by tuning active species and oxygen defects for zinc-air batteries. *ChemElectroChem* 2020, 7, 4949-4955. doi:10.1002/celec.202001419

Co-author attribution statement:

Co-author	Conception and design	Methodology and data acquisition	Data processing and analysis	Interpretation and discussion	Manuscript writing, revision and finalization	Final Approval
Jie Dai		×		×		×
	I acknowledge that these represent my contribution to the above result output.				Signed.	
Xiaomin Xu				×	×	×
	I acknowledge that these represent my contribution to the above result output.				Signed.	
Chao Su				×	×	×
	I acknowledge that these represent my contribution to the above result output.				Signed.	
Zongping Shao	×			×	×	×
	I acknowledge that these represent my contribution to the above result output.				Signed.	

Chapter 5 is reprinted (adapted) from the below publication. The coauthor attribution statement for this paper is given in the following table.

Publication detail:

Yijun Zhong, Xiaomin Xu, Pengyun Liu, Ran Ran, San Ping Jiang, Hongwei Wu, Zongping Shao, A function-separated design of electrode for realizing high-performance hybrid zinc battery. *Adv. Energy Mater.* 2020, 10, 2002992. doi:10.1002/aenm.202002992

Co-author attribution statement:

Co-author	Conception and design	Methodology and data acquisition	Data processing and analysis	Interpretation and discussion	Manuscript writing, revision and finalization	Final Approval
Xiaomin Xu				×	×	×
	I acknowledge that these represent my contribution to the above result output.				Signed.	
Pengyun Liu		×		×		×
	I acknowledge that these represent my contribution to the above result output.				Signed.	
Ran Ran				×	×	×
	I acknowledge that these represent my contribution to the above result output.				Signed.	
San Ping Jiang				×	×	×
	I acknowledge that these represent my contribution to the above result output.				Signed.	
Hongwei Wu				×	×	×
	I acknowledge that these represent my contribution to the above result output.				Signed.	
Zongping Shao	×			×	×	×
	I acknowledge that these represent my contribution to the above result output.				Signed.	